

PDF hosted at the Radboud Repository of the Radboud University Nijmegen

The following full text is a publisher's version.

For additional information about this publication click this link.

<http://hdl.handle.net/2066/114013>

Please be advised that this information was generated on 2018-11-11 and may be subject to change.

X-RAY ABSORPTION OF
TRANSITION METAL OXIDES



Frank de Groot

X-RAY ABSORPTION OF TRANSITION METAL OXIDES

Een wetenschappelijke proeve op het gebied van
de natuurwetenschappen

Proefschrift

ter verkrijging van de graad van doctor aan
de Katholieke Universiteit Nijmegen,
volgens besluit van het college van decanen
in het openbaar te verdedigen op
maandag 25 november 1991,
des namiddags om 1.30 uur precies.

door

FRANCISCUS MARTINUS FREDERIKUS DE GROOT
geboren te Eindhoven
op 10 februari 1964

Druk: Krips Repro, Meppel
1991

Promotor: Prof. Dr. J.C. Fuggle, PhD., D.Sc.

ISBN: 90-9004479-5

All mathematicians would (therefore) be intuitive if they had good sight, because they do not draw false conclusions from principles that they know And intuitive minds would be mathematical if they could adapt their sight to the unfamiliar principles of mathematics.

Pascal, *Pensées*, 512

*Voor mijn ouders
Voor Hedwig*

MOTIVATION

The electrons are ultimately responsible for all the electronic, magnetic and structural properties of a material. Ever since the discovery of quantum mechanics in the beginning of the century, extended efforts have been made to describe the electronic structure of solids. These efforts have been relatively successful in some extreme limits, especially for periodic, weakly correlated systems for which one electron approaches are effective, and also for strongly correlated systems, which show properties related to those of isolated atoms. However a large number of materials cannot be described by these extreme limits and in those cases understanding can only be achieved by a close combination of experimental studies with model calculations. Due to major technological developments the field of x-ray absorption spectroscopy, which yields new and useful data for studies of the electronic structure of solids, has recently gained in importance enormously. Some of the important experimental developments are summarized in chapter 2, but equally important have been developments in the theoretical methods made only within the last six years. When my work on this thesis started, some of the most important developments had not been applied to real systems for comparison with experiment.

In this thesis I present new investigations on a wide variety of materials in an attempt to define which theoretical models are appropriate under which circumstances and to illustrate the range of new information which can be obtained from the combination of the new theoretical and experimental possibilities. At the outset of this study various models to interpret the x-ray absorption spectral shapes were in use:

- The weakly correlated limit can be calculated in great detail by making use of one electron theories to determine the N-particle density of states. The one electron theories include band structure calculations and multiple scattering calculations. In recent years several successful attempts have been made to mimic the effect of the core hole by extending one electron density of states calculations by inclusion of an impurity with a core hole.
- For the strongly correlated limit, in particular the $3d$ and $4d$ edges of the rare earths, atomic multiplet theory has been applied. For the $2p$ and $3p$ x-ray absorption edges of the ionic $3d$ -compounds the atomic multiplets have been extended to include a cubic crystal field. Throughout this thesis extensive use is made of a crystal field multiplet program as developed by Theo Thole.

The mere possibility to study the various models in detail was stimulated enormously by the recent improvement of the soft x-ray monochromators: the DRAGON monochromator at NSLS Brookhaven reached an unprecedented resolution of about $1 : 10^4$ and a similar resolution has been obtained in an improved version of the SX700 at BESSY Berlin. I am very grateful for being given the opportunity to use both these monochromators.

The dominating interactions determining the electronic structure of weakly correlated solids are the interatomic hybridizations, or in other words the chemical bonding, which characterizes the solid as such. In the study of $3d$ transition metal oxides the key feature of the chemical bonding is the cubic crystal field. The cubic crystal field affects the $3d$ -states, which are partly filled in transition metal oxides. The main result of the cubic crystal field, which originates from the hybridization of the metal $3d$ -states with the oxygen $2p$ -states, is an overall division of the ten $3d$ -electrons in two symmetries, t_{2g} and e_g , which have different energies. The dominating interaction in strongly correlated solids are the electron repulsion effects within narrow bands, which give rise to the formation of a specific non-uniform distribution of the valence electrons in the ground state. The interplay between the cubic crystal field and the intra-atomic electron repulsion effects determines the symmetry of the ground state of a transition metal oxide.

In the final state of an x-ray absorption process additional interactions occur due to the core hole created:

- The valence electrons react to the core potential as if the core has one extra positive charge.
- The metal $2p$ core hole has a strong spin-orbit coupling which gives rise to the splitting into an L_2 and an L_3 edge and furthermore the wavefunction of the $2p$ core hole overlaps strongly with that of the $3d$ electrons which gives rise to multipole core hole interactions, hence an x-ray absorption spectrum dominated by multiplet effects.

In this thesis I will try to determine the limits of the validity as well as the utility of the available models for the description the spectral shape of metal $2p$ and oxygen $1s$ x-ray absorption of $3d$ -transition metal oxides. The validity of the respective models is closely connected with a correct description of the ground state. Ideally the models have to incorporate *all interactions* which determine the electronic structure of the ground state, as well as the specific, experiment dependent, final state. However for the utility of a model a primary objective is the derivation of useful information for other fields of research, and for this purpose the *simplicity* of the model is a prerequisite. During the work of this thesis it became clear that the crystal field multiplet model not only describes the metal $2p$ x-ray absorption spectra in great detail, but this relatively straightforward description also yields useful information such as the valency of the $3d$ -metal ion and its ground state symmetry. Consequently efforts were made to start the usage of $2p$ x-ray absorption in material oriented fields of research. Also results are reported which indicate possibilities for the use of oxygen $1s$ x-ray absorption spectra for the study of the electronic structure.

CONTENTS

Preface	i
1 Introduction	1
1.1 The electron-electron interaction	2
1.2 The electron-photon interaction	5
1.3 X-ray absorption in relation to other spectroscopies	7
2 Experimental	15
2.1 Synchrotron radiation	16
2.2 X-ray monochromators	17
2.3 Measurement conditions	20
2.4 Detection techniques	21
2.4.1 Total electron yield	23
3 Theory of the x-ray absorption spectral shapes	27
3.1 History of x-ray absorption	27
3.1.1 Atomic transitions in solids	29
3.2 The crystal field multiplet model	34
3.2.1 Atomic multiplets	34
3.2.2 The cubic crystal field	38
3.2.3 Core hole effect on the crystal field multiplet	43
3.3 Metal $2p$ x-ray absorption of $3d^0$ compounds	45
3.4 Metal $2p$ x-ray absorption of $3d$ transition metal compounds	56
3.5 Spin-orbit coupling and non-cubic symmetries	67
3.5.1 Effects of $3d$ spin-orbit coupling	68
3.5.2 Effects of non-cubic symmetries	70
3.6 Polarization dependence	72
3.6.1 Non-cubic compounds	74
3.6.2 Surfaces and adsorbates	78
3.6.3 Magnetic materials	78
3.7 Multiplets and hybridization	80
3.8 Electronic structure calculations	87
3.8.1 The Localized Spherical Wave method	88
3.8.2 LSW calculation of the density of states of SrTiO_3	90
3.8.3 Inclusion of core hole effects	96
	iii

4	The electronic structure of transition metal oxides	105
4.1	Introduction	105
4.2	Oxygen 1s edges of binary 3d-metal oxides	116
4.3	LiCo and LiMn oxides	126
4.3.1	Introduction	126
4.3.2	The cobalt 2p edges of the LiCo-oxides	128
4.3.3	The manganese 2p edges of the LiMn-oxides	132
4.3.4	The oxygen 1s edges of the LiCo-oxides	137
4.3.5	The oxygen 1s edges of the LiMn-oxides	140
4.3.6	Conclusions	141
4.4	The $\text{La}_{1-x}\text{Sr}_x\text{TMO}_3$ perovskites	144
4.4.1	The metal 2p x-ray absorption spectra	144
4.4.2	The oxygen 1s x-ray absorption spectra	151
4.4.3	Conclusions	158
4.5	Vanadium oxides	160
4.5.1	The binary vanadium oxides	160
4.5.2	The $\text{Zn}_{1-x}\text{Li}_x\text{V}_2\text{O}_4$ spinel system	164
4.5.3	The phase transition of VO_2	168
4.5.4	Conclusions for the vanadium oxides	173
4.6	Conclusions concerning the electronic structure	173
5	Applications	179
5.1	Bioinorganics	180
5.1.1	Manganese $L_{2,3}$ edges	181
5.2	Superconducting oxides	188
5.2.1	Oxygen 1s x-ray absorption of $\text{BaPb}_{1-x}\text{Bi}_x\text{O}_3$	189
5.3	Minerals	199
5.3.1	2p x-ray absorption of titanium in minerals	200
5.4	Surfaces	212
5.4.1	The calcium 2p edge of $\text{CaF}_2/\text{Si}(111)$	212
	Summary	227
	Samenvatting	229
	List of publications	231
	Acknowledgements	235
	Index: Metal 2p spectra	237
	Index: Oxygen 1s spectra	238
	Curriculum vitae	239

1. INTRODUCTION

If an x-ray enters a solid it can be absorbed and in this absorption process a core electron is excited to an empty state. If the energy of the x-ray is much larger than the binding energy of the core state the excited electron behaves like a 'free' electron in the solid. If however the x-ray energy is just enough to excite a core electron it will occupy the lowest available empty state. The probability for these edge absorption processes is large. If the x-ray energy is too small to reach an empty state no excitation can occur. Thus if the x-ray energy is varied from below the binding energy of the core state to about 100 eV above the edge, a spectrum as given in figure 1.1 is observed.

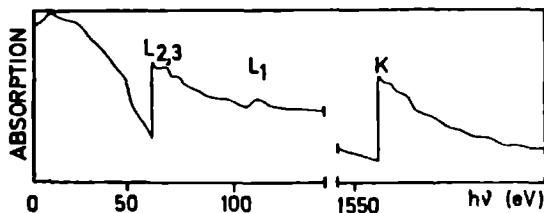


Figure 1.1: X-ray absorption edges of aluminium. The K edge corresponds to an electron excitation from the $1s$ core state. L_1 corresponds to $2s$ and $L_{2,3}$ to $2p$ core states. (Figure taken from Ref. 1).

An edge jump is followed by a slowly decaying structure, which can be related to the variations in the number of empty states which can be reached from the core state. An alternative picture to identify this structure originates from the idea that the 'free' electron, created in the absorption process at a specific site in the solid, is subject to scattering due to the core potentials of neighbouring atoms. It can be shown that both viewpoints, if worked out rigorously in their mathematical frameworks, predict equivalent x-ray absorption spectra [25]. Close to the edge the created electron has low energy and the density of states picture is more appealing but for electrons created some 50 eV or more above the edge the scattering picture is preferred because in that energy region (the so-called extended x-ray absorption fine structure, EXAFS, region) the spectrum is dominated by single-scattering events which yield useful structural information [3]. However in this thesis the emphasis will be completely on the first 30 eV of the spectrum. As a result of the experimental progress in the soft x-ray monochromators, the attainable resolution has improved to about $1 : 10^4$ [4]. This resulted in high resolution metal $2p$ and oxygen $1s$ x-ray absorption edges of $3d$ -metal compounds, which showed a large amount of structure at the edge and which thereby made a detailed analysis possible. The analysis of the high resolution spectra is a main subject of

this thesis.

Scope

Section 1.1 discusses the electron-electron interactions which are important for the electronic structure and consequently for the interpretation of the x-ray absorption results. The impact of the x-ray, that is the electron-photon interaction, is discussed in section 1.2. In chapter 2 the experimental aspects of the x-ray absorption process are discussed and chapter 3 deals with the detailed theoretical analysis of the x-ray absorption spectral shape. Chapter 4 focuses on the electronic structure of 3d-metal oxides, which because of their intermediate character in between the weakly correlated and strongly correlated limits, are as yet only partially understood. Chapter 5 gives examples of novel applications of the x-ray absorption technique to material science, mineralogy, bioinorganics and surface studies. An important subject which is left out of this thesis is the use of x-ray absorption for the study the magnetic structure of materials [5].

1.1. The electron-electron interaction

The general starting point for describing electron-electron interactions is the quantum mechanical formalism. The system is described with a wavefunction (Φ_N), which is dependent on the position of all electrons. An observable can be found by acting on the wavefunction with the corresponding operator. The eigenvalue problem of the energy operator, the Hamiltonian (\mathcal{H}), is known as the Schrödinger equation [6]:

$$\mathcal{H}\Phi_N = E_N\Phi_N \tag{1.1}$$

The most important ingredient of the quantum mechanical description of electrons is the Pauli principle, which states that the wavefunction of a system consisting of a collection of electrons must be antisymmetric for the interchange of two electrons [7]. The next step is to define the system and usually a molecule or a solid is visualized as a collection of atomic nuclei surrounded by electrons. As the mass of the proton is 1860 times that of the electron, the wavefunctions of the nuclei are decoupled from the wavefunctions of the electrons: the Born-Oppenheimer approximation [8]. The system which will be described with the wavefunction Φ is thus the collection of all electrons in a particular atom, molecule or solid with the nuclei in fixed positions.

The Hamiltonian consists of the kinetic (T) and potential (V) energy of the electrons. The potential energy includes the interactions between the electrons and the nuclei (V_N) and the electron-electron interactions (V_{ee}). Though relativistic effects are not treated explicitly, one of their consequences, the spin-orbit coupling, will prove to be essential for a proper description of x-ray absorption. Inclusion of relativistic effects results in three additional terms in the Hamiltonian [9] of which the coupling between the angular momentum and the spin ($V_{LS} \sim l_i \cdot s_i$) is essential. For many electron systems also consideration must be given to the inter-electronic couplings $l_i \cdot l_j$, $l_i \cdot s_j$, and $s_i \cdot s_j$. Though these couplings possibly can have some effect on the ground state they will be neglected throughout this thesis.

Also the coupling to the spin of the nucleus, used in nuclear magnetic resonance (NMR) techniques, will be neglected as it is too small to influence the electronic structure as far as x-ray absorption is concerned.

From these considerations the Hamiltonian to solve is:

$$\mathcal{H} = T + V_N + V_{LS} + V_{ee} \quad (1.2)$$

For a system with more than one electron the Schrödinger equation 1.1 is not exactly solvable because the V_{ee} -term in equation 1.2 is dependent on two electrons. To find the optimum numerical solution of a system with more than one electron a number of methods have been developed. Central to all is matrix calculation [10]: the wavefunction Φ is developed in a series of basis functions. For a full description of Φ an infinite series of basis functions is necessary, thus the specific choice of a certain limited basis set introduces an approximation intrinsic to matrix calculation. Important for the success of the numerical matrix methods is the variation principle which states that any approximate wavefunction Ψ will yield an energy which is larger than the ground state energy obtained with the ground state wavefunction.

single particle wavefunctions

To solve the electron-electron interactions in an atom or a solid it is useful to rewrite the many-particle wavefunction Φ in terms of single-particle wavefunctions $\phi(i)$. This problem was dealt with by Hartree who simply rewrote the wavefunction Φ as the product function of the single-particle wavefunctions [11]:

$$\Phi(1, n) = \phi(1) \cdot \phi(2) \cdot \dots \cdot \phi(n) \quad (1.3)$$

The antisymmetrization of the wavefunctions Φ was accomplished by Fock and Slater [10, 12], and the method which resulted is called Hartree-Fock. The result is that the single particle wavefunctions are described by a so-called Slater determinant, build from the chosen basis functions. As the Hamiltonian is dependent on the wavefunctions and vice-versa, the problem is solved with a self-consistent iterative procedure. The energies (ϵ_i) of these Slater determinants have in principle no physical meaning, but it is an appealing picture to identify them with the binding energy of a single electron: Koopmans' theorem states that if an electron is removed from the system, the ionization energy (E^I) is equal to (ϵ_i) under the assumption that the remaining electron wavefunctions are not modified [13].

The Hartree-Fock method does not treat electron correlations, apart from a partial effect due to the Pauli principle. The straightforward way to include the correlation effects is to form a linear combination of the Slater determinants: the configuration interaction method. This method will yield, within the chosen basis set, the correct many electron ground state energy. For a two-electron system a full configuration interaction calculation is still feasible [14], but for three or more electrons a specific subset of configurations has to be chosen.

Local potentials for atoms

An enormous simplification and reduction of the computational time can be achieved if the two-electron integrals are reduced to effective single particle integrals, or in other words if the potential V_{ee} is reduced to a local potential V_i . The simplest local potential is obtained if the original Hartree method is used [11, 15]. Instead of inclusion of the exchange by the use of Slater determinants, as in the non-local Hartree-Fock potential, a statistical exchange term can be included [16]. Because the Hartree term excludes self-interaction, self-exchange effects have to be excluded too. In further developments correlation corrections have been added [15], and the resulting Hartree plus statistical exchange method has been in the atomic multiplet calculations discussed in chapter 3. As far as atomic core level binding energies are concerned the correlation corrected Hartree plus statistical exchange calculations are superior to Hartree-Fock results as well as to the results from density functional theory [17].

Local potentials for solids

The situation for solids is far more complicated as the number of electrons is effectively infinite. Thomas considered an electron j as interacting with a spherical symmetric density distribution function, representing all other electrons [18]. Though the Thomas-Fermi potential [19, 20] gives a rather poor agreement with experiment, it is historically important as it concentrates on the electron density instead of the wavefunctions. Dirac included a statistical exchange-term into the Thomas-Fermi potential [21] and later Slater combined this statistical exchange term with the direct interaction term of the Hartree-Fock method [22]. It has been found that agreement with experiment was improved by rescaling the statistical exchange term to a value α in between 2/3 and 1: the so-called $X\alpha$ -method [23].

For solids an important step was taken when Hohenberg and Kohn introduced their density functional theorems [24, 25], which state that the ground state energy of a system can be expressed as functionals of the electron density alone. The practical implementation of the density functional theorems was greatly enhanced after Kohn and Sham introduced their local density approximation (LDA) [26], in which the energy is equal to:

$$E[n] = T_0[n] + E_H[n] + E_{zc}[n] \tag{1.4}$$

In the local density approximation both exchange and correlation are combined in a total exchange correlation potential V_{zc} . As all terms except the exchange correlation potential can be calculated exactly, this equation can be viewed as the definition of the exchange correlation potential. The former identification of the exchange potential with the Pauli principle and the correlation term with the effect of the electron under consideration on the electron density is lost. In fact the exchange correlation potential includes also part of the kinetic energy. There are several different formulations of the exchange correlation potential and also a whole range of numerical methods to solve the local density equations. (See the review of Jones and Gunnarsson and references therein [25]). The local density approximation is basically valid for weakly correlated systems, hence its limitations are more evident if correlation effects are important.

Limitations of local density calculations

In contrast to the atomic Hartree plus statistical exchange calculations with which the Slater integrals are calculated explicitly [17], the local spin density calculations do not include the effects due to the non-spherical symmetry of the wavefunctions [25, 27, 28]. These effects are important if the ground state consists of a partly filled *d* or *f* band. Recently they were included in the local spin density calculations under the heading of orbital polarization [29, 30].

A second drawback is, as discussed before, the incomplete cancelation of the self-interactions. For local spin density calculations this was studied by Perdew and Zunger [31–33]. Recently Svane and Gunnarsson performed self-interaction corrected density functional calculations for the 3*d*-metal oxides; their results yield band gaps as well as magnetic moments in close agreement with experiment [16]. The self-interaction causes problems only if the states are localized, as its limit for extended states is zero [17].

A final drawback of density functional methods is the neglect of many body effects as far as excitations are concerned. Many body calculations invoke a clever selection of the most important effects. For example in the *GW*-approach a series expansion of the screened potential *W* is used [36, 37]. The main effort of the *GW*-approach is to transform the non-observable *N*-particle density of states to an occupied *N*-1 plus an unoccupied *N*+1 description.

Model Hamiltonians

In cases which are as yet not tractable with the *ab-initio* methods of the weakly correlated limit, one has to rely on a model Hamiltonian¹ designed for the specific problem of interest. A successful model Hamiltonian for the description of the electronic structure of systems with highly correlated valence electrons has been found in the Anderson impurity model [38]. In this impurity model some dominating many body effects are included explicitly. For example for the rare earths the 4*f*-band is approximated as a set of distinct 4*f^N*-configurations which are separated by the 'Hubbard *U*' [39]. The localized ground state is then found by performing a configuration interaction calculation [40]. In the chapters 3 and 4 the Zaanen-Sawatzky-Allen (*ZSA*) model will be discussed because as yet it is the most direct model to interpret the x-ray and electron spectroscopies of the 3*d*-metal compounds [41].

1.2. The electron-photon interaction

The second basic ingredient for the analysis of x-ray absorption spectra is the interaction of electromagnetic radiation with matter. The probability for absorption of a photon is (in the dipole approximation) equal to a transition matrix element squared times a delta function

¹The usage of the term model Hamiltonian is rather arbitrary; for example the local density method uses in principle also a 'model Hamiltonian', valid for the weakly correlated limit.

describing the conservation of energy; Fermi's golden rule [43]:

$$W_{abs} = \frac{8\pi e^2 \omega^3 n}{\hbar c^3} \cdot |\langle \Phi_f | \mathbf{p}_q | \Phi_i \rangle|^2 \cdot \delta(E_f - E_i + E_{h\nu}) \quad (1.5)$$

The momentum operator \mathbf{p}_q (q accounts for the polarization degrees of freedom) can be replaced by the position operator \mathbf{r} as $[\mathbf{r}, \mathcal{H}] = (i\hbar/m) \cdot \mathbf{p}$. This replacement is correct only if the same Hamiltonian is used in initial and final states. Equation 1.5 in principle refers to a final state with infinite lifetime. If the finite lifetime is accounted for the δ -function is replaced by a Lorentzian [42].

In theoretical treatments of the x-ray absorption cross section it is customary to reformulate equation 1.5 in terms of a correlation function [40,41]. Though the golden rule notation is used throughout this thesis, the correlation function is given for convenience. The squared matrix element $|\langle \Phi_f | \mathbf{r} | \Phi_i \rangle|^2$ is rewritten as $\langle \Phi_i | \mathbf{r} | \Phi_f \rangle \cdot \langle \Phi_f | \mathbf{r} | \Phi_i \rangle$. The radial operator \mathbf{r} is rewritten in second quantization as $T = \sum_v W_v \phi_v^\dagger \phi_c$. ϕ_c annihilates a core electron and ϕ_v^\dagger creates a valence electron. The finite lifetime of the excited state (Γ) is included and the delta function $\delta(E_f - E_i + E_{h\nu})$ is rewritten as (one over π times) the imaginary part of a Green's function \mathcal{G} :

$$\mathcal{G} = \frac{1}{\mathcal{H} - E_i + E_{h\nu} - \frac{1}{2} \cdot i\Gamma} \quad (1.6)$$

After these modifications the total equation takes the shape of a correlation function:

$$W_{abs} \sim -\frac{1}{\pi} \Im \langle \phi_i | T^\dagger \mathcal{G} T | \phi_i \rangle \quad (1.7)$$

T and T^\dagger project the initial state wavefunction on a series of final states for which the Green's function is evaluated.

Selection Rules for x-ray absorption

In case of an atom the wavefunctions in equation 1.5 can be given J and M (or M_J) quantum numbers. The matrix element $\langle \phi(JM) | \mathbf{r}_q | \phi(J'M') \rangle$ can be separated into a radial and an angular part according to the Wigner-Eckart theorem [44]:

$$\langle \phi(JM) | \mathbf{r}_q | \phi(J'M') \rangle = (-1)^{J-M} \begin{pmatrix} J & 1 & J' \\ -M & q & M' \end{pmatrix} \langle \phi(J) || \mathbf{r}_q || \phi(J') \rangle \quad (1.8)$$

The triangle relations of the 3J-symbol [45] give directly the selection rules for x-ray absorption. They read as follows: because the x-ray has an angular momentum of $l_{h\nu} = +1$, conservation of angular momentum gives $\Delta l_i = +1$ or -1 ; the angular momentum of the excited electron differs by 1 from the original core state. As x-rays do not carry spin, conservation of spin gives $\Delta s_i = 0$. Given these restrictions the overall momentum quantum number cannot be changed by more than 1, thus $\Delta J = +1, 0$ or -1 , with $J + J' \geq 1$. The magnetic quantum number M is changed according to the polarization of

the x-ray, i.e. $\Delta M = q$. The x-ray absorption experiments are performed with linearly polarized synchrotron radiation (see chapter 2). Thus if the x-ray impinges on a sample under normal incidence $q = +1$ or -1 , while for grazing incidence $q = 0$. This can give rise to angular dependent x-ray absorption spectra if the sample under consideration has a non-cubic symmetry [46]. In section 3.6 these polarization dependent effects will be dealt with in more detail.

Extended final states

For extended final states (the Bloch-like wavefunctions in density functional methods) J and M are not good quantum numbers and the only selection rules are $\Delta l_i = +1$ or -1 and $\Delta s_i = 0$. Thus in case of an excitation from a $1s$ core state only p -final states can be reached and from a p core state s and d final states can be reached. The absorption cross section is reformulated as the matrix element squared times the local projected density of states [47, 48]:

$$W_{abs} \sim |\langle \Phi_{l-1} | \mathbf{r}_q | \Phi_l \rangle|^2 \cdot \mathcal{P}_{l-1} + |\langle \Phi_{l+1} | \mathbf{r}_q | \Phi_l \rangle|^2 \cdot \mathcal{P}_{l+1} \quad (1.9)$$

This approximation assumes that both the extra valence electron and the core hole do not modify the calculated density of states significantly. Thus it is assumed that $\mathcal{P}_N \approx \mathcal{P}_{N+1}$, which is a rather valid approximation for weakly correlated systems like simple metals, but which can give problems for strongly correlated narrow band systems like the $3d$ -metal oxides. Additionally it is assumed that $\mathcal{P}_N \approx \mathcal{P}_{\epsilon N}$. The complete neglect of the core hole is a rather drastic assumption, as will become evident in chapters 3 and 4.

1.3. X-ray absorption in relation to other spectroscopies

In this section the x-ray absorption technique is compared with related spectroscopies. Discussed are the relation to other photon absorption techniques, the equivalence of electron energy loss spectroscopy (EELS) and the relation to other core level spectroscopies.

X-rays versus UV, visible and IR radiation

The absorption of electromagnetic radiation is generally divided into a number of energy regions. Originally the division has been made into infrared (IR), visible (VIS) and ultra-violet (UV) radiation, on the basis of the sensitivity of the human eye. This division is still dominant, but a conceptually clearer division is to separate the electromagnetic spectrum into the kind of excitations they produce: x-rays produce core level excitations, UV/VIS light produces valence band excitations and IR radiation produces roto-vibrational excitations. Optical absorption (absorption of UV/VIS light) excites a valence state to an empty state, hence the spectral shape has to be described as the joint density of states. Because the excited electron interacts with the hole, the optical transition can generate an exciton (electron hole pair) with an energy below the bandgap.

Though the main transition in x-ray absorption is that of a core state to an unoccupied state, this by no means excludes additional vibrational effects. For example the $1s \rightarrow 2p$ x-ray absorption spectra of simple molecules like N_2 or CO have fine structure originating from vibrational effects [49, 50]. In general any low energy excitation can accompany the main excitation (if allowed for by selection rules, etc). A technique which makes specific use of optical transitions accompanying the main x-ray transition is x-ray excited optical luminescence (XEOL). After the decay of the core hole a system will in general not be back at its ground state. It is possible that an intermediate state is reached which is optically active, hence its luminescence can be measured [51].

Equivalence of x-ray absorption with EELS

It has been shown that (core level) electron energy loss spectroscopy (EELS) can result in identical spectra to x-ray absorption. In EELS the electronic transition is caused by a high energy electron, typically several hundreds of keV [52]. The spectrum is measured in transmission mode and the detector is placed at an angle Θ to the normal. For example the Karlsruhe spectrometer uses 170 keV electrons and the detector is placed at an angle of 4 mrad. Under these conditions the wave vector $|\vec{q}| \simeq q_{\perp} \simeq k\Theta$. The interaction Hamiltonian for electrons contains the term $e^{-i\vec{q}\vec{r}}$, instead of $e^{i\vec{e}\vec{p}}$ for photons. For small $|\vec{q}|$ this term can be expanded as $1 - i\vec{q}\vec{r} - (\vec{q}\vec{r})^2/2$. If the wave vector $|\vec{q}|$ is much smaller than the inverse of the core wave function mean diameter ($1/\langle R_c \rangle$), all terms except $i\vec{q}\vec{r}$ vanish and the dipole approximation retains its validity. A disadvantage of a transmission mode experiment is the necessity to use thin samples. An advantage of EELS is the possibility to modify the wave vector in order to allow for non-dipole transitions. Additionally it is possible to use an electron microscope, to allow for a spatial resolution of the order of nanometers. The present status of the detectors used in EELS makes possible a resolution of about 0.2 eV at the oxygen edge (500 eV). This is in the same order of magnitude as the presently used x-ray absorption monochromators (see chapter 2).

Core level spectroscopies

X-ray absorption excites an electron from a core state to an empty state and because the core level binding energies are specific to a certain chemical element, x-ray absorption (as well as all other core level spectroscopies) is element specific [53]. Other core level spectroscopies are x-ray photo-emission (XPS) x-ray emission (XES) and Auger electron spectroscopy (AES). Figure 1.2 sketches schematically the four core level spectroscopies.

The nomenclature of core level spectroscopies is not uniformly used. Historically the main quantum number is given a letter in alphabetic order starting with K [54]. Within this main quantum number the levels are numbered from high energy to low energy (the numbers are given either in roman or arabic). In electronic structure calculations the orbital names are used for the core states, i.e. the main quantum number n is given a number and the angular quantum number l is denoted as respectively s , p , d , f and thereafter alphabetically. For instance absorption from a $2p$ core state is called the $L_{2,3}$ edge. Table 1.1 makes a comparison of both nomenclatures.

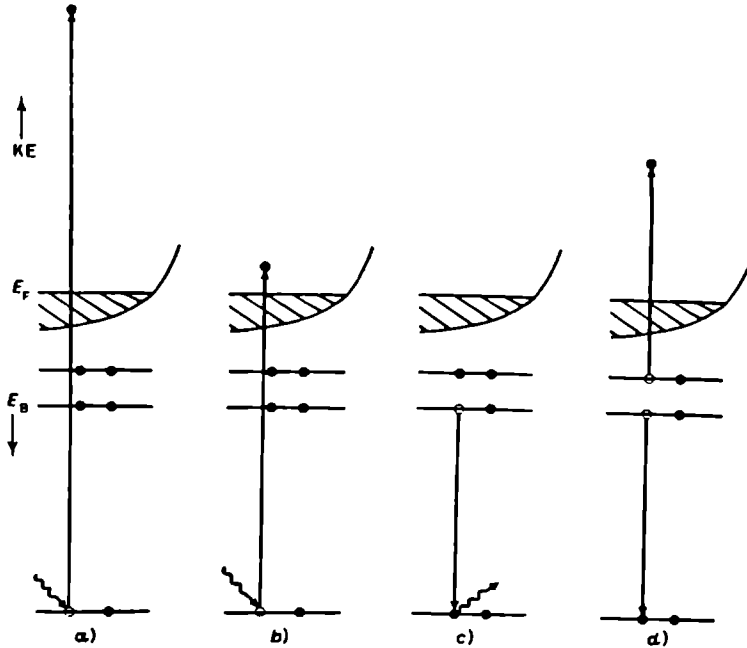


Figure 1.2: Core level spectroscopies; from left to right (a) x-ray photoemission, (b) x-ray absorption, (c) x-ray emission and (d) Auger electron spectroscopy.

Core state	Spectroscopic name
$1s$,	K
$2s, 2p$	$L_1, L_{2,3}$
$3s, 3p, 3d$	$M_1, M_{2,3}, M_{4,5}$
$4s, 4p, 4d, 4f$	$N_1, N_{2,3}, N_{4,5}, N_{6,7}$

Table 1.1: Nomenclature as used in x-ray spectroscopies.

Throughout this thesis both notations will be used. X-ray absorption and x-ray photoemission can be completely described with this notation. However as there can be many different Auger and x-ray emission decay processes, these spectroscopies need more complex identifications. The Auger process consists of three core or valence states, one in the initial state and two in its final state. An Auger process which transfers a $2p$ core electron to a $1s$ core hole with the simultaneous ejection of another $2p$ core electron is called $1s2p2p$ -Auger or alternatively $KL_{2,3}L_{2,3}$ -Auger. Valence electrons are given the symbol V in both notations, i.e. KL_1V , etc. X-ray emission processes are possible from any core state above the core

hole present, given that they are allowed to couple from symmetry arguments. In principle therefore a two core state notation could be used, i.e. $KL_{2,3}$ x-ray emission. However for historical reasons the usual notation has developed into a rather complicated set of names. For instance the transition from L_2 to K is denoted as $K\alpha$ and the transition $M_3 \rightarrow L_2$ is called $L_{II}\beta_{17}$, etc. The full table of historical notations is given in Ref. 125.

Decay spectroscopies

An important division which can be made is between spectroscopies which create excited states, like x-ray absorption and x-ray photoemission, and spectroscopies which monitor the decay of an excited state like Auger electron spectroscopy and x-ray emission spectroscopy. Neglecting finite temperature, the initial state in x-ray absorption is clearly defined as the ground state of the system. On this ground state a specific perturbation is applied, which creates a core hole and brings the system into an excited state. In contrast for Auger electron spectroscopy the initial state is in general not be a single core hole state, but a specific set of core hole states depending on the x-ray energy of the core hole creation process and the reaction of the system under consideration to the core hole creation. For instance in cases where the lowest energy core hole state does not significantly couple to the ground state the majority of states generated will consequently be of higher energy. These states can relax to the lowest ground state with the core hole present, or alternatively they can decay directly via an Auger or an x-ray emission decay process depending on the subsequent transition probabilities. For a detailed description of the decay spectroscopies these effects should be known or at least kept in mind if a specific approximation is made. For example in Auger electron spectroscopy it is often tacitly assumed that the initial state is uniquely defined, which must surely lead to errors in some cases.

Spectral functions

The ground state density of states (\mathcal{P}_N) does in itself not have any real (i.e. observable) meaning as it presents the optimized distribution of effective one particle states and the occupied states yield the correct ground state total energy of the system. For x-ray absorption the spectral function is equal to $\mathcal{P}_{\underline{c}N+1}^-$ ($- \equiv$ the unoccupied part). Under the assumption that $\mathcal{P}_{\underline{c}N+1}^- \approx \mathcal{P}_N^-$, the spectral shape is approximated with the density of states as calculated with a ground state calculation. For this assumption to be valid two conditions must be met: (1) the core hole should not influence the spectral shape and (2) the extra valence electron should not be correlated with the other valence electrons. These conditions however are in general not met for strongly correlated systems like $3d$ -metal compounds. It should be noted that the core hole and the extra valence electron are, from an electrostatic viewpoint, counteracting effects. In other words the total charge is conserved locally and consequently the disturbance on the system is not large.

The overall charge is not conserved in photoemission and inverse photoemission. Thus as can be checked in table 1.2 inverse photoemission relates to the $(N+1)$ -particle density of empty states and because the counteracting effect of the core hole is not present, the inverse photoemission spectrum will be more sensitive to correlation effects. The last column of

Spectroscopy	Spectral Function	Ground state DOS
x-ray absorption	$\mathcal{P}_{\epsilon N+1}^-$	$\approx \mathcal{P}_N^-$
inverse photoemission	\mathcal{P}_{N+1}^-	$\approx \mathcal{P}_N^-$
photoemission	\mathcal{P}_{N-1}^+	$\approx \mathcal{P}_N^+$
x-ray emission	\mathcal{P}_N^+	$= \mathcal{P}_N^+$
optical	$\mathcal{P}_{N-1}^+ \cdot \mathcal{P}_{N+1}^-$	$\approx \mathcal{P}_N^+ \cdot \mathcal{P}_N^-$
core XPS	\mathcal{P}_ϵ (relaxed)	\mathcal{P}_ϵ

Table 1.2: Spectral functions of the different spectroscopies. All spectroscopies have to be multiplied with their respective matrix elements.

table 1.2 is the spectral shape if correlation is not important as is met closest for free electron metals. Thus for free electron metals one can expect the spectral shapes to be closely related to the ground state density of states. For correlated systems this condition is not met; thus the 'amount of disagreement' between ground state density of states and the spectral shape indicates the importance of correlations in the system. Because the 'amount of disagreement' is a highly qualitative concept, model calculations are required for a quantitative discussion. From the table it is found that the XPS spectrum should correspond to a single peak, representing the core level binding energy. This makes core level XPS a good candidate to study correlation effects: if the spectrum does not correspond to a single peak some sort of correlation effect is important. Important correlation effects are, depending on the specific system, (1) multiplets, (2) charge transfer satellites, (3) electron hole pairs and (4) plasmon satellites. For x-ray absorption of 3d-metal oxides specifically multiplets and charge transfer are important, as will be discussed in chapter 3.

Resonant techniques

If the electron and photon spectroscopies discussed are combined, a whole series of novel possibilities arise. The x-ray energy can be changed through an x-ray absorption edge and for every x-ray energy the corresponding photoemission and/or Auger spectrum can be measured. Figure 1.3 sketches the energy positions of some Auger and photoemission peaks as a function of the x-ray energy. For simplicity, level splittings, correlations and core hole effects are neglected. As they resemble a core state of a specific binding energy, the photoemission peaks vary linearly with the x-ray energy. The Auger peaks have a constant kinetic energy as they relate to the energy difference between three core states, which is independent of the x-ray energy.

In the schematic example of figure 1.3 the 2p binding energy is 30 eV and the 1s binding energy is 100 eV, i.e. the 2p-photoemission peak has a kinetic energy of the x-ray energy minus 30 eV and the 1s2p2p Auger peak has a kinetic energy of 100 - 60 = 40 eV. An interesting phenomena occurs if an Auger process interferes with a photoemission process. At the x-ray energy indicated with the arrow the 2p-photoemission process ($1s^2 2p^6 V^N \rightarrow 1s^2 2p^5 V^N + e^-$) interferes with the Auger process ($1s^2 2p^6 V^N \rightarrow 1s^1 2p^6 V^{N+1} \rightarrow 1s^2 2p^5 V^N +$

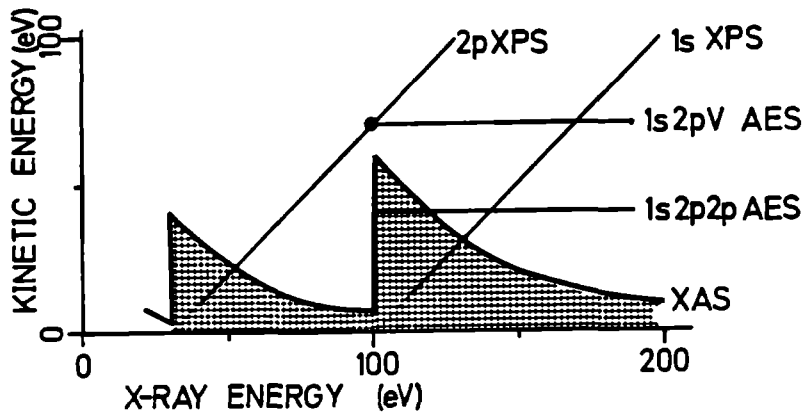


Figure 1.3: Energy dependence of Auger and photoemission peaks.

e^-). In case of resonant enhancement of valence band photoemission, information concerning the partial density of states in the valence band can be obtained [52]. If for example the valence band of CuO is measured with the x-ray energy varying through the copper 3p edge, the spectrum is clearly modified [167]. However because the overall process can be complicated the interpretation is in general not straightforward [81].

Spin polarization, x-ray polarization and angular dependence

The techniques discussed can be extended if use is made of extra degrees of freedom, for example the electron spin and the polarization of the x-ray. All electron spectroscopies can be modified to a spin-polarized version, with detection and/or creation of spin dependency. Also the x-rays can be used in a linear or circular polarized fashion, selecting only specific transitions. This can yield an overwhelming amount of extra obtainable information, specifically concerning the magnetic structure of materials [59].

Another degree of freedom is the angular variation of the material of investigation with respect to the incoming/outgoing electron/photon. For example angular resolved photoemission (ARPES) gives information concerning the \mathbf{k} -dependence of the states and from the spectral shapes an 'experimental band structure' can be obtained. X-ray diffraction (XD) gives information concerning the bulk structure whereas (low energy) electron diffraction (LEED) gives information concerning the surface structure. Photo-electron diffraction (PED) and Auger electron diffraction (AED) use an internal electron source. [60]. In this thesis the possibilities of spin polarization and diffraction are not considered. The use of the polarization of the x-ray is discussed in section 3.6 and an application concerning surfaces is discussed in section 5.4.1.

References

- [1] Jeroen Goedkoop, PhD. thesis: *X-ray dichroism of rare earth materials* (University of Nijmegen, 1989).
- [2] R. Natoli and M. Benfatto, *J. Phys. Coll.C8* **47**, 11 (1986).
- [3] *X-ray Absorption Fine Structure VI*, (*Proc. of the 6th Inter. XAFS Conf., York, 1990*), Ed. S.S. Hasnain, (Ellis Horwood, Chichester, 1991); references therein.
- [4] C.T. Chen, *Nucl. Instr. Meth. A* **256**, 595 (1987); C.T. Chen and F. Sette, *Rev. Sci. Instr.* **60**, 1616 (1989).
- [5] The study of the magnetic structure of materials with core level spectroscopies has been subject of other theses from our group: Jeroen Goedkoop, PhD. thesis: *X-ray dichroism of rare earth materials* (University of Nijmegen, 1989); Hans van Acker, PhD. thesis: *Magnetism and covalence: the electronic structure of localized perturbations* (University of Nijmegen, 1990); Harry Borsje, PhD. thesis: *Experimental investigations of surface magnetism* (University of Nijmegen, 1990); Ronald Kappert, PhD. thesis, (University of Nijmegen, to be published).
- [6] E. Schrödinger. "Quantisierung als Eigenwertproblem", I, II, III, IV: *An. der Physik* **79**, 361 (1926); *ibid.* **79**, 489 (1926); *ibid.* **80**, 437 (1926); *ibid.* **81**, 109 (1926).
- [7] W. Pauli, *Z. Physik* **31**, 765 (1925).
- [8] M. Born and J.R. Oppenheimer, *Ann. Physik* **84**, 457 (1927).
- [9] R.D. Cowan, *The Theory of Atomic Structure and Spectra*; (Univ. of California Press, Berkeley, 1981); chapter 3.
- [10] J.C. Slater, *Phys. Rev.* **34**, 1293 (1929).
- [11] D.R. Hartree, *Proc. Cam. Phil. Soc.* **24**, 111 (1928).
- [12] V. Fock, *Z. Physik* **61**, 126 (1930); *ibid.* **62**, 795 (1930); V. Fock and M.J. Petrashen, *Physik Z. Sowjetunion* **6**, 368 (1934).
- [13] T. Koopmans, *Physica* **1**, 104 (1934).
- [14] P. Wormer and F. de Groot, *J. Chem. Phys.* **90**, 2344 (1989).
- [15] Ref. 9; chapter 7.
- [16] R.D. Cowan, *Phys. Rev.* **163**, 54 (1967).
- [17] Ref. 9; chapter 8.
- [18] L.H. Thomas, *Proc. Cam. Phil. Soc.* **23**, 542 (1927).
- [19] E. Fermi, *Atti accad. Lincei* **6**, 602 (1927).
- [20] E. Fermi, *Z. Physik* **48**, 73 (1928).
- [21] P.A.M. Dirac, *Proc. Cam. Phil. Soc.* **26**, 376 (1930).
- [22] J.C. Slater, *Phys. Rev.* **81**, 385 (1951).
- [23] J.C. Slater, T.M. Wilson and J.H. Wood, *Phys. Rev.* **179**, 28 (1969).
- [24] P.C. Hohenberg and W. Kohn, *Phys. Rev.* **136**, 864 (1964).
- [25] R.O. Jones and O. Gunnarsson, *Rev. Mod. Phys.* **61** 689 (1989).
- [26] W. Kohn and L.J. Sham, *Phys. Rev.* **140**, 1133 (1965).
- [27] R.O. Jones and O. Gunnarsson, *Phys. Rev. Lett.* **55**, 107 (1985).
- [28] O. Gunnarsson and R.O. Jones, *Phys. Rev. B* **31**, 7588 (1985).
- [29] O. Eriksson, L. Nordström, A. Pohl, L. Severin, A.M. Boring and Börje Johansson, *Phys. Rev. B* **41**, 11807 (1990); O. Eriksson, Börje Johansson, R.C. Albers, A.M. Boring and M.S.S. Brooks, *Phys. Rev. B* **42**, 2707 (1990).
- [30] M.R. Norman, *Phys. Rev. Lett.* **64**, 1162 (1990); (E) 2466 (1990).
- [31] J.P. Perdew, *Chem. Phys. Lett.* **64**, 127 (1979).

- [32] A. Zunger, J.P. Perdew and G.L. Oliver, *Solid State Comm.* **34**, 933 (1980).
- [33] J.P. Perdew and A. Zunger, *Phys. Rev. B.* **23**, 5048 (1980).
- [34] A. Svane and O. Gunnarsson, *Phys. Rev. Lett* **65**, 1148 (1990).
- [35] Y. Ishii and K. Terakura, *Phys. Rev. B.* **42**, 10924 (1990).
- [36] M.S. Hybertsen and S.G. Louie, *Phys. Rev. B.* **34**, 223 (1987).
- [37] M. Godby, M. Schlüter and L.J. Sham, *Phys. Rev. B.* **37**, 1059 (1988).
- [38] P.W. Anderson *Phys. Rev.* **115**, 2 (1959).
- [39] J. Hubbard, *Proc. Roy. Soc. A.* **276**, 238 (1963); *ibid.* **277**, 237 (1964); *ibid.* **281**, 401 (1967).
- [40] O. Gunnarsson and K. Schönhammer, *Phys. Rev. B.* **28**, 4315 (1983); *ibid.* **31**, 4815 (1985).
- [41] Jan Zaanen, PhD. thesis *The electronic structure of transition metal compounds in the impurity model*, (University of Groningen, 1986).
- [42] M. Weissbluth, *Atoms and Molecules* (Academic Press, San Diego, 1978).
- [43] The golden rule is named after E. Fermi, who created its name; the inventor of the rule itself is P.A.M. Dirac.
- [44] E. Wigner *Z. Physik* **43**, 624 (1927); C. Eckart, *Rev. Mod. Phys.* **2**, 305 (1930).
- [45] E.P. Wigner in: *Quantum Theory of Angular Momentum*, Ed. L.C. Biedenharn and H. van Dam (Academic Press, New York, 1965).
- [46] C. Brouder *J. Phys. C.* **2**, 701 (1990).
- [47] L.F. Mattheis and R.E. Dietz, *Phys. Rev. B* **22**, 1663 (1980).
- [48] J.E. Müller and J.W. Wilkins, *Phys. Rev. B.* **29**, 4331 (1984).
- [49] C.T. Chen, Y. Ma and F. Sette, *Phys. Rev. A.* **40**, 6737 (1989).
- [50] M. Domke, C. Xue, A. Puschman, T. Mandel, E. Hudson, D.A. Shirley and G. Kaindl, *Chem. Phys. Lett.* **173**, 122 (1990).
- [51] J. Goulon, P.Tola, M. Lemonnier and J. Dexpert-Ghys, *Chem. Phys.* **78**, 347 (1983); C. Gauthier, I. Ascone, J. Goulon, R. Cortes, J.-M. Barbe, R. Guillard, *Chem. Phys.* **147**, 165 (1990).
- [52] J. Fink, *Recent developments in EELS*, in: *Adv. in El. and El. Phys.* (Academic Press, Orlando, 1990).
- [53] Core level spectroscopies are not unique in their element specificity; e.g. nuclear magnetic resonance (NMR) is also element specific due to the element specific nuclear spin.
- [54] The historical origin of this K, L, M nomenclature is the use of these letters by C.G. Barkla (*Phil. Mag.* **22**, 396 (1911)), who supposedly took the letters from his name. See R. Stumm von Bordwehr, *Ann. Phys. Fr.* **14**, 377 (1989).
- [55] Ref. 9; page 585, reproduced from J.A. Baerden, *Rev. Mod. Phys.* **39**, 78 (1967).
- [56] L.C. Davis, *J. Appl. Phys.* **59**, R25 (1986).
- [57] J. Ghijsen, L.H. Tjeng, J. van Elp, H. Eskes, J. Westerink, G.A. Sawatzky and M.T. Czyżyk, *Phys. Rev. B.* **41**, 5613 (1990).
- [58] J. van Elp, PhD. thesis: *The electronic structure of doped late transition metal monoxides* (University of Groningen, 1991).
- [59] R.J.H. Kappert, H.R. Borsje and J.C. Fuggle, *J. Magn. Magn. Mat.* **100**, in press.
- [60] B. Sinkovic, D.J. Friedman and C.S. Fadley, *J. Magn. Magn. Mat.* **92**, 301 (1991); B. Hermsmeier, B. Osterwalder, D.J. Friedman, B. Sinkovic, T. Tran and C.S. Fadley, *Phys. Rev. B.* **42**, 1895 (1990); references therein.

2. EXPERIMENTAL

An x-ray absorption spectrum is measured as the amount of the incoming x-ray which is absorbed by the substrate. The normal set-up to measure x-ray absorption is in transmission mode as sketched in Figure 2.1. The intensity of the x-ray is measured before and after the substrate and the percentage of transmitted x-rays is determined. The x-ray absorption spectrum is generated by repeating the experiment for a series of x-ray energies.

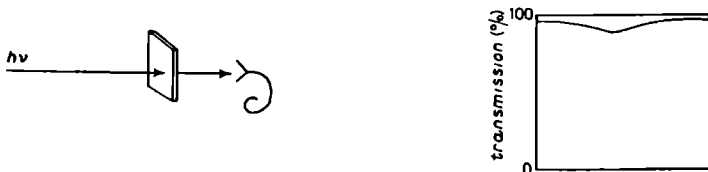


Figure 2.1: Transmission mode experiment of x-ray absorption.

Transmission mode experiments are standard for hard x-rays, though for soft x-rays they are difficult to perform because of the strong interaction of soft x-rays with matter. In order to obtain a detectable signal the substrate has to be thin, typically $\sim 0.1\mu\text{m}$. This poses a (too) large technological problem for most materials. Soft x-rays also have a large absorption cross section with air, hence the experiments have to be performed in vacuum.

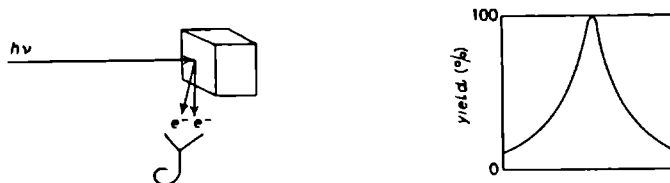


Figure 2.2: Yield-mode experiment of x-ray absorption.

An alternative to the transmission mode experiments has been provided by measuring the decay products of the core hole which is created in the absorption process. The decay of the core hole gives rise to an avalanche of electrons, photons and ions escaping from the

surface of the substrate. Figure 2.2 shows a yield mode experiment of the x-ray absorption cross section, with which it is possible to measure samples of arbitrary thickness.

X-ray absorption experiments have been made since the beginning of this century, but they were severely restricted because the only available intense x-ray sources had only a restricted set of sharply defined energies. The advent of synchrotron radiation sources, which provide an intense and continuum spectrum of electromagnetic radiation, created the possibility of improving immensely the x-ray absorption spectra. Additionally high-resolution monochromators dedicated to synchrotron radiation have been developed. In this chapter the various experimental aspects of the x-ray absorption experiments are discussed. To be discussed are:

- synchrotron radiation
- x-ray monochromators
- sample conditions
- detection techniques

2.1. Synchrotron radiation

Synchrotron radiation is produced when a charged particle, with an energy $E \gg mc^2$, is deflected in a magnetic field. The development of synchrotron radiation is based on the work of Ivanenko and Pomaranchuk [1] and Schwinger [2] in the forties [3, 4]. The original synchrotrons were used for high energy physics and the radiation was considered merely as a side product. The experiments which made use of the radiation were performed in a parasitic fashion. However the interesting results which emerged led to the development of dedicated synchrotron radiation sources in the early seventies and the SRS in Daresbury can be considered as the first dedicated storage ring for synchrotron radiation. The original emphasis was on the optimization of the life-time, the current and the energy of the beam. In the early eighties the emphasis switched to an optimization of the brilliance and also to the development of insertion devices to increase the intensity of high energy photons [4]. Figure 2.3 sketches the development of the available x-ray flux during the last century.

Most experiments for this thesis were performed at the Berliner Elektronen-speicherring Gesellschaft für Synchrotronstrahlung (BESSY) [5], which is an electron storage ring with a circumference of about 62 meters. From each of the twelve bending magnets synchrotron radiation is directed to a number of experimental stations. The energy of the electrons stored in the ring is 754 MeV and to keep the electrons in orbit they are accelerated at one point in the ring to compensate the energy-loss due to emission of radiation in the bending magnets. The position of the electrons is corrected, but nevertheless the stored current slowly decreases because of scattering with remnant gas, imperfect orbit correction, etc. The typical life-time at BESSY is two hours.

The deflection of the electrons in the bending magnets creates electromagnetic radiation with an energy-distribution as sketched in figure 2.4 [1, 2, 6]. The critical energy, E_c , is

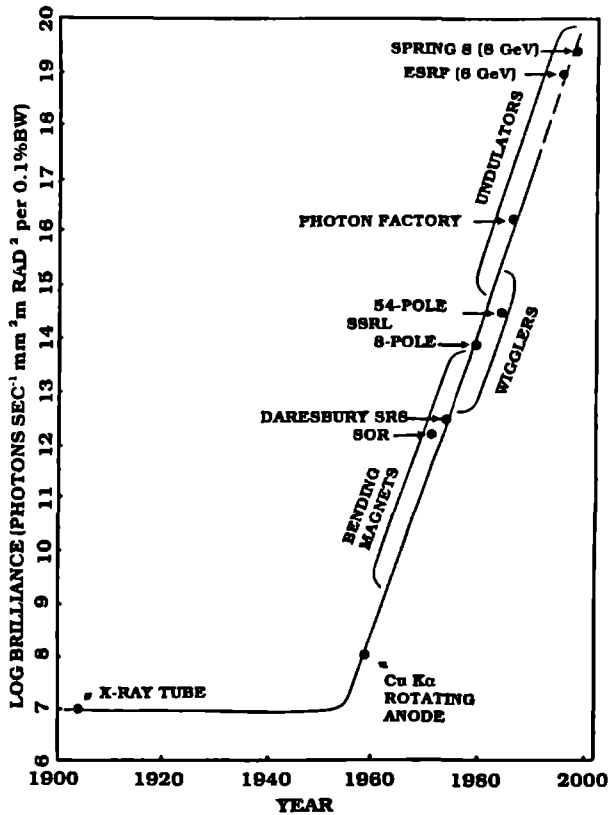


Figure 2.3: The historical development of the brilliance of the available x-ray sources. (Taken from Ref. 4).

determined by the magnetic field in the magnets and the energy of the electrons stored. For BESSY the critical energy is about 600 eV.

Figure 2.5 shows the radial distribution of the radiation for three typical x-ray energies (relative to the critical energy e_c). The radiation in the plane of the orbiting electrons is linearly polarized. Out-of-plane radiation is partly circularly polarized. By selecting part of this out-of-plane radiation, the circularly polarized x-rays can be used. However the intensity of out-of-plane radiation decreases quickly, especially for soft x-rays. The intensity of the circularly polarized x-rays can be increased with the use of special insertion devices such as asymmetric wigglers.

2.2. X-ray monochromators

In order to perform soft x-ray absorption measurements of the oxygen 1s edge and the metal 2p edges of 3d-metal oxides, it is crucial that the soft x-rays are monochromatized with high resolution. The edges of interest lie in the difficult energy range in between 200 and 1000 eV, that is in between the traditional regions of grating monochromators ($E < 200$ eV)

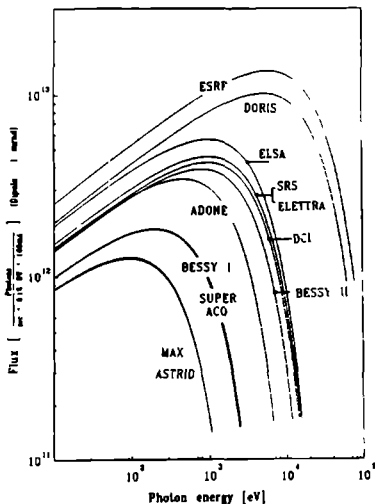


Figure 2.4: Intensity distribution of the radiation in the European synchrotron radiation facilities. ESRF, ELETTRA and BESSY II are as yet not operational. DORIS and ELSA are used parasitically. (Taken from Ref. 4).

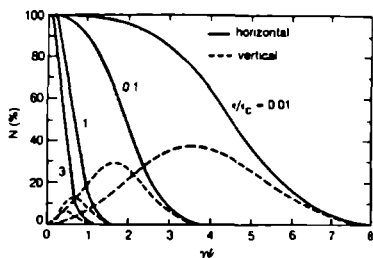


Figure 2.5: Radial distribution of intensity. $\gamma\psi$ is the angle (in mrad) with the plane of the electron-orbit.

and crystal monochromators ($E > 800$ eV).

Crystal monochromators

For energies above 800 eV the usual way to monochromatize the x-ray is by means of a double crystal monochromator. The x-ray beam impinges on the first crystal and the x-ray energy which satisfies Bragg's equation ($n\lambda = 2d\sin\theta$) is reflected. In principle one crystal is enough to monochromatize the beam; the second crystal improves the resolution by a factor of $1/\sqrt{2}$ but it is used primarily because it allows for a constant direction of the outgoing monochromatized x-ray. The energy range of the double crystal monochromator is defined by the lattice spacing of the crystals used, given that the angle of incidence (θ) is limited between 10 and 80 degrees. For energies above 2 keV artificial silicon crystals ($2d = 6.271 \text{ \AA}$) are used. The difficult energy range in between 800 and 1500 eV is covered by natural beryl crystals ($2d = 15.95 \text{ \AA}$). For energies lower than 800 eV one has to use crystals with a lattice spacing larger than beryl. The organic crystals with this property are

however not resistant to the full power of the synchrotron beam. A solution to this problem has been found by using an artificial multilayer as a pre-mono-chromator [8]. Although the double crystal monochromators with organic crystals reach a rather good resolution of about $1 : 10^3$, its development has been largely overtaken by recent developments with grating monochromators.

Grating monochromators

The monochromatizing element is in this case an artificial grating with typically 1000 lines per mm ($2d \approx 5 \cdot 10^{-7}$ meter). The soft x-ray range can be covered by using the grating monochromators in grazing incidence ($\theta \rightarrow 0$). The grazing incidence grating monochromators are divided according to the shape of the grating, which can be toroidal, plane or circular. The toroidal grating monochromators (TGM's) dominate in the energy range up to 200 eV. At present the energy region in between 200 eV and 800 eV is best served with either a plane grating monochromator like the SX700, or with a cylindrical (or spherical) grating as is present in the DRAGON.

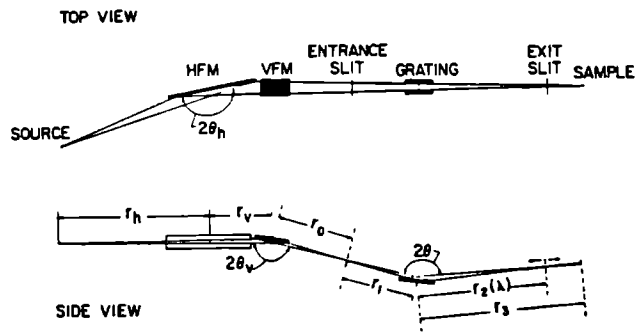


Figure 2.6: Lay-out of the DRAGON monochromator (Taken from Ref. 10).

Part of the experiments have been performed on the DRAGON monochromator [9,10] at the National Synchrotron Light Source (NSLS) at Brookhaven. The DRAGON monochromator reached an unprecedented high resolution of $1 : 10^4$ for the soft x-ray range. It is based on a novel design for a soft x-ray monochromator using cylindrical optical elements. The idea was to design a monochromator with a relatively simple arrangement of optical components [9]. Figure 2.6 sketches the lay-out of the DRAGON. The entrance slit improves the resolution by making the monochromator less dependent on the source size. The exit slit moves during an energy-scan. The mirrors are situated before the grating which facilitates the monochromator positioning to out-of-plane (circularly polarized) radiation. A design in which the beam is split in the mirrorbox and radiation from above and below the

synchrotron plane is guided to the sample simultaneously, that is using a switching device, is under construction [12].

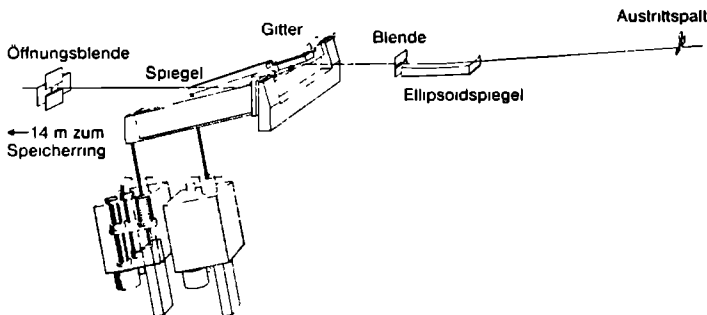


Figure 2.7: Lay-out of the SX700 monochromator. (Taken from Ref. 15).

The experiments at BESSY have been performed with the SX700 monochromators [13, 14], which were designed to monochromatize the synchrotron radiation onto a fixed exit slit, without the necessity of an entrance slit. This can be achieved by a combined movement of the plane grating and the mirrors. Figure 2.7 sketches the lay-out of the SX700. The first plane pre-mirror is used to satisfy the focusing condition of the plane grating [13]. The second ellipsoidal mirror refocuses the radiation onto the curved exit slit. The resolution is mainly source limited because there is no entrance slit. The resolution of the SX700(I) is about $1 : 10^3$ and the SX700(II) monochromator has an improved resolution of about $1 : 10^4$. A resolution of $1 : 10^4$ is at present reached by the DRAGON-like monochromators at NSLS-Brookhaven and at SSRL-Stanford [11]. The SX700-based monochromators which obtain a similar resolution can be found at BESSY-Berlin, ISA-Aarhus and MAXLAB-Lund.

2.3. Measurement conditions

All soft x-ray experiments have been performed in ultra high vacuum, with a typical pressure 10^{-10} torr. It is necessary to work under ultra high vacuum conditions to assure a clean surface because the detection (total electron yield) is rather surface sensitive. As far as the penetration of the soft x-ray is concerned it is in principle possible to perform experiments in a vacuum of 10^{-5} torr. The measured materials are single crystals or sintered polycrystalline pellets. They are scraped in vacuum with an alumina or a diamond file. For angular dependent studies on single crystals scraping cannot be used and preferably the sample should be cleaved in situ. If surface cleanliness can not be guaranteed the polarization dependent measurements on the single crystal can be performed and afterwards the sample is scraped and remeasured to check for surface contamination. If not checked for surface cleanliness, total electron yield data from unscraped samples should be treated with

extreme caution. The problems concerning surface cleanliness can be avoided by measuring in fluorescence yield (see next section).

Effects from exposure to the x-ray beam

During an x-ray absorption measurement the dose of soft x-rays which is impinging on the sample is relatively low because the experiments are performed with high resolution and only an extremely small proportion of the beam reaches the sample. Due to the high efficiency of total electron yield this is still enough to measure a spectrum in typically 15 minutes. Beam damage effects can be neglected, given that the sample is not exposed to the white light, which at the present synchrotrons has a radiation dose of typically 10^{17} photons/cm². Depending on the material this dose will cause moderate to severe damage [16]. Also charging problems are in general not crucial for x-ray absorption experiments, in contrast to XPS. However the samples should be grounded to prevent macroscopic charging effects.

2.4. Detection techniques

As sketched in figure 2.2 the absorption cross section can be measured by means of electrons which escape from the surface as a result of the decay of the core hole. Instead of electrons, also photons or ions can be detected and the electron, fluorescence and ion yield methods present an alternative to the transmission mode experiments. In this section the different methods are discussed, specifically with regard to the conditions under which a specific yield measurement represents the x-ray absorption cross section. Closely related to this is the probing depth of the specific yield method. That transmission mode experiments are indeed difficult for soft x-ray energies is clear from the analysis of the manganese $2p$ x-ray absorption spectra of MnF_2 as given by Nakai et al. [18]. They used transmission mode detection through a thin film of about 2000 Å. From comparison with theory as well as with yield experiments (see section 5.1), the spectrum given in Ref. 18 is found to be completely saturated.

Auger electron yield

The theoretically clearest yield method is a measurement of the intensity of a specific Auger decay channel of the core hole. The energy of the Auger electron is not dependent on the energy of the incoming x-ray and from the universal curve [18] it is found that the mean free path of a 500 eV Auger electron is of the order of 20 Å. Hence the number of Auger electrons emitted is equal to the number of core holes which are created in the first 20 Å from the surface. Because the mean free path of the incoming x-ray is of the order of 1000 Å, the number of core holes created in the first 20 Å is equal to the absorption cross section. Effectively the Auger electron yield method is a measurement of only 20 Å of material, hence the Auger electron yield is rather surface sensitive.

Fluorescence Yield

Instead of the Auger decay also the fluorescent decay of the core hole can be used as the basis for the absorption measurement. The amount of fluorescent decay is increased with energy [19], and a comparison of the amount of Auger decay with fluorescent decay shows that for the atomic number $Z \leq 20$ Auger decay dominates for all core levels and for $Z \leq 50$ Auger decay dominates all edges apart the K edges for which fluorescent decay starts to dominate [20]. Thus for the 3d-metals, the K edges show strong fluorescence and all other edges mainly Auger decay. The photon created in the fluorescent decay has a mean free path of the same order of magnitude as the incoming x-ray, which excludes any surface effect. On the other hand it means that there will be large saturation effects if the sample is not dilute. That is, in the limit that there is only absorption process, all x-rays photons which enter the material contribute to the fluorescence yield signal, hence its intensity will not be equal to the absorption cross section. The relation between the intensity of the fluorescence yield (I_f) and the absorption cross section (μ) is [21]:

$$I_f \sim \frac{\mu_x(E)}{\mu_x(E) + \mu_b(E) + \mu_x(E_f) + \mu_b(E_f)} \quad (2.1)$$

For dilute materials, that is if the the background absorption (μ_b) dominates the absorption of the specific edge (μ_x), the measured intensity is approximately equivalent to the absorption coefficient ($I_f \sim \mu_x$). For less dilute materials the spectral shape is modified and the highest peaks will appear compressed with respect to the lower peaks, known as saturation effects. For a given material the background absorption is known and in principle can be corrected for afterwards. However this correction procedure affects the statistics considerably. For concentrated systems, ($\mu_x > \mu_b$), the spectral modifications are too large for a sensible analysis. The $M_{4,5}$ edges of rare earths and to a lesser extend also the $L_{2,3}$ -edges of transition metals are relatively strong, hence the fluorescence yield signal will be completely saturated for the pure metals. Also the binary oxides and other compounds with low-Z elements only will show distorted x-ray absorption spectra. The oxygen K edge of metal oxides will show relatively small saturation effects, especially if some high-Z elements are present as is the case for $YBa_2Cu_3O_{7-\delta}$ and related compounds [22]. Equation 2.1 shows that apart from saturation effects, there can be effects due to so-called self-absorption. If the fluorescent decay of a core hole takes place at an energy (E_f) which is strongly reabsorbed, the spectral shape is modified in a rather complicated manner and the spectrum is difficult to interpret.

Though fluorescent yield is complicated for concentrated materials due to its large escape depth. On the other hand the large escape depth makes fluorescence yield extremely suited for the measurement of impurities, which are difficult to measure with a surface sensitive technique such as Auger yield. The suitability of fluorescence yield for impurities, for example metal ions in bioinorganic cluster compounds or even complete enzymes. has led to the large efforts in the development of fluorescence yield detectors [23].

Ion yield

A third decay product of the core holes are ions. If the absorption process takes place in the bulk and the core hole decays via an Auger process a positively charged ion is formed, but due to further decay and screening processes the original situation will be restored after some time. However if the absorption process takes place at the surface, the possibility exists that the atom which absorbs the x-ray is ionized by Auger decay and escapes from the surface before relaxation processes can bring it back to the ground state. If the escaping ions are analysed as a function of x-ray energy the signal will again be related to the absorption cross section. Because only atoms from the top-layer are measured, ion yield is extremely surface sensitive. The mere possibility of obtaining a measurable signal from ion yield means that the surface is irreversibly distorted, but as there are of the order of 10^{13} surface atoms per mm^2 , this does not necessarily mean that a statistically relevant proportion of the surface is modified. From these considerations it is clear that the possibility of ion yield will be highly material dependent. In section 5.4 ion yield is used to study the calcium atoms in the surface layer of CaF_2 .

2.4.1. Total electron yield

The most abundant yield detection technique, which is also the most unclear in its nature, is total electron yield. The difference with Auger electron yield is that the energy of the outgoing electrons is not selected and simply all escaping electrons are counted. It is clear that the signal is dominated by secondary electrons which are created in the cascade process of the Auger decay electrons [24, 25]. The ease of detection and the large signal make total electron yield a much used technique, but questions which remain are the specific processes which take place and specifically the probing depth and the related surface sensitivity are only roughly known. A rough estimate for the probing depth is to use the Auger probing depth as the lower boundary and something of the order of 200 Å as the upper boundary. As the creation, migration and escape of secondary electrons will be highly material dependent, the probing depth of total electron yield will certainly be material dependent too.

To study the mean probing depth of total electron yield quantitatively the oxygen K edge of thin layers of Ta_2O_5 on tantalum metal has been studied [26]. The tantalum oxide overlayers can be prepared with great accuracy and they are extremely stable with respect to further oxidation if the layers have a thickness of 20 Å or more [28]. The oxygen K edge of samples with a Ta_2O_5 -thickness ranging from 0 to 1200 Å have been measured. To increase the reliability of the data the spectra have been measured several times. Figure 2.8 shows the results for a layer thickness in between 20 and 80 Å. Layer thicknesses of more than 80 Å (160 Å, 320 Å, etc) give identical results to the 80 Å sample. The 10 Å layer has an intensity equal to the 20 Å layer which indicates additional oxidation.

Analysis of the data points reveals that total electron yield is already saturated for layers of the order of 40 Å, which is shorter than often assumed. It is probable that the probing depth of total electron yield is similar for the oxygen K edge of other oxides. It is concluded that the probing depth of total electron yield detection of soft x-ray absorption in oxides is of the order of 40 Å. More details concerning the processes which determine the probing

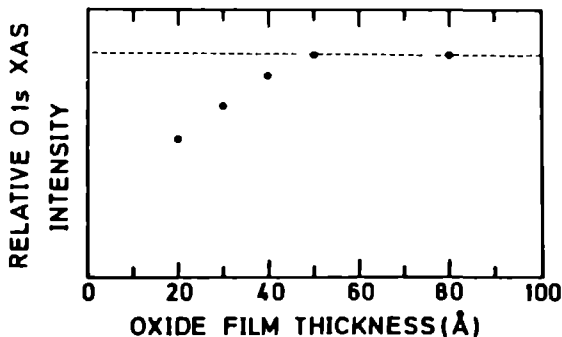


Figure 2.8: Relative oxygen K edge x-ray absorption intensity as a function of the thickness of the Ta_2O_5 layer (Taken from Ref. 26).

depth are given in Refs [24–27]. In conclusion table 2.1 gives the best estimates of the probing depths of the different yield methods if applied to 3d-metal oxides.

Detection technique	Probing depth
Ion yield	$\sim 2 \text{ \AA}$
Auger electron yield	$\sim 20 \text{ \AA}$
Total electron yield	$\sim 40 \text{ \AA}$
Fluorescence yield	$> 1000 \text{ \AA}$

Table 2.1: Probing depths of yield detection of soft x-ray absorption experiments of 3d-metal oxides

References

- [1] D. Ivanenko and J. Pomeranchuk, *Phys. Rev.* **65**, 343 (1944).
- [2] J. Schwinger, *Phys. Rev.* **70**, 798 (1946); *ibid.* **75**, 1912 (1949).
- [3] E.E. Koch, B. Kunz and B. Sonntag, *Phys. Reports* **29**, 153 (1977).
- [4] I.H. Munro, C.A. Boardman and J.C. Fuggle, *World Compendium of Synchrotron Radiation Facilities*, (European Synchrotron Radiation Society, 1991).
- [5] S. Bernstorff et al., *Physica Scripta* **36**, 15 (1987).
- [6] I.M. Ternov, V.V. Mikhailov and V.R. Khalilov, *Synchrotron Radiation and its Applications* (Harwood Academic Publishers, 1985).
- [7] Jeroen Goedkoop, PhD. thesis *X-ray dichroism of rare earth materials* (University of Nijmegen, 1989).
- [8] G van der Laan, J.B. Goedkoop and A.A. MacDowell, *J. Phys. E.* **20**, 1496, (1987).
- [9] C T. Chen, *Nucl. Instr. Meth. A.* **256**, 595 (1987).
- [10] C T Chen and F. Sette, *Rev. Sci. Instr.* **60**, 1616 (1989); C.T. Chen and F. Sette, *Physica Scripta* **T31**, 119 (1990)

-
- [11] P.A. Heimann *et al.*, *Physica Scripta* **T31**, 127 (1990).
- [12] The so-called double headed DRAGON is under construction; C.T. Chen, F. Sette and N.V. Smith, *Applied Optics* **29**, 4235 (1990).
- [13] H. Petersen, *Opt. Commun.* **40**, 402 (1982); German Patent No 30 45 931, European Patent No. 00 53 723, US Patent No. 4,553,253.
- [14] H. Petersen, *Nucl. Instrum. Meth. A* **246**, 260 (1986).
- [15] Reimund Torge, Fritz Riemer, Erich Heynacher and Wolfgang Opitz, *Zeiss Inform.* **29**, 55 (1986).
- [16] F.J. Himpsel, U.O. Karlsson, A.B. McLean, L.J. Terminello, F.M.F. de Groot, M. Abbate, J.C. Fuggle, J.A. Yarmoff, B.T. Thole and G.A. Sawatzky, *Phys. Rev. B* **43**, 6899 (1991).
- [17] S.-I. Nakai, A. Kawata, M. Ohashi, M. Kitamura, C. Sugiura, T. Mitsuishi and H. Maezawa, *Phys. Rev. B* **37**, 10895 (1988).
- [18] M.P. Seah and W.A. Dench, *Surf. Interface Anal.* **1**, 2 (1979).
- [19] P.H. Citrin, P. Eisenberger and B.M. Kincaid, *Phys. Rev. Lett.* **36**, 1346 (1976).
- [20] J.C. Fuggle, *Core Level Spectroscopies and Synchrotron Radiation*, in: *Proc. Int. School of Physics*, Ed. R. Rosei (N. Holland, Amsterdam, 1990).
- [21] J. Jaklevic, J.A. Kirby, M.P. Klein, A.S. Robertson, G.S. Brown and P. Eisenberger, *Solid State Comm.* **23**, 679 (1977).
- [22] L. Tröger, D. Arvanitis, H. Rabus, L. Wenzel and K. Baberschke, *Phys. Rev. B* **41**, 7297 (1990).
- [23] S.P. Cramer, O. Tench and G.N. George, *Nucl. Instr. Meth. A* **266**, 586 (1988); S.P. Cramer, H. Kraner, S.J. George, L. Rogers, S. Rescia, V. Radeka, M. Yocum, J. Coloresi, O. Tench and O.C. Mullins in: *X-ray Absorption Fine Structure*, Ed. S.S. Hasnain, (Ellis Horwood, Chichester, 1991): page 640.
- [24] A. Erbil, G.S. Cargill III, R. Frahm and R.F. Boehme, *Phys. Rev. B* **37**, 2450 (1988).
- [25] B.L. Henke, J. Liesegang and S.D. Smith, *Phys. Rev. B* **19**, 3004 (1979).
- [26] M. Abbate, J.B. Goedkoop, F.M.F. de Groot, M. Grioni, J.C. Fuggle, S. Hoffman, H. Petersen and M. Sacchi, submitted.
- [27] A. Krol, C.J. Sher and Y.H. Kao, *Phys. Rev. B* **42**, 3829 (1990).
- [28] J.M. Sanz and S. Hoffman, *Surf. Interface Anal.* **5**, 210 (1983).

3. THEORY OF THE X-RAY ABSORPTION SPECTRAL SHAPES

In this chapter the theory of the x-ray absorption spectral shapes is discussed. In section 3.1 a short historical account of x-ray absorption is given. The emphasis is on the strongly correlated limit; the history of the weakly correlated limit is described in detail in Ref. 1. Sections 3.2 to 3.7 describe the crystal field multiplet model, which is used to describe the metal $2p$ x-ray absorption spectra. Section 3.2 gives a theoretical introduction to the important effects: atomic multiplets, the cubic crystal field and the multipole core hole interactions. Section 3.3 contains a paper which discusses the crystal field multiplet model to explain the metal $2p$ spectra for compounds with an empty $3d$ -band and the paper in section 3.4 describes the spectra of systems with partly filled $3d$ -bands. Section 3.5 discusses the effects of the $3d$ spin-orbit coupling and distortions from cubic crystal fields, section 3.6 the effects of polarization dependence and finally in section 3.7 the limits of the crystal field multiplet model are discussed. The chapter is concluded with a section describing the weakly correlated limit with electronic structure calculations within density functional theory.

3.1. History of x-ray absorption

The historical development of x-ray absorption started almost immediately after the discovery of the x-rays by W.C. Röntgen in 1895 [2]. Some important landmarks in the development of the x-ray absorption technique are outlined with the emphasis on the use of the x-ray absorption edge structure and the manner to derive information concerning the electronic structure of solids. The discussion of the early developments is mainly based on *A History of x-ray absorption fine structure* from R. Stumm von Bordwehr [1].

X-rays and atomic energy levels

The first big step in the use of x-rays came in 1913 with Moseley's identification of the x-ray energies with Bohr's atomic energy levels [3]. In the years before it was recognized that metals emit characteristic x-rays (Sagnac, 1898 [4]). This observation was systemized by Barkla, who notified two distinct series of characteristic x-ray energies which he named K and L [5]. In 1913 Bohr developed his atomic energy level theory [6], which was directly used by Moseley who found that the x-ray energies varied with the atomic number squared [3].

From lines to spectra

The next step was the recognition of the existence of 'fine structure' in the x-ray absorption lines. In his thesis W. Stenström noted that:

This intense absorption band is followed by an emission region and then by a weak second band (W. Stenström, 1918 [7]).

This notion that the transition does not involve single lines, but can be structured was shown more convincingly for the chromium K edge by Fricke in 1920 [8]. With respect to the origins of the fine structure the notions of W. Kossel are important.

The greatest work has been done during the transition from the core to the surface, and the various paths that can still remove it from the immediate vicinity of the atom require only a small energy, [...] One is hopefully able to draw other conclusions concerning the phenomena that occur on the atom surface. This surface must depend, for instance, on the number of electrons that occupy it, i.e. on the ionization state of the atom. This is the point where the external conditions of the atom can have an influence on the Röntgen rays (W. Kossel, 1920 [1,9]).

This notion is important because if the x-ray absorption process would yield only intra-atomic information it would be of little use in the study of the electronic structure of solids. The discovery of the fine structure is therefore the first sign that the electronic structure around the 'surface of the atom', or in other words the chemical bonding, is important for the x-ray absorption fine structure. Related to this are the first observations that the valency influences the energy of the x-ray absorption edge [10]. The trends were explained by Pauling as the effect of screening from the neighbouring atoms [11].

X-ray absorption spectra of atoms

After the foundation of quantum mechanics [12,13], the explanation of the x-ray absorption spectra of hydrogen developed quickly and a detailed ab-initio picture evolved [14]. Thereafter the development of the interpretation of more complex atoms was hampered mainly by the 'mathematical' problems to describe the electron-electron interaction. If the wavefunctions of the initial state and final state configurations are determined, the calculation of the transition probability is accomplished with the application of the Wigner-Eckart theorem, with its implicit selection rules, and the calculation of the radial overlap [15].

X-ray absorption spectra of solids

The interpretation of x-ray absorption spectra in solids and the related theory of the electronic structure of solids developed much slower. An important step was taken by Kronig, who developed a scattering theory to explain the intensity modulations in the x-ray absorption spectrum [16,17]. From Kronig's theory there is an almost straightforward development to the interpretation of the extended x-ray absorption fine structure (EXAFS):

The later progress of x-ray absorption spectra calculations was to gradually free oneself from Kronig's hypotheses (C. Brouder, 1989 [18]).

An important experimental result which confirmed the importance of the crystal structure was given by Veldkamp who showed that the iron K edge of fcc-NiFe is equivalent to fcc-nickel and not bcc-iron [19]. Kronig's theory was developed further by Smoluchowski [20] who found good agreement for his 'single scattering' theory with all structures above 50 eV from the edge.

In the thirties it became evident that Kronig's scattering theory did not take into account the transition rules correctly. The overlap of the core state with the final state is more important for shallow core levels, especially if the principal quantum number is not modified. In the band structure model the transition probability is equal to the transition matrix element times the partial density of states [22, 23]. In principle this formula is still used as the basis for x-ray absorption calculations, though the original method to calculate the partial density of states has been shown to be incorrect [24]. The band structure approach developed to explain the near edge structure, with its implicit assumption of the neglect of the effects of the core hole as well as the extra valence electron as will be discussed in section 3.8. The scattering theory developed for the analysis of the EXAFS spectra and the multiple scattering formalism became the usual model for determination of the near edge structure of hard x-ray spectra [25].

3.1.1. Atomic transitions in solids

Both the band structure and the multiple scattering approaches are valid within the weakly correlated limit. Systems which are strongly correlated are not described correctly within this limit and during the years it became evident that some x-ray absorption spectra were completely dominated by the intra-atomic interactions with none or little influence from the electronic structure of the valence electrons.

The development of the strongly correlated limit, largely excluded from Ref. 1, can be traced back to the thirties, but really started with Rule's 1945 paper on the 3d ($M_{4,5}$) edge of samarium, in which he observed a subsidiary absorption maximum on the low energy side of the principal absorption [28]. He attributed this, following the ideas of Lindberg [26] and Sandström [27], to a pre-edge structure related to localized 3d to 4f transitions, while the remainder was attributed to the principal $M_{4,5}$ edge.

This division into localized 3d \rightarrow 4f transitions and the 'true' edge, was maintained in the initial studies of the Leicester group [29, 30] For example in his study on the 3d edges of praseodymium, neodymium, samarium and europium (oxides), Zandy used this division and identified the localized pre-edge peaks in all edges except the M_5 edge of europium [30]. In 1966 K.C. Williams, also from the Leicester group, recognized that the division into pre-edge and 'true' absorption edge was basically incorrect [31]. He concluded that the whole edge structure is related to the localized $3d^{10}4f^N \rightarrow 3d^94f^{N+1}$ transition:

Absorption into the 4f shell is permitted by the x-ray absorption selection rules and may be generally represented by the transition of an electron from an initial

state $3d^{10}4f^N$ to a final state $3d^94f^{N+1}$. If strict η -coupling is assumed between the $3d^9$ and $4f^{N+1}$ groups, then for Yb one transition is possible for the M_5 edge and none for the M_4 . In the case of Tm, three M_5 transitions are possible and one M_4 . This evidence seems to indicate that most of the large increase in $M_{4,5}$ absorption for these elements can be explained by attributing it to transitions into the $4f$ shell and that very little 'edge' absorption is occurring (K.C. Williams, 1966 [31]).

For the $M_{4,5}$ edge of Eu_2O_3 ($\text{Eu}^{3+}-4f^6$) Williams concludes:

For the particular case of trivalent Eu, it is possible for 107 M_5 and 79 M_4 transitions to occur into the $4f$ shell. It is scarcely surprising therefore that the absorption spectra should be banded and complex, as illustrated (K.C. Williams, 1966 [31]).

Although Williams' arguments can be considered as quite convincing the 1967 paper of Zandy [32] and the 1968 paper of Combley et al. [33] still used the original division into 'pre-edge' and main edge.

Also in 1966 high resolution x-ray absorption spectra of the $4d$ ($N_{4,5}$) edges of rare earth metals became available through the work of the Leningrad group [34, 35]. The spectra showed apart from the main absorption edge a whole series of small and extremely sharp 'pre-edge' peaks as is shown in figure 3.1. These peaks were, like the $M_{4,5}$ edges, were identified as atomic $4d$ to $4f$ transitions:

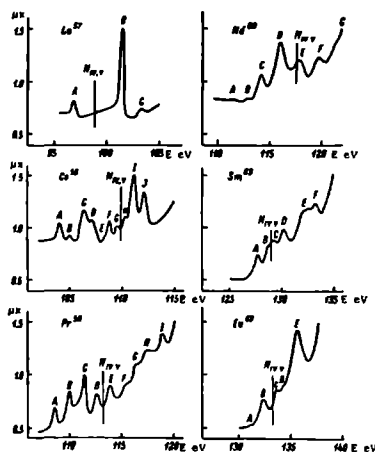


Figure 3.1: The $4d$ x-ray absorption spectrum of lanthanum, cerium, praseodymium, neodymium, samarium and europium. Taken from Fomichev et al. [35].

It is possible that the structure of the spectra corresponds to the transition of positive ions of the metals from an initial state with electronic configuration $4f^N$ to a final state $4d^94f^{N+1}$, the ions being bound in a solid state lattice. (Fomichev et al., 1966 [35]).

In 1970 the first synchrotron experiments on the $4d$ edges of the rare earths were performed by Haensel et al. [36]. They measured cerium, praseodymium and neodymium and found that for Pr and Nd the spectra of the oxides were identical to those of the pure metal, which confirmed the atomic nature of the transitions, or in other words the insensitivity of the $4d$ edge to chemical variations.

Williams' qualitative arguments for the attribution of the whole spectrum to transitions to the $4f$ states were shown to be correct in the early seventies when atomic multiplet calculations were performed in the groups of Fano and Cooper. Based on the interpretation of x-ray absorption in atoms [37], the 'atomic transitions in solids' were described in a series of papers by Dehmer, Starace, Sugar, Fano and Cooper [38–42]. The emphasis was on the rare earth $4d$ edges which are marked by a series of small, sharp peaks (see figure 3.1), followed by a strong and asymmetric absorption edge.

The basic idea was that the complete spectrum can be described as the transition from the $4f^N$ ground state to $4d^0 4f^{N+1}$ final states. The separation into the low energy and high energy part originates from the so-called centrifugal barrier [38]: the high energy states autoionize which gives them their asymmetric Fano lineshape [37], whereas for the low energy peaks autoionization is prevented by the centrifugal barrier. Therefore the low energy states are relatively stable and thus sharp. The calculations showed that the final state multiplet is dominated by the df Slater integrals and is spread over about 20 eV, whereby nearly all intensity goes to the high energy states. The calculations used the computer code of C. Froese [43] to determine the Hartree-Fock values of the Slater integrals, and the resulting dipole spectrum was in agreement with the main features of the experimental results [38]. To optimize the result the df Slater integrals were reduced to 75% and the ff Slater integrals were taken from optical experiments [44].

The success of the calculations led Dehmer et al. to the prediction that their model could be extended to the $3p$ edges of the $3d$ transition metals. Simultaneously E.J. McGuire [45] predicted strong autoionization for the $3p$ edges due to the super Coster-Kronig process $3p^5 3d^{N+1} \rightarrow 3p^6 3d^{N-1} \epsilon f$; ϵf denotes a continuum state of f -symmetry. At that time some spectra had been measured with line sources during the fifties [46] and a first set of high resolution spectra had been taken in 1969 with the DESY synchrotron by Sonntag et al. [47]. The spectra were broad and did not show a sharp edge but a rising intensity over some eV, which could be interpreted within the autoionization framework. A more detailed interpretation was not possible as the spectra were rather monotonic and did not show any pre-edge structures. The ideas concerning autoionization were developed further by Dietz et al. [48]; they were generalized by Davis and Feldkamp [49, 50] and definitively confirmed by the high resolution data on manganese atoms [51]. In the following parts emphasis is given to the multiplet structures; more information concerning the autoionization effects can be found in the review article of Davis [52].

In 1974 S.-I. Nakai et al. measured the $3p$ edges of the $3d$ -metal halides which, in contrast to the metals, showed sharp pre-edge peaks [53]. Their original interpretation was mainly bandstructure oriented and they used the distinction into localized $3p \rightarrow 3d$ transitions for the pre-peaks and a density of states interpretation for the 'main edge'. Figure 3.2 gives the results for some manganese halides. From these figures Nakai et al. conclude:

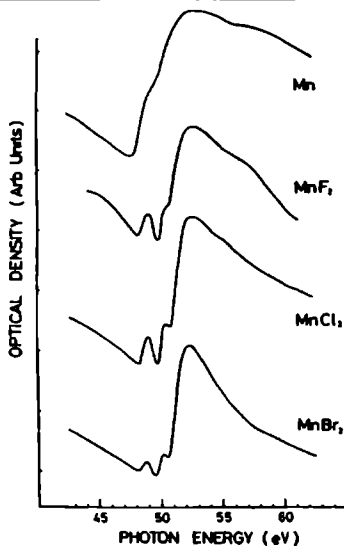


Figure 3.2: 3p x-ray absorption spectrum of manganese halides. Taken from Nakai et al. [53].

The absorption curves of MnF_2 , $MnCl_2$ and $MnBr_2$ are very similar to one another, nevertheless these halides have different crystal structures.... The detailed structures in the low energy structures may be due to the $3p^5 3d^{N+1}$ multiplet (including the crystalline field splitting). (Nakai et al.,1974, [53]).

In their 1981 paper Shin et al. present the 3d spectra of $KMnF_3$ and $KCoF_3$ [54]. The spectra shown are identical to those of the halides, but the interpretation changed:

We assign the most part of the observed $M_{2,3}$ spectra to the $3p^6 3d^N \rightarrow 3p^5 3d^{N+1}$ transitions, contrary to the propositions given for other transition metal compounds in Refs. 53, 55 (Shin et al.,1981 [54]).

The spectra were consequently calculated with a crystal field multiplet program (discussed in detail in the next sections). The multiplet approach was originally developed simultaneously in Tokyo [56–58] and Winnipeg [59, 60] to study core level photoemission spectra. Though the core level photoemission experiments were in 'good agreement with the calculations' [60, 61], the shortcomings of the approach were already indicated by Asada et al., who, following Refs. 62, 63, noted that the satellites are related to electron transfer from the ligand to the metal. In their 1976 paper, Asada and Sugano combined the multiplet model with charge transfer [64]. The hypothesis of charge transfer was shown to be correct by the calculations of Zaanen et al. who, using an Anderson impurity model, could explain all divalent nickel-halide spectra consistently [65]. For x-ray absorption the crystal field multiplet approach proved to be better suited (see section 3.2): Shin et al. neglected all states but the Hund's rule ground state and calculated the multiplet spectrum, neglecting also the 3d spin-orbit coupling. The 3d3d interactions were taken from experiment and the 3p3d multipole interactions were taken from atomic spectra but were reduced to approximately 60% [66]. The analysis was developed further in Ref. 67, 68. Figure 3.3 is reproduced from

Ref. 68 and shows the spectral variations with changes in the cubic crystal field, from which it can be concluded that the spectral variations are not large and, given the uncertainties in the atomic parameters, it is difficult to use the $3p$ spectra for a detailed optimisation of the cubic crystal field value. However the calculations convincingly explain the spectral variations. The asymmetric lineshape of the high energy lines was explained qualitatively as autoionization [37, 52].

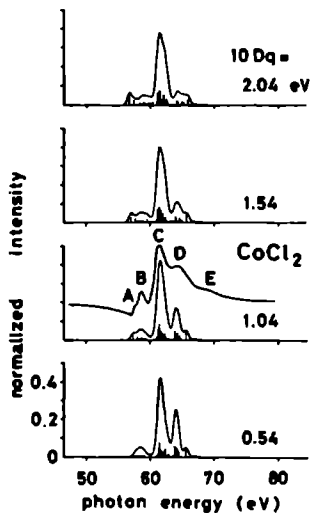


Figure 3.3: Cubic crystal field calculation for divalent cobalt. Taken from Shin et al. [68].

The calculations were generalized for all transition metal ions and for the $2p$ x-ray absorption as well as $2p$ XPS by Yamaguchi et al. [69, 41]. In 1985 Thole et al. calculated all $4f^N \rightarrow 3d^9 4f^{N+1}$ transitions for the divalent and trivalent rare earth ions [71], using Cowan's atomic Hartree-Fock program [15, 72]. Basically the calculations are equivalent to those performed by the groups of Fano and Cooper in the early seventies [38–41], but the improvement in computers made it possible to calculate a general $3d^9 4f^{N+1}$ multiplet in intermediate coupling, making use of (scaled) Hartree-Fock calculated Slater integrals and spin-orbit couplings. The agreement with experiments on rare earth metals convincingly confirmed the basic correctness of the method [71]. The atomic multiplet method was also used for the calculation of the $3d^5 \rightarrow 2p^5 3d^6$ multiplet to simulate spectra of manganese impurities in noble metals [73]. Again a basic agreement was found and the ground state could be identified as the Hund's rule ground state. The method was extended by B.T. Thole to include crystal field effects. The output of the atomic multiplet program was connected with the general group theoretical program of Butler [53]. The method is similar to the one used by Yamaguchi et al. [69, 41], but it is made more general as $3d$ spin-orbit coupling can be included and the group theoretical projection can be made to any point group of interest. The first results of the method were given in Refs. 75, 76.

3.2. The crystal field multiplet model

In this section the basic ingredients of the crystal field multiplet model are discussed. Sections 3.3 and 3.4 are reproductions of papers on the results of the calculations with a cubic crystal field. Limitations and extensions of the model are discussed in section 3.5 to 3.7.

3.2.1. Atomic multiplets

The general starting point for the strongly correlated limit is the atomic multiplet theory which describes the correlated electronic states in partly filled atomic shells. A single $3d$ electron has ten possibilities, respectively spin-up and spin-down states with m_l ranging from -2 to 2. The overall quantum numbers L and S of a $3d^1$ configuration are 2 and $\frac{1}{2}$. The total J quantum number has two possibilities, respectively $\frac{3}{2}$ ($L-S$) and $\frac{5}{2}$ ($L+S$). In term symbol notation, representing irreducible representations in spherical symmetry: ${}^{2S+1}L_J = {}^2D_{\frac{5}{2}}$ and ${}^2D_{\frac{3}{2}}$. LS-coupling is a correct description for the valence electron couplings of the light elements because the $3d$ spin-orbit coupling is rather small [77]. Thus the spin and angular momenta of the $3d$ -electrons are first coupled to an overall L and S . In pure LS-coupling the 45 combinations of a $3d^2$ -configuration are grouped in the term symbols 1G , 3F , 1D , 3P and 1S . If jj-coupling is considered as a small perturbation the irreducible representations are indicated by their general ${}^{2S+1}L_J$ term symbol, i.e. 1G_4 , 3F_4 , 3F_3 , 3F_2 , 1D_2 , 3P_2 , 3P_1 , 3P_0 and 1S_0 . However if the jj-coupling becomes more dominant this term symbol notation loses its meaning as the states with equal J 's start to mix and the states have to be described as linear combinations of term symbols. Finally in pure jj-couplings only 5 irreducible representations remain, distinguishable by their J -value only. The 'transition' from LS to jj coupling is indicated in figure 3.4.

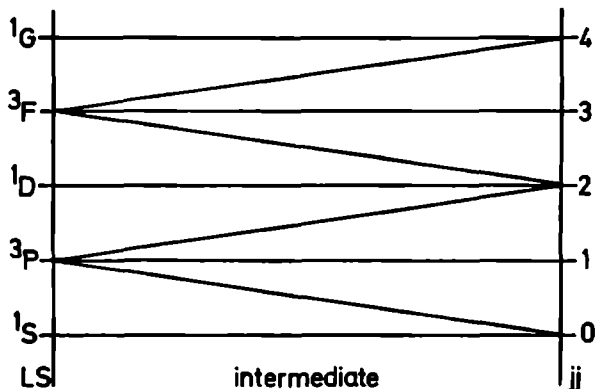


Figure 3.4: $LS \rightarrow jj$ transition for $3d^2$. In table 3.2 the physical ordering for LS-coupling is given.

If a $3d^3$ -configuration is coupled according to LS-coupling there are 120 configurations divided over the term symbols: 4F , 4P , 2H , 2G , 2F , 2D (2 times) and 2P . The main problem to solve is to find the wavefunctions of these term symbols. One way to proceed is

to couple first two electrons to $|d^2\mathbf{LS}\rangle$ and subsequently couple this with the third electron. From symmetry arguments and recoupling formulae it can be shown [15] that the overall wavefunction $|d^3\mathbf{L}'\mathbf{S}'\rangle$ can be formed by a summation over all LS combinations of the two-electron wave functions multiplied by a specific coefficient:

$$|d^3\mathbf{L}'\mathbf{S}'\rangle = \sum_{\mathbf{L},\mathbf{S}} |d^2\mathbf{LS}\rangle \cdot c_{\mathbf{LS}} \quad (3.1)$$

For example the quartet F state of $3d^3$ is built from its parent triplet states as:

$$|d^3[{}^4F]\rangle = \frac{4}{5}|d^2[{}^3F]\rangle - \frac{1}{5}|d^2[{}^3P]\rangle \quad (3.2)$$

Similarly all other $3d^3$ states can be built. They are denoted as $(d^2LS\{\}\alpha LS)$ and are called *Coefficients of Fractional Parentage*, because the $3d^2$ -states can be considered as the 'parents' of the $3d^3$ -states. The coefficients for all partly filled d and f states are tabulated by Nielsen and Koster [78].

Core hole effect on atomic multiplets

Up to now only partly filled $3d$ -states were considered. In the final state of the metal $2p$ x-ray absorption process a $2p^53d^{N+1}$ configuration is formed. As the dominant interaction is the core hole spin-orbit coupling, the actual coupling scheme is given as jj-coupling for the core hole and LS-coupling for the valence electrons. The overall coupling scheme is a mixture of both. The simplest $2p3d$ coupling is the $2p^53d^1$ state. The configurations are found from multiplying (the symmetries of) the $2p^5$ state with the $3d^1$ state.

$${}^2P \otimes {}^2D = {}^1P_1 + {}^1D_2 + {}^1F_3 + {}^3P_{0,1,2} + {}^3D_{1,2,3} + {}^3F_{2,3,4} \quad (3.3)$$

Figure 3.5 sketches the transition from pure LS to jj coupling for the pd -multiplet. For configurations with two or more $3d$ electrons (and the $2p$ core hole) the intermediate coupling scheme makes a term symbol assignment of the states inappropriate.

In section 1.2 it was discussed that for x-ray induced transitions the dipole selection rules are applicable, i.e. $\Delta L = \pm 1$, $\Delta S = 0$ and $\Delta J = \pm 1, 0$ with $J + J' \geq 1$. Therefore in LS-coupling the transition from $3d^0 \rightarrow 2p^53d^1$ is a non-degenerate single line, because the the dipole selection rules allow only a 1P final state. In jj-coupling the selection rules yield a (threefold degenerate) $J = 1$ final state; in the actual intermediate coupling scheme three states exist. In figure 3.5 it is shown that the degeneracy of the $J = 1$ is lifted. The actual states are described as linear combinations of the 1P_1 , 3P_1 and 3D_1 term symbols.

Slater integrals, Racah parameters and Hund's rules

The origin of the term splittings can be found in the electron-electron interactions and the spin-orbit coupling. The usual method of determining the 2-electron integrals is by

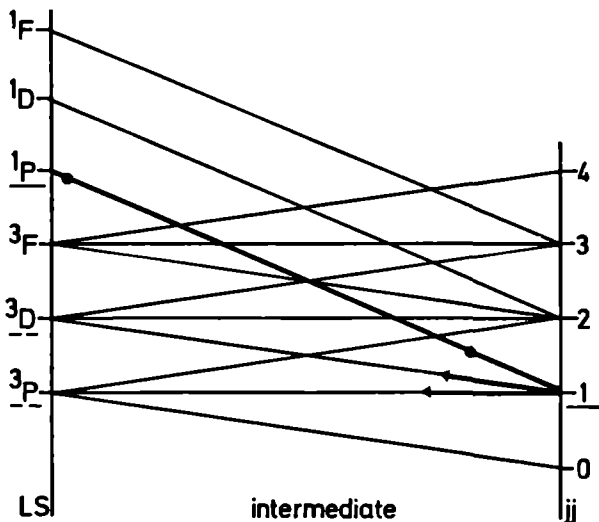


Figure 3.5: $LS \rightarrow jj$ transition for $2p^5 3d^1$. In LS-coupling only the 1P_1 -state can be reached, but in intermediate coupling there is admixture of the 1P_1 -state with the 3P_1 -state and the 3D_1 -state.

expanding them as a series of Legendre polynomials [15, 79, 12]. The radial part reduces to the integrals:

$$R^k(ab, cd) = \int_{r_1} \int_{r_2} \frac{r_{<}^k}{r_{>}^{k+1}} \cdot P_1(a)P_2(b)P_1(c)P_2(d) dr_1 dr_2 \quad (3.4)$$

It is common practice to divide the radial integrals in Coulomb terms and exchange terms. The Coulomb terms are denoted as $F^k(ab, ab) \Rightarrow F^k(a, b)$ and the exchange terms as $G^k(ab, ba) \Rightarrow G^k(a, b)$, the so-called Slater integrals. The angular part composes strong selection rules on the k -values in the series expansion, i.e. for two $3d$ -electrons only F^0 , F^2 and F^4 are possible and for a pd -interaction F^0 , F^2 , G^1 and G^3 have to be considered. Instead of the F^k , G^k superscript notation two alternative notations are used: in the subscript F_k notation the F^k Slater integrals are renormalised with a common k -dependent denominator D_k [79]. Another common notation for dd -interactions are the Racah parameters A, B and C. Table 3.1 gives their relation to the Slater integrals.

The effect of the electron-electron interaction on the $3d^2$ configuration is that the term symbols have the relative energies as given in table 3.3. The energy positions in this table reveal that the ground state of the $3d^2$ configuration is the 3F state, which is an example of the rule that for a general $3d^N$ configuration the ground state is always the state with highest S, and for these states the state with the highest L: *Hund's rules* [82]. The Hund's rules are a direct consequence of the multipole dd -interaction described with the Slater integrals: S (and L) are maximized because the electron-electron repulsion is minimized if the electrons belong to different m_l -orbitals and also because electrons with parallel spin have an additional exchange interaction which lowers the total energy. If the 3F -state is split due to $3d$ spin-orbit coupling the ground state is, according to Hund's third rule, the state with the lowest J (the 3F_2 -state); in case more than five $3d$ -electrons are present, the highest J-value has lowest energy. Notice that the Hund's rules do not explain the ordering

Racah	Slater	Integrals
A	=	$F^0 - F^4/9$
B	=	$(9F^2 - 5F^4)/441$
C	=	$5F^4/63$

Table 3.1: Relation of Slater integrals with Racah parameters for 3d-electrons

Symmetry	Relative energy	
$E(^1S)$	$14B + 7C$	+4.2 eV
$E(^1D)$	$-3B + 2C$	+0.5 eV
$E(^1G)$	$+4B + 2C$	+1.2 eV
$E(^3P)$	$+7B$	+0.7 eV
$E(^3F)$	$-7B$	-0.8 eV

Table 3.2: Relative energy positions of a $3d^2$ configuration. For the values in the third column the representative values $B=0.1$ eV and $C=0.4$ eV are used.

of the states, but only the symmetry of the ground state. In the final state of the metal $2p$ x-ray absorption process the dominant interaction is the core hole spin-orbit coupling (ξ_{2p}). Its magnitude ranges from about 3 eV for titanium to about 10 eV for nickel. If only this spin-orbit coupling is considered the $2p$ spectra are split in two, the L_3 and the L_2 edge, separated by $\frac{3}{2} \cdot \xi_{2p}$. The pd Coulomb and exchange terms, F_{pd}^2 , G_{pd}^1 and G_{pd}^3 , are of the order of 5 to 10 eV and from table 3.3 it can be seen that the dd -interactions cause splittings of the order of 5 eV. The combination of the core hole spin-orbit interaction and the $3d3d$ and $2p3d$ electron-electron interactions gives for the general case of a $2p^53d^N$ configuration a complex distribution of states. The $3d$ spin-orbit coupling is small and possible effects are discussed in section 3.5.

The specific values of the pd -Slater integrals and the $2p$ spin-orbit coupling give the atomic multiplet spectrum of the $3d^0 \rightarrow 2p^53d^1$ transition two intense lines with an additional small 'pre-edge' peak (see section 3.4). The atomic multiplet for $3p$ x-ray absorption is described with exactly the same coupling scheme. However because the $3p$ spin-orbit coupling is relatively small and the $3p3d$ Slater integrals large, the coupling scheme is almost pure LS and more than 99% of the transition goes to the final state of 1P -symmetry¹.

¹The energy of the 1P -state is about 10 eV above the lowest state, and this is the origin of the 'delayed onset' in $3p$ resonant photoemission experiments.

3.2.2. The cubic crystal field

Atomic multiplet theory can be extended to describe the 3d-metal ions by incorporation of the dominating cubic crystal field. As an introduction first the cubic crystal field, which is the central phenomenon in describing the electronic structure of 3d transition metal ions [12, 44], is introduced:

In an octahedral environment the potential of the central ion has cubic (O_h) symmetry which divides the 5-fold degenerate 3d-orbitals into two distinct representations of T_{2g} and E_g symmetry. The twofold degenerate E_g state contains orbitals which point towards the center of the cube faces, that is directly towards the position of the ligands. Consequently they interact stronger, electrostatically as well as covalently, with the ligands. The three t_{2g} orbitals point towards the corners of the cube and therefore their interaction with the octahedral ligands is considerably lower. The five 3d electron-pairs, ($|JM_J\rangle =$) $|20\rangle$, $|\bar{1}0\rangle$, $|00\rangle$, $|10\rangle$ and $|20\rangle$, are regrouped by a cubic crystal field as indicated in table 3.3.

representation	orbital name	atomic states	Cartesian notation
E_g	d_{z^2}	$ 20\rangle$	$\frac{1}{2}(3z^2 - r^2)$
	$d_{x^2-y^2}$	$\frac{1}{\sqrt{2}} 2\bar{2}\rangle + \frac{1}{\sqrt{2}} 22\rangle$	$\frac{\sqrt{3}}{2}(x^2 - y^2)$
T_{2g}	d_{xy}	$\frac{1}{\sqrt{2}} 2\bar{2}\rangle - \frac{1}{\sqrt{2}} 22\rangle$	$\sqrt{3}(xy)$
	d_{yz}	$\frac{1}{\sqrt{2}} 2\bar{1}\rangle + \frac{1}{\sqrt{2}} 21\rangle$	$\sqrt{3}(yz)$
	d_{zx}	$\frac{1}{\sqrt{2}} 2\bar{1}\rangle - \frac{1}{\sqrt{2}} 21\rangle$	$\sqrt{3}(zx)$

Table 3.3: Effect of a cubic crystal field on a 3d electron

In the following the effects of the cubic crystal field on the electronic structure of a partly filled 3d-band are considered. For this purpose two models are used:

- A simplified 'spin dependent molecular orbital' model which accounts only for the effects of the cubic crystal field on the Hund's rule ground state and therefore can be viewed as an effective single particle model.
- A more complete crystal field multiplet model which takes both atomic multiplets as well as the cubic crystal field into account.

The molecular orbital model can be described with two parameters, the cubic crystal field strength ($10Dq$ or \mathcal{D}) and an effective exchange splitting \mathcal{K} which gives the energy gain of two parallel spins. Henceforth this model is called the \mathcal{DK} -model; it allows for a direct qualitative assignment of the peaks in the observed oxygen 1s x-ray absorption spectra. In the crystal field multiplet model the atomic symmetries are projected to cubic symmetry. Table 3.4 gives the projection rules for cubic symmetry.

Spherical	Cubic
<i>S</i>	A_1
<i>P</i>	T_1
<i>D</i>	$E + T_2$
<i>F</i>	$A_2 + T_1 + T_2$
<i>G</i>	$A_1 + T_1 + T_2 + E$
<i>H</i>	$T_1 + T_1 + T_2 + E$
<i>I</i>	$A_1 + A_2 + T_1 + T_1 + T_2 + E$

Table 3.4: The $SO_3 \rightarrow O_h$ Branching rules in the Schönflies notation.

The $3d^0$ to $3d^3$ configurations

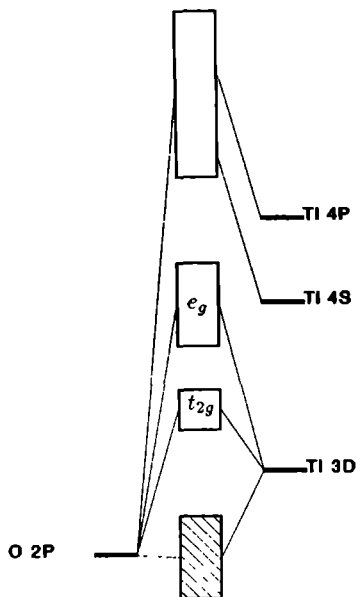


Figure 3.6: Schematic N-particle density of states of TiO_2 , based on a molecular orbital description. The oxygen $2p$ -band is filled and the empty $3d$ -band is split into a t_{2g} and an e_g sub-band.

A system with a $3d^0$ configuration, like TiO_2 or CaF_2 , has an electronic configuration with only completely filled or completely empty bands. Figure 3.6 sketches a simplified density of states picture of a $3d^0$ compound. The narrow $3d$ -band is situated in between the filled

oxygen $2p$ -band and the empty metal $4sp$ band. The $3d$ -band is split in two and the t_{2g} sub-band is positioned at lower energy and is considerably sharper (less interaction) than the e_g sub-band. The filled oxygen $2p$ -band contains a considerable amount of metal $3d$ -character and correspondingly the empty $3d$ -band contains states of oxygen $2p$ -character. For example the band structure calculation of SrTiO_3 yields a titanium $3d$ occupation of 1.5 electrons (see section 3.8). The electron addition spectrum of a $3d^0$ compound shows respectively a t_{2g} -peak, an e_g -peak and a structure related to the $4sp$ -band. In the final state there is only one electron in the $3d$ -band, hence no multipole correlation effects.

A $3d^1$ configuration has a ground state of 2T_2 -symmetry and the electron addition spectrum (in the DK -model) contains four peaks related to the filling of respectively a t_{2g}^+ , t_{2g}^- , e_g^+ or e_g^- orbital. The splitting between the t_{2g}^+ and the e_g^+ state is equal to the cubic crystal field strength (\mathcal{D}), and the splitting between the t_{2g}^+ and the t_{2g}^- state is equal to \mathcal{K} . The exchange interactions are slightly different for respectively t_{2g} and e_g electrons. The exchange interactions are taken from Ref. 83 and a calculation for the atomic Slater integrals of Mn^{IV} shows that $\mathcal{K}_{ee} \approx 1.05$ eV, $\mathcal{K}_{tt} \approx 0.92$ eV and $\mathcal{K}_{et} \approx 0.79$ eV. For trivalent and divalent manganese the values are slightly lower. Figure 3.7 sketches the energy situation (in the final state) of a $3d^1$ ground state.

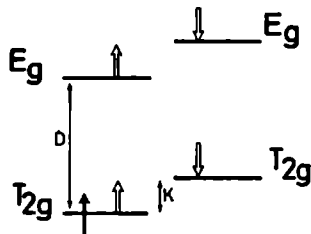


Figure 3.7: The DK -model for a $3d^1$ -configuration

In the crystal field multiplet model the electron addition spectrum consists of all atomic multiplets split by the cubic crystal field: the 3F -state splits into 3T_1 , 3T_2 and 3A_2 , the 3P -state to 3T_1 . The energy positions are determined by the Slater integrals and the cubic crystal field. The difference between the models is that the DK -model effectively neglects the Slater integrals apart from the energy difference between singlet and triplet states and as a consequence only states are considered which contain at least one t_{2g}^+ electron, as other states do not couple to the ground state under neglect of the Slater integrals. A $3d^2$ -configuration contains two (t_{2g}^+) electrons and its symmetry is 3T_1 . That is the 3F ground state splits in three (3T_1 , 3T_2 and 3A_2), of which 3T_1 has the lowest energy. As the 3P -state also projects onto a 3T_1 -state, the actual 3T_1 ground state is a combination of the two states of this character [12]. Figure 3.8 shows the effect of increasing cubic crystal field, the so-called Tanabe-Sugano diagram, for $3d^2$. Electron addition in the DK -model gives four peaks at the energies 0, \mathcal{D} , $2\mathcal{K}$ and $\mathcal{D} + 2\mathcal{K}$. For \mathcal{K} the value for \mathcal{K}_{te} are used. In the crystal field multiplet model the electron addition states relate again to all $3d^3$ states, which can couple to the ground state of the $3d^2$ -state with the addition of a $3d$ -electron. A $3d^3$ -configuration contains three (t_{2g}^+) electrons which form a ground state of 4A_2 -symmetry. Electron addition in the DK -model gives only three peaks as the t_{2g}^+ -state is full.

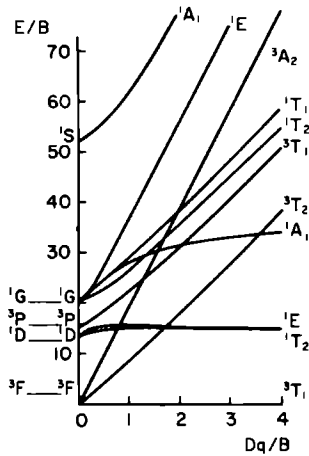


Figure 3.8: Tanabe Sugano diagram for a $3d^2$ ground state in cubic symmetry. Taken from Ref. 44.

High-spin versus low-spin

If four electrons have to be accommodated in the five $3d$ -orbitals in an octahedral surrounding, two different situations can occur. If $3\mathcal{K}_{(te)} > \mathcal{D}$, a high spin $(t_{2g}^+)^3(e_g^+)^1$ -configuration with 5E -symmetry is formed from the Hund's rule 5D ground state. If however $3\mathcal{K} < \mathcal{D}$, a low spin $(t_{2g}^+)^3(t_{2g}^-)^1$ -configuration with 3T_1 -symmetry, originating from five atomic triplet states, is formed [44, 12]. Figure 3.9 sketches the addition of an electron to respectively the high-spin and the low-spin ground state. In case of low-spin the addition of an electron in the e_g^- -band costs \mathcal{D} but one gains $3\mathcal{K}_{te}$; with the addition of an electron in the t_{2g} -band one gains \mathcal{K}_{tt} . The e_g^+ -band is positioned at an energy \mathcal{D} above the t_{2g}^+ -band and the relative energy of the t_{2g}^- -band is $-\mathcal{D} + 3\mathcal{K}_{te} - \mathcal{K}_{tt}$. This places the t_{2g}^- -band at an energy $3\mathcal{K}_{te} - \mathcal{K}_{tt}$ above the t_{2g}^+ -band. Because the energy difference between \mathcal{K}_{te} and \mathcal{K}_{tt} is only 0.1 eV it is neglected, and the expression for the relative energy of the t_{2g}^- -band reduces to $2\mathcal{K}$ as given in the figure. To simplify the discussion the difference between \mathcal{K}_{te} and \mathcal{K}_{tt} is neglected in the following sections. If the t_{2g}^- -level and the e_g^+ -level are close to degenerate, they give rise to an intermediate spin state if $3d$ spin-orbit coupling is included [75] (see section 3.5). For $3d^5$, $3d^6$ and $3d^7$ ground states the high-spin versus low-spin dichotomy exist. Table 3.5 gives the respective configurations, symmetries and electron addition states (in the \mathcal{DK} -model).

Table 3.5 shows that for $3d^5$ to $3d^7$ the high-spin states consist only of two electron addition states, split by \mathcal{D} , as only spin-down electrons can be added. The low-spin $3d^6$ has only one electron addition state as the e_g^+ and e_g^- states are exactly degenerate because of the singlet ground state. Because the number of final states is limited the electron addition states of $3d^7_{HS}$ are a good example to show the actual difference between the \mathcal{DK} -model and the crystal field multiplet model. The ground state has 4T_1 -symmetry, thus the electron addition $3d^8$ -states must be triplet states. In the atomic $3d^8$ multiplet there are only two triplet states: 3F and 3P . In the \mathcal{DK} -model there are also only two available states:

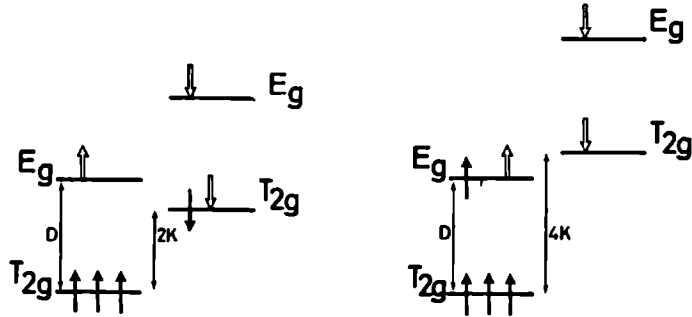


Figure 3.9: The \mathcal{DK} -model for a $3d^4$ -configuration: (left) low spin; (right) high-spin. The energy difference between \mathcal{K}_{te} and \mathcal{K}_{tt} has been neglected.

state	configuration	symmetry	energy of		
			one electron addition		
$3d_{HS}^4$	$(t_{2g}^+)^3(e_g^+)^1$	5E	\mathcal{D}	$4\mathcal{K}$	$\mathcal{D} + 4\mathcal{K}$
$3d_{LS}^4$	$(t_{2g}^+)^3(t_{2g}^-)^1$	3A_2	\mathcal{D}	$2\mathcal{K}$	$\mathcal{D} + 2\mathcal{K}$
$3d_{HS}^5$	$(t_{2g}^+)^3(e_g^-)^2$	6A_1	$5\mathcal{K}$	$\mathcal{D} + 5\mathcal{K}$	
$3d_{LS}^5$	$(t_{2g}^+)^3(t_{2g}^-)^2$	2T_2	\mathcal{D}	\mathcal{K}	$\mathcal{D} + \mathcal{K}$
$3d_{HS}^6$	$(t_{2g}^+)^3(e_g^+)^2(t_{2g}^-)^1$	5T_2	$4\mathcal{K}$	$\mathcal{D} + 4\mathcal{K}$	
$3d_{LS}^6$	$(t_{2g}^+)^3(t_{2g}^-)^3$	1A_1	\mathcal{D}		
$3d_{HS}^7$	$(t_{2g}^+)^3(e_g^+)^2(t_{2g}^-)^2$	4T_1	$3\mathcal{K}$	$\mathcal{D} + 3\mathcal{K}$	
$3d_{LS}^7$	$(t_{2g}^+)^3(t_{2g}^-)^3(e_g^+)^1$	2E	\mathcal{D}	$\mathcal{D} + \mathcal{K}$	

Table 3.5: Symmetries of the $3d^N$ ground state configurations and the 'electron addition states' in the \mathcal{DK} -model.

$(t_{2g}^+)^3(e_g^+)^2(t_{2g}^-)^3$ and $(t_{2g}^+)^3(e_g^-)^2(t_{2g}^-)^2(e_g^-)^1$, or in hole notation $(e_g^-)^2$ and $(e_g^-)(t_{2g}^-)$ or simply \underline{ee} and \underline{et} . The atomic multiplet model takes into account the Slater integrals only, whereas the \mathcal{DK} -model allows for one electron addition only. The crystal field multiplet model allows for multi-electron transitions to the whole crystal field multiplet and figure 3.10 sketches the transition from the atomic multiplet (in LS-coupling) to the one electron addition model for a cubic crystal field.

The 3F state splits into states of 3A_2 , 3T_2 and 3T_1 symmetry and the 3P state transforms to 3T_1 symmetry. Increasing the cubic crystal field (divided by the Slater integrals) trans-

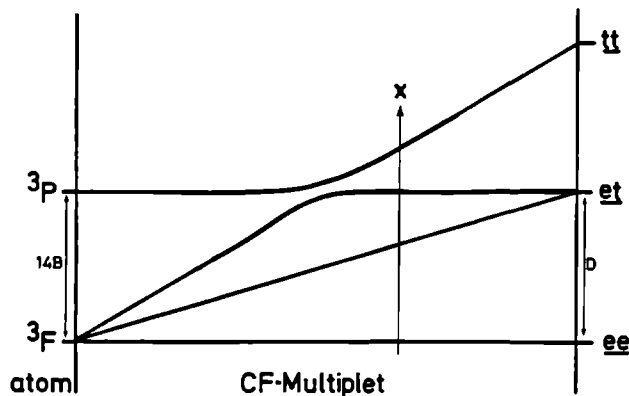


Figure 3.10: Transformation between the states in an atomic multiplet (right) and one electron DK -model (left). The crystal field multiplet model refers to a situation in between these extremes. For the DK -model the tt state has zero intensity as it cannot be reached by one electron addition to the $(t_{2g}^+)^3(e_g^+)^2(t_{2g}^-)^2$ ground state.

forms the 3A_2 -state to the pure ee -state and the 3T_2 -state to the et -state. The situation for the 3T_1 -state is more complicated as there are two states of the same symmetry. The 3T_1 state originating from the 3P atomic state has to transform to the et -state, whereas the 3T_1 state originating from the 3F atomic state has to transform to the tt -state, i.e. the overall atomic states are spherical symmetric (${}^3F \rightarrow ee + et + tt$ and ${}^3P \rightarrow et$). From figure 3.10 it can be seen that the 3T_1 -like states tend to cross, which is forbidden as they have the same symmetry. Therefore the two 3T_1 -states repel each other; both states have strongly mixed atomic 3P plus 3F states, or alternatively strongly mixed te plus tt crystal field character. The pure tt state does not couple to the ground state and therefore in the DK -model only two states can be reached. The crystal field multiplet model has four allowed states. In table 3.6 the number of states is given for the atomic multiplet, the crystal field multiplet (without core hole) and the DK -model for all $3d^N$ -configurations. In case of a ground state with A_1 -symmetry the number of final states is relatively small, because only T_2 and E states can be reached. Because the 6A_1 -state only the quintet states can be reached, only two states is found in the crystal field multiplet.

3.2.3. Core hole effect on the crystal field multiplet

A central phenomena of the x-ray absorption process is the creation of a core hole. In the final state the core hole gives rise to additional interactions, as discussed for the atomic case. If the valence electrons are described by a crystal field multiplet similar effects occur. The dominant effect of the core hole is that the symmetries of the valence band crystal field multiplet have to be multiplied with the spin-orbit split ${}^2P_{3/2}$ and ${}^2P_{1/2}$ -symmetries of the core hole. This gives rise to two distinct multiplets related to the L_3 and the L_2 edge. As discussed before additional core hole effects occur due to considerable overlap of the $2p$ and $3d$ wavefunctions. Because of this the existence of a $2p$ core hole gives rise to strong correlations with $3d$ electrons, and the multipole F_{pd}^2 and the (multipole) exchange G_{pd}^1 and G_{pd}^1 Slater integrals cause a drastic reordering of the crystal field multiplet. Therefore it is

state	symmetry	atom	CFM	DK
$3d^1$	2T_2	5	16	4
$3d^2$	3T_1	8	32	4
$3d^3$	4A_2	7	10	3
$3d^4_{HS}$	5E	5	11	3
$3d^4_{LS}$	3T_1	15	20	3
$3d^5_{HS}$	6A_1	1	2	2
$3d^5_{LS}$	2T_2	14	36	3
$3d^6_{HS}$	5T_2	2	3	2
$3d^6_{LS}$	1A_1	6	9	1
$3d^7_{HS}$	4T_1	2	4	2
$3d^7_{LS}$	2E	5	11	2
$3d^8$	3A_2	1	1	1
$3d^9$	2E	1	1	1

Table 3.6: Comparison of the number of states in the crystal field multiplet model (CFM) as compared with the DK-model and the atomic multiplet.

more appropriate to discuss the complete $2p$ crystal field multiplet at once in an intermediate coupling scheme. The crystal field multiplet program as developed by B.T. Thole takes all interactions within the $2p^53d^{N+1}$ final state into account simultaneously. The symmetries of the atomic states, calculated with an atomic multiplet program, are projected according to the branching rules [53]. The papers included in the sections 3.3 and 3.4 give the actual effects of the cubic crystal field on the spectral shape of the atomic multiplets of a series of $3d$ -metal ions. Section 3.5 discusses the low-energy splittings originating from the $3d$ spin-orbit coupling and non-cubic crystal fields and section 3.6 deals with the effects of polarization dependence. The limitations of the model are discussed in section 3.7.

3.3. Metal 2p x-ray absorption of $3d^0$ compounds

Reproduced from *Physical Review B.*, volume 41, page 928-937 (1990).

This paper contains the crystal field multiplet calculations for compounds with an empty $3d$ -band. The crystal field multiplets of the $3d^0 \rightarrow 2p^5 3d^1$ transition are calculated. The effects of the cubic crystal field on the theoretical spectral shape is studied in detail. The theoretical results are compared with $2p$ x-ray absorption spectra of FeTiO_3 , TiO_2 , Sc_2O_3 , ScF_3 , CaF_2 and the potassium halides. The peaks in the experimental spectra can be related to single final states of the crystal field multiplet. This makes it possible to measure the broadening of the individual transitions in the $3d^0 \rightarrow 2p^5 3d^1$ multiplet. The origins of the different mechanisms for the symmetry dependent broadening effects are discussed.

**$L_{2,3}$ x-ray-absorption edges of d^0 compounds:
 K^+ , Ca^{2+} , Sc^{3+} , and Ti^{4+} in O_h (octahedral) symmetry**

F M F de Groot and J C Fuggle

Research Institute for Materials, University of Nijmegen, Toernooiveld, 6525 ED Nijmegen, The Netherlands

B T Thole and G A Sawatzky

Materials Science Centre, University of Groningen, Nijenborgh 18, Paddepoel, 9747 AG Groningen, The Netherlands

(Received 17 July 1989)

The $L_{2,3}$ x-ray-absorption edges of d^0 compounds are calculated with use of an atomic description of the $2p^63d^0$ to $2p^53d^1$ excitation, with the inclusion of the crystal field. For reasons of clarity, we confine ourselves to d^0 compounds in octahedral symmetry, but the same approach is applicable to all other d^N compounds in any point-group symmetry. The experimental spectra of $FeTiO_3$, Sc_2O_3 , ScF_3 , CaF_2 , and the potassium halides are well reproduced by the present calculations, including the previously misinterpreted small leading peaks. The splitting between the two main peaks in both the L_3 and L_2 edge are related, though not equal, to the crystal field splitting. Comparison to experiment showed that the broadening of the main multiplet lines is different. This can be related to Coster-Kronig Auger processes for the L_2 edge and to a solid-state broadening which is a combination of vibrational (phononic) and dispersive broadenings. With the full treatment of the atomic multiplets, the atomic effects can be separated from solid-state effects, which offers a better description of the latter. This includes vibrational broadenings, the covalent screening of the intra-atomic Coulomb and exchange interactions, via the position of small leading peaks, and surface effects. The same general framework can be used to discuss crystal-field effects in both lower symmetries, with the possibility of polarization-dependent spectra (e.g., TiO_2), and partly filled d bands.

I. INTRODUCTION

In the past few years experimental progress in the field of soft-x-ray absorption has been tremendous. The attainable experimental resolution has improved to its present best value of 30 meV at 300 eV.^{1,2} This technical progress has opened the possibility to measure the transition metal $L_{2,3}$ x-ray-absorption edges, including also K and Ca, with great accuracy.³

Theoretical developments have lagged behind those of experiment but the improvement in resolution has created the need for a much more advanced description. In this paper we contribute to a description of the transition metal $L_{2,3}$ x-ray-absorption spectra.⁴ The starting point is an atomic multiplet calculation.⁵⁻⁷ We then treat those cases where the most prominent effect of the solid state is the crystal field, the breaking of the spherical symmetry around the atom. We prefer to use the term crystal field rather than ligand field, because in principle we only change the point-group symmetry. The crystal field is put in as a parameter fit to the experiment. In this manner the hybridization effect of the ligands is implicitly taken into account. Dispersive effects, which have been treated earlier for the elemental transition metals,^{8,9} are not taken explicitly into account here.

Using group-theory formalism,¹⁰⁻¹² it is possible to project the atomic spectrum (spherical symmetry) onto a specific symmetry group. All point-group symmetries can be addressed in this way. However, the lower the

symmetry, the more parameters are needed to account for all possible interactions. In this paper we only consider O_h symmetry, which accounts for both sixfold (octahedral) and eightfold (simple-cubic) surroundings. We will show that with the restriction to O_h symmetry we are already able to obtain excellent results, even for some cases in which the actual symmetry is lower. To limit the complexity of the theory presented, we postpone the discussion of lower symmetries.

We start with an outline of the theoretical approach (Sec II). In Sec III we will present some general results for the d^0 compounds, where we take Ti^{4+} as an example. We show that the splittings in the x-ray-absorption spectroscopy (XAS) spectrum are due to, but do not directly scale with, the crystal-field parameter $10Dq$. In Sec IV we will make a comparison to experimental results of K^+ , Ca^{2+} , Sc^{3+} , and Ti^{4+} compounds.

II. THEORY

We calculated the excitation from the d^0 ground state to the final-state $2p^53d^1$ multiplet by means of an optical dipole transition. The central point in our analysis will be the crystal field. First it is necessary, however, to calculate the atomic multiplet.

A. Atomic multiplet theory

For reasons of clarity we will briefly repeat atomic multiplet theory as can be found in the standard text-

books^{13,14} The Hamiltonian for atomic multiplets can be written as

$$H = H_{av} + L \cdot S(p) + L \cdot S(d) + g(i, j)$$

H_{av} consists of the kinetic term and the interaction with the nuclei. It gives the average energy of the multiplet and does not contribute to the multiplet splittings. The splittings in the multiplet are caused by the spin-orbit couplings, $L \cdot S$, for the 2p and 3d electron, and by the Coulomb repulsion term, $g(i, j)$. This two-electron operator can be expressed in terms of spherical harmonics,¹³ which necessitates the division of radial and angular parts. The radial part, $R^k(l_1 l_2, l_3 l_4)$ is divided in direct Coulomb terms, $F^k(l_1 l_2, l_1 l_2)$, and exchange terms, $G^k(l_1 l_2, l_2 l_1)$. The angular part of $g(i, j)$ results in the selection rules, or in other words it gives the possible K values. For the direct Coulomb term, no odd K values are allowed, and the maximum K value is two times the minimal l value. For the $p^2 d^1$ multiplet this results in F^0 and F^2 , while for a d^2 multiplet F^4 also comes into play. The K values in the exchange term equal $|l_1 - l_2|$, $|l_1 - l_2 + 2k|$, $l_1 + l_2$. For the $p^2 d^1$ multiplet this results in G^1 and G^3 . Thus we can evaluate the two-electron operator $g(i, j)$ for the $p^2 d^1$ multiplet in terms of four interactions F^0 , F^2 , G^1 , and G^3 . F^0 only contributes to the average energy and is taken into H_{av} . The *ab initio* calculated Coulomb, exchange and spin-orbit parameters (F^2 , G^1 , G^3 , $L \cdot S_p$, and $L \cdot S_d$) of K^+ , Ca^{2+} , Sc^{3+} , and Ti^{4+} are given in Table I. For the actual crystal-field calculations, the *ab initio* (Hartree-Fock) values of F^2 , G^1 , and G^3 are scaled down to 80% of their original value to account for many-body corrections.¹⁵

B. The atomic excitation from 2p⁴3d⁰ to 2p³3d¹

The ground state d^0 consists of one single 1S state. Therefore with x-ray absorption, following the optical transition selection rule, only the 1P final state is within reach in LS coupling, thus only one peak would appear in the XAS spectrum. Turning on the spin-orbit coupling of the 2p core hole, but still neglecting the spin-orbit coupling of the 3d electron and the Coulomb repulsion term, $g(i, j)$, leads to the well-known approximation of two peaks with an intensity ratio of 1:2, denoted by the L_3

TABLE I Values for the atomic multiplet, from an *ab initio* calculation. E_{av} gives the average energy of the multiplet and $L \cdot S$ gives the parameters for the spin-orbit coupling. The *ab initio* value of the Coulomb and exchange parameters or Slater integrals F^2 , G^1 , and G^3 are given, they are normalized to 80% of their *ab initio* value in the real calculation, to simulate configuration interaction.

Ion	K ⁺	Ca ²⁺	Sc ³⁺	Ti ⁴⁺
E_{av}	298.40	350.37	405.75	464.81
$L \cdot S(p)$	1.88	2.4	3.03	3.78
$L \cdot S(d)$	0.005	0.011	0.020	0.032
F^2_{pd}	2.20	3.79	5.09	6.30
G^1_{pd}	1.32	2.51	3.58	4.62
G^3_{pd}	0.74	1.42	2.03	2.63

and L_2 edge. This is caused by the transformation from LS to JJ coupling which results in the mapping of 1P (LS) onto 1P , 3P , and 3D (JJ), of which both triplet states have equal energy.⁸ As is directly evident from the values of Table I, the direct Coulomb and exchange terms F^2 , G^1 , and G^3 are not negligible. The result is a splitting of the L_3 edge and consequently three absorption lines. The intensities of these lines are also strongly redistributed by F^2 , G^1 , and G^3 . Figure 1 gives only the result for Ti^{4+} as the atomic spectra for K^+ , Ca^{2+} , and Sc^{3+} are similar. The small leading peak has predominantly triplet character and is mixed through the spin-orbit interaction and the Coulomb repulsion into the main L_3 edge. This small leading peak retains its intensity when the crystal field is considered and will give rise to a general small leading peak in x-ray-absorption spectra of d^0 compounds. We stress this atomic multiplet feature as it has been overlooked in some x-ray-absorption literature.

C. Crystal-field effect on the 2p³3d¹ multiplet

We now consider the crystal field. In terms of group theory the effect of an octahedral crystal field is the reduction of symmetry from O_3 to O_h . All irreducible representations (henceforth referred to as IR) in spherical symmetry are projected onto the O_h group. We have to consider separately (1) the ground state IR, (2) the final state IR's, and (3) the transition IR.

Using JJ coupling in O_3 symmetry, there exists one IR per J value, with a degeneracy of $2J + 1$. The d^0 ground state has a J value of 0, and the transition has a J value of 1. The accessible final states are thus restricted to those with a J value of 1. The 60 possible states of the $p^3 d^1$ multiplet are distributed over five IR's with J values of 0, 1, 2, 3, and 4, and with degeneracies of, respectively, 1, 3, 4, 3, and 1. Notice that in LS coupling the $p^3 d^1$ multiplet has six IR's: singlet and triplet F , D , and P .

We have to transform these O_3 IR's to O_h symmetry, where there are five possible IR's. Their standard notation is A_1 , A_2 (one-dimensional), E (two-dimensional), T_1 , and T_2 (Ref. 14) (three-dimensional). The transformation from O_3 to its subgroup O_h , mostly called the O_3 - O_h branching, can be found in the work of Butler.¹⁰

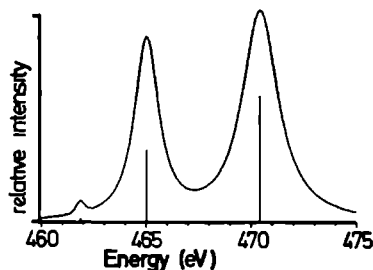


FIG 1 Atomic multiplet spectrum for the 3d⁰ to 2p³3d¹ excitation of Ti^{4+} , the Slater integrals are reduced to 80% of their Hartree-Fock values.

TABLE II The branching table from O_3 to O_h is given for integer values of J in O_3 (as occur for the p^3d^1 multiplet) See Butler for more details and all other branching tables

O_3	\rightarrow	O_h
$J=0$	\rightarrow	A_1
$J=1$	\rightarrow	T_1
$J=2$	\rightarrow	$E + T_2$
$J=3$	\rightarrow	$T_1 + T_2 + A_2$
$J=4$	\rightarrow	$A_1 + T_1 + E + T_2$

The essential details are repeated in Table II

The ground state and the transition IR are transformed to, respectively, A_1 and T_1 . The entire effect of the crystal field to split and shift the peaks in the spectrum is thus concentrated in the final state. All possible final states must have T_1 symmetry, otherwise the transition matrix element equals zero. The T_1 IR can be reached not only from the $J=1$ IR, but also from the $J=3$ and $J=4$ IR's (see Table II). The $J=1$ and $J=3$ IR's are both threefold degenerate and the $J=4$ IR is nondegenerate. This results in seven possible T_1 IR's in O_h symmetry, or, in other words, seven possible final states. The XAS spectrum consists, in principle, of seven lines, as can be seen in Fig. 2, where the T_1^{4+} XAS spectrum for a crystal-field splitting ($10Dq$) of 1.8 eV is calculated.

D Generality of the method

The method used starts with the calculation of the atomic (initial and final) multiplets. The Slater integrals (F^2 , G^1 , and G^3) are scaled down to 80% of their *ab initio* values. Then the reduced matrix elements of all necessary operators in the spherical group are calculated with the use of Cowan's atomic multiplet program.⁷ To obtain the reduced matrix elements in any point group, Butler's program is used for the calculation of all necessary factors ($3J$ symbols). With this general approach, the program is, in principle, capable of calculating the transition probabilities between any two configurations in

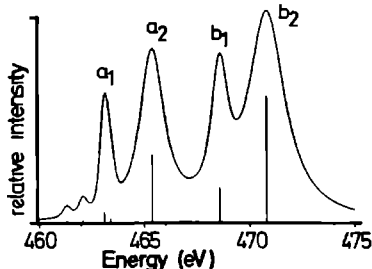


FIG. 2 Multiplet spectrum for the $3d^0$ to $2p^3d^1$ excitation of Ti^{4+} in octahedral symmetry, the crystal field parameter $10Dq$ was taken as 1.8 eV. The 80% reduction of the Hartree Fock values was used.

XAS, x ray photoemission spectroscopy (XPS), or bremsstrahlung isochromat spectroscopy (BIS) in all point-group symmetries.^{7,16}

This means that for the $L_{2,3}$ XAS edges any transition from a d^N ground state to a p^3d^{N+1} final state can be calculated. The number of final states increases drastically if $N > 0$. Also, ground-state crystal-field effects become important, which complicates the analysis. We have calculated the complete d^N series in O_h symmetry, which will be published elsewhere.¹⁷ The calculation of lower symmetries, using the necessary branchings, means that the number of parameters increases. For example, O_h needs only one parameter while D_{4h} needs three, which makes the analysis more difficult. Another important effect of lower symmetries such as D_{4h} is the polarization dependence of the spectrum. The possibility to use lower symmetries to correctly describe x-ray-absorption spectra was used for rutile TiO_2 .¹⁸

III RESULTS FOR d^0 COMPOUNDS

Experimentally it is found that the crystal field splits the L_3 and L_2 x-ray absorption edges. Often this is pictured as a splitting of both edges into two, with the energy difference between both peaks assumed equal to the crystal-field parameter $10Dq$. Using the crystal field program we have calculated the p^3d^1 multiplet for a number of $10Dq$ values. Figure 3 gives the results for Ti^{4+} using both positive and negative values, related to, respectively, sixfold (octahedral) and eightfold (simple cubic) surroundings. The crystal field has to compete with all intra atomic interactions [F^2 , G^1 , G^3 , $LS(p)$, and $LS(d)$]. The result is a complex change of the spectrum as a function of $10Dq$. The value of the crystal-field splitting is indicated as the distance between the vertical line and the diagonal. In Fig. 4 the distance between the two main peaks in the L_3 (peak a_1 and a_2) and L_2 (peak b_1 and b_2) edge is given as a function of the crystal field. The result is evident: *The energy splitting in the XAS spectra, is, in general, not equal to $10Dq$.*

Starting with the atomic calculation (Fig. 4, $10Dq=0$) and turning on a small crystal field, a small energy splitting immediately appears. This does not mean that the atomic lines are split in two, but that other final states are mixed in. These states were not accessible in spherical symmetry as discussed in Sec. II. The intensities of these new transitions (opened channels for O_h) are small for low crystal fields as can be seen in Fig. 5.

The following picture then emerges. In O_h symmetry the p^3d^1 multiplet consists of seven lines, four of which are forbidden in spherical symmetry. The crystal field has the effect of (1) shifting the seven final states in energy (see Figs. 3 and 6) and (2) redistributing the absorption intensity over all seven lines (see Fig. 5).

The crystal field has a slightly different, though equivalent, effect on the L_3 edge, compared to the L_2 edge. This small difference between the L_3 and L_2 edge can also be seen in the experimental spectra, but this was not extensively discussed until now. With the present improvement in resolution,² it is possible to show the ine-

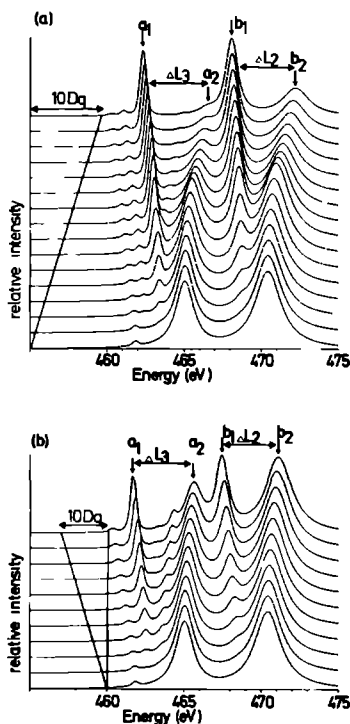


FIG 3 Ti^{4+} $2p^33d^1$ excitation spectra in O_h symmetry as a function of the crystal-field splitting $10Dq$. (a) The value of $10Dq$ is positive and ranges from 0.0 to 4.5 eV, indicated by the diagonal line, (b) the value of $10Dq$ is negative. ΔL_3 measures the distance between the peaks a_1 and a_2 , split by the crystal field

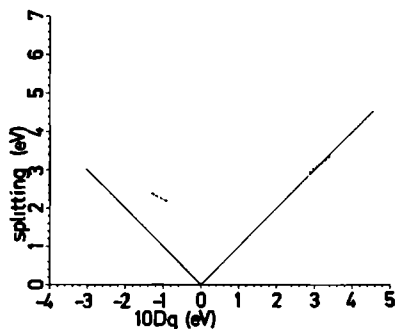


FIG 4 The splitting between peaks a_1 and a_2 (ΔL_3 , dashed line) and between peaks b_1 and b_2 (ΔL_2 , dotted line) is given as a function of the crystal-field parameter $10Dq$. For the solid line, the assumption of a splitting equal to $10Dq$ is made

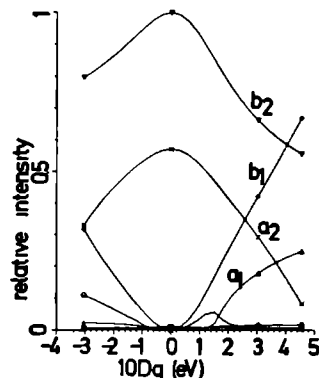


FIG 5 For Ti^{4+} in O_h symmetry the changes in intensity are given as a function of the crystal field splitting $10Dq$. The symbols correspond to the seven absorption lines ordered for increasing energy (see Fig 6)

quivalence of peak separations in the L_2 and L_3 peaks convincingly. The clearest case is CaF_2 (see Sec IV C)

IV. COMPARISON WITH EXPERIMENT

We compare our results for the $2p^33d^1$ optical transition multiplet with x-ray-absorption spectra for K^+ , Ca^{2+} , Sc^{3+} , and Ti^{4+} compounds. We start with Ti^{4+} in ilmenite, $FeTiO_3$ (Sec IV A). A comparison to the Sc^{3+} compounds Sc_2O_3 and ScF_3 is given in Sec IV B. The

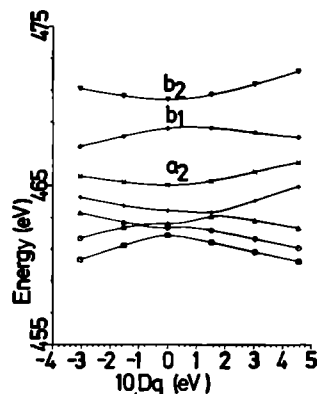


FIG 6 For Ti^{4+} in O_h symmetry the changes in energy position are given as a function of the crystal-field splitting $10Dq$. The symbols correspond to the seven absorption lines ordered for increasing energy

scandium compounds show well separated peaks, from which we can show that it is possible to make more accurate comparisons with the exact position of the small leading peaks. Section IVC deals with CaF_2 , whose (bulk) spectrum is completely reproduced. We end with a comparison with a series of potassium-halide $\text{K } L_{2,3}$ edges,¹⁹ which will be discussed in Sec. IV D.

A. The $\text{Ti } L_{2,3}$ XAS spectrum of FeTiO_3

We have compared the titanium $L_{2,3}$ edge of FeTiO_3 with the calculation of Ti^{4+} in O_h symmetry. The exact structure of FeTiO_3 (see Table V) (Refs. 20 and 21) and the resulting point group of Ti^{4+} are not critical for our analysis. Figure 7 gives the FeTiO_3 spectrum compared with the calculation in O_h symmetry, which shows good agreement and justifies the approximation of octahedrally surrounded Ti^{4+} ions. Although we will not discuss the theoretical Ti^{3+} spectrum we calculated, we note that the experimental $\text{Ti } L_{2,3}$ XAS spectrum of FeTiO_3 is only consistent with Ti^{4+} , not Ti^{3+} .²²

To obtain the optimum agreement with experiment, it is necessary to choose different Lorentzian broadenings for the four peaks. The optimum values for the broadening are given in Table III. After the Lorentzian broadening the whole spectrum was convoluted with a Gaussian broadening of 0.15 eV (Ref. 23) to simulate the experimental resolution. From this choice of broadenings and from the resulting agreement with experiment, it is clear that each peak in the $L_{2,3}$ XAS spectrum has its own characteristic broadening. Noticing this we will try to find the underlying reasons. The extra broadening of the peaks belonging to the L_2 edge (peak b_1 and b_2) originates from the shorter lifetime of the $p_{1/2}$ states. A $p_{1/2}$ state has an extra decay channel, the Coster-Kronig (CK) Auger decay process,²⁴ by which it can fall back to a $p_{3/2}$ hole, with the simultaneous ejection of a d electron. The energy difference between a $2p_{1/2}$ and a $2p_{3/2}$ hole, due to the ($2p$) spin-orbit coupling, must be larger than the binding energy of the d electron, otherwise the CK Auger decay channel is closed.

From Table III we conclude that the CK Auger broadening of the L_2 edge (peak a_2 and b_2) is 0.4 eV. Subtracting this broadening,²⁵ both peaks a_2 and b_2 have an extra broadening of about 0.5 eV with respect to peaks a_1 and b_1 . The origin of this broadening could be due to (1) a lifetime effect similar to the L_2 CK Auger decay, (2) an effect of the actual point-group symmetry, (3) vibrational (phononic) broadening, and (4) dispersive broadening.

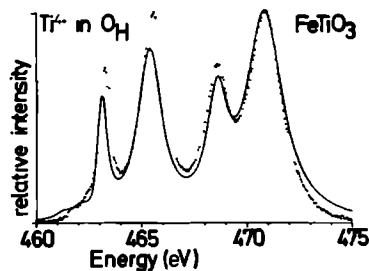


FIG. 7. The experimental FeTiO_3 spectrum (dotted), measured with the SX700 monochromator at Berliner Elektronenspeicherung-Gesellschaft für Synchrotronstrahlung m. b. H. (BESSY), is compared with a multiplet calculation in O_h symmetry. The crystal-field parameter is 1.8 eV, the broadening factors are tabulated in Table III.

The possibility of a large broadening effect of a decay process (1) seems unlikely. The energy difference with respect to the lowest main peak is only about 2 eV, which prohibits real Auger decay processes, though virtual processes cannot be excluded. The effect of an actual lower point-group symmetry may be important in the special case of FeTiO_3 . Because in the other compounds which we will discuss O_h symmetry is better obeyed and their broadenings are equivalent (see Table IV), we do not expect a large extra broadening effect of the reduced symmetry, though in the case of FeTiO_3 it may be considerable. In Sec. V we will come back to the possible effect of a lower symmetry and make a connection with the vibrational broadening mechanism. We will now further concentrate on effects (3) and (4), the vibrational and dispersive broadening mechanisms, which can be combined under the heading solid-state broadening.

In a simple picture of a transition metal in octahedral symmetry, the two peaks in both the L_3 and the L_2 edge can be related to t_{2g} (d_{xy} , d_{xz} , and d_{yz} orbitals) and e_g (d_{z^2} and $d_{x^2-y^2}$ orbitals) symmetry.¹⁴ Although in a full atomic multiplet plus crystal-field description this division is not exact, it is a good starting point. In octahedral symmetry e_g orbitals point to the ligands, while t_{2g} orbitals point in between them. This causes the e_g orbitals to bind more strongly to the ligands and conse-

TABLE III. The broadening factors for the FeTiO_3 spectrum. The total broadening (Γ) is divided in the Coster-Kronig Auger broadening (α) and the solid-state broadening (β). From the adjustment to experiment it is found that $\alpha = 0.4$ eV and $\beta = 0.5$ eV (see Fig. 7).

Peak	Total Γ	CK Auger α	$\Gamma - \alpha$	Solid state β	$\Gamma - \alpha - \beta$
a_1	0.1 eV		0.1 eV		0.1 eV
a_2	0.6 eV		0.6 eV	0.5 eV	0.1 eV
b_1	0.5 eV	0.4 eV	0.1 eV		0.1 eV
b_2	1.0 eV	0.4 eV	0.6 eV	0.5 eV	0.1 eV

quently to a higher energy of the (antibonding) e_g state, compared to the (antibonding) t_{2g} state. This is in fact the origin of the crystal-field splitting¹⁴. We can now conclude that, independent of the exact symmetry, the second peak will always be related to a state that has a larger hybridization with the ligands.

Large hybridization, which arises when the states are directed towards the ions, also means that the equilibrium interatomic distances are strongly dependent on occupation of the levels. In x-ray absorption the antibonding levels become occupied, which means that the final-state interatomic distance is larger than the equilibrium ground-state interatomic distance. This is indicated in Fig 8 [$R^*(e_g) > R$]. Following the Franck-Condon principle²⁶ this means a large final-state vibrational broadening (see Fig 8). For small hybridization (i.e., the t_{2g} orbitals) this Franck-Condon broadening will be smaller. Thus the larger hybridization can cause the extra broadening of the a_2 and b_2 peak. We would also expect a large temperature dependence because of the occupancy of excited vibrational states in the (electronic) ground state. Thermal effects will broaden both the " t_{2g} " and " e_g " states, but the effect on the e_g state will be larger. This thermal broadening more or less scales with the final-state vibrational broadening, which is also present at 0 K [see Fig 8, compare the energy widths for e_g and t_{2g} at 0 K and at finite temperature (T^*)].

The possibility of dispersive broadening is related to the amount of hybridization. The larger hybridization of the e_g states results in larger bandwidths in the solid state. This dispersion can, however, be reduced or eliminated by excitonic effects due to the large core-hole 3d attraction, which localizes the 3d electron²⁷. The conclusion is that the a_2 and b_2 peaks, because of their larger

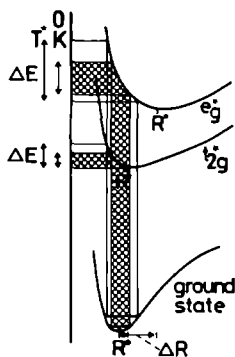


FIG 8 Because an electron is added to an antibonding e_g or t_{2g} orbital, the equilibrium interatomic distance (R) becomes larger. The largest ΔR occurs for the e_g^* orbital. Following the Franck-Condon principle this leads to the largest broadening (ΔE). Raising the temperature from 0 K (T) to a finite temperature (T^*) enlarges ΔE both for the e_g and t_{2g} peaks.

hybridization, can have stronger vibrational broadening and possibly also stronger dispersive broadening. We do not see a possibility to separate these two broadening mechanisms. Therefore we would like to denote the experimentally found broadening of the e_g peaks in general as a solid-state broadening. This solid-state broadening is found to be 0.5 eV in FeTiO_3 (see Table III). From the discussion of the potassium-halide spectra (Sec IV D), vibrational broadening is found to be the major broadening mechanism.

The analysis procedure of the FeTiO_3 $L_{2,3}$ XAS spectrum can be generalized in the following way. First measure the experimental splittings between the a_1 and a_2 peak (ΔL_1) and between the b_1 and b_2 peak (ΔL_2). The splittings found can be related to the value of $10Dq$ with use of the theoretical ΔL versus $10Dq$ lines as given in Fig 4. With the observed $10Dq$ value, the spectrum can be simulated and from a comparison with the experimental spectrum the exact broadening factors are found.

Although we will not discuss other symmetries in detail, it is interesting to see what happens for a strongly distorted system, such as rutile TiO_2 ²⁸. The strong distortion makes it impossible to simulate its XAS spectrum with the $\text{Ti}^{4+} p^3d^1$ multiplet in O_h symmetry. If the symmetry is reduced to D_{4h} , however, good agreement with experiment can be reached (see Fig 9)²⁹. We have used the same range of broadenings as found for FeTiO_3 . In D_{4h} symmetry the p^3d^1 multiplet consists of 22 lines (seven in O_h). Also one has to consider three crystal-field parameters (only one in O_h) and the polarization dependence of the spectrum. Further discussion of D_{4h} symmetry and the TiO_2 spectrum will be given elsewhere¹⁸.

B. The $\text{Sc} L_{2,3}$ edge of Sc_2O_3 and ScF_3

Figure 10 shows the $\text{Sc} L_{2,3}$ edge of Sc_2O_3 overlaid with a calculated spectrum for a crystal field of 1.83 eV. The broadening factors used are given in Table IV. The ScF_3 spectrum, Fig 11, was measured by Chen *et al* at Brookhaven National Laboratory (BNL)¹⁹.

The ScF_3 spectrum is similar to Sc_2O_3 , but some interesting differences can be seen. The broadening factors for the fluoride are smaller than for the oxide (see Table

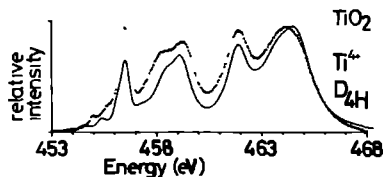


FIG 9 The experimental TiO_2 spectrum (dotted), measured with the SX700 monochromator at BESSY, is compared with a multiplet calculation in D_{4h} symmetry. The crystal-field parameter ($10Dq$) is 1.8 eV and the values for the 420 and 220 branches are 0.75 and 0.3 eV, respectively, the broadening factors are similar to those for FeTiO_3 .

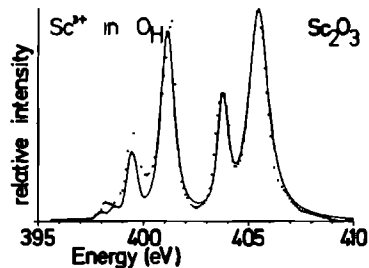


FIG 10 The experimental Sc_2O_3 spectrum (dotted), measured with the SX700 monochromator at BESSY, is compared with a multiplet calculation in O_h symmetry. The crystal-field parameter is 18 eV, the broadening factors are tabulated in Table IV.

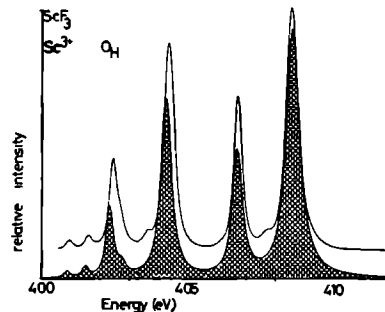


FIG 11. The experimental ScF_3 spectrum (solid line), measured with the "dragon" monochromator at Brookhaven National Laboratory (BNL) Chen *et al.*, is compared with a multiplet calculation in O_h symmetry (shaded area). The crystal-field parameter is 17 eV; the broadening factors are tabulated in Table IV.

IV). Notice that this is no resolution effect, which is taken care of by the extra Gaussian broadening. The small leading peaks come out more clearly in the ScF_3 spectrum: Close comparison of the calculated multiplets with FeTiO_3 and Sc_2O_3 (Figs. 7 and 10), shows small discrepancies in the energy position of the leading peaks. In the experimental spectra they are situated closer to the rest of the spectrum. This discrepancy is not found in ScF_3 (and CaF_2 , see the next section), which indicates that for the fluorides the Coulomb and exchange parameters (F^2 , G^1 , and G^3), which dominate the precise energy position of the leading peaks, have the atomic value, and thus are not screened. In our present calculations we used a 20% reduction from the *ab initio* Hartree Fock (HF) values. The reduction to 80% of the HF values originate from the practice of fitting calculated multiplets to atomic data.¹⁵ The reduction results from the inclusion of many-body corrections (configuration interaction) leading to effective parameters.

We can conclude that, while for ScF_3 the atomic approach works out well, the spectra of the oxides indicate that the effective Coulomb and exchange parameters must be further reduced. This leads to leading peaks

closer to the rest of the spectrum, but another result is a change in the intensity distribution of the main peaks resulting in a change in the L_3/L_2 branching ratio^{8,9,30,31} The reduction of the intra-atomic interactions in the oxides means that solid-state effects are more important. Covalent screening can cause reduced effective values of the intra-atomic interactions. We find that these screening effects do not play a significant role in ScF_3 and CaF_2 (see Fig. 13), which marks a clear distinction between fluorides and oxides. This agrees with the clearly larger solid-state broadening in the oxides compared with the fluorides (see Table IV) and with the concept that fluorides are more ionic.

C. The $\text{Ca } L_{2,3}$ edge of CaF_2

CaF_2 has been frequently studied because of its interesting theoretical and practical aspects.³²⁻³⁵ With our calculations we are able to disprove the suggestion that the small leading peaks in the $L_{2,3}$ XAS spectrum of

TABLE IV The broadening parameters for Lorentzian broadening of the individual peaks. σ is the Gaussian broadening factor which simulates the experimental resolution. The individual numbers should not be taken too literally. The trend in the values for the CK Auger (α) and the solid-state broadening (β) is, however, clear. The crystal-field splitting ($10Dq$) shows a trend similar to the broadening. Notice that all KX spectra were fitted with the same broadenings, which were not fully optimized and from which it is not possible to derive values for α and β .

Compound	a_1	a_2	b_1	b_2	Peaks			$10Dq$
					σ	α	β	
KX	0.14	0.22	0.20	0.22	0.03			0.6 (KF) 1.1 (KI)
CaF_2	0.08	0.15	0.10	0.18	0.03	0.02	0.07	-0.9
ScF_3	0.13	0.20	0.19	0.26	0.03	0.06	0.07	1.7
Sc_2O_3	0.10	0.30	0.25	0.45	0.15	0.15	0.20	1.8
FeTiO_3	0.10	0.60	0.50	1.00	0.15	0.40	0.50	1.8

CaF_2 are related to $\text{Ca}^+ (4s)^{32}$ Figure 12 shows the spectrum with a crystal-field splitting ($10Dq$) of about -0.9 eV, which compares well with the experimental result for bulk CaF_2 (Ref 34) [and also for seven layers of CaF_2 on Si (Refs 32 and 33)] Notice that negative values of $10Dq$ are used, because the calcium ion is in eightfold coordination (simple-cubic) The two main lines are reproduced, as well as the small leading peaks In this case the leading peaks also include the low-energy peaks of the crystal-field doublet, the a_1 and b_1 peak, which have low intensity because of the small and negative value of $10Dq$ The ΔL_2 and ΔL_3 splittings deviate strongly from $10Dq$ and from each other, which prohibits a direct explanation of the individual peaks and thus necessitates a full atomic multiplet calculation Including the crystal field, this can fully explain the Ca $L_{2,3}$ XAS spectrum and the small leading peaks come out "automatically," without recourse to the $4s^1$ configuration

In Fig 12 there are some small discrepancies In the experimental spectrum there exists an extra peak at ~ 352.3 eV (b') and also the a' peak at ~ 348.7 eV is considerably more intense We believe that this originates from a shifted superposition of the spectrum as a result of surface (or damage) effects This shift is also observed in a surface study of CaF_2 on Si,^{32,31} in which it is suggested that in the surface layer of CaF_2 the Ca ions have an extra $4s$ electron The (formally) monovalent Ca^+ ions shift the spectrum to lower energy If this is correct the spectrum originates from a $4s^1$ to $2p^3 3d^1 4s^1$ transition, which can result in a modified multiplet spectrum To check this we performed a series of calculations with different crystal fields We calculated the $\text{Ca}^+ 2p^3 3d^1 4s^1$ in O_h

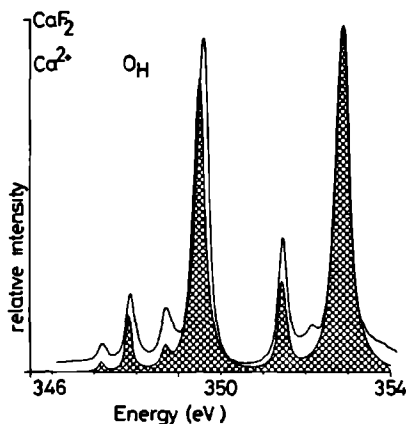


FIG 12 The experimental CaF_2 spectrum (solid line), measured with the "dragon" monochromator at BNL by Chen *et al*, is compared with a multiplet calculation in O_h symmetry (shaded area) The crystal field parameter is -0.9 eV, the broadening factors are tabulated in Table V

symmetry and also in lower symmetries (D_{4h} and D_{3d}) to make a better simulation of the surface symmetry Experimentally a polarization dependence is found,³² which clearly proves the existence of a symmetry lower than O_h In a future paper we will focus on CaF_2 and discuss the different multiplet calculations in detail³⁶

D. The $K L_{2,3}$ edges of potassium halides

To complete the series of d^0 compounds, we have calculated the potassium $L_{2,3}$ edges from the $\text{K}^+ 2p^3 3d^1$ multiplets with the crystal-field parameter between 0 and 1 eV, and compared the results with the data of the potassium halides from Sette *et al*³⁷

Our calculations are in excellent agreement with the experimental results In Fig 13 the experimental results are compared with approximately the corresponding calculated $\text{K}^+ p^5 d^1$ multiplets We did not optimize our results accurately to the experimental spectra, but the excellent visual agreement makes one sure of the possibility to do so With the use of the relation between $10Dq$ and the splittings between the main peaks (see Fig 4), the values for $10Dq$ can be extracted from the experimental spectra The small inequality of the L_3 and L_2 splittings (Fig 4) and the small leading peaks are visible in the experiment The small peaks in between the L_3 and L_2 edge, and the bumps around 300 eV, are not explained by the present multiplet calculation They are probably related to the $4s$ bands, although there is also a possibility that they originate from a lower symmetry, eventually in combination with surface effects (as for CaF_2)

The four calculated spectra in Fig 13 are broadened

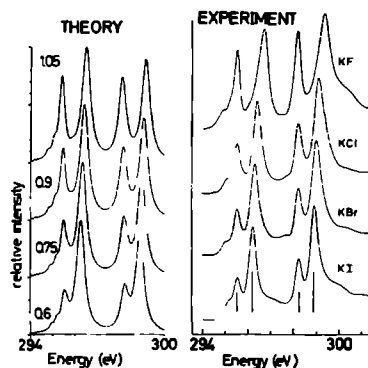


FIG 13 Four $\text{K}^+ 2p^3 3d^1$ excitation spectra in O_h symmetry (right side) are compared with the four potassium halide spectra, measured with the dragon monochromator at BNL by Chen *et al* (left side) The calculated spectra are not completely optimized to the experiment The broadenings used are adjusted to KI Notice that the KF spectrum is broader (see text)

with identical broadening factors (see Table IV). Close comparison to the experimental spectra reveals that the a_2 and b_2 peaks are extra broadened for KF compared to KI. Or in other words, the solid-state broadening of the e_g peaks (see Sec. IV B) is considerably larger for KF. Going through the halide series the dominant change is the potassium-halide interatomic distance, as given in Table V. We will examine their relation to the possibility of vibrational and dispersional broadening.

A shorter interatomic distance means that the final-state vibrational broadening will be larger. A shorter distance results in a larger expansion (ΔR) after the filling of the antibonding e_g orbital. KF has shorter interatomic distances than KI, thus KF should have a larger broadening.³⁸ The trend in the vibrational broadening is thus in agreement with experiment.

Considering the dispersional effects a distinction can be made between broadening due to K^+ -halide hybridization and K^+ - K^+ hybridization. The direct cation interactions are expected to be smaller and in general they can be neglected for ioniclike compounds. We will, however, shortly consider both possible sources of dispersion. The hybridization with the ligand is expected to be largest for iodide, which would lead to the largest broadening for KI, opposite to the experimental trend. Thus ligand hybridization cannot explain the observed broadenings. Direct cation-cation interactions (K^+ - K^+ hybridization) should in rocksalt structure be larger for the t_{2g} orbitals, compared to the e_g orbitals. This is also in contrast with the experimental observation that the a_2 and b_2 peaks (corresponding largely to e_g orbitals) are broader than the a_1 and b_1 peaks (corresponding largely to t_{2g} orbitals).

The conclusion is that both possible sources of dispersional broadening do not agree with the experimental observation. Thus the extra broadening for the e_g peaks in KF is caused by vibrational broadening, which also suggests that, at least for the potassium halides, final-state vibrational broadening is the dominant broadening factor. As can be seen in Table IV the amount of broadening scales with the interatomic distance for all compounds discussed.

TABLE V The crystal structure and nearest neighbor metal-ligand distances (R_{ML}) of the discussed compounds. Data from Ref. 28.

Compound	Crystal structure	R_{ML}
KF	rocksalt	2.66
KCl	rocksalt	3.14
KBr	rocksalt	3.29
KI	rocksalt	3.53
CaF ₂	fluorite	2.27
ScF ₃	cubic ReO ₃	2.11*
Sc ₂ O ₃	Re ₂ O ₃ C	2.01*
FeTiO ₃	ilmenite	1.92(3)
		2.06(3)
TiO ₂	rutile	1.94(4)
		1.99(2)

*Reference 27

V CONCLUDING REMARKS

We have shown that an atomic multiplet calculation followed by a transformation to a cubic crystal field (O_h symmetry) can reproduce excellently the transition-metal $L_{2,3}$ x-ray-absorption edges of the d^0 compounds discussed. Within this description it becomes clear that the splitting between the two main peaks in both the L_3 and L_2 edge is related, though not equal to the crystal-field splitting $10Dq$. Also the small leading peaks can be explained as a part of the p^2d^1 multiplet. Their position is controlled by the Coulomb and exchange parameters (F^2 , G^1 , and G^3). The crystal field does not influence them strongly, which causes their uniform appearance in the spectra.

Each main peak has its own individual broadening, which is caused by the Coster-Kronig Auger decay process of the L_2 edge and by the solid-state broadening of the " e_g " peaks. From the discussion of the potassium-halide spectra it becomes clear that the dominant solid-state broadening effect is the final-state vibrational broadening.

The central discriminating factor for the e_g broadening is the interatomic radius. A small radius results in a large broadening and also a large crystal-field splitting. This causes the broadening trend for the potassium halides to be $F^- > Cl^- > Br^- > I^-$, in agreement with the trend in the radii. From this observation it can be concluded that for the potassium halides the crystal-field splitting originates dominantly from ionic factors. The covalent contribution, which can be expected to be largest for iodide, can be neglected in first approximation.

It is shown that the small leading peaks in the fluoride spectra (CaF₂ and ScF₃) fully agree with the "atomic" multiplet spectra. In the oxide spectra, however, the leading peaks are closer to the rest of the spectrum, which is a mark of decreased intra-atomic Coulomb and exchange parameters. In the oxides the effects of the solid state (covalent screening) are so large that the intra-atomic interactions (on the empty $3d$ electron states) are rescaled, while for F^- no effect is found. This marks a different "nature" of the oxides compared to the fluorides. Fluorides can be considered as ionic, while oxides have some important covalent character.

We have shown that with our calculations, which treat the atomic multiplet effects in detail, it becomes possible to separate out the atomic effects from solid-state effects. This makes it possible to study the latter, i.e., the broadening of the peaks, related to the final-state vibrational broadening and the CK Auger decay, the exact position of the small leading peaks, related to the covalent screening of intra-atomic (pd) Coulomb and exchange interactions, and the presence of extra peaks, related to surface effects and/or reduced symmetry.

Finally we point out the relationship between vibrational broadening and the (static) lowering of the symmetry. Vibrations can be viewed as dynamical distortions of the site symmetry. The Franck-Condon principle states that x-ray absorption is a fast process with respect to vibrations. The symmetry of the absorbing (transition-metal) cation is constantly changing. This affects the

XAS spectrum, which in this picture can be viewed as a superposition of all possible distorted site symmetries. The difference with a static symmetry breaking is that in that case a specific point-group symmetry can be applied to all cations, which results in a different spectrum, as for TiO_2 . For cases like $FeTiO_3$, with structureless peaks it is not trivial to separate the (small) static lowering of symmetry from the dynamical (vibrational) symmetry-breaking effects. To answer the questions concerning these effects it would be desirable to study a compound more closely, experimentally as well as theoretically. Measurements at low temperatures can reduce the dynamical effects and possibly reveal the static symmetry effects. Theoretically all lower point groups can be calculated, and in principle also the dynamical effects can be simulated.

ACKNOWLEDGMENTS

We are grateful to the staff of the Berliner Elektronenspeicherung-Gesellschaft für Synchrotronstrahlung (BESSY) for their support during the XAS experiments. This work was supported, in part, by the Dutch Foundation for Chemical Research [Stichting Scheikundig Onderzoek Nederland (SON)] with financial assistance of the Netherlands Organization for Scientific Research [Nederlandse Organisatie voor wetenschappelijk Onderzoek (NWO)] and by the Committee for the European Development of Science and Technology (CODEST) program. We also thank C T Chen, F Sette, and F J Himpsel for permission to reproduce previously unpublished results.

- ¹Examples of high-resolution (1 1000) monochromators in the 300–800-eV range include the SX700 at BESSY, H Petersen, Nucl Instrum Methods A 246, 260 (1986), and the 10-m grazing incidence monochromator at Photon Factory, H Maezawa, S Nakai, S Mitani, A Mikuni, T Namioaka, and T Sasaki, *ibid* 246, 310 (1986).
- ²An even better resolution (up to 1 10 000) is reached by the dragon monochromator at BNL. C T Chen, Nucl Instrum Methods A 256, 595 (1987).
- ³Compare the present resolution with, e.g., the resolution reached in 1982 as can be found in R D Leapman, L A Grunes, and P L Fejes, Phys Rev B 26, 614 (1982).
- ⁴A former description has been given by T Yamaguchi, S Shibuya, S Suga, and S Shin, J Phys C 15, 2641 (1982).
- ⁵This approach has been proven very successful for the rare-earth $M_{4,5}$ edges, see, e.g., B T Thole, G van der Laan, J C Fuggle, G A Sawatzky, R C Karnatak, and J M Esteve, Phys Rev B 32, 5107 (1985).
- ⁶For the $L_{2,3}$ x-ray absorption edges the atomic approach is not sufficient and the crystal field has to be included, see, e.g., B T Thole, R D Cowan, G A Sawatzky, J Fink, and J C Fuggle, Phys Rev B 31, 6856 (1985).
- ⁷The theoretical basis for this method can be found in R D Cowan, J Opt Soc Am 58, 808 (1968), and R D Cowan, *The Theory of Atomic Structure and Spectra* (University of California Press, Berkeley, 1981).
- ⁸J Zaanen, G A Sawatzky, J Fink, W Speier, and J C Fuggle, Phys Rev B 32, 4095 (1985).
- ⁹J Fink, Th Müller-Heinzerling, B Scheerer, W Speier, F U Hillebrecht, J C Fuggle, J Zaanen, and G A Sawatzky, Phys Rev B 32, 4899 (1985).
- ¹⁰P H Butler, *Point Group Symmetry, Applications, Methods and Tables* (Plenum, New York, 1981).
- ¹¹J R Derome and W T Sharp, J Math Phys 6, 1584 (1965).
- ¹²P H Butler and B G Wybourne, Int J Quantum Chem 10, 581 (1976).
- ¹³E U Condon and G H Shortley, *The Theory of Atomic Spectra* (Cambridge University Press, Cambridge, 1964).
- ¹⁴This part is also nicely discussed by C J Ballhausen, in *Introduction to Ligand Field Theory* (McGraw-Hill, New York, 1962).
- ¹⁵R D Cowan, *The Theory of Atomic Structure and Spectra* (University of California Press, Berkeley, 1981), p 464, and references therein.
- ¹⁶G van der Laan, B T Thole, and G A Sawatzky, Phys Rev B 37, 6587 (1988).
- ¹⁷F M F de Groot, B T Thole, and G A Sawatzky (unpublished).
- ¹⁸F M F de Groot, B T Thole, and G A Sawatzky (unpublished).
- ¹⁹C T Chen and F Sette (private communication).
- ²⁰A F Wells, *Structural Inorganic Chemistry*, 3rd ed (Clarendon, Oxford, 1962), p 486.
- ²¹R E Newham, J H Fang, and R P Santoro, Acta Crystallogr 17, 240 (1963).
- ²²J B Goodenough, Phys Rev 117, 1442 (1960), Prog Solid State Chem 5, 145 (1972).
- ²³With a Gaussian broadening of 0.15 eV we mean that the parameter σ is chosen as 0.15 eV, this also applies for the Lorentzian broadenings.
- ²⁴J Zaanen and G A Sawatzky, Phys Rev B 33, 8074 (1986).
- ²⁵This procedure is not exact, but it is good enough for the accuracy needed.
- ²⁶C-O Almladh and L Hedin, in *Handbook on Synchrotron Radiation*, edited by E E Koch (North-Holland, Amsterdam, 1983), Vol 1, p 635.
- ²⁷D K G de Boer, C Haas, and G A Sawatzky, Phys Rev B 29, 4401 (1984).
- ²⁸A F Wells, Ref 20, p 461.
- ²⁹Our spectrum is equivalent to the EELS spectrum of Brydson *et al.*, R Brydson, B G Williams, W Engel, H Sauer, E Zettler, and J M Thomas, Solid State Commun 64, 609 (1987).
- ³⁰B T Thole and G van der Laan, Phys Rev B 38, 3158 (1988).
- ³¹G van der Laan and B T Thole, Phys Rev Lett 60, 1977 (1988).
- ³²D Rieger, F J Himpsel, U O Karlsson, F R McFreely, J F Morar, and J A Yarmoff, Phys Rev B 34, 7295 (1986).
- ³³F J Himpsel, U O Karlsson, J F Morar, D Rieger, and J A Yarmoff, Phys Rev Lett 56, 1497 (1986).
- ³⁴C T Chen and F Sette, Phys Rev Lett 60, 160 (1988).
- ³⁵F J Himpsel, U O Karlsson, J F Morar, D Rieger, J A Yarmoff, Phys Rev Lett 60, 161 (1988).
- ³⁶F J Himpsel *et al.* (unpublished).
- ³⁷F Sette, B Sinkovic, Y J Ma, and C T Chen, Phys Rev B 39, 11 125 (1989).

3.4. Metal $2p$ x-ray absorption of $3d$ transition metal compounds

Metal $2p$ x-ray absorption of $3d$ transition metal compounds

Reproduced from *Physical Review B.*, volume **42**, page 5459 - 5468 (1990).

This paper contains the crystal field multiplet calculations for compounds with a partially filled $3d$ -band. The crystal field multiplets of the $3d^N \rightarrow 2p^5 3d^{N+1}$ transitions are given for the common valencies of the $3d$ -metal ions. A comparison with $2p$ x-ray absorption experiments is made for VF_3 , MnF_2 and CoF_2 and excellent agreement is found. (Due to an error in a plotting routine, some multiplets for $10Dq = 0$ as given in the paper are not correct. The correct spectra will be almost equal to the spectra as given for $10Dq = 0.3$ eV in all cases).

2p x-ray absorption of 3d transition-metal compounds: An atomic multiplet description including the crystal field

F M F de Groot and J C Fuggle

Research Institute for Materials, University of Nijmegen, Toernooiveld, 6525 ED Nijmegen, The Netherlands

B T Thole and G A Sawatzky

Materials Science Centre, University of Groningen, Nijenborgh 18, Paddepoel, 9747 AG Groningen, The Netherlands

(Received 30 January 1990, revised manuscript received 4 June 1990)

The metal 2p x-ray absorption spectra (or $L_{2,3}$ edges) of 3d transition-metal compounds are calculated, using atomic multiplet theory with inclusion of the cubic crystal field. A general overview of the effect of the cubic crystal field on the shape of the $3d^N$ to $2p^5 3d^{N+1}$ excitation spectrum is given for 14 common valencies of 3d transition metal ions. Comparison to some high resolution 2p x-ray absorption spectra shows excellent agreement, which confirms the validity of the approach. Possible refinements of the theory, including lower-symmetry calculations and the inclusion of configuration interaction, are discussed.

1. INTRODUCTION

As a result of the experimental progress in the field of (soft-) x-ray-absorption spectroscopy (XAS), the attainable resolution has improved to its present best value of 1/10000.¹ The high-resolution 2p x-ray-absorption spectra of transition-metal compounds show a large amount of structure at the edge, which now can be investigated in detail. In this paper we present a theoretical analysis of these spectra, based on atomic multiplet theory with the inclusion of the cubic crystal field. A similar method has been used by Yamaguchi *et al*.²

We summarize briefly the general description of the absorption process to clarify the difference of our approach with the more common single-particle density of states (DOS) and multiple-scattering approaches. The x-ray-absorption cross section is given by³

$$\sigma(E_x) \sim \sum_f |(\phi_i | X | \phi_f)|^2 \delta(E_i + E_x - E_f), \quad (1)$$

where E_x , E_i , and E_f are, respectively, the energy of the photon, the initial state, and the final state. X is the perturbation acting on the system, which in this case is the absorption process of the photon, for which we will use the dipole approximation.³ ϕ_i and ϕ_f are the initial- and final-state wave functions. In the single-particle DOS approach, ϕ_i is taken as a core state and ϕ_f is an empty state, which is coupled via the dipole selection rules. For 2p x-ray absorption, the dipole-allowed transitions are $2p \rightarrow 3d$ and $2p \rightarrow 4s$, but as transitions to 3d states dominate over transitions to 4s states, the latter will be neglected. This leads to the expression

$$\sigma_{2p}(E_x) \sim |(\phi(2p) | X | \phi(3d))|^2 \mathcal{P}_{3d}(E_x - E_{2p}), \quad (2)$$

where $\mathcal{P}_{3d}(E)$ is the unoccupied 3d-projected DOS. The (projected) DOS is normally calculated using density-functional theory (DFT).⁴ For the description of x-ray absorption, real-space multiple-scattering (MS) methods,

which have been shown to be equivalent to DFT,⁵ are also used.

We follow another approach in treating the x-ray-absorption cross section. Our main assumption is that for 3d transition-metal compounds, the 3d-3d as well as the 2p-3d two-particle interactions are most important for the description of the 2p XAS spectrum. It is these two-particle interactions which define the ground state of the transition-metal ion and which split the XAS final state into a large number of configurations. In the single-particle DOS approximations, the 3d-3d and 2p-3d two-particle interactions are not included. Because we want to calculate them explicitly, we start with the calculation of the atomic multiplets, thereby neglecting all solid-state effects. In the atomic approach the 2p XAS cross section for $3d^N$ transition-metal ions is,

$$\sigma_{2p}(E_x) \sim \sum_j |(\phi_G(3d^N)_{O(3)} | X | \phi_{f_j}(2p^5 3d^{N+1})_{O(3)})|^2 \delta(E_G + E_x - E_{f_j}), \quad (3)$$

where $\phi_G(3d^N)_{O(3)}$ is the ground state of the $3d^N$ multiplet in spherical $O(3)$ symmetry. $\phi_{f_j}(2p^5 3d^{N+1})_{O(3)}$ is state j in the final-state atomic multiplet spectrum. To include solid-state effects, a cubic-crystal-field term is added to the Hamiltonian. The cubic crystal-field coupling is treated as a free parameter to be varied to obtain the best fit to experiment. Distortions from cubic symmetry are not considered.

In Sec II we repeat some general aspects of atomic multiplet theory as far as what is important for partly filled initial states. In Sec III we will present an overview of the effect of the cubic crystal field on the $3d^N$ to $2p^5 3d^{N+1}$ excitation for 14 common valencies of transition-metal ions. We will use crystal-field strengths between 0 and 2.5 eV. As examples for the validity of our method, we will compare the results with some high-

resolution experimental results of $3d$ transition-metal fluorides in Sec IV Section V describes possible reasons for discrepancies and possible refinements

II. THEORY

The calculations consist of three steps. First, the energy levels in the initial-state $3d^N$ multiplet and the final-state $2p^3 3d^{N+1}$ multiplet are calculated in $O(3)$ symmetry. Then the atomic multiplet spectrum is calculated by means of the dipole transition from the ground state (in the initial-state multiplet) to all final states. The third part is the projection of the $O(3)$ multiplets to cubic (O_h) symmetry.

A. Atomic multiplet spectrum

The Hamiltonian of the $3d^N$ initial-state multiplet consists only of the $3d$ - $3d$ Coulomb interaction (H_{dd}), which is developed in spherical harmonics.⁶ The radial parts F_{dd}^0 , F_{dd}^2 , and F_{dd}^4 are calculated within the Hartree-Fock (HF) limit and corrected by hand to 80% of the HF result to include intra-atomic configuration interaction (CI).⁷ The isotope interaction ($f_0 F_0^0$) does not affect the multiplet, but causes a shift in the average energy position. Our calculation is not suited for the calculation of the absolute energy position. Therefore, we simply shift our calculated multiplet for comparison to experiment. The multiplet splitting is determined by the multipole terms of the $3d$ - $3d$ interaction, F_{dd}^2 and F_{dd}^4 , which also determine the Hund's-rule ground state within the initial-state $3d^N$ multiplet.⁸ The $3d$ spin-orbit coupling is small and is neglected as hybridization and temperature effects will mix the spin-orbit-split states.

The $2p^3 3d^{N+1}$ final-state Hamiltonian is extended with two terms related to the $2p$ core hole: first, the spin-orbit coupling of the $2p$ hole (H_{LS}), which causes the division of the $2p$ edge into the $2p_{3/2}$ (L_3) and $2p_{1/2}$ (L_2). In our calculation we will always consider the full $2p$, thus $L_{2,3}$ spectrum. The second term which originates from the core hole is the $2p$ - $3d$ Coulomb and exchange interaction (H_{cd}). Again, the radial parts of the $2p$ - $3d$ Coulomb (F_{pd}^0 and F_{pd}^2) and exchange (G_{pd}^1 and G_{pd}^3) multipole interactions are calculated *ab initio*. The isotropical $2p$ - $3d$ Coulomb interaction $f_0 F_{pd}^0$ is equal for all final states (in a specific $2p^3 3d^{N+1}$ multiplet). The total Hamiltonian for the atomic multiplet then is

$$H_A = H_{dd} + H_{LS} + H_{cd}$$

B. Cubic-crystal-field effect on the $2p^3 3d^{N+1}$ multiplet

To simulate the solid we add an extra term to the Hamiltonian describing the cubic crystal field (H_{CCF}). In the present calculations we assume that the cubic-crystal-field parameter ($10Dq$) is equal for initial and final states.

In terms of group theory, the effect of a cubic crystal field is the reduction of symmetry from $O(3)$ to O_h . The group-theoretical treatment of the transformation from $O(3)$ symmetry to its subgroup O_h , further called $O(3)-O_h$

branching, can be found in Refs 9-11. In our paper on the d^0 compounds, we considered it in more detail.¹²

The cubic crystal field splits the initial-state multiplet. For small cubic crystal fields, the ground state does not change character and originates from the atomic ground state, which according to Hund's rules is high spin. For strong crystal fields a change of character can occur and the ground state can become low spin. That is, it originates from an excited state in the initial-state atomic multiplet. The general results of the influence of the cubic crystal field on the initial-state $3d^N$ multiplet can be found in the Tanabe-Sugano diagrams.¹³

The crystal field also splits the final-state multiplet. If the character of the ground state is not changed from the atomic situation, the same final states are reached. In this case the changes in the spectrum are a result from the crystal-field effect on the final state. Levels are split and/or shifted, and the transition matrix elements are modified due to changes in the final-state wave functions. This modifies the spectrum. If a change of the ground-state character occurs, this is immediately visible in the spectral shape as the dipole transitions from this new ground state reach a totally new set of final states. The dipole transition operator is not split in cubic symmetry, which means that no polarization dependence can occur.

In the Hamiltonian we neglect all other crystal-field couplings related to lower symmetries, taken together in H_{LCF} , the $3d$ spin-orbit coupling, (H_{LS}), magnetic interactions (H_{ex}), and any form of CI, intra-atomic (e.g., $3d^{N-1}4p$) as well as extra-atomic (e.g., $3d^{N+1}L_k$). H_{LCF} , H_{LS} , and H_{ex} all will influence the ground-state character. But for the total, polarization-averaged XAS spectrum their influence is negligible as the effects on the final-state multiplet are too small. However, for polarization-dependent XAS measurements, a more accurate determination of the character of the ground state is needed and some extra terms will have to be added to the Hamiltonian. In Sec V we will discuss possible refinements of the calculations in more detail.

III. CALCULATIONS

The intra-atomic interaction parameters, as calculated in the Hartree-Fock limit, are collected in Table I. The Coulomb and exchange parameters (F_{dd}^2 , F_{dd}^4 , F_{pd}^2 , G_{pd}^1 , and G_{pd}^3) are renormalized to 80% of the HF values to account for intra-atomic CI. The multiplet of the $3d^N$ initial state and the $2p^3 3d^{N+1}$ are calculated, and the ground state $\phi_G(3d^N)_{O(3)}$ is determined. The XAS cross section is calculated. According to Eq (3), the result is a series of lines at energies ($E_G - E_{fj}$) with respective intensities $|\langle \phi_G(3d^N)_{O(3)} | X | \phi_{fj}(2p^3 3d^{N+1})_{O(3)} \rangle|^2$. Figure 1 gives the atomic multiplet for $d^5 Mn^{2+}$. Addition of the cubic-crystal-field changes the energy positions and matrix elements. Figure 2 shows the result if the cubic-crystal-field parameter ($10Dq$) is 0.9 eV.

To compare with experiment, the spectra have to be broadened. Besides the experimental broadening, there are several intrinsic broadening mechanisms. These include lifetime effects, vibrations, and hybridization (covalency), all of which are compound and final state

dependent. Because of the hundreds of (unresolvable) final states, this creates an enormous problem to solve quantitatively. For compounds with a $3d^0$ ground state, information of the final-state dependence of the broadening can be found experimentally as each of the main multiplet lines can be resolved.¹² Analysis showed that for fluorides, vibrational broadening dominates, but for ox-

ides, also covalence causes broadening. A general result is that the lifetime broadening of the L_2 part is increased due to the opening of Coster-Kronig Auger decay channels. As a detailed analysis of the broadening is not possible from XAS alone, we decided to use an equal broadening for every line. For the L_3 part, a Lorentzian broadening with $\sigma = 0.1$ eV (Ref. 14) is used; for the L_2

TABLE I Hartree-Fock values of the parameters used in the multiplet calculation. Given are the multipole terms of the $3d$ - $3d$ interaction (F_{dd}^2 and F_{dd}^4) of the ground and final states. The final-state $3d$ -spin-orbit interaction ($L \cdot S_d$), $2p$ -hole-spin-orbit interaction ($L \cdot S_p$), and multipole terms of the $2p$ - $3d$ interaction (F_{pd}^2 , G_{pd}^1 , and G_{pd}^3). In the actual multiplet calculation, the multipole terms are normalized to 80% of their *ab initio* value, to account for intra-atomic configuration interaction (all values in eV)

d_n	Ion	F_{dd}^2		F_{dd}^4		$L \cdot S_d$	$L \cdot S_p$
		final states	(g.s.)	final states	(g.s.)		
d^1	Ti^{1+}	10 343	(0 000)	6 499	(0 000)	0.027	3 776
	V^{4+}	11 965	(0 000)	7.554	(0.000)	0.042	4.650
d^2	V^{1+}	10 974	(10.127)	6 888	(6 354)	0.036	4.649
d^3	Cr^{1+}	11.596	(10.777)	7.270	(6 755)	0.047	5.667
	Mn^{4+}	13 177	(12.416)	8.299	(7 820)	0.066	6 845
d^4	Cr^{2+}	10.522	(9.649)	6 552	(6.002)	0.041	5.668
	Mn^{1+}	12 210	(11 415)	7.649	(7 148)	0 059	6 845
d^4	Mn^{2+}	11 155	(10.316)	6.943	(6.414)	0.053	6.846
	Fe^{1+}	12 818	(12.043)	8.023	(7 535)	0 074	8.199
d^6	Fe^{2+}	11 779	(10 966)	7 327	(6 815)	0 067	8 200
	Co^{1+}	13.422	(12.663)	8.395	(7.917)	0 092	9.748
d^7	Co^{2+}	12 396	(11 605)	7 708	(7 209)	0.083	9 746
	Ni^{1+}	14.022	(13.277)	8.764	(8 295)	0.112	11.506
d^8	Ni^{2+}	0 000	(12 234)	0 000	(7.598)	0.102	11 507
d_n	Ion	F_{pd}^2		G_{pd}^1		G_{pd}^3	
d^1	Ti^{1+}	5.581		3 991		2.268	
	V^{4+}	6 759		5.014		2.853	
d^2	V^{1+}	6 057		4.392		2.496	
d^3	Cr^{1+}	6 526		4.788		2.722	
	Mn^{4+}	7 658		5.776		3.288	
d^4	Cr^{2+}	5 841		4.024		2.388	
	Mn^{1+}	6.988		5.179		2 945	
d^5	Mn^{2+}	6 321		4.606		2 618	
	Fe^{1+}	7 446		5.566		3.166	
d^6	Fe^{2+}	6.793		5 004		2 844	
	Co^{1+}	7.900		5 951		3 386	
d^7	Co^{2+}	7 260		5 397		3 069	
	Ni^{1+}	8.350		6.332		3.603	
d^8	Ni^{2+}	7 721		5.787		3 291	

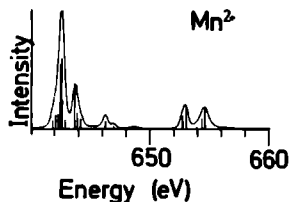


FIG. 1. Mn^{2+} $3d^1$ to $2p^3 3d^5$ atomic multiplet spectrum. The line spectrum is broadened as described in the text.

part, $\sigma' = 0.3$ eV. Then the spectra are convoluted with a Gaussian with $\sigma = 0.15$ eV. We expect these broadening procedures to represent early transition-metal fluoride spectra taken with the present high-resolution monochromators¹ Oxide and late transition-metal fluoride spectra will in general be broader (see Sec. V). Figures 1 and 2 show the effect of the broadening procedure on the two Mn^{2+} multiplet spectra.

Figures 3–16 show the effect of increasing cubic crystal field on the x-ray-absorption spectrum. The calculated energy scale is used; for comparison to experiment the spectra will have to be shifted over some eV (see Sec. IV). The $10Dq$ value is given on the right. The changes as a function of $10Dq$ are in general smooth and reflect the influence of the cubic crystal field on the final-state multiplet as discussed in Sec. II. In cases where the ground state changes character, from high to low spin, a sudden change in the spectral shape occurs as a new subset of final states is reached. This is visible for, e.g., Cr^{2+} (d^4) and Co^{3+} (d^6) between 2.1 and 2.4 eV. Because of the clear difference between high- and low-spin spectra, the actual situation is easy to determine from experiment. Some care has to be taken because the presented calculations are performed in a standard way and do not give the $10Dq$ value for this transition very accurately. Furthermore, $10Dq$ can be slightly different in initial and final states. There is no problem to include this, but it does need dedicated, compound-specific calculations.

Two ions with an equal number of $3d$ electrons, such as $d^1 \text{V}^{4+}$ and Ti^{3+} , have a similar atomic multiplet spectrum. The only differences are the atomic parameter values of the intra-atomic interactions (see Table I),

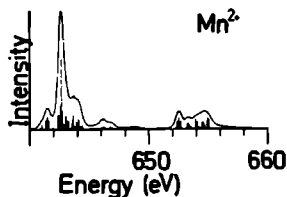


FIG. 2. Mn^{2+} $3d^1$ to $2p^3 3d^5$ multiplet spectrum, projected to O_h . The cubic-crystal-field parameter ($10Dq$) is 0.9 eV. The line spectrum is broadened as described in the text.

60

which slightly modify the spectra.

However, more important is the fact that multiplets do change significantly as the number of $3d$ electrons is changed. Compare for example, Mn^{2+} , Mn^{3+} , and Mn^{4+} . Besides the shift to higher energy with higher valency, the spectral shape does change significantly, which makes determination of the valency, and its cubic-crystal-field splitting, straightforward.

IV. COMPARISON TO EXPERIMENT

To show the validity of our approach, we make a comparison to some high-resolution $2p$ x-ray-absorption data of transition-metal fluorides obtained with the Dragon monochromator by Chen and Sette.¹⁵

In our paper on the $3d^0$ compounds, we showed the excellent agreement with potassium, calcium, scandium, and titanium oxides and fluorides. As the final-state $p^5 d^1$ is simple and well resolved, it was possible to obtain detailed information, such as individual broadenings for each state. Such detailed analysis is not possible for the $p^5 d^{N+1}$ multiplets (for $N > 0$), as the individual lines are not resolved (there are typically 600 lines spread over 20 eV). Therefore, the standard broadening as discussed in Sec. III is used.

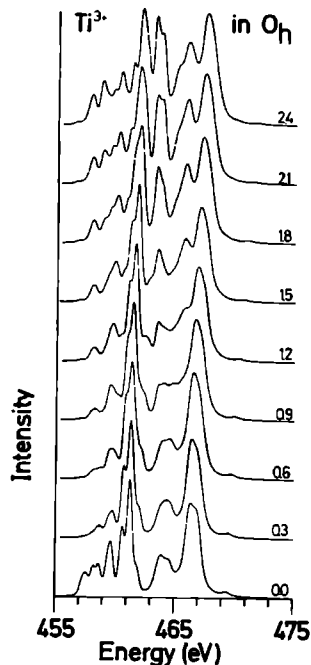


FIG. 3. Ti^{3+} $3d^1$ to $2p^3 3d^2$ transition in cubic crystal fields. $10Dq$ ranges from 0.0 (bottom) to 2.4 eV.

In Fig. 17 the theoretical spectra of V^{3+} (d^2), Mn^{2+} (d^5), and Co^{2+} (d^7) are compared with the experimental spectra of VF_3 , MnF_2 , and CoF_2 (see Table II for the crystal structures) as obtained with the Dragon,¹³ The cubic-crystal-field parameters ($10Dq$) used are, respectively, 1.5, 0.75, and 0.75 eV. The overall agreement found is good for all compounds. From this we conclude that the atomic multiplet approach with the inclusion of the cubic crystal field gives a good description of all spectral details of the $2p$ x-ray-absorption spectra of $3d$ transition-metal fluorides. This also shows that the tetragonal symmetry of the metal site in CoF_2 and MnF_2 (Table II) is a too-small distortion from cubic symmetry to cause clear disagreement between experiment and the present cubic symmetry simulation. However, for the description of polarization-dependent spectra of a tetragonal site, the inclusion of the exact lower symmetry is absolutely necessary. In other words, with polarization-dependent measurements small tetragonal distortions will show up. Unfortunately, a rutile crystal structure is not suitable for polarization-dependent studies because of different orientations of the tetragonal sites.

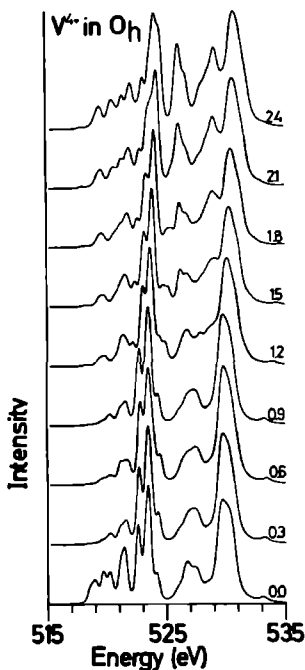


FIG. 4. V^{4+} $3d^1$ to $2p^1 3d^2$ transition in cubic crystal fields. $10Dq$ ranges from 0.0 (bottom) to 2.4 eV.

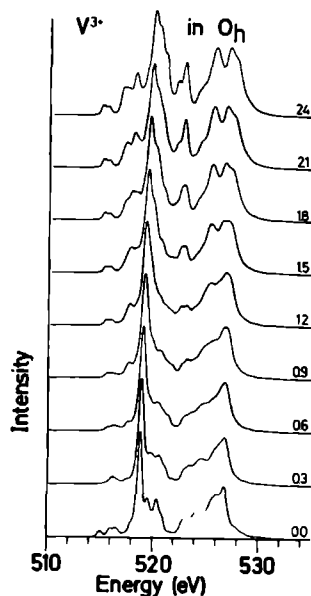


FIG. 5. V^{3+} $3d^2$ to $2p^1 3d^1$ transition in cubic crystal fields. $10Dq$ ranges from 0.0 (bottom) to 2.4 eV.

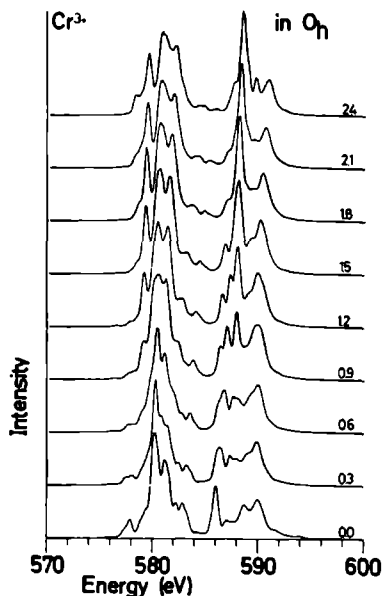


FIG. 6. Cr^{3+} $3d^3$ to $2p^1 3d^4$ transition in cubic crystal fields. $10Dq$ ranges from 0.0 (bottom) to 2.4 eV.

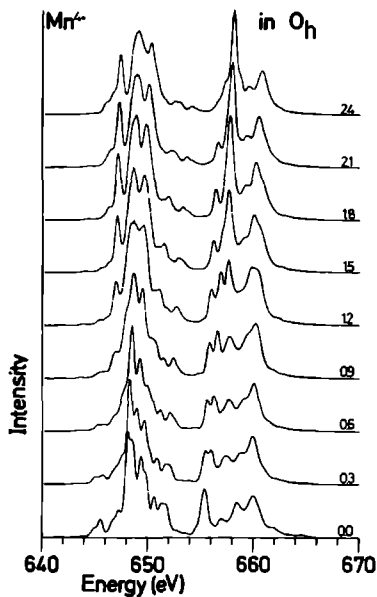


FIG. 7. $Mn^{4+} 3d^1$ to $2p^1 3d^4$ transition in cubic crystal fields. $10Dq$ ranges from 0.0 (bottom) to 2.4 eV

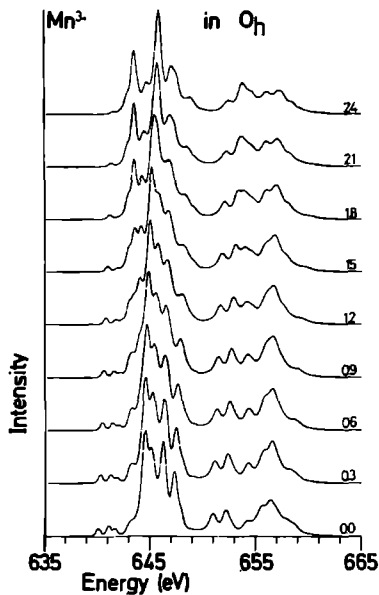


FIG. 9. $Mn^{3+} 3d^4$ to $2p^1 3d^4$ transition in cubic crystal fields. $10Dq$ ranges from 0.0 (bottom) to 2.4 eV

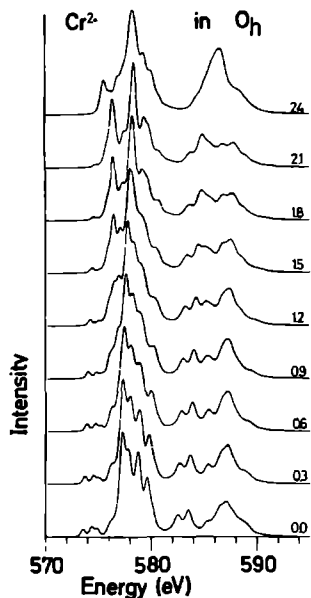


FIG. 8. $Cr^{2+} 3d^4$ to $2p^1 3d^4$ transition in cubic crystal fields. $10Dq$ ranges from 0.0 (bottom) to 2.4 eV

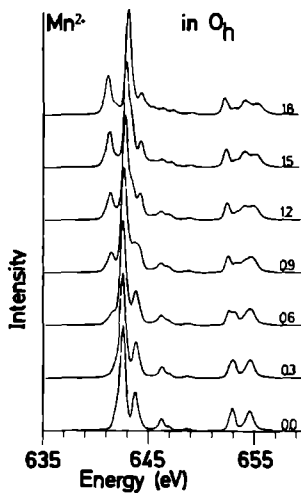


FIG. 10. $Mn^{2+} 3d^5$ to $2p^1 3d^5$ transition in cubic crystal fields. $10Dq$ ranges from 0.0 (bottom) to 1.8 eV.

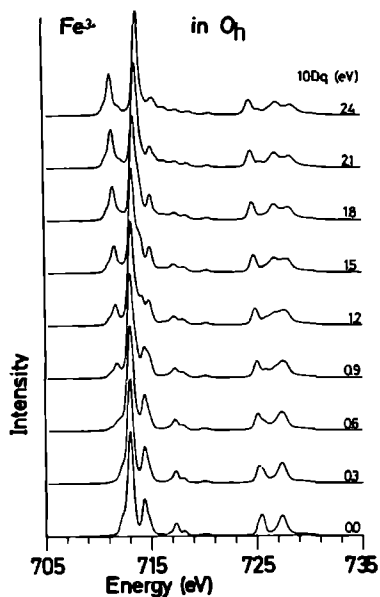


FIG. 11. $\text{Fe}^{2+} 3d^6$ to $2p^5 3d^6$ transition in cubic crystal fields. $10Dq$ ranges from 0.0 (bottom) to 2.4 eV

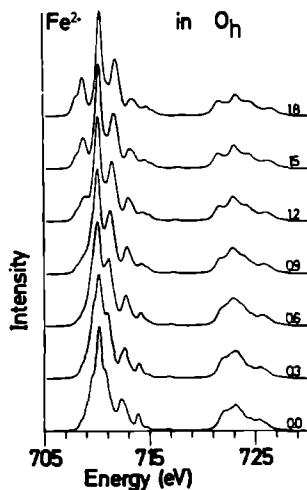


FIG. 12. $\text{Fe}^{2+} 3d^6$ to $2p^5 3d^7$ transition in cubic crystal fields. $10Dq$ ranges from 0.0 (bottom) to 1.8 eV.

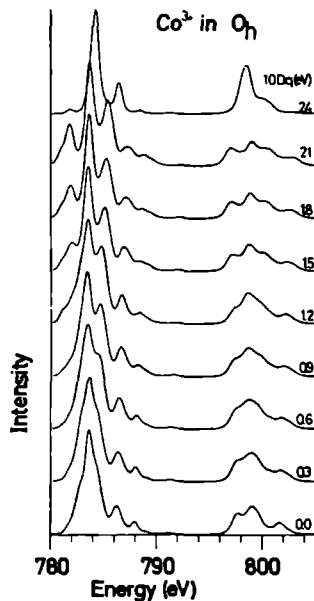


FIG. 13. $\text{Co}^{3+} 3d^6$ to $2p^5 3d^7$ transition in cubic crystal fields. $10Dq$ ranges from 0.0 (bottom) to 2.4 eV

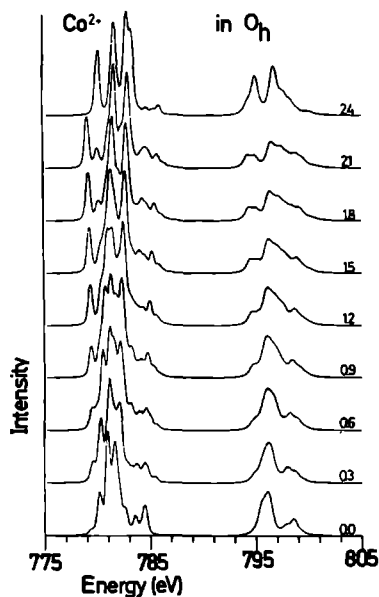


FIG. 14. $\text{Co}^{2+} 3d^7$ to $2p^5 3d^8$ transition in cubic crystal fields. $10Dq$ ranges from 0.0 (bottom) to 2.4 eV.

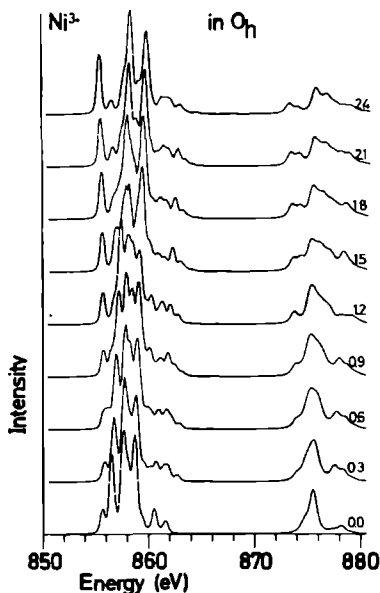


FIG 15 $Ni^{3+} 3d^7$ to $2p^5 3d^8$ transition in cubic crystal fields $10Dq$ ranges from 0.0 (bottom) to 2.4 eV

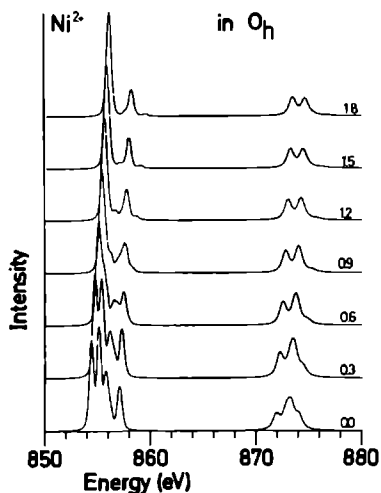


FIG 16. $Ni^{2+} 3d^8$ to $2p^5 3d^9$ transition in cubic crystal fields $10Dq$ ranges from 0.0 (bottom) to 2.4 eV.

V. LIMITATIONS OF THIS APPROACH

There are two main limitations in the present approach to explain the $2p$ x-ray-absorption edges. First, the character of the ground state is not considered in detail. Second, the effects on the spectral shape of hybridization, vibrations, lifetime, and experimental resolution are treated very roughly as a general Lorentzian-plus-Gaussian broadening.

In Sec. II we already mentioned the necessity to include the exact lower-site symmetries (H_{LCF}), magnetic

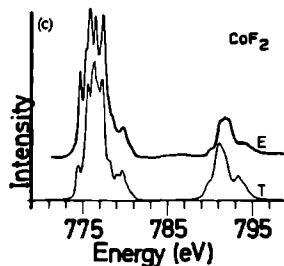
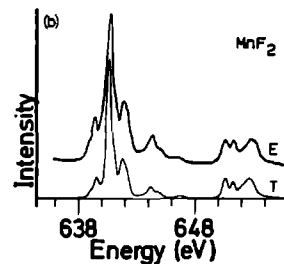
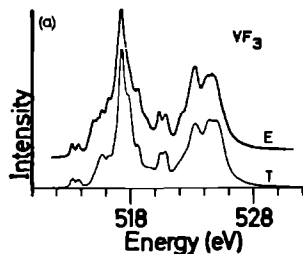


FIG. 17 $2p$ x-ray-absorption spectra of (a) VF_3 , (b) MnF_2 , and (c) CoF_2 , compared, respectively, with the d^2V^{1+} (1.5 eV), the d^4Mn^{2+} (0.75 eV), and the d^7Co^{2+} (0.75 eV) multiplet calculations. The used values of $10Dq$ are given in parentheses. The theoretical spectra are shifted, by about 2 eV to lower energy, to align with experiment

TABLE II Crystal structures of the 3d transition metal fluorides (Ref 26)

Compound	Crystal structure	Point group of metal ion
VF ₃	(intermediate) close packed	O _h (octahedral)
MnF ₂	rutile	D _{4h} (tetragonal)
CoF ₂	rutile	D _{4h} (tetragonal)

field effects (H_{ex}), and 3d spin-orbit coupling (H_{LS}) to describe the character of the ground state more accurately. H_{LCF} and H_{ex} will not influence the polarization-averaged spectral shape because the effects are generally too small to be seen in the final-state multiplet. That is, even if they modify the ground-state character considerably, the polarization-averaged (ρ) matrix elements hardly change. Only for strongly distorted sites can a visible effect be expected. However, for the polarization-dependent spectra, knowledge of the ground-state character is crucial for the determination of the respective matrix elements for $\Delta m = +1$, -1 , or 0.^{16,17} Then the interplay of H_{LCF} , H_{ex} , and H_{LS} will determine the exact ground state and, consequently, the differences in spectral shape for linear (difference between $\Delta m = 0$ and $+1/-1$) and circular (difference between $\Delta m = 1$ and -1) dichroism.

The 3d spin-orbit coupling might influence the spectral shape for solids. Its influence on the polarization-averaged spectra will be directly evident from the branching ratio between L_1 and L_2 .¹⁸ Its influence will be largest, if present at all, for the late 3d transition metals (see Table I), and indeed for CoF₂ [see Fig. 17(c)] the branching ratio, as well as the total spectral shape, is improved if the 3d spin-orbit coupling is included.¹⁹

We now turn to the second limitation, the use of an equal broadening for all final states in the L_1 and L_2 parts to simulate effects such as hybridization, vibrations, and lifetime. These effects will be different for every compound and even for every line in the 600-line final-state multiplet, making a detailed description totally out of reach. However, some aspects are becoming clear. For the d^0 compounds it was shown that the e_g -like states show more broadening than the t_{2g} -like states, which we related to vibrational effects. For the $2p^5 3d^{N+1}$ multiplets such conclusions cannot be drawn, but similar effects can be expected.

Hybridization, which can be treated as extra-atomic configuration interaction, will modify the spectrum considerably. Especially for more covalent materials, such as oxides, the amount of extra-atomic configuration interaction cannot be neglected. The coupling of $3d^N$ with $3d^{N+1}L$ becomes more prominent, introducing more $3d^{N+1}L$ character in the ground state. These aspects can be taken into account by performing a real CI calculation, as was done for the early 3d transition metals²⁰ and for the nickel-dihalides.²¹ For the cases considered here, such a CI approach is at present not a routine task, but this line will certainly be followed in future efforts.

An alternative route is to include the effects of hybridization effectively in the atomic multiplet calculations. Hybridization, the mixing of the transition metal 3d orbitals with the ligand p orbitals, has the effect of delocal-

izing the d functions, thereby reducing their mutual interactions—the nephelauxetic effect.²² This effect can be simulated by an extra reduction of the two-particle interaction parameters F_{dd}^2 and F_{dd}^4 . Also the final-state interactions with the core hole will be affected. Preliminary calculations, where we reduced all parameters by the same amount, are encouraging, although the possible accuracy has to be investigated,²³ and shake-up satellites will not be reproduced properly.

The last effect which is not treated in detail is the lifetime broadening. It can be expected that the lifetime is different for about everyone of the 600 final states. The states at higher energy can lose energy by Coster-Kronig-like Auger decay to lower states, and the other decay routes will be different also. This problem relates to the more general question of the coupling of core-hole creation and decay, and its influence on the spectral shape of the different spectroscopic techniques. The answer will have to be formed by a combination of normal x-ray absorption and x-ray photoemission with "resonance" experiments, in which the x-ray energy is scanned through the $L_{2,3}$ XAS energy range, and the resulting x-ray-emission spectra,²⁴ Auger spectra,²⁵ and/or photoemission spectra are measured.

VI CONCLUDING REMARKS

We have shown that the atomic multiplet approach with the inclusion of the cubic crystal field reproduces the metal 2p x-ray-absorption spectra of 3d transition-metal fluorides. For more covalent compounds, such as oxides, the presented spectra are probably less accurate, although this remains to be checked. As discussed, this can be improved upon by an effective reduction of the 3d-3d Coulomb interactions. By comparison to experiment an accurate measure of the crystal-field-strength parameter $10Dq$ can be obtained. In fact, the final-state value of $10Dq$ is found, which can be different from the "initial"-state values that are found by optical spectroscopy. A study of this would be of quite some interest.

The field of application of the atomic multiplet plus crystal-field approach as presented here will probably be limited to the more ionic 3d transition-metal compounds. For the pure metals and alloys, band-structure effects may be of equal or greater importance than the atomic multiplet effects.²⁰ A systematic experimental study of band-versus-atomic effects would be of great interest in this regard.

ACKNOWLEDGMENTS

We are grateful to C. T. Chen and Francesco Sette for making available their unpublished results of the

transition-metal fluorides, taken with the high-resolution Dragon monochromator. This study was supported in part by the Dutch Foundation for Chemical Research [Stichting Scheikundig Onderzoek in Nederland (SON)] with financial assistance of the Netherlands Organization

for Scientific Research [Nederlandse Organisatie voor wetenschappelijk Onderzoek (NWO)], and by the Committee for the European Development of Science and Technology (CODEST) Program

- ¹A resolution up to 1 10000 is reached by the Dragon monochromator at Brookhaven National Laboratory (Upton, NY). C T Chen, *Nucl Instrum Methods A* **256**, 595 (1987). Other high-resolution monochromators in the 300–800-eV range include the SX700 at BESSY, Berlin. H Petersen, *ibid* **246**, 260 (1986), and the 10-m-focal-length grazing-incidence monochromator at the Photon Factory. H Maezawa, S Nakai, S Mitani, A Mikuni, T Namiooka, and T Sasaki, *ibid* **246**, 310 (1986).
- ²T Yamaguchi, S Shibuya, and S Sugano, *J Phys C* **15**, 2625 (1982), T Yamaguchi, S Shibuya, S Suga, and S Shin, *ibid* **15**, 2641 (1982).
- ³S Gasiorowicz, *Quantum Physics* (Wiley, New York, 1974), Chap 22.
- ⁴The use of DFT for x-ray absorption is worked out in J E Müller and J W Wilkins, *Phys Rev B* **29**, 4331 (1984).
- ⁵C R Natoli and M Benfatto, *J Phys Colloq* **47**, C8-11 (1986).
- ⁶The theoretical basis for this method can be found in R D Cowan, *J Opt Soc Am* **58**, 808 (1968), and R D Cowan, *The Theory of Atomic Structure and Spectra* (University of California Press, Berkeley, 1981).
- ⁷R D Cowan, *The Theory of Atomic Structure and Spectra* (University of California Press, Berkeley, 1981), p 464, and references therein.
- ⁸See, e.g., C J Ballhausen, *Introduction to Ligand Field Theory* (McGraw-Hill, New York, 1962).
- ⁹P H Butler, *Point Group Symmetry, Applications, Methods and Tables* (Plenum, New York, 1981).
- ¹⁰J R Derome and W T Sharp, *J Math Phys* **6**, 1584 (1965).
- ¹¹P H Butler and B G Wybourne, *Int J Quantum Chem* **10**, 581 (1976).
- ¹²F M F de Groot, J C Fuggle, B T Thole, and G A

- Sawatzky, *Phys Rev B* **41**, 928 (1990).
- ¹³S Sugano, Y Tanabe, and H Kamimura, *Multiplets of Transition Metal Ions in Crystals* (Academic, New York, 1970), Chap 5 1.
- ¹⁴For the late 3d transition metals, the Lorentzian broadening of 0.1 eV is too small, as only lifetime effects will cause a larger broadening. See, e.g., J C Fuggle and S Alvarado, *Phys Rev A* **22**, 1615 (1980), and references therein.
- ¹⁵C T Chen and F Sette (private communication).
- ¹⁶R D Cowan, Ref 7, p 403.
- ¹⁷We have made several observations of such effects in cooperation with various other groups, and these will be published in the near future.
- ¹⁸B T Thole and G van der Laan, *Phys Rev B* **38**, 3158 (1988).
- ¹⁹F M F de Groot (unpublished).
- ²⁰J Fink, Th Müller-Heinzerling, B Scheerer, W Speier, F U Hillebrecht, J C Fuggle, J Zaanen, and G A Sawatzky, *Phys Rev B* **32**, 4899 (1985), J Zaanen, G A Sawatzky, J Fink, W Speier, and J C Fuggle, *ibid* **32**, 4905 (1985).
- ²¹J Zaanen, C Westra, and G A Sawatzky, *Phys Rev B* **33**, 8060 (1986).
- ²²C K Jorgensen, *Absorption Spectra and Chemical Bonding in Complexes* (Pergamon, Oxford, 1962), Chap 8.
- ²³F M F de Groot *et al* (unpublished).
- ²⁴J -E Rubensson, D Mueller, R Schuker, D L Ederer, C H Zhang, J Jia, and T A Callcott, *Phys Rev Lett* **64**, 1047 (1990).
- ²⁵D D Sarma, C Carbone, P Sen, and W Gudat, *Phys Rev B* **40**, 12 542 (1989).
- ²⁶A F Wells, *Structural Inorganic Chemistry*, 4th ed (Clarendon, Oxford, 1975), pp 350–355, and references therein.

3.5. Spin-orbit coupling and non-cubic symmetries

In sections 3.2 to 3.4 the ground state of the partly filled $3d$ -band is assumed not to be influenced by the $3d$ -spin-orbit coupling. In this section the limits of this approximation are investigated. The treatment of the $3d$ -spin-orbit coupling in the crystal field multiplet program are discussed and arguments are given concerning the actual physical effects of the spin-orbit coupling.

For the projection of the spin symmetries from spherical to cubic symmetry the same branching rules as for the angular momentum apply. Compounds with an even number of $3d$ electrons have an integer spin and the branching rules as given in table 3.4 can be used. For compounds with an odd number of $3d$ electrons the spin will be $1/2$, $3/2$ or $5/2$. The atomic $S = 1/2$ state projects to E_1 -symmetry in a cubic crystal field. Similarly $S = 3/2$ projects to G -symmetry and $S = 5/2$ is split into states of E_2 -symmetry and of G -symmetry.

state	symmetry	spin-projection	overall symmetry	degeneracy
$3d^1$	2T_2	E_1	$E_2 + G$	2
$3d^2$	3T_1	T_1	$E + T_1 + T_2 + A_1$	4
$3d^3$	4A_2	G	G	1
$3d_{HS}^4$	5E	$E + T_2$	$A_1 + A_2 + E + T_1 + T_2$	5
$3d_{LS}^4$	3T_1	T_1	$E + T_1 + T_2 + A_1$	4
$3d_{HS}^5$	6A_1	$G + E_2$	$G + E_2$	2
$3d_{LS}^5$	2T_2	E_1	$E_2 + G$	2
$3d_{HS}^6$	5T_2	$E + T_2$	$A_1 + E + 2 \cdot T_1 + 2 \cdot T_2$	6
$3d_{LS}^6$	1A_1	A_1	A_1	1
$3d_{HS}^7$	4T_1	G	$E_1 + E_2 + 2 \cdot G$	4
$3d_{LS}^7$	2E	E_1	G	1
$3d^8$	3A_2	T_1	T_2	1
$3d^9$	2E	E_1	G	1

Table 3.7: Effects of spin-orbit coupling on $3d^N$ ground state

If the $3d$ spin-orbit coupling is taken into consideration, the overall symmetry of the spin plus the angular momentum must be determined. In spherical symmetry this is accomplished by multiplying L with S to all possible J 's. Similarly in cubic symmetry the irreducible representations of the spin must be multiplied with those of the angular momentum. Table 3.7 gives the results for the low-spin and high-spin configurations of all $3d^N$ states. It can be seen that in cubic symmetry the multiplicity of the spin $(2S+1)$ does not directly relate to the total number of states. For example the 5T_2 state is split in six (and not in five!) different states. The crystal field multiplet program uses in all cases the branchings for both spin and angular momentum and thus the overall symmetries of the states as given in table 3.7. If the $3d$ spin-orbit coupling is neglected all states with the same angular symmetry are degenerate because the spin in itself does not influence the energy of

the state.

3.5.1. Effects of 3d spin-orbit coupling

3d spin-orbit coupling has a large effect on partly filled t_{2g} states, that is the ground states of the $3d^1$, $3d^2$, $3d_{LS}^4$, $3d_{LS}^5$, $3d_{HS}^6$ and $3d_{HS}^7$ symmetries. The effects on states of E -symmetry are considerably smaller [12]. The difference in effect on T_2 -states respectively E -states is directly related to the way in which a t_{2g} , respectively an e_g wavefunction is build from the atomic wavefunctions. As has been shown in table 3.3 an e_g wavefunction can be build from $m_l = 0$ or 2 (or -2) functions. A spin-orbit coupling effect can only affect states which differ by one in their m_l -value, hence in first order the e_g states are not affected, in contrast to the t_{2g} states (See for example Ref. 12 for the mathematical details). Spin-orbit coupling does not affect states of A_1 or A_2 symmetry.

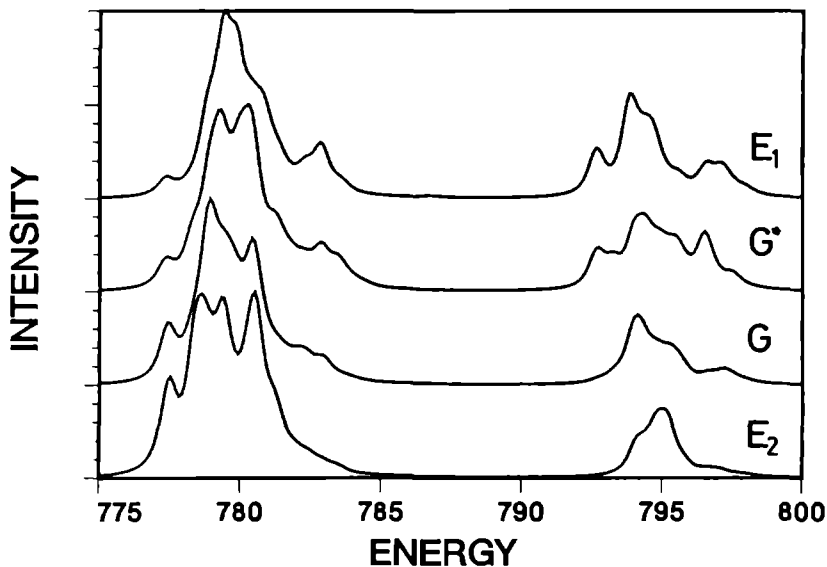


Figure 3.11: Theoretical x-ray absorption spectra for the $3d_{HS}^7[\Gamma_1] \rightarrow 2p^5 3d^8$ transition for the four different 3d spin-orbit split symmetries of the 4T_1 ground state. The respective symmetries are from bottom to top: E_2 , G , G^* and E_1 .

The magnitudes of the 3d spin-orbit coupling of the 3d-metal ions were given in section 3.3. Because the spin-orbit coupling strength increases with the atomic number, the best case to investigate the effect of 3d spin-orbit coupling is the $3d_{HS}^7$ configuration. The $3d_{HS}^7$ ground state configuration is found in for example CoF_2 and CoO . In section 3.4 the CoF_2 spectrum is compared with a crystal field multiplet calculation in which the 3d spin-orbit coupling is neglected. From table 3.7 it is found that if 3d spin-orbit coupling

is included, the 4T_1 ground state of the $3d_{HS}^7$ -configuration splits in four states of E_1 , E_2 and two times G -symmetry. The actual multiplet calculation with the atomic value of the $3d$ spin-orbit coupling (83 meV) and a cubic crystal field strength of 0.9 eV gives the four states at energies of respectively 0 (E_2), 44 meV (G), 115 meV (G^*) and 128 meV (E_1). Figure 3.11 gives the crystal field multiplets of the $3d_{HS}^7[\Gamma_1] \rightarrow 2p^5 3d^8$ transition for the four different symmetries. Given this spread in the initial states, the room temperature (25 meV) spectrum is dominated by the lowest state of E_2 -symmetry, with a 17% contribution of the first excited state of G -symmetry.

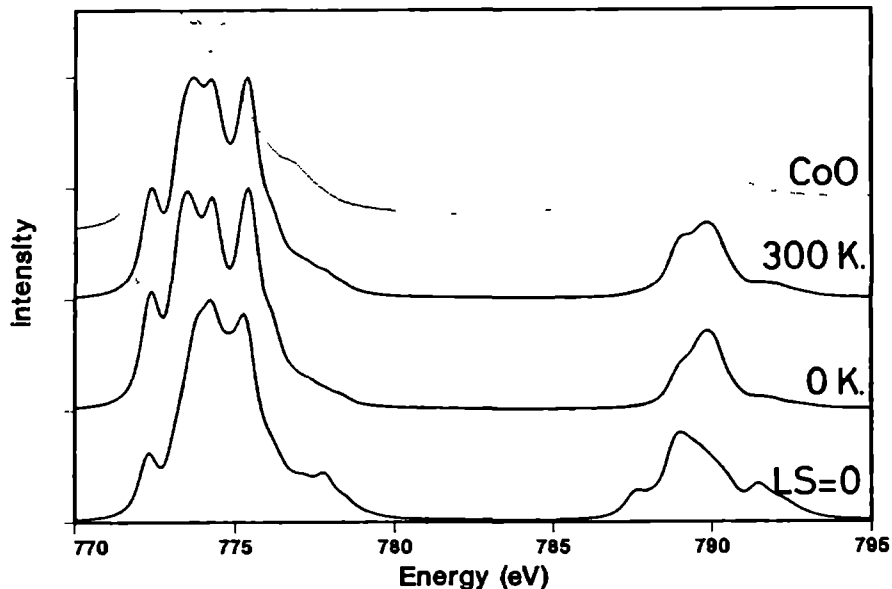


Figure 3.12: Comparison of the theoretical spectra of (from bottom to top) (a) the spectrum under neglect of $3d$ spin orbit coupling, (b) the ground state, and (c) the spectrum at 300 Kelvin, with the experimental spectrum of CoO.

Figure 3.12 gives the theoretical spectra corresponding respectively to the ground state E_2 spectrum, the 300 Kelvin spectrum and the spectrum under neglect of $3d$ spin-orbit coupling. It is clear that the inclusion of the $3d$ spin-orbit coupling enhances the agreement considerably. The good agreement between theory and experiment makes it possible to determine the energies of the low-lying excited states from an analysis of the experimental spectrum, preferably measured for a series of temperatures. Hence it can be concluded that in potential temperature dependent x-ray absorption experiments can reveal the magnitude of the $3d$ spin-orbit coupling (which can differ from the atomic value).

Above it has been shown that the $3d$ spin-orbit coupling has a detectable influence on the spectral shape of divalent cobalt $3d_{HS}^7$ -compounds. Another configuration which is influenced considerably is $3d_{LS}^4$, which has 3T_1 -symmetry and splits in four states if the $3d$

spin-orbit coupling is included. The trivalent manganese oxides have a $3d^4$ ground state. In these compounds the cubic crystal field strength is approximately equal to the effective exchange splitting which places the trivalent manganese oxides close to the high-spin low-spin transition point. As a result of $3d$ spin-orbit coupling the low-spin 3T_1 -state splits in four and the high-spin 5E -state splits in five though its actual splittings will be small. In table 3.7 it can be checked that the overall symmetries of the spin-orbit split high-spin and low-spin states contain E , T_1 , T_2 and A_1 irreducible representations. Hence, if the high-spin and low-spin states are close to degenerate these representations are allowed to form bonding and anti-bonding admixtures. The spin-state of these combinations (thus of the ground state) will not be pure high-spin ($S=2$) or low-spin ($S=1$) but have an effective spin-state with S in between 1 and 2. This concept will be used in section 4.3 to explain the spectral shape of the manganese $2p$ x-ray absorption spectrum of LiMnO_2 . The formation of admixtures of spin states has been used also in a study of iron phthalocyanine ($3d^6$ in a D_{4h} point group) by Thole et al. [84].

3.5.2. Effects of non-cubic symmetries

Another type of low-energy splittings of the crystal field multiplet is caused by distortions from cubic symmetry. A difference can be made between initial state effects and final state effects. Initial state splittings can be important for room temperature experiments if they are of the order of 25 meV. Final state effects will be visible only if they cause spectral changes over an energy range of about 200 meV or more (depending on the specific multiplet, amount of covalency, etc). From this consideration it might be expected that initial state effects of symmetry distortions from cubic symmetry will cause large spectral changes in almost all compounds. However if the actual effects of the lower crystal fields on the spectral shapes are studied it is found that even if a symmetry distortion causes initial state splittings of the order of 100 meV, the spectral shape of the ground state is hardly modified from the spectral shape of the ground state of the non-distorted spectrum. Hence in order to show a visible effect on the spectral shape the demand of initial state splittings of the order of 25 meV is in itself not enough to cause spectral changes, and considerably larger splittings are needed. In this respect it is important to notice that a splitting of 50 meV will show drastic effects on the spectral shape if caused by $3d$ spin-orbit coupling, but the same splitting will cause hardly any effect if caused by distortions from cubic symmetry.

Large initial state effects of lower symmetries are found if the cubic $3d^N$ ground state contains a partly filled e_g band. Elongation of the z -axis lifts the degeneracy of the e_g orbitals: the Jahn-Teller effect [85]. A similar effect occurs in case of a partly filled t_{2g} , but the energy effects of the tetragonal distortion are larger for partly filled e_g -states. (Notice that in contrast $3d$ spin-orbit coupling has a considerably larger effect on partly filled t_{2g} -states) Partly filled e_g states occur for $3d_{HS}^4$, $3d_{LS}^7$ and $3d^9$. The effects on the $3d_{HS}^4$ -state are well-known for divalent chromium-compounds. As discussed above in the trivalent manganese oxides the high-spin and low-spin configuration are close to degenerate, and the Jahn-Teller distortion of the high-spin state will further complicate the analysis (see the discussion of LiMnO_2 in section 4.3). The $3d_{LS}^7$ -configuration does not occur as such and for

example the 'low-spin like' trivalent nickel compounds are dominated by $3d^8 \underline{L}$ -character (see chapter 4). The tetragonal distortion (or in other words the square planar surrounding) of the $3d^9$ -configuration is well known, for example in the CuO-based high T_C superconductors.

Final state effects of lower symmetries can be important for all $3d^N$ configurations if the site geometry is strongly distorted from cubic. Final state effects of lower symmetries are best observable for $3d^0$ -compounds due to their simple spectral shape in which all multiplet transitions are resolved as individual peaks. In rutile (TiO_2) the site symmetry of titanium is D_{2h} and the effective configuration is $3d^0$. Effects of the symmetry reduction can be expected for the $2p^5 e_g^1$ -like states and indeed the rutile spectrum (given in section 3.3) clearly shows a splitting of the e_g -peak which is reproduced in a calculation for D_{4h} -symmetry.

Similar final state effects of lower symmetries are expected for systems with a partly filled $3d$ -band. However it can be argued that crystal field effects, including distortions from cubic symmetry, are more important for early $3d$ -metal oxides compared with the late $3d$ -metal oxides. The important parameters are the radial extend of the wavefunctions of the $3d$ -electrons (r_ϕ) and the inter-atomic distances (R). It is known that the ratio r_ϕ/R decreases in the 3-metal series [86,87], and especially in systems with one or more occupied e_g orbital, relatively large inter-atomic distances are found [88]. Crystal field effects scale with r_ϕ/R , hence effects of lower symmetries (and also the cubic crystal field strengths) are largest for the early $3d$ -metals.

Branching rules for lower symmetries

The crystal field multiplet program can handle any point group symmetry. As an example, the branching rules of a D_{2h} point group are given in figure 3.13. The projection from spherical symmetry to D_{2h} symmetry is accomplished in three steps. First the symmetry is reduced to cubic, in the second step the cubic (O_h) to tetragonal (D_{4h}) symmetry reduction is included and the third step goes to D_{2h} symmetry. The necessary extra crystal field terms in the Hamiltonian can be deduced directly from this figure: The Hamiltonian has A_1 -symmetry, thus all branchings to A_1 -symmetry take part in the Hamiltonian. For cubic symmetry, apart from the S -state, the G -state projects to the A_1 -state. This $G \rightarrow A_1$ branching describes the inclusion of cubic crystal field term in the Hamiltonian. Similarly for tetragonal symmetry the cubic E -state projects to the A_1 -state. In turn the cubic E -state has two parent states in spherical symmetry, hence there are two additional paths $D \rightarrow E \rightarrow A_1$ and $G \rightarrow E \rightarrow A_1$. In other words there are two additional crystal field parameters in the Hamiltonian of D_{4h} symmetry. The total number of crystal field parameters of a specific point group can be found directly from the total number of different paths leading to the A_1 -symmetry state. It should be noticed that the 'route' to reach the D_{2h} point group is not uniquely defined, and instead of the route via O_h (as given in the figure) an alternative route via $D_{\infty h}$ can be chosen. The choice of the route determines the meaning of the crystal field parameters and because of the central place of the cubic crystal field strength, in general the route via O_h symmetry is used. The different branchings for all point groups and also all possible choices for the routes to reach a specific point group are given in Ref. 53.

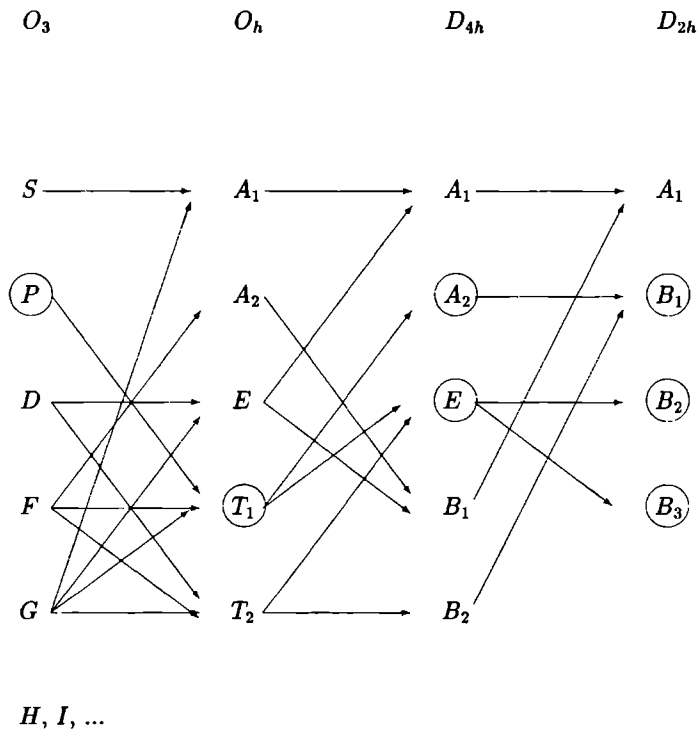


Figure 3.13: Schematic branchings from O_3 -symmetry (atomic) to D_{2h} -symmetry, via O_h and D_{4h} . Encircled are all representations which can be reached from atomic P -symmetry. (Notice that this also describes symmetry effects on the polarization dependence of a dipole transition, see section 3.6).

3.6. Polarization dependence

In the foregoing the discussion has been limited to the total x-ray absorption cross section. The x-ray absorption spectrum however depends on the polarization of the incoming x-ray. The polarization dependence can be found directly from the angular part of the transition matrix elements. This angular part is (see equation 1.7 on page 7) given as the 3J-symbol:

$$\begin{pmatrix} J & 1 & J' \\ -M & q & M' \end{pmatrix} \quad (3.5)$$

The triangle relations of the 3J-symbol give $\Delta M = M' - M = -q$. With the use of this equation one tacitly assumes only dipole transitions to occur. Quadrupole transitions have possibly some effect on specific edges [89], but as far as the transition metal $2p$ edges are concerned they do not play any role.

As discussed in the experimental section synchrotron radiation is linearly polarized in the plane of the orbiting electrons and out of plane it is partly circularly polarized. If the x-ray impinges on a substrate under normal incidence linearly polarized light, sometimes denoted as s -polarized, can give rise to $\Delta M = +1$ or -1 transitions. Right circular polarized light ($q = -1$) allows $\Delta M = +1$ transitions and left circular polarized light decreases M by one. If the substrate is turned to grazing incidence the $\Delta M = \pm 1$ transitions decrease whereas $\Delta M = 0$ transitions increase.

Dichroism

The difference between normal incident and grazing incident spectra taken with linear polarized x-rays is usually denoted as (linear) x-ray dichroism. Circular dichroism is the difference between the absorption of left and right polarized x-rays under normal incidence. The condition for the occurrence of polarization dependence is a macroscopic asymmetry in the electronic and/or magnetic structure. Thus non-magnetic crystals with a cubic symmetry do not show any polarization dependence because they have inversion symmetry and their x , y and z directions are equivalent. Also a non-magnetic (random) polycrystalline solid is symmetric and dichroism is prohibited by selection rules. Therefore either single crystals or oriented polycrystalline materials must be used for dichroism experiments.

The symmetry criterion which determines a possible polarization dependence is given by the space group of the crystal and not by the point group of the atom. This can be illustrated with system which has a cubic space group but in which the atom which absorbs the x-ray has a tetragonal point group (hence the elongated direction of the tetragonal point group is for some atoms directed along the x -axis, but for others along the y -axis respectively the z -axis). In this case the spectral shape is determined by the point group, however no dichroism is found because the potentially dichroic effect of the three differently oriented atoms cancels each other exactly [90]. The actual polarization dependence of all space groups can be deduced directly from the symmetry branching rules as were given in the foregoing section (figure 3.13). The polarization dependence is determined by the splittings of the irreducible representation of the dipole transition which is P -like ($\Delta J = +1, -1$ or 0) in the atom. From figure 3.13 it can be checked that in octahedral symmetry no polarization dependence can occur, in contrast to tetragonal symmetry. For a D_{2h} space group there are three different representations (directions), which can be denoted as trichroism [90]. From this figure it is clear that the polarization dependence of quadrupolar transitions (which have atomic D -symmetry) is different, and already in octahedral symmetry polarization dependence occurs.

Linear dichroism can be caused by both electric and magnetic effects, but electric fields (such as the crystal fields) can never cause a difference between the $\Delta M = -1$ and $\Delta M = +1$ transitions. This is a direct consequence of Kramer's theorem [91] which states that the

lowest state in a static electric field is always at least twofold degenerate. The only way to break the degeneracy of the Kramer's doublet is by means of a time asymmetric field (such as a magnetic field). Thus crystal field effects can only cause linear dichroism whereas magnetic effects can also cause circular dichroism.

The potential use of polarization dependent x-ray absorption experiments is illustrated with examples from non-cubic compounds, surfaces and adsorbates, and magnetic materials.

3.6.1. Non-cubic compounds

Non-cubic compounds contain at least one axis which is distinguishable from the others, hence the x-ray absorption spectra are polarization dependent with respect to this axis. Both BaCoF_4 and TiO_2 are non-cubic and their polarization dependent x-ray absorption spectra are discussed.

Cobalt 2p x-ray absorption of BaCoF_4

BaCoF_4 crystallizes in a $C_{2v}^{12}(A_{21am})$ space group [92]. Along the [001] direction (a -axis) a macroscopic electric polarization has been found, which can be reversed by reordering the CoF_4 -sheets. At room temperature BaCoF_4 is ferroelectric and paramagnetic. Below $T_N = 68$ Kelvin it is antiferromagnetic [92]. Given these properties it is expected that BaCoF_4 shows an x-ray dichroism effect with respect to the a -axis. In principle the C_{2v} -symmetry allows for a further dichroic behaviour of the b -axis with respect to the c -axis, which is not considered here. Figure 3.14 shows the cobalt 2p x-ray absorption spectra taken at three different temperatures and for $E \perp a$ and for $E \parallel a$. A clear linear dichroism is observed, which furthermore shows a clear temperature dependence.

Crystal field multiplet calculations have been performed to simulate the spectra. For the calculations the Co^{II} -ions are described with a $3d_{HS}^7$ ground state. The Slater integrals as given in section 3.4 have been used. In section 3.5 it was shown that $3d$ spin-orbit coupling is important for divalent cobalt and hence it is included in the calculations. The cubic crystal field is optimized and found to be 0.9 eV. The effects of lower symmetry are included as a tetragonal distortion. The possible effects of reduction to D_{2h} -symmetry have been neglected. The calculations are performed for the paramagnetic phase, hence no exchange splitting is included. Table 3.8 sketches the initial state effects of. in order of decreasing magnitude, the Slater integrals, the cubic crystal field, the $3d$ spin-orbit coupling, the tetragonal crystal field and the exchange field. The tetragonal crystal field does not split the E_2 -symmetry ground state but it does affect the first excited state of G-symmetry. After inclusion of the tetragonal field the state is split and the two resulting states are called G_1 and G_2 . In the crystal field multiplet calculation, which is optimized to simulate the 30 Kelvin spectra, the G_1 and G_2 are found at respectively 39 meV and 51 meV above the E_2 ground state. Assuming a Boltzmann distribution over the low-lying states this means that at 30 Kelvin these states are not populated but at 300 Kelvin their population is respectively 21% and 13%.

Figure 3.15 shows the calculated crystal field multiplet spectra for $E \parallel a$ ($\Delta M = \pm 1$) and $E \perp a$ ($\Delta M = 0$) for the 3 low lying states E_2 , G_1 and G_2 . Comparison of the crystal

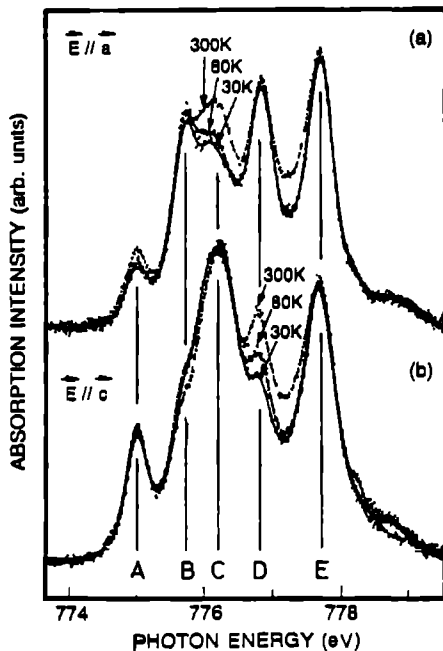


Figure 3.14. Cobalt 2p x-ray absorption spectra of BaCoF_4 . The experiments were performed with the Dragon monochromator by B. Sinkovic et al. [93].

Ground state symmetry	Physical effect	Excited states symmetry	Ground state degeneracy
$3d^7$			120
\downarrow	Slater integrals		
4F		$+^4P, ^2P$, etc	28
\downarrow	cubic crystal field		
4T_1		$+^4T_2, ^4A_2$	12
\downarrow	$3d$ Spin-orbit coupling		
E_2		$+G, G^*, E_1$	2
\downarrow	tetragonal crystal field		
E_2		but: $G \rightarrow G_1 + G_2$	2
\downarrow	magnetic exchange field		
E_2^+		$+E_2^-$	1

Table 3.8: Splitting of the initial state multiplet of a $3d^7$ -configuration. The tetragonal crystal field (or any other lower symmetry field) does not split the 'Kramers doublet' E_2 ground state, but the first excited state of G -symmetry is split.

field multiplet calculation with experiment shows that the main features, including the dichroism effects, are reproduced. Some minor discrepancies exist: The D peak is too high in the calculated $E \perp a$ spectrum (it is close to absent in the experimental 30 K spectrum)

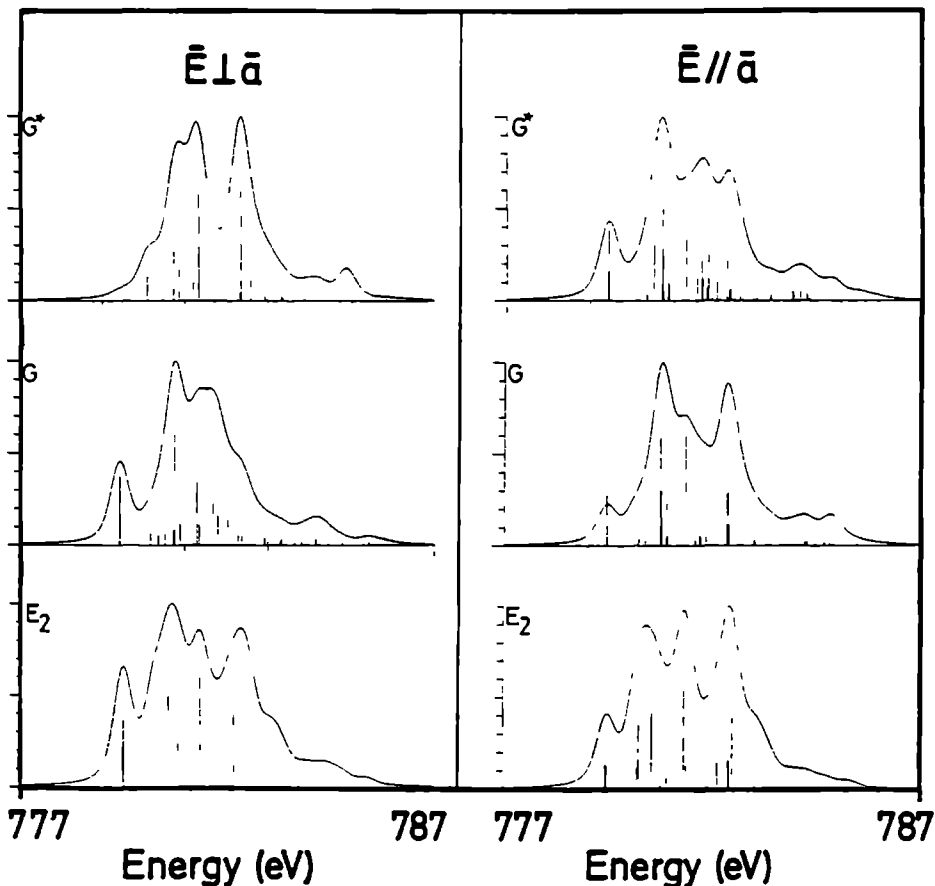


Figure 3.15: Calculated $3d^7 \rightarrow 2p^5 3d^8$ multiplets for E_2 , G_1 and G_2 .

and the E peak is too broad. As can be checked in figure 3.16, which gives the theoretical 30 Kelvin and 300 Kelvin spectra for $E \perp a$, the reversal of the asymmetry of peaks B and C is nicely reproduced. From the accuracy of the description the following conclusions can be drawn:

- The crystal field multiplet model is capable of reproducing the main features of the dichroism and its temperature dependence, despite uncertainties in the precise magnitudes of the parameters used (Slater integrals, crystal field couplings and $3d$ spin-orbit coupling).
- Above T_N the ground state of BaCoF_4 is a Kramer's doublet of E_2 symmetry with states originating from cubic G -symmetry at excitation energies in the range of kT , thereby creating a large temperature dependence between 80 Kelvin and 300 Kelvin. (From the present analysis it is not possible to be more precise about the exact energy

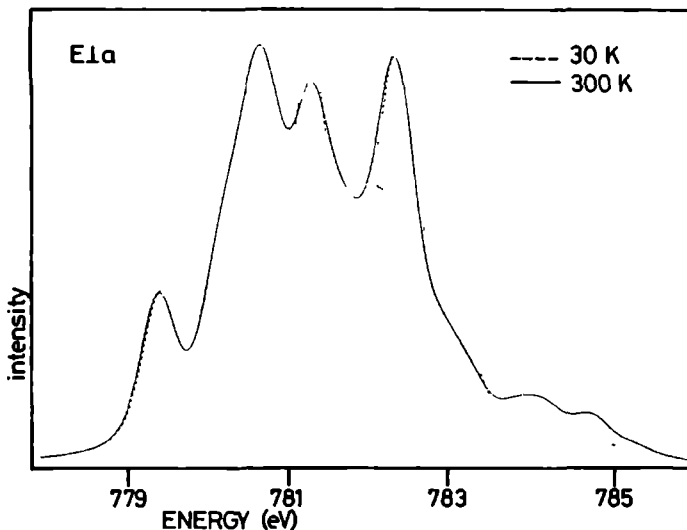


Figure 3.16: Calculated $3d^7 \rightarrow 2p^5 3d^8$ multiplet for $E \perp a$ for 30 Kelvin (dashed line) and 300 Kelvin (solid line).

differences and symmetries, also because the actual symmetry is D_{2h} and the symmetry lowering from D_{4h} influences the G states as well as the transition matrices).

- Below T_N an additional effect from the splitting of the Kramer's doublet occurs, which modifies the linear dichroism, and additionally causes circular dichroism effects.

More detailed temperature dependent measurements of B. Sinkovic et al. [94] reveal that above T_N the amount of linear dichroism, detected from specific peak-ratios, follows a smooth trend originating from population effects of excited states in agreement with the present analysis. At T_N a jump in the peak-ratios occurs which indicates the additional dichroic effect of the exchange splitting. The effects of the exchange splitting can be tested directly with use of circular polarised x-rays.

Titanium 2p x-ray absorption of TiO_2

TiO_2 has a D_{4h}^{14} space group symmetry in the rutile crystal structure and the point group of titanium is D_{2h} . Titanium has six oxygen neighbours, 2 at 1.98 Å and 4 at 1.94 Å, forming a quasi-tetragonal (D_{4h}) environment which is slightly distorted. The overall spectrum can be simulated with tetragonal crystal field parameters of the order of 0.75 eV. Thus the tetragonal symmetry distortion is strong and effects on the spectrum are clearly visible. From this observation one expects a large linear dichroism effect. However a closer look at the crystal structure of rutile reveals that there are two titanium sites which have their elongated axis rotated over 90° . Thus within the ab -plane the angular dependent effect of the tetragonal symmetry distortion, the main lower symmetry effect on the spectral shape, exactly cancels and no dichroism is expected. In principle a dichroism effect might

be expected because the c -axis is different from the ab -plane. However in experiments performed thus far no dichroism has been observed. In contrast to the $2p$ edge, the pre-edge region of the titanium $1s$ x-ray absorption spectrum of rutile shows a clear angular dependence [95, 96]. Angular dependent measurements within the ab -plane clearly reveal angular dependence of the quadrupolar transitions, for which the two (90° rotated) sites are in phase [90]. Thus from the angular dependence observed the leading peak is proven to be (at least partly) related to quadrupolar transitions [95].

3.6.2. Surfaces and adsorbates

A surface presents a clear breaking of the (x, y, z) -symmetry, and will therefore always present a rather large linear dichroism between polarizations in the surface plane and perpendicular to it. A linear polarized x-ray impinging perpendicularly upon a surface excites core electrons to bonds lying in the surface plane. A grazing incident x-ray excites exclusively bonds perpendicular to the surface plane, which can be used to determine the surface electronic structure.

A problem with electron yield is that due to its mean probing depth of the order of 30 Å, the surface signal is overwhelmed by the signal from the bulk. To separate the surface signal it is fruitful to use ion yield which, with its probing depth of only 1 or 2 layers, is a true surface probe. The combination of ion-yield and electron yield detection has been applied to the CaF_2 -Si(111)-system. The paper included in section 5.4.1 confirms that it is indeed possible to pick out the surface signal with ion yield detection.

Surface dichroism effects are particularly useful for adsorbates. A nice example is given for the absorption of boron on a silicon (111) surface, for which the sharp boron π -peak, related to the silicon-boron bond, is visible solely with p-polarized x-rays [102]. Given that the adsorbates are present on the surface only, the x-ray absorption spectrum can be measured with any method [98, 99]. Because electron yield measurements are easier in their use, adsorbates are usually measured with (partial) electron yield. Besides an interest in the structure of the x-ray absorption edges, the surface extended x-ray absorption fine structure (SEXAFS) is important for the determination of for example the surface bond lengths [100]. The common procedure of analysis for the 'near edge structure' is by means of multiple scattering calculations. Emphasis is given to the complicated problem of correct determination of the surface structure [101]; the problems regarding the limitations of the one-electron approach are generally not considered. Specifically if a $3d$ -metal surface (or adsorbate) is analysed the applicability of one-electron like models, like multiple scattering, is doubtful.

3.6.3. Magnetic materials

As has been discussed magnetic fields can cause linear as well as circular dichroism. Because circular dichroism effects can not be caused by symmetry effects from surfaces and crystal fields they present a direct measure of the magnetic structure of materials. Circular dichroism has been studied in the hard x-ray range by the groups of G. Schütz [103, 104] and A. Fontaine / E. Dartyge [105], and clear magnetic circular dichroism (MCD) effect have been

found for the $L_{2,3}$ of rare earths and the K edges of $3d$ -metals. Recently it became possible to extend the circular dichroism experiments to the soft x-ray range and as yet some rare earth $M_{4,5}$ edges [106–108] and $3d$ -metal $L_{2,3}$ edges [108, 109] have been measured.

For the interpretation of the MCD effects the common methods to explain the x-ray absorption spectra have been extended to include magnetic fields:

- The band structure approach, mainly used for the metal K edges and rare earth $L_{2,3}$ edges, has been modified to perform spin-dependent relativistic calculations by Ebert et al. [110].
- The multiple scattering method has been modified by C. Brouder et al. [111].
- The circular dichroism of the atomic multiplet spectra of rare earth $M_{4,5}$ edges has been analysed by J. Goedkoop [112], using the results of B.T. Thole, and also by Imada and Jo [113].
- G. van der Laan and B.T. Thole calculated all MCD spectra for the $L_{2,3}$ edges of transition metal compounds in cubic crystal fields [114].
- The MCD spectrum of nickel has been explained with a band structure approach with empirically optimized exchange and spin-orbit values [115], and also with an Anderson impurity model (including the crystal field multiplet) [116].

In the crystal field multiplet approach the addition of a magnetic field splits the Kramer's doublet. Mathematically the symmetry is reduced from cubic symmetry to C_4 symmetry via the branching $O_h \rightarrow D_{4h} \rightarrow D_4 \rightarrow C_4$ with inclusion of an exchange splitting in the z direction. As the effects of crystal field symmetry reduction have been neglected in Ref. 114, the linear dichroism spectra apply to pure octahedral symmetry only. The discussion of the linear dichroism of $BaCoF_4$ in the last section reveals that the inclusion of lower symmetries is crucial for the correct description of linear dichroism effects.

Magnetic effects on linear dichroism

Magnetic effects generate circular dichroism, but additionally they can have a large effect on the linear dichroism of rare earth $M_{4,5}$ -edges as was first shown by van der Laan et al. [117]. The basic reason is the strong correlation between ΔM_J and ΔJ transitions as a result of the properties of the $3J$ -symbol (equation 3.5). Under the assumption that only the $M_J = -J$ magnetic level of the ground state is filled, this correlation is given in table 3.9.

Because the J -values for the rare earths are found to be in between $5/2$ and 8 , the correlation is rather strong and $\Delta J = \pm 1$ transitions are almost exclusively correlated with $q = \Delta M_J = \pm 1$ transitions. The polarization averaged spectrum is formed from a combination of all transitions from the $4f^N$ ground state of specific J to all $3d^0 4f^{N+1}$ final states of $J + 1$, J and $J - 1$. Figure 3.17 shows the atomic multiplet spectrum for Tm^{3+} .

The M_5 edge has three possible transitions, the first one with $\Delta J = 0$ (dashed line) and the two others with $\Delta J = -1$ (chain-dotted line) Due to the Jq -correlation the transitions to $\Delta J = -1$ are solely visible in the $q = \pm 1$ spectrum, and the $\Delta J = 0$ transition is largely

$(\Delta M_J = -q)$	-1	0	+1
ΔJ			
-1	1	0	0
0	$\frac{1}{J+1}$	$\frac{J}{J+1}$	0
+1	$\frac{1}{(2J+3)(J+1)}$	$\frac{2J+1}{(2J+3)(J+1)}$	$\frac{(2J+1)(J+1)}{(2J+3)(J+1)}$

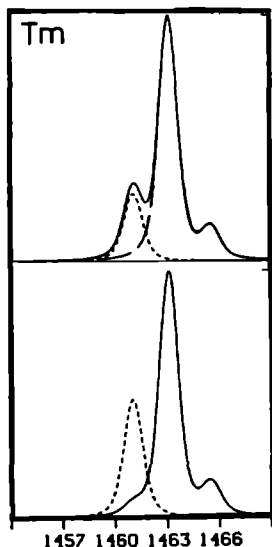
Table 3.9: Correlation between ΔJ and ΔM_J 

Figure 3.17: Atomic multiplet calculation of M_5 edge of thulium. Top spectrum: dashed line corresponds to $\Delta J = 0$ and chain-dotted line to $\Delta J = -1$. Bottom spectrum: the resulting spectra for $E \perp M$ (dashed) and $E \parallel M$ (solid).

restricted to $q = 0$ polarized x-rays. The small low-energy shoulder in the $q = \pm 1$ spectrum is an effect of the incomplete correlation. The linear and circular dichroism of the $M_{4,5}$ spectra of all rare earths, including the effects of finite temperature, have been given in Ref. 112. It has been shown experimentally that magnetic effects indeed cause a large linear dichroism [112, 118], though in some cases it is difficult to distinguish the magnetic effects from the electrostatic (surface) effects [112, 119, 120]

3.7. Multiplets and hybridization

The crystal field multiplet calculations assume the ground state to be represented by a single $3d^N$ -configuration. This configuration is found from the atomic multiplet calculation and

its projections to cubic symmetry. The errors introduced in this approach are known to be not negligible. The errors are all related to the fact that the actual ground state is not single configurational but contains an admixture of a series of configurations. In an atom a number of excited configurations can be included in multi-configurational Hartree-Fock calculations. In a solid the most obvious extension is to account for hybridizational effects by means of the admixture of extra-atomic configurations such as the charge transfer states $3d^{N+1}\underline{L}$, etc. In this section some of the possible extensions of the crystal field multiplet model are discussed.

Multi-configurational atomic multiplet calculations

The obvious extension of the calculational scheme is to include excited configurations in a configuration interaction calculation. The situation is not favourable for actual calculations because there are an infinite number of small effects. Theoretical studies indicate that it is possible to approximate the infinite series of excited configurations with a single configuration which has an equivalent LS-dependence as the ground state but an opposite sign [121–124]. This finding gives a partial justification of the reduction of the Hartree-Fock values of the Slater integrals to 80% of their original values [125].

A recent effort to overcome these problems and to actually perform a multi-configurational calculation has been made by Sarpal et al. [126]. Using a multi-configurational Dirac-Fock (= relativistic Hartree-Fock) calculational scheme, the $M_{4,5}$ edges of divalent samarium and thulium atoms were calculated. The advantage of these configuration interaction calculations is that no parameter adjustments are necessary. However from comparison with experiment it appears that for the multi-configurational spectrum the agreement is not perfect and even more the (reduced) Hartree-Fock result from Thole et al. [127] compare far better with the experimental spectrum. Figure 3.18 shows the multi-configurational result in comparison with experiment. The result from Ref. 127 is given at the top This indicates that the correct configuration-interactional solution of the atomic multiplet spectra is as yet not found. Hence, for practical purposes the reduced Slater integral approach is preferred, especially because of its transparent computational method.

The effects of hybridization in solids

In contrast to atoms where an improvement was found in a more rigorous multi-configurational treatment to avoid empirical parameter adjustments, for solids the multiplet calculations are embedded in model Hamiltonians to account for solid state effects. For solids the number of possible effects on the actual ground state increases. Apart from intra-atomic configuration interaction effects, there are effects from extra-atomic hybridization. In this context it is by no means guaranteed that the intra-atomic configuration interaction effects are equal to those in the atom, if it is possible at all to separate the intra-atomic effects from extra-atomic effects.

Lynch and Cowan used an approach in which they reduced the Slater integrals from their atomic values. To simulate the hybridization of ligand character $|L\rangle$ into the original atomic $|4f\rangle$ wavefunction the ff -Slater integrals were reduced by 20% and the df -Slater

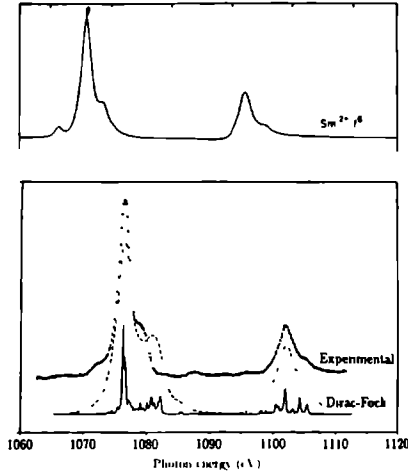


Figure 3.18: Top: Scaled down Hartree-Fock calculation from Thole et al. [127]; bottom: experimental Sm^{2+} spectrum compared with multi-configurational Dirac-Fock calculation from Sarpal et al. [126].

integrals by 10% (as the core state are not modified in a solid) [128]. Their results on the $M_{4,5}$ edges of Ce^{3+} and Pr^{3+} showed a complex reordering of states as result of the Slater integral reduction. The method of reducing the Slater integrals is rather limited and effects like extra broadenings and satellites are not reproduced. Also the intrinsic approximation is used that the radial wavefunction are identical for all states.

An alternative approach to include covalency effects is to implement the multiplet calculation into an Anderson impurity model. This model has been developed (for spectroscopy) by Gunnarsson and Schönhammer [129,130] and was used extensively to study the core level spectra of cerium [131–135]. The groups of Kotani and Jo [136–142] used the Anderson impurity method to account for both the atomic multiplets and the interaction of the localized levels with bands, and they have been able to simulate the cerium x-ray absorption and x-ray photoemission spectra with great success. The basic idea of the Anderson impurity model is to describe the effects of the interaction (V_{fk}) of a correlated localized state (ϵ_f) with a non-correlated band ($\sum_k \epsilon_k$). The electron correlation shifts the localized state to higher energy (over U_{ff}) upon electron addition. The Anderson impurity Hamiltonian is written as:

$$\mathcal{H}_{AI} = \epsilon_f n_f + \sum_k \epsilon_k n_k + V_{fk} \sum_k (a_f^\dagger a_k + a_k^\dagger a_f) + U_{ff} n_f n_f \quad (3.6)$$

In this equation second quantization is used and a_f^\dagger denotes the creation of the localized f -state; $n_f (= a_f^\dagger a_f)$ is the occupation-number operator of the localized state. For cerium compounds their 2 or 3-peaked 3d-XPS spectrum could be accounted for by a ground state consisting of f^0 -state plus a $f^1 \underline{k}$ state where one electron is transferred from the band to the localized state, (plus eventually a $f^2 \underline{k} \underline{k}'$ -state). In the final state the effects of the core hole, the core level binding energy (ϵ_c) and the core hole potential (U_{cf}), are added to

the Hamiltonian. The model parameters, ε_f , V_{fk} , U_{ff} and U_{cf} have to be optimized from experiment. Alternatively these parameters have to be calculated from ab-initio calculations, and for example density functional and cluster calculations have been applied to determine these model parameters [143-145].

To include multiplet effects in the Anderson impurity description the different symmetries of the $4f$ -electron states and the $3d$ -core hole states have to be accounted for. This can be accomplished by an explicit summation over these symmetries (with a double summation over the U-terms) [133]. As in this procedure each individual atomic configuration is accounted for, it is possible to include the atomic multiplet terms. For the ground state this includes the Slater integrals F_{ff}^2 , F_{ff}^4 and F_{ff}^6 and the $4f$ spin-orbit coupling. In the final state the Slater integrals concerning the df -coupling and the $3d$ spin-orbit coupling have to be included. The final state Hamiltonian uses eight Slater integrals, taken from the Hartree-Fock calculation (and reduced to 80%), two spin-orbit coupling strengths from the Hartree-Fock calculation, and empirical or calculated values for ε_f , ε_d , U_{ff} , U_{fd} , V_{fk} and $\sum_k \varepsilon_k$ (the shape of the band). Despite the numerous parameters needed, it has been shown convincingly that the model reached an unprecedented efficiency for systems like CeO_2 or CuO and related compounds. However for a reliable application to new systems it is necessary to perform extensive parameter optimizations whereby difficulties can arise because some parameters have counteracting effects on the spectral shape. Additional problems can arise in the study of systems in the middle of transition metal or rare earth series as the number of configurations is too large for the use of a similar rigorous approach. For $3d$ x-ray absorption on cerium compounds it has been found that the main effect of the implementation into the impurity model is a narrowing of the atomic multiplet [137]. For the heavily debated $4d$ x-ray absorption spectrum of CeO_2 Kotani et al. convincingly showed that the actual spectral shape is a direct consequence of the interplay between atomic multiplets and the interactions of the localized states with the band [138].

The impurity model for transition metal compounds

The impurity model has been applied to transition metal compounds by the Groningen group. The many body description has been started by van der Laan et al. in the description of the photoemission spectra of copper dihalides [152]. Zaanen et al. applied the Anderson impurity model to the nickel dihalides, whose ground state is dominated by a $3d^8$ configuration but in which going from the fluoride to the iodide the admixture of the $3d^9\bar{L}$ configuration becomes more dominant as a result of a decreasing charge transfer energy (Δ) [65]. Compared to the cerium-compounds for the nickel halides the correlations are smaller and the interaction between the localized state and the band is larger which results, given the variations in Δ , in a complicated, but nicely explained, variation of the nickel $2p$ XPS spectral shape. Comparison of the $2p$ XPS spectra with the $2p$ XAS spectra of the nickel dihalides shows that whereas the XPS spectra showed drastic spectral changes, the x-ray absorption spectra resemble each other much more closely and furthermore the main features of all spectra are reasonably accounted for by a single configuration crystal field multiplet calculation. The agreement is increased considerably after implementation of the

multiplets in the impurity model. The main result is, apart from the appearance of small satellites, a reduction of the multiplet splittings [151], a result similar to that obtained for cerium compounds [137].

The impurity model versus Slater integral reduction

From the foregoing it can be concluded that there are two approaches to include hybridization effects in the single configuration multiplet spectra: (1) the reduction of the Slater integrals from their atomic values and (2) the implementation of the atomic multiplets into the impurity model. The impurity model is more rigorous and has been proven to account well for the experimental spectra. Its disadvantage however is that it is a more complicated calculation. Specifically for compounds in the middle of the transition metal series (with a large number of configurations), impurity calculations similar to those performed for the nickel halides [65] are not possible. Therefore it would be of great help if Slater integral reduction would reproduce the experimental spectra (apart from the intensity coming from the satellites, which is not accounted for in this approach). Because only the Slater integrals are modified the calculation is exactly equivalent to a normal crystal field multiplet calculation.

To test the validity of Slater integral reduction and to compare it with the impurity model, the nickel dihalide spectra are simulated. Divalent nickel presents a special case for the crystal field multiplet calculations as the $2p^53d^9$ final state contains only a single $3d$ -hole and thus does not contain any dd -correlations. This simplifies the multiplet calculation and, apart from the spin-orbit coupling which is not essential for this problem, only two sets of Slater integrals remain: F_{dd}^2 and F_{dd}^4 for the initial state and F_{pd}^2 , G_{pd}^1 and G_{pd}^3 for the final state. Furthermore the x-ray absorption spectral shape is not sensitive to the actual values of the ground state dd integrals as the 3A_2 ground state is the sole state of this symmetry and consequently does not mix with any excited state. Thus the only set of parameters which determine the spectral shape are the final state pd -Slater integrals. To test the Slater integral reduction they were stepwise reduced from their atomic values and figure 3.19 shows the corresponding spectral changes. It should be noted that a cubic crystal field a value of 0.9 eV is used, in agreement with the values (for all nickel halides) determined from optical spectroscopy. In the original paper on the impurity model a crystal field value of 1.5 eV had been used (corresponding to NiO).

For comparison the experimental spectra are reproduced from Ref. 151. It can be seen that with the reduction of the pd Slater integrals the splitting between the main peak and its high-energy shoulder is reduced, a similar effect to that obtained in the impurity model calculations. The experimental spectra show exactly the same trend in going from the fluoride to the iodide. Also the modifications in the L_2 edge are reproduced nicely. From this agreement it can be concluded that in case of the nickel dihalides the Slater integral reduction gives a good account of the main spectral modification upon increasing hybridization (apart from the satellite structure). It is important to note that the amount of Slater integral reduction gives an alternative measure of the amount of hybridization. For the halides it is found that whereas the fluoride corresponds to the atomic values, for chloride,

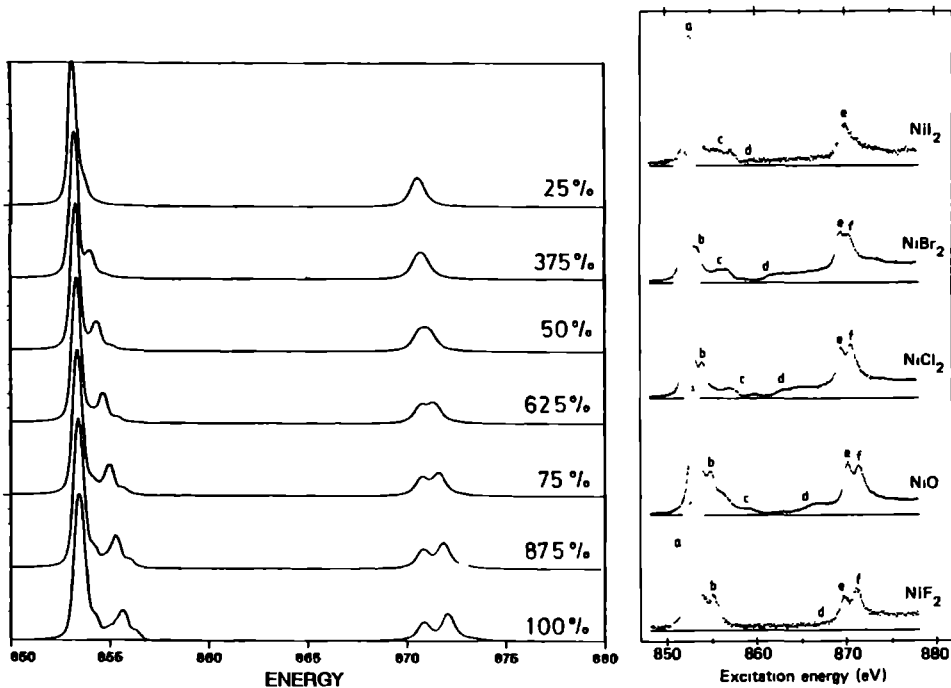


Figure 3.19: Reduction of Slater integrals (left) compared with experiment (right). The experimental data are reproduced from Ref. 65. (100 % relates to the atomic values).

bromide and iodide the Slater integrals have to be approximately reduced to respectively 75%, 65% and 25% of their atomic value. This trend is a nice example of the so-called 'nephelauxetic series' obtained from the analysis of optical spectra [154, 155]. There is also a close relation between the Slater integral reduction and the ratio of the charge transfer energy (Δ) and the interaction strength with the band (V_{dk} or T). For NiF₂ (Δ/T)² is 0.09 [153] and the atomic Slater integrals are correct. For NiI₂ (Δ/T)² is 1.8 and the effects of the Slater integrals on the spectral shape is negligible. For NiCl₂ and NiBr₂ the values are respectively 0.3 and 0.6, and an intermediate situation occurs for which the values of the Slater integrals are reduced but still they have considerable influence on the spectral shape.

Why are the satellites so small in x-ray absorption ?

In this section it is argued why the charge transfer satellites are small or absent in $2p$ x-ray absorption spectra, in contrast to their importance in the $2p$ XPS spectra of ionic $3d$ -metal compounds. Furthermore the absence of satellite structures is an additional justification of the Slater integral reduction method.

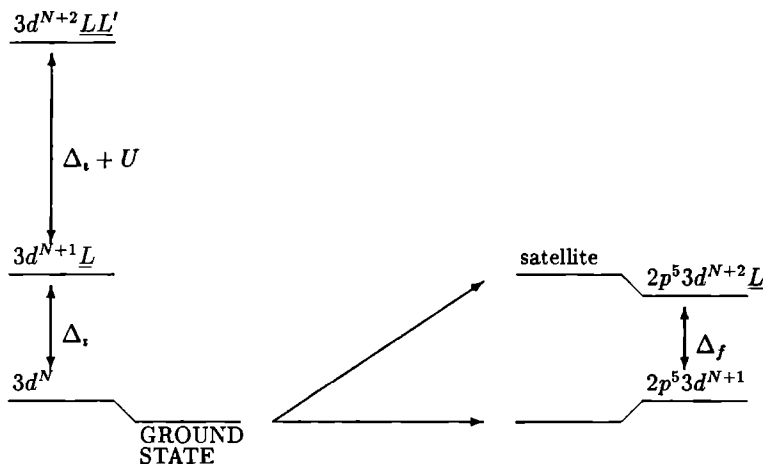


Figure 3.20: Initial and final states of metal $2p$ x-ray absorption in the charge transfer model. The ground state is formed by the bonding combination of $3d^N + 3d^{N+1}\underline{L}$. The arrows indicate the transitions to the bonding and anti-bonding (= charge transfer satellite) final states.

Figure 3.20 sketches the energy levels in the charge transfer model. The ground state has $3d^N$ -character which mixes with $3d^{N+1}\underline{L}$ character after hybridization is taken into account. The energy of the $3d^{N+2}\underline{L}\underline{L}'$ is large and its contribution to the ground state can be neglected. The consequence of the interaction between $3d^N$ and $3d^{N+1}\underline{L}$ -character is the forming of bonding and anti-bonding states which both consist of admixtures of these two configurations. Similarly in the final state the interaction between $2p^5 3d^{N+2}\underline{L}$ and $2p^5 3d^{N+1}$ -character gives rise to bonding and anti-bonding combinations. In the charge transfer model it is found that the amount of admixture of $3d^{N+1}\underline{L}$ -character in the ground state is given as the hopping (T) over the energy difference (Δ) squared. In the final state Δ_f is approximately equal to $\Delta_i - Q + U$ and because Q is in general slightly larger than U , Δ_f is slightly decreased which results in an increased hybridization. Possibly the hopping is increased in the final state which will further increase the hybridization [65]. Under the assumption that the hybridization is not modified, all intensity goes to the

bonding combination of the final state. Furthermore under neglect of interference effects the overall spectral shape is given as the superposition of the crystal field multiplets of the $3d^N \rightarrow 2p^5 3d^{N+1}$ and the $3d^{N+1} \underline{L} \rightarrow 2p^5 3d^{N+2} \underline{L}$ transitions. Thus the crystal field multiplet analysis as used in section 3.3 and 3.4 is extended with the superposition of the transitions from the $3d^{N+1} \underline{L}$ -character of the ground state. If the hybridization is increased the main effect will be that the amount of $2p^5 3d^{N+1}$ -character in the anti-bonding state increases with respect to (the $3d^N$ -character in) the initial state. This will result in transitions to the anti-bonding combination, hence to a charge transfer satellite as is for example observed for the nickel-halides [151]. In summary it can be concluded that hybridization itself gives rise to a reduction of the energy splittings in the multiplet and to the superposition of transitions from $3d^{N+1} \underline{L}$ -character, but that only the *changes* in the hybridization will give rise to a satellite structure.

In x-ray absorption the change in hybridization is considerably smaller than for XPS, which is a direct consequence of the charge conservation. The mere absence of charge transfer satellites explains the good agreement of the x-ray absorption spectra with the crystal field multiplet calculations and additionally it is a partial justification of the Slater integral reduction method.

3.8. Electronic structure calculations

In contrast to sections 3.2 to 3.7, in this section the emphasis will be on the weakly correlated limit. The electronic structure of ordered solids is, in the weakly correlated limit, accurately described with density functional theory within the local density approach [156,157]. As discussed in chapter 1 the x-ray absorption cross section is in the weakly correlated limit related to the unoccupied density of states with one extra valence electron and with the presence of a core hole ($\mathcal{P}_{\underline{c}N+1}$): the final state rule [158,159]. Under the additional assumption that the effects of the core hole as well as the extra valence electron are negligible, the density of states which results from a ground state calculation, the non-observable N-particle density of states (\mathcal{P}_N), bears close resemblance to the spectral shape ($\mathcal{P}_N \approx \mathcal{P}_{\underline{c}N+1}$). Evidently this assumption breaks down completely for the rare earth metals and their compounds. In the preceding sections it was shown that also for the metal $2p$ x-ray absorption edges of the $3d$ -metal compounds, this assumption is violated and correlation effects dominate the spectral shape. Despite the fact that from the metal $2p$ spectra the conclusion is drawn that $3d$ -metal oxides are highly correlated, in this section the model of a weakly correlated system is tested for the analysis of the oxygen $1s$ x-ray absorption spectra of the $3d$ -metal oxides. There are some favourable factors for the use of the description within the weakly correlated limit:

- The oxygen $1s$ core hole bears no angular momentum and hence there are no multipole interactions of the core hole with the electrons in the valence band. (The G_{pp}^1 Slater integral (exchange coupling) is neglected).
- X-ray absorption is a local process which is charge conserving with the consequences that the modifications in the hybridization are small and mainly local (also it places

x-ray absorption close to the adiabatic limit).

- The core hole is located on the oxygen site and the 3d valence electrons are localized mainly on the metal sites, hence (the effect of) the core hole potential is small. However still the oxygen 1s core hole will attract the valence electrons to the oxygen site and thereby it tends to counteract the correlations within the 3d-band.

The density of states is calculated within the local density approximation of density functional theory, which as discussed in the introduction presents an accurate ab-initio method to solve the Schrödinger equation for weakly correlated, ordered solids. The Hamiltonian to solve includes respectively the kinetic term, the Hartree term, the nuclear term and the exchange-correlation term:

$$\mathcal{H} = -\frac{1}{2}\nabla^2 + \int \frac{n(r')}{|r-r'|} d^3r' + V_N(r) + \frac{\partial E_{xc}[n]}{\partial n} \quad (3.7)$$

The exchange-correlation energy is approximated according to the Hedin-Lundqvist expression [160]. The Hamiltonian itself is dependent on the electron density (the wavefunctions as far as occupied), hence the solution is found in a self-consistent iterative procedure. A specific starting set of wavefunctions $\phi^{in}(r)$ is chosen, the Hamiltonian is determined and thereafter the eigenvalue-problem is solved which yields a new set of wavefunctions $\phi^{out}(r)$. This new set of wavefunctions can be used for the next cycle of the calculation. The actual iterative procedure uses a specific combination of the wavefunction-sets to speed up the convergence. For example a linear combination of $\phi_{N-1}^{out}(r)$ and $\phi_{N-1}^{in}(r)$ can be used.

3.8.1. The Localized Spherical Wave method

To tackle the calculation of an actual solid a number of numerical methods have evolved, differing in specific choices with respect to the treatment of the valence and core electrons, the division of space and the effectiveness to shape the calculation into a manageable form. The specific method used is the Localized Spherical Wave (LSW) method, which originates from the Augmented Spherical Wave (ASW) method of Williams et al. [161]. With respect to ASW, there are two essential developments:

- The idea of tight-binding (localized) muffin-tin orbitals, suggested by Andersen and Jepsen for the linearized muffin-tin orbital (LMTO) method [162, 163], has been reformulated and implemented for the ASW method by F. Springelkamp et al. [164].
- The extended basis set option was added to LSW in order to describe appropriately the unoccupied states in the energy range higher than a few eV above the Fermi level [165].

The LSW method, including the extended basis sets has been applied to a number of systems, including Ag_2O [165, 166], CuO [167, 168], TiSi and other silicides [166, 169] and MoNi -alloys [170].

Treatment of valence electrons

All band structure methods divide the electrons into core and valence electrons of which only the latter are expanded in reciprocal space to derive the band structure. The LSW method uses spherical waves to expand the valence electrons, contrary to linearized augmented plane wave (LAPW) and LMTO methods which use plane waves. For each angular quantum-number and for each site the wavefunction is written as a radial Hankel function [161] times the respective spherical harmonics (Y_{LM}). The Hankel functions of a specific site are at another site expanded in a series of Bessel functions [171].

Treatment of core electrons

The core electrons can be treated in two ways: they can be frozen to their atomic values or alternatively they can be calculated after each step in the iteration procedure. This second approach, which is used in the LSW calculation, allows one to detect the reaction of the core levels on the hybridizational effects of the valence electrons.

Division of space

A major problem in all density functional methods is to divide the space of the unit cell into manageable sections. There are two main approaches known as muffin-tin and atomic sphere approximation. In the muffin-tin approach each atom is surrounded by a sphere in such a way that, if possible, they just touch each other. Inside the spheres an atomic potential is used and the interstitial region outside the spheres is approximated with a flat potential. In the atomic sphere approximation a similar approach is followed but the radii of the spheres are chosen as to fill a volume equal to the total volume of the unit cell. This procedure creates overlapping spheres, so there are regions inside the unit cell which are encompassed in two or sometimes three spheres. Additionally in the atomic sphere approximation the total space of the interstitial regions is much smaller than in the muffin-tin approach. As each atomic site is surrounded by a sphere the overlap occurs in the bonding directions whereas the interstitial regions are found in non-bonding directions. The choice of the atomic radii is important and for this purpose one can use tables of radii in the ionic and covalent limits [172]. However many, if not all, interesting compounds contain an intermediate character and the radii have to be optimized. In crystal structures which have a filling which is rather far from closed-packed the overlapping spheres give rise to numerical problems and therefore a method has been developed to improve the division of space by creating empty spheres, that is spheres which are allocated to open places in the crystal structure and which consequently have no ion core.

Number of basisfunctions

In standard LSW calculations one Hankel function per site and per l -value is used. In SrTiO_3 there are 5 atoms per unit cell [57] and in the self-consistent iteration process s , p and d Hankel functions are allocated to the strontium, titanium and oxygen sites. It is

necessary to include empty spheres at a 12-fold degenerate site and a Hankel function of s -symmetry is assigned to each empty sphere. As a result the total size of the matrix is 5 times 9 for the atoms, plus 12 (times 1) for the empty spheres. The set of Bessel functions used in the expansion is limited to $l \leq 3$. For the empty spheres only s , p and d Bessel functions are included.

Extended basis sets

In order to give an accurate description of the states above the Fermi level, which is essential for the comparison with the x-ray absorption cross section, it is necessary to increase the number of basis-functions to more than one per angular momentum [165]. Because the potential is dependent only on the occupied states, which are hardly influenced by the addition of new states at high energies, it is possible to use the potential as determined with the smaller basis. Thus it is not necessary to repeat the self-consistent calculation and one can manage with a single calculation to determine the density of states within the extended basis set.

3.8.2. LSW calculation of the density of states of SrTiO₃

SrTiO₃ has (at room temperature) a cubic perovskite crystal structure (O_h^1). The positions of the ions in the unit cell are given in table 3.10. For numerical reasons, it is necessary to include empty spheres at the 12-fold degenerate $(\frac{1}{2}, x, x)$ -positions with the x as given in the table. Two sets of radii have been used. A covalent set with a small oxygen radius (I), and a more ionic set with an increased oxygen radius (II). The two sets of radii given in table 3.10 are optimized touching spheres. The actual radii are renormalized from these values by multiplication with the total volume of the unit cell over the total volume of the given spheres. The renormalization values ($V_{WS}/\sum_i V_i$) are given in table 3.10. The densities of states emerging from these two sets of radii are, within the accuracy needed for x-ray absorption, equal to each other which is an additional check for the correctness of the density of states.

The basis set used in the calculation is given in table 3.11. The size of the Hamiltonian is 57. It was checked that inclusion of the $2p$ -Hankel functions for the empty spheres, which increases the Hamiltonian size to 83, did not have any detectable effect. The k -points in the self-consistent iteration procedure are chosen in a 8 by 8 by 8 grid in the unit cell, which from symmetry arguments reduces to 35 points. The iteration procedure converges after approximately 25 cycles. With the self-consistent potential the density of states is calculated with an extended basis set, in which apart from the Hankel functions as given in table 3.10, also oxygen $3s$ and $3p$ states are included. Furthermore the strontium and titanium $4f$ -states have been included in the Hamiltonian, which increases its size to 83. The density of states is calculated with a 16 by 16 by 16 grid of k -points, which is reduced to 165 points in the irreducible zone.

Results

El.	site		radii (I)	radii (II)
Sr	(0, 0, 0)	<i>1a</i>	1.70	1.57
Ti	($\frac{1}{2}, \frac{1}{2}, \frac{1}{2}$)	<i>1b</i>	1.05	0.92
O	($\frac{1}{2}, \frac{1}{2}, 0$)	<i>3c</i>	0.90	1.03
Ze	($\frac{1}{2}, x, x$)	<i>12j</i>	0.51	0.50
			($x = 0.19$)	($x = 0.13$)
$\cdot V_{WS} / \sum_i V_i$			1.130	1.147

Table 3.10: Unit cell parameters and sets of radii used in the LSW-calculation

El.	core	Hankel	N_H	Bessel	N_{tot}
Sr	<i>1s2s2p</i>	<i>5s</i>		<i>+4f</i>	
(1)	<i>3s3p3d</i>	<i>5p</i>	9		16
	<i>4s4p</i>	<i>4d</i>			
Ti	<i>1s2s2p</i>	<i>4s</i>		<i>+4f</i>	
(1)	<i>3s3p</i>	<i>4p</i>	9		16
		<i>3d</i>			
O	<i>1s</i>	<i>2s</i>		<i>+4f</i>	
(3)		<i>2p</i>	9		16
		<i>3d</i>			
Ze		<i>1s</i>	1	<i>+2p</i>	9
(12)				<i>+3d</i>	

Table 3.11: Number of Hankel functions in the Hamiltonian (N_H) and number of Bessel functions used in the expansion at other sites.

Figure 3.21 shows from bottom to top the total density of states and the partial density of states for the strontium, the titanium and the oxygen sites. The zero refers to the highest filled state. The main features in the DOS are the oxygen *2p*-band between -5 and 0 eV. It is dominated by oxygen *2p* character, which can be checked from figure 3.22 in which the oxygen states are projected to the respective angular momenta. The oxygen *2p*-band is split in two sub-bands: the (lower) bonding band has a relatively larger contribution of titanium and strontium than the non-bonding band. Figures 3.22 give the angular momentum projected states for respectively titanium, strontium and oxygen.

The first band of unoccupied states is the rather narrow band between 2 and 4 eV,

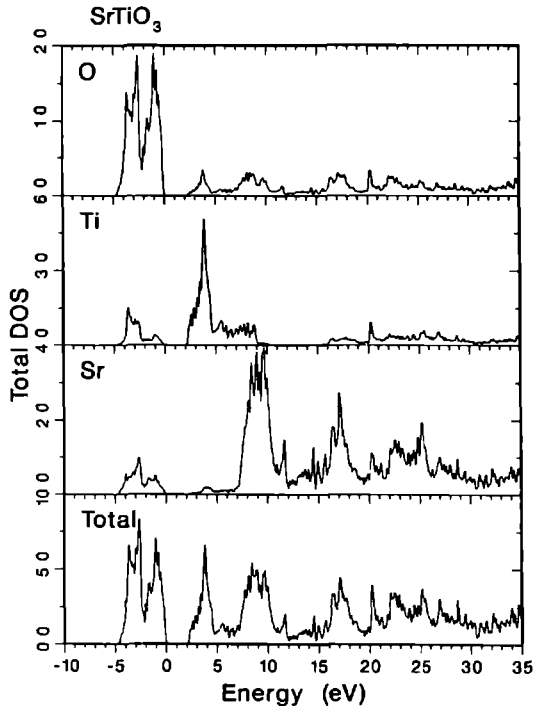


Figure 3.21: SrTiO₃ density of states. The total density of states (bottom) is split in the partial strontium, titanium and oxygen density of states.

which is dominated by titanium 3*d*-character. It represents the *t*_{2*g*} states which in a tight-binding picture are only π anti-bonding. The next band, between 4 and 9 eV, is related to the titanium 3*d* states of *e*_g character. It has rather low intensity and a relatively large dispersion. The *e*_g-band overlaps with the strontium 5*d* band between 7 and 10 eV. Notice that the strontium 6*s*-band is split into a part below and above the 5*d*-band.

Under the assumption that SrTiO₃ can be described in the weakly correlated limit and with the approximation that $\mathcal{P}_{eN+1} \approx \mathcal{P}_N$, the oxygen *p*-projected density of states simulates the oxygen 1*s* x-ray absorption spectral shape. In principle the density of states has to be modified with the transition matrix elements which are energy dependent, though it is expected that the effects of the matrix elements are not essential [174]. The oxygen *p*-projected density of states as given in figure 3.22 is broadened with a Lorentzian to mimic the lifetime of the oxygen 1*s* core hole and with a Gaussian to mimic the experimental resolution. Figure 3.23 compares the broadened oxygen *p*-projected density of states with the oxygen 1*s* x-ray absorption spectrum. The peaks in the broadened spectrum relate to respectively the oxygen *p* contribution to the *t*_{2*g*}-band at about 3.5 eV and the strontium 5*d*-band between 7 and 10 eV. The shoulder at 12 eV relates mainly to oxygen *p*-character hybridized with strontium 6*s*-states as can be checked in figure 3.22. The peak at about 17 eV marks the onset of the titanium 4*sp*-band and the structure at about 23 eV also relates to this band. The experimental spectrum bears resemblance to the theoretical curve and the peaks discussed can also be found in the experiment, though their calculated energy position

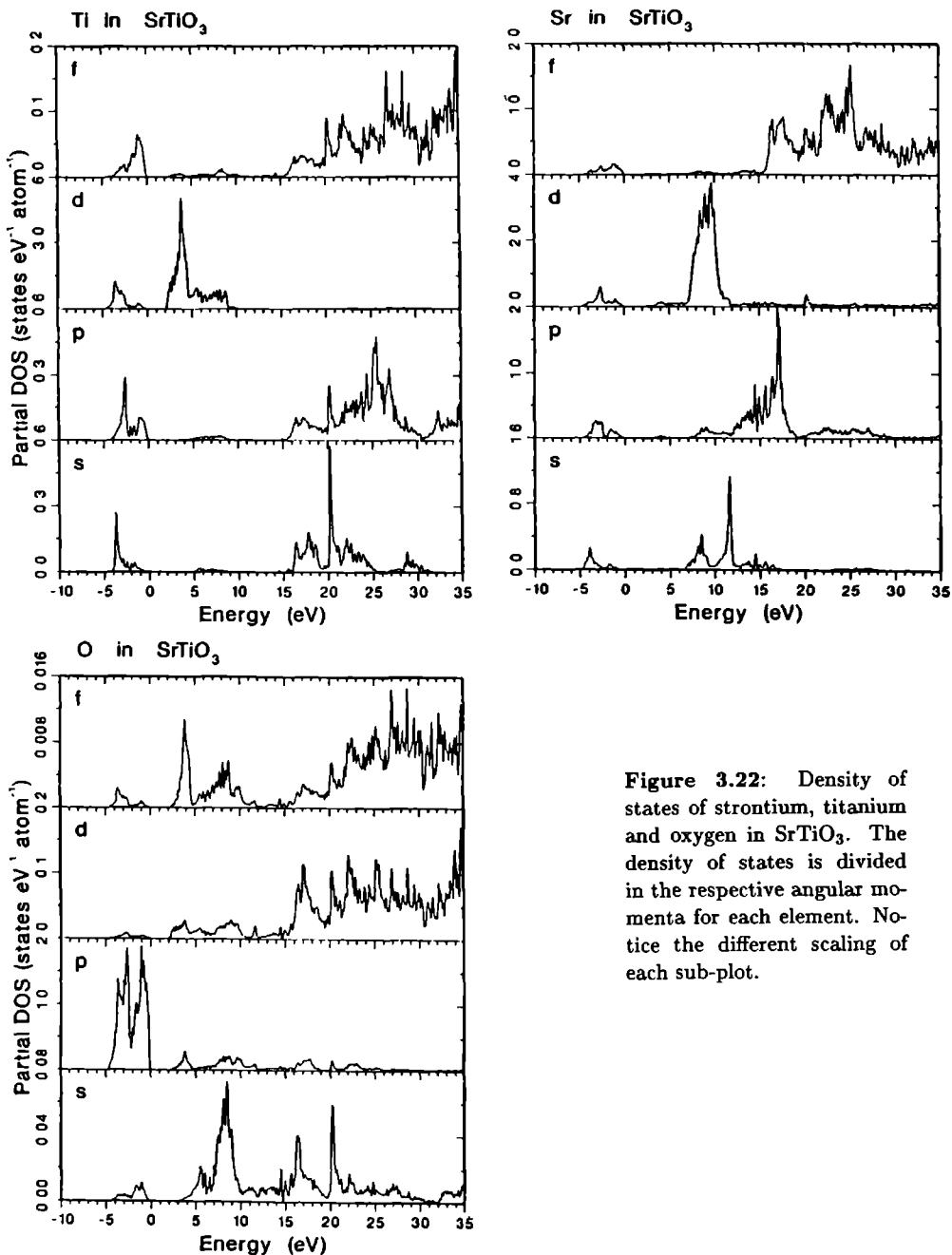


Figure 3.22: Density of states of strontium, titanium and oxygen in SrTiO₃. The density of states is divided in the respective angular momenta for each element. Notice the different scaling of each sub-plot.

is slightly off. The spectrum is aligned at the sharp t_{2g} -peak at threshold. The strontium

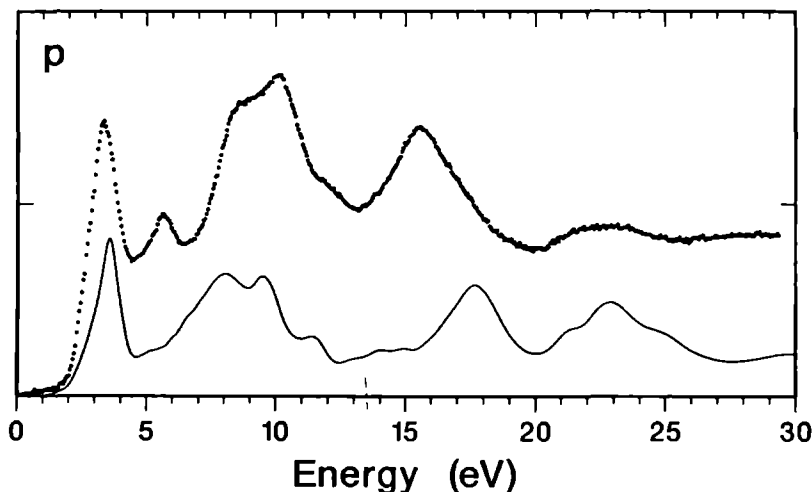
Oxygen k edge of SrTiO_3 

Figure 3.23: The oxygen $1s$ x-ray absorption spectrum of SrTiO_3 (dots) compared with the broadened oxygen p projected density of states (solid line). The scaling of the y -axis is arbitrarily.

$5d$ -band including its $6s$ -shoulder are found at slightly higher energy in the experiment whereas the peaks related to the titanium $4sp$ -band are found at slightly lower energy. The sharp e_g -peak present in the experiment is visible as a weak shoulder only in the calculated density of states.

As indicated an approximation of the present analysis is the usage of the ground state density of states. Qualitatively it can be expected that an oxygen $1s$ core hole affects the spectral shape mainly as an attractive potential which pulls weight to the bottom of the respective bands (see also next section). Especially the narrow $3d$ -bands are sensitive to the core hole potential and it is to be expected that the final state oxygen p density of states pile up at the bottom of the t_{2g} and the e_g -band. The t_{2g} -band is already narrow in the ground state and after the broadening little effect will be visible. However the e_g -band is expected to form a peak at the bottom of the band, as is indeed observed. From the comparison with experiment it is noticed that the bands related to strontium are found at higher energy compared with the bands related to titanium, which might indicate a stronger core hole effect on the states which are bonded to the titanium sites (as compared with the strontium sites). Additional effects which might explain part of the discrepancies observed include correlations effects, which are not treated correctly in the local density methods. As far as the major structures are concerned the agreement between the calculated oxygen p density of states and the observed oxygen $1s$ x-ray absorption spectrum is reasonably good, but the fine details as well as the exact energy-positions are influenced by effects not included in the N -particle density of states.

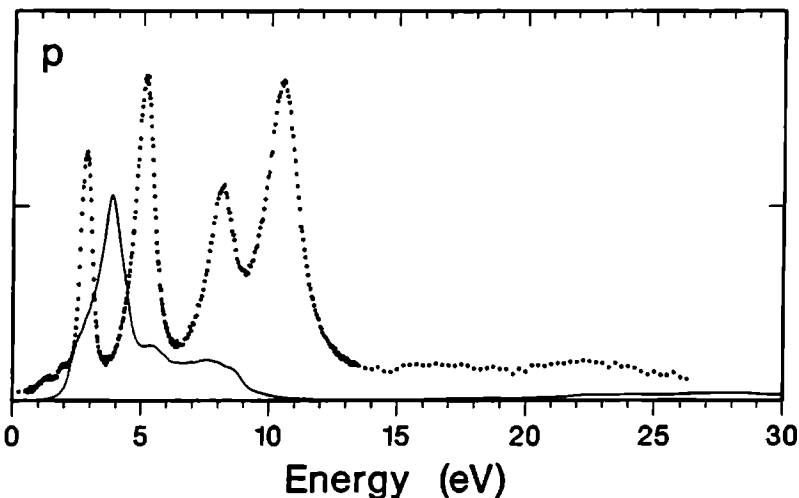
Titanium 2p edge of SrTiO₃

Figure 3.24: The titanium 2p x-ray absorption spectra of SrTiO₃ (dots) compared with the broadened titanium d projected density of states (solid line). The scaling of the y-axis is arbitrarily.

To show the importance of correlation effects for the metal 2p x-ray absorption edge, as discussed in the preceding sections, figure 3.24 compares the experimental spectrum with the titanium 3d-projected density of states. The multipole correlation effects in combination with the 2p spin-orbit coupling and the cubic crystal field give rise to a multiplet structure consisting of seven sharp peaks which was explained in detail in section 3.3. These interactions make a N-particle density of states approach to the spectrum useless as is obvious from the large disagreement.

An LSW-calculation similar to the one described for SrTiO₃ has been performed for LaTiO₃. In section 4.4 the density of states description of SrTiO₃ and LaTiO₃ is used to discuss the oxygen 1s x-ray absorption spectra of the series of La_{1-x}Sr_xTiO₃-compounds and a series of similar perovskites with respectively manganese, iron and cobalt.

LSW results for CuO

To place the calculation of SrTiO₃ in perspective, a similar LSW for CuO (3d⁹) is discussed shortly. The details are discussed by Grioni et al. [168]. The 3d-band in CuO contains 9 electrons and is situated between -3 and +1 eV and the oxygen 2p band is with respect to SrTiO₃ shifted to lower energy (-7.5 to -3 eV). Above the 3d-band there is a gap of approximately 2 eV followed by a slowly rising copper 4sp-band. The density of states calculation has a band crossing the Fermi level, which is in contrast to the finding that CuO is an insulator. This error is most likely a consequence of the incomplete treatment of

correlation (and/or the incorrect treatment of the spin and orbital polarization).

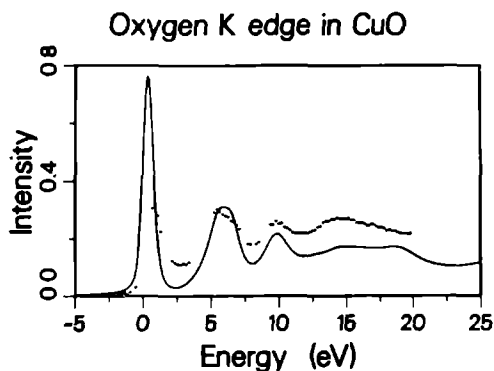


Figure 3.25: The oxygen $1s$ x-ray absorption spectrum of CuO compared with the broadened oxygen p -projected density of states. Reproduced from Ref. 168.

As there is one $3d$ -hole per copper this hole will tend to localize, thereby prohibiting electric conduction. Figure 3.25 compares the oxygen $1s$ x-ray absorption spectrum with the broadened oxygen $2p$ density of states. The agreement is good apart from the $3d$ -band which has an offset of 0.5 eV and an intensity which is far too high theoretically. The high intensity in the theoretical spectrum is greatly reduced after inclusion of the core hole. The energy offset however cannot be related to the core hole as it is also present in the BIS spectrum [167]. The offset is therefore related to an incomplete treatment of (correlation within) the $3d$ -band

3.8.3. Inclusion of core hole effects

The core hole can be included in the LSW electronic structure calculations by the removal of a core electron of one of the atoms. To reduce non-physical interactions between two sites with a core hole, the size of the unit cell is increased and a so-called supercell calculation is performed. This supercell calculation is a complete new self-consistent calculation of \mathcal{P}_{eN+1} instead of \mathcal{P}_N and according to the final state rule [158, 159], the correct spectral shape (within the weakly correlated limit) is calculated in this manner. This approach has been applied successfully to the $L_{2,3}$ -edges of Ag_2O [165, 166] and the silicon K edges of $TiSi$ and $TiSi_2$ [166, 169].

An LSW calculation with an oxygen $1s$ core hole has been performed for $LiCoO_2$ [175]. In this compound cobalt has the low-spin $3d^6$ -configuration (1A_1 -symmetry). Consequently the density of states consists of the oxygen $2p$ band and the t_{2g} -band, which both are filled. The empty bands are the e_g -band and at higher energy the $4sp$ -band and bands related to lithium. The oxygen $1s$ x-ray absorption spectrum probes the e_g -band and at higher energies the other empty bands. Figure 3.26 gives the comparison of the x-ray absorption spectrum with the density of states, with and without inclusion of the core hole. A general agreement is found and the overestimation of the intensity of the e_g -band is clearly removed

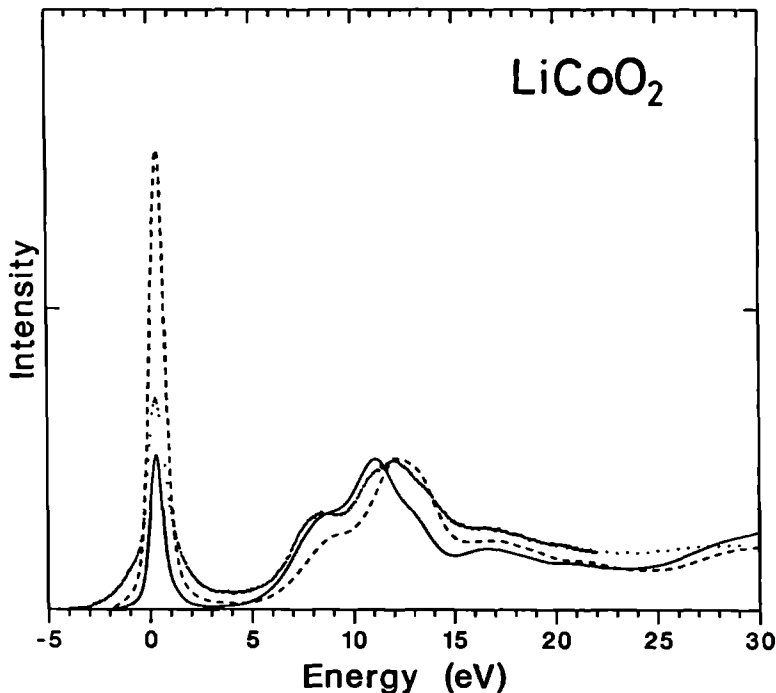


Figure 3.26: The oxygen $1s$ x-ray absorption spectrum of LiCoO₂ compared with the broadened oxygen p -projected density of states. The dashed line refers to the ground state density of states. The solid line refers to the density of states after inclusion of the oxygen $1s$ core hole: \mathcal{P}_{cN+1} .

after inclusion of the core hole. In fact the density of states is slightly too low in the core hole calculation.

The core hole effect as calculated for the LiCoO₂ spectrum confirms that an oxygen $1s$ core hole will locally pull down states to the bottom of the bands. The result for $3d$ -metal oxides is that the intensity of the narrow $3d$ -band is reduced. The bands at higher energy are less influenced because they are more extended. The main effect is a redistribution of spectral weight which in general results in an increase of intensity at the bottom of each band. As a final remark it is noticed that though the core hole LSW-calculations give the correct final state density of states needed to describe the x-ray absorption spectrum within the weakly correlated limit, for narrow band materials like the $3d$ -metal oxides there will be omissions as the dd -correlations (or in other words fluctuations) are not treated correctly.

References

- [1] R. Stumm von Bordwehr, *Ann. Phys. Fr.* **14**, 377 (1989).
- [2] W.C. Röntgen, *Sitzungsberichte Phys. Mediz. Gesellschaft zu Würzburg* **137**, 132 (1895);

- English translation in: *Nature* **53**, 274 (1896).
- [3] H.G.J. Moseley, *Phil. Mag.* **26**, 1024 (1913).
 - [4] R. Sagnac, *Ann. Chim. Phys. Ser. VII* **23**, 145 (1901).
 - [5] C.G. Barkla, *Phil. Mag.* **22**, 396 (1911); C.G. Barkla and V. Collier, *Phil. Mag.* **23**, 987 (1912).
 - [6] N. Bohr, *Phil. Mag.* **26**, 1 (1913); *ibid.* **26**, 476 (1913); *ibid.* **26**, 857 (1913).
 - [7] W. Stenström, *Ann. Phys. (Leipzig)* **57**, 347 (1918).
 - [8] H. Fricke, *Phys. Rev.* **16**, 202 (1920).
 - [9] W. Kossel, *Z. Phys.* **1**, 119 (1920).
 - [10] J. Bergengren, *Z. Phys.* **3** 247 (1920).
 - [11] L. Pauling, *Phys. Rev.* **34**, 954 (1929); based on K. Fajans, *Z. Phys.* **50**, 531 (1928).
 - [12] W. Heisenberg, *Z. Phys.* **33**, 879 (1925).
 - [13] E. Schrödinger, *Ann. Phys. (Leipzig)* **79**, 361 (1926); *ibid.* **79**, 489 (1926); *ibid.* **80**, 437 (1926); *ibid.* **81**, 109 (1926)
 - [14] H. Hall, *Rev. Mod. Phys.* **8**, 358 (1936).
 - [15] R.D. Cowan, *The Theory of Atomic Structure and Spectra* (Univ. of California Press, Berkeley, 1981).
 - [16] Ref. 1; chapter 3.
 - [17] R. de L. Kronig, *Z. Phys.* **70**, 317 (1931).
 - [18] Ref. 1; page 399.
 - [19] J. Veldkamp, *Z. Phys.* **77**, 250 (1932).
 - [20] R. Smoluchowski, *Z. Phys.* **94**, 775 (1935).
 - [21] P.A.M. Dirac, *Proc. Roy. Soc. A.* **114**, 243 (1927).
 - [22] H.M. O'Bryan and H.W.B. Skinner, *Phys. Rev.* **45**, 370 (1934).
 - [23] H. Jones, N.F. Mott and H.W.B. Skinner, *Phys. Rev.* **45**, 379 (1934).
 - [24] J.E. Müller and J.W. Wilkins, *Phys. Rev. B.* **29**, 4331 (1984).
 - [25] R. Natoli and M. Benfatto, *J. Phys. Coll. C8.* **47**, 11 (1986).
 - [26] E. Lindberg, *Diss. Nova Acta Reg. Soc. Sci. Uppsalenus* **7**, IV, 7 (1931).
 - [27] Sandström, *Diss. Nova Acta Reg. Soc. Sci. Uppsalenus* **9**, IV, 2 (1935).
 - [28] K.C. Rule *Phys. Rev.* **68**, 246 (1945).
 - [29] E.A. Stewardson and P.A. Lee, *Proc. Phys. Soc. A.* **64**, 318 (1951); E.A. Stewardson and J.E. Wilson, *ibid.*, **69**, 93 (1956).
 - [30] H.F. Zandy, *Proc. Phys. Soc. A.* **65**, 1015 (1952).
 - [31] K.C. Williams, *Proc. Phys. Soc.* **87**, 983 (1966).
 - [32] H. F. Zandy, *Phys. Rev.* **162**, 1 (1967).
 - [33] F.H. Combley, E.A. Stewardson and J.E. Wilson, *J. Phys. B.* **1**, 120 (1968).
 - [34] T.M. Zimkina, V.A. Fomichev, S.A. Gribovskii and I.I. Zhukova, *Sov. Phys. Sol. State* **9**, 1128 (1967).
 - [35] V.A. Fomichev, T.M. Zimkina, S.A. Gribovskii and I.I. Zhukova, *Sov. Phys. Sol. State* **9**, 1163 (1967).
 - [36] R. Haensel, P. Rabe and B. Sonntag *Solid State Comm.* **8**, 1845 (1970).
 - [37] U. Fano, *Phys. Rev.* **124**, 1866 (1961); J.W. Cooper, *Phys. Rev. Lett.* **13**, 762 (1964); U. Fano and J.W. Cooper, *Rev. Mod. Phys.* **40**, 441 (1968).
 - [38] J. L. Dehmer, A.F. Starace, U. Fano, J. Sugar and J.W. Cooper, *Phys. Rev. Lett.* **26**, 1521 (1971).
 - [39] A.F. Starace, *Phys. Rev. B* **5**, 1773 (1972).

- [40] J. Sugar, *Phys. Rev. B* **5**, 1785 (1972).
- [41] J.L. Dehmer and A.F. Starace, *Phys. Rev. B* **5**, 1792 (1972).
- [42] J.L. Dehmer, *J. Chem. Phys.* **56**, 4496 (1972).
- [43] C. Froese, *Can. J. Phys.* **41**, 1895 (1963).
- [44] S. Sugano, Y. Tanabe and H. Kitamura, *Multiplets of Transition Metal Ions* (Academic Press, New York, 1970).
- [45] E.J. McGuire, *J. Phys. Chem. Solids* **33**, 577 (1972).
- [46] N.N. Axelrod and M.P. Givens, *Phys. Rev.* **120**, 1205 (1960).
- [47] B. Sonntag, R. Haensel and C. Kunz, *Solid State Comm.* **7**, 597 (1969).
- [48] R.E. Dietz, E.G. McRae, Y. Yafet and C.W. Caldwell, *Phys. Rev. Lett.* **33**, 1372 (1974).
- [49] L.C. Davis and L.A. Feldkamp, *Phys. Rev. B* **15**, 2961 (1977).
- [50] L.C. Davis and L.A. Feldkamp, *Phys. Rev. B* **23**, 6239 (1981).
- [51] R. Bruhn, B. Sonntag and H.W. Wolff, *Phys. Lett. A* **69**, 9 (1978).
- [52] L.C. Davis, *J. Appl. Phys.* **59**, R25 (1986).
- [53] S.-I. Nakai, H. Nakamori, A. Tomita, K. Tsutsumi, H. Nakamura, C. Sugiura, *Phys. Rev. B* **4**, 1870 (1974).
- [54] S. Shin, S. Suga, H. Kanzaki, S. Shibuya and T. Yamaguchi, *Solid State Comm.* **38**, 1281 (1981).
- [55] F. Brown, C. Gähwiller and A.B. Kunz, *Solid State Comm.*, **9**, 487 (1971).
- [56] S. Asada, C. Satako and S. Sugano, *Technical Report of the Institute of Solid State Physics* (Univ. of Tokyo, 1974) A, 671.
- [57] S. Asada, C. Satako and S. Sugano, *J. Phys. Soc. Jap.* **37**, 855 (1975).
- [58] T. Yamaguchi and S. Sugano, *J. Phys. Soc. Jap.* **42**, 1949 (1977).
- [59] R.P. Gupta and S.K. Sen, *Phys. Rev. B* **10**, 71 (1974).
- [60] R.P. Gupta and S.K. Sen, *Phys. Rev. B* **12**, 15 (1975).
- [61] S.P. Kowalczyk, L. Ley, F.R. McFreely and D.A. Shirley, *Phys. Rev. B* **11**, 1721 (1975).
- [62] T. Novakov, *Phys. Rev. B* **3**, 2693 (1971).
- [63] A. Kotani and Y. Toyozawa, *J. Phys. Soc. Jap.* **37**, 912 (1974).
- [64] S. Asada and S. Sugano, *J. Phys. Soc. Jap.* **41**, 1291 (1976).
- [65] J. Zaanen, C. Westra and G.A. Sawatzky, *Phys. Rev. B* **33**, 8060 (1986).
- [66] This in contrast to the calculations in this thesis for which essentially the atomic values are used and in general no reduction is applied.
- [67] S. Suga, S. Shin, M. Taniguchi, K. Inoue, M. Seki, I. Nakada, S. Shibuya and T. Yamaguchi, *Phys. Rev. B* **25**, 5487 (1982).
- [68] S. Shin, S. Suga, M. Taniguchi, H. Kanzaki, S. Shibuya and T. Yamaguchi, *J. Phys. Soc. Jap.* **51**, 906 (1982).
- [69] T. Yamaguchi, S. Shibuya, S. Sugano, *J. Phys. C* **15**, 2625 (1982).
- [70] T. Yamaguchi, S. Shibuya, S. Suga, S. Shin, *J. Phys. C* **15**, 2641 (1982).
- [71] B.T. Thole, G. van der Laan, J.C. Fuggle, G.A. Sawatzky, R.C. Karnatak and J.-M. Esteve, *Phys. Rev. B* **32**, 5107 (1985).
- [72] R.D. Cowan, *J. Opt. Soc. Am.* **58**, 808 (1968).
- [73] B.T. Thole, R.D. Cowan, G.A. Sawatzky, J. Fink and J.C. Fuggle, *Phys. Rev. B* **31**, 6856 (1985).
- [74] P.H. Butler, *Point Group Symmetry Applications: Methods and Tables* (Plenum Press, New York, 1981).
- [75] B.T. Thole, G. van der Laan and P.H. Butler, *Chem. Phys. Lett.* **149**, 295 (1988).

- [76] G. van der Laan, B.T. Thole, G.A. Sawatzky and M. Verdaguer, *Phys. Rev. B* **37**, 6587 (1988).
- [77] K.M. Karplus and R.N. Porter, *Atoms and Molecules* (Benjamin Publ., Marlo Park, 1970).
- [78] C.W. Nielson and G.F. Koster, *Spectroscopic Coefficients for the p^N , d^N and f^N Configurations* (M.I.T. Press, Cambridge Massachutes, 1963).
- [79] E.U. Condon and G.H. Shortley, *The Theory of Atomic Spectra* (Univ. Press, Cambridge, 1935).
- [80] J.S. Griffith, *The Theory of Transition Metal Ions* (Univ. Press, Cambridge, 1964).
- [81] J. van Elp, PhD. thesis: *The electronic structure of doped late transition metal monoxides*, (University of Groningen, 1990).
- [82] F. Hund, *Linienspektren und Periodisches System der Elemente* (Julius Springer, Berlin, 1927), page 124 ff.
- [83] C.J. Ballhausen, *Introduction to Ligand Field Theory*, (McGraw-Hill, New York, 1962).
- [84] B.T. Thole, G. van der Laan and P.H. Butler, *Chem. Phys. Lett.* **149**, 295 (1984).
- [85] Jahn and Teller, *Proc. Roy. Soc.* **161**, 220 (1937).
- [86] D. van de Marel, PhD. Thesis, (University of Groningen, 1985).
- [87] J.C. Fuggle, G.A. Sawatzky and J.W. Allen (Eds): *Narrow Band Phenomena* (Plenum Press, New York, 1988); page 3.
- [88] J.A. Wilson, *Adv. Phys.* **19**, 1 (1970).
- [89] P. Carra and M. Altarelli, *Phys. Rev. Lett.* **64**, 1286 (1990).
- [90] C. Brouder, *J. Phys. C* **2**, 701 (1990).
- [91] K. Kramers, *Akad. van Wetenschappen*, **33**, 959 (Amsterdam, 1930).
- [92] E.T. Keve, S.C. Abrahams and J.L. Bernstein, *J. Chem. Phys.* **53**, 3279 (1970).
- [93] B. Sinkovic, private comm.; C.T. Chen and F. Sette, *Physica Scripta* **T31**, 119 (1990).
- [94] B. Sinkovic et al. to be published.
- [95] C. Brouder, J.-P. Kappler and E. Beaurepaire, *Conference Proceedings of the 2nd European Conference on Progress in X-ray Synchrotron Radiation Research*, Eds. A. Balerna, E. Bernieri and S. Mobilio (SIF, Bologna, 1990), page 19.
- [96] B. Poumellec, R. Cortes, G. Tourillon and J. Berthon, *Conference Proceedings of the 2nd European Conference on Progress in X-ray Synchrotron Radiation Research*, Eds. A. Balerna, E. Bernieri and S. Mobilio (SIF, Bologna, 1990), page 23.
- [97] F.J. Himpsel, U.O. Karlsson, A.B. McLean, L.J. Terminello, F.M.F. de Groot, M. Abbate, J.C. Fuggle, J.A. Yarmoff, B.T. Thole and G.A. Sawatzky, *Phys. Rev. B* **43**, 6899 (1991).
- [98] J. Somers, *X-ray absorption spectroscopy of small molecules in: Unoccupied Electronic States*, Eds: J.C. Fuggle and J. Inglesfield, (Springer, Berlin, 1991).
- [99] M. Pedio, J.C. Fuggle, J. Somers, E. Umbach, J. Haase, Th. Lindner, U. Höfer, M. Grioni, F.M.F. de Groot, B. Hilert, L. Becker and A. Robinson, *Phys. Rev. B* **40**, 7924 (1989).
- [100] *X-ray Absorption Fine Structure VI*, Ed. S.S. Hasnain, (Ellis Horwood, Chichester, 1991); chapter IV, pages 191-282; references therein.
- [101] M. Pedio, L. Becker, B. Hillert, S.D. Addato and J. Haase, *Phys. Rev. B* **41**, 7462 (1990).
- [102] A.B. McLean, L.J. Terminello and F.J. Himpsel, *Phys. Rev. B* **41**, 7694 (1990).
- [103] G. Schütz, W. Wagner, W. Wilhelm, P. Kienle, R. Zeller, R. Frahm and G. Materlik, *Phys. Rev. B* **58**, 737 (1987).
- [104] G. Schütz, R. Wienke, W. Wilhelm, W.P. Zeper, H. Ebert and K. Spörl, *J. Appl. Phys.* **67**, 4456 (1990).
- [105] F. Baudalet, E. Dartyge, A. Fontaine, C. Brouder, G. Krill, J.P. Kappler and M. Piecuch,

- Phys. Rev. B.* **43**, 5857 (1991).
- [106] P. Fisher, G. Schütz, M. Knülle, S. Stähler, A. Puschmann and W.D. Brewer, *BESSY-report 1990* (1991): page 197.
- [107] M. Sacchi, unpublished results.
- [108] F. Sette, C.T. Chen, Y. Ma, S. Modesti and N.V. Smith, *X-ray Absorption Fine Structure VI* Ed. S.S. Hasnain, (Ellis Horwood, Chichester, 1991).
- [109] C.T. Chen, F. Sette, Y. Ma and S. Modesti, *Phys. Rev. B.* **42**, 7262 (1990).
- [110] H. Ebert, G. Schütz and W.M. Temmerman, *Solid State Comm.* **76**, 475 (1990).
- [111] C. Brouder and M. Hikam, *Phys. Rev. B.* **43**, 3809 (1991).
- [112] J.B. Goedkoop, PhD. Thesis, *X-ray dichroism of rare earth materials* (University of Nijmegen, 1989).
- [113] S. Imada and T. Jo, *J. Phys. Soc. Jap* **59**, 3358 (1990).
- [114] G. van der Laan and B.T. Thole, *Phys. Rev. B* **43**, 13401 (1991).
- [115] C.T. Chen, N.V. Smith and F. Sette, *Phys. Rev. B.* **43**, 6785 (1991).
- [116] T. Jo and G.A. Sawatzky, *Phys. Rev. B.* **43**, 8771 (1991).
- [117] G. van der Laan, B.T. Thole, G.A. Sawatzky, J.B. Goedkoop, J.C. Fuggle, J.-M. Esteva, R.C. Karnatak, J.P. Remeika and H.A. Dabkowska, *Phys. Rev. B.* **34**, 6529 (1986).
- [118] M. Sacchi, R.J.H. Kappert, J.C. Fuggle and E.E. Marinero, *Appl. Phys. Lett.*, accepted for publication.
- [119] M. Sacchi, O. Sakho and G. Rossi, *Phys. Rev. B.* **43**, 1276 (1991).
- [120] R.J.H. Kappert, PhD. Thesis, (University of Nijmegen, in print).
- [121] K. Rajnak and B.G. Wybourne, *Phys. Rev.* **132**, 280 (1963).
- [122] K. Rajnak and B.G. Wybourne, *Phys. Rev.* **134**, 596 (1964).
- [123] B.G. Wybourne, *Phys. Rev.* **137**, 364 (1965).
- [124] B.G. Wybourne, *Spectroscopic Properties of Rare Earths*, (Interscience, New York, 1965), chapter 2,17.
- [125] R.D. Cowan, *The Theory of Atomic Structure and Spectra*, (University of California Press, Berkeley, 1981), page 464.
- [126] B.K. Sarpal, C. Blancard, J.P. Connerade, J.M. Esteva, J. Hormes, R.C. Karnatak and U. Kuetgens, *J. Phys. B.* **24**, 1593 (1991).
- [127] B.T. Thole, G.A. Sawatzky, R. Karnatak and J.-M. Esteva, *Phys. Rev. B.* **33**, 4253 (1986).
- [128] D.W. Lynch and R.D. Cowan, *Phys. Rev. B.* **36**, 9228 (1987).
- [129] O. Gunnarsson and K. Schönhammer, *Phys. Rev. B.* **28**, 4315 (1983).
- [130] O. Gunnarsson and K. Schönhammer, *Phys. Rev. B.* **31**, 4815 (1985).
- [131] A. Kotani, H. Mizuta, T. Jo and J.C. Parlebas, *Solid State Comm.* **85**, 805 (1985).
- [132] T. Jo and A. Kotani, *Solid State Comm.* **54**, 451 (1985).
- [133] T. Jo and A. Kotani, *J. Phys. Soc. Jap.* **55**, 2457 (1986).
- [134] A. Kotani, T. Jo, K. Okada, T. Nakano, M. Okada, A. Bianconi, A. Marcelli and J.C. Parlebas, *J. Magn. Magn. Mat.* **70**, 28 (1987).
- [135] A. Kotani, *Many body effects in core-level spectroscopy of solids* in: *Core Level Spectroscopy*, Eds: J. Kanamori and A. Kotani, (Springer, 1988), page 3.
- [136] T. Jo and A. Kotani, *theory of high energy spectroscopy in CeO₂* in: *Core Level Spectroscopy*, Eds: J. Kanamori and A. Kotani, (Springer, 1988), page 34.
- [137] T. Jo and A. Kotani, *J. Phys. Soc. Jap.* **57**, 2288 (1988).
- [138] A. Kotani, H. Ogasawara, K. Okada, B.T. Thole and G.A. Sawatzky, *Phys. Rev. B.* **40**, 65 (1989).

- [139] T. Jo, *J. Phys. Soc. Jap.* **58**, 1452 (1989).
- [140] S. Imada and T. Jo, *J. Phys. Soc. Jap.* **58**, 402 (1989).
- [141] S. Imada and T. Jo, *J. Phys. Soc. Jap.* **58**, 2665 (1989).
- [142] S. Imada and T. Jo, *Physica Scripta* **41**, 115 (1990).
- [143] O. Gunnarsson, O.K. Andersen, O. Jepsen and J. Zaanen, *Phys. Rev. B.* **39**, 1708 (1989).
- [144] M.S. Hybertsen, M. Schlüter and N.E. Christensen, *Phys. Rev. B.* **39**, 9028 (1989).
- [145] A.K. McMahan, R.M. Martin and S. Satpathy, *Phys. Rev. B.* **38**, 6650 (1988).
- [146] A. Kotani, T. Ikeda, K. Okada and H. Ogasawara, *J. El. Spec. Rel. Phen.* **51**, 229 (1990).
- [147] T. Ikeda, K. Okada, H. Ogasawara and A. Kotani, *J. Phys. Soc. Jap.* **59**, 622 (1990).
- [148] J.-I. Igarashi, *J. Phys. Soc. Jap.* **59**, 1868 (1990).
- [149] J.-I. Igarashi, *J. Phys. Soc. Jap.* **59**, 348 (1990).
- [150] H. Eskes and G.A. Sawatzky, *Phys. Rev. Lett.* **61**, 1415 (1988).
- [151] G. van der Laan, J. Zaanen, G.A. Sawatzky, R. Karnatak and J.-M. Esteve, *Phys. Rev. B.* **33**, 4253 (1986).
- [152] G. van der Laan, C. Westra, C. Haas and G.A. Sawatzky, *Phys. Rev. B.* **23**, 4369 (1981).
- [153] Values derived from table II in Ref. 65.
- [154] C.K. Jorgensen, *Absorption Spectra and Chemical Bonding in Complexes*, (Pergamon Press, Oxford, 1962).
- [155] C.K. Jorgensen, *Modern Aspects of Ligand Field Theory*, (North Holland, Amsterdam, 1971).
- [156] P.C. Hohenberg and W. Kohn, *Phys. Rev.* **136**, 864 (1964).
- [157] W.Kohn and L.J. Sham, *Phys. Rev.* **140**, 1133 (1965).
- [158] U. von Barth and G. Grossman, *Solid State Comm.* **32**, 645 (1979); U. von Barth and G. Grossman *Phys. Rev. B.* **25**, 5150 (1982).
- [159] G.D. Mahan, *Phys. Rev. B.* **21**, 1421 (1980).
- [160] L. Hedin and B.I. Lundqvist, *J. Phys. C.* **3**, 2065 (1971).
- [161] A.R. Williams, J. Kübler and C.D. Gelatt Jr., *Phys. Rev. B.* **19**, 6094 (1979).
- [162] O.K. Andersen and O. Jepsen, *Phys. Rev. Lett.* **53**, 2571 (1984).
- [163] O.K. Andersen, O. Jepsen and D. Glötzel, *Highlights of Condensed Matter Theory*, Eds. F. Bassani, F. Fumi and M. Tosi (North-Holland, Amsterdam, 1985); page 59 ff.
- [164] F. Springelkamp, M.T. Czyżyk and R.A. de Groot, (1987), unpublished; see also H. van Leuken, A. Lodder, M.T. Czyżyk, F. Springelkamp and R.A. de Groot, *Phys. Rev. B.* **41**, 5613 (1990).
- [165] M.T. Czyżyk, R.A. de Groot, G. Dalba, P. Fornasini, A. Kisiel, F. Rocca and E. Burattini, *Phys. Rev. B.* **39**, 9831 (1989).
- [166] M.T. Czyżyk and R.A. de Groot, *Conference Proceedings of the 2nd European Conference on Progress in X-ray Synchrotron Radiation Research*, Eds: A. Balerna, E. Bernieri and S. Mobilio (SIF, Bologna, 1990); page 47.
- [167] J. Ghijsen, L.H. Tjeng, J. van Elp, H. Eskes, J. Westerink, G.A. Sawatzky and M.T. Czyżyk, *Phys. Rev. B.* **41**, 5613 (1990).
- [168] M. Grioni, M.T. Czyżyk, F.M.F. de Groot, J.C. Fuggle, B.E. Watts, *Phys. Rev. B.* **39**, 4886 (1989).
- [169] P.J.W. Weijs, M.T. Czyżyk, J.F. van Acker, W. Speier, J.B. Goedkoop, H. van Leuken, H.J.M. Hendriks, R.A. de Groot, G. van der Laan, K.H.J. Buschow, G. Wiech and J.C. Fuggle, *Phys. Rev. B.* **41**, 11899 (1990).
- [170] M.T. Czyżyk, K. Lawniczak - Jablonska, S. Mobilio, *Phys. Rev. B.*, submitted.
- [171] Methfessel, PhD. Thesis: *Multipole Green Functions for Electronic Structure Calculations*

- (University of Nijmegen, 1986); references therein.
- [172] L.A. Shuvalov, *Modern Crystallography IV; Physical properties of crystals* (Springer series in Solid State Sciences, Berlin, 198x).
- [173] R.W.G. Wyckoff, *Crystal Structures II* (Interscience, New York, 1964).
- [174] J.J.M. Michiels et al., *Phys. Rev. B.*, submitted.
- [175] M.T. Czyżyk and G.A. Sawatzky, *Phys. Rev. B.*, submitted.
- [176] L.F. Mattheis, *Phys. Rev. B.* **6**, 4718 (1972).

4. THE ELECTRONIC STRUCTURE OF TRANSITION METAL OXIDES

In this chapter the emphasis will be on the electronic structure of transition metal oxides. In the introduction some important concepts concerning the electronic structure are given. In the subsequent sections the emphasis will be on a specific group of $3d$ -metal oxides: the binary $3d$ -metal oxides are discussed in section 4.2, which contains a reproduction of a paper concerning their oxygen $1s$ x-ray absorption spectra. The subsequent sections deal with doped $3d$ -metal oxides: Section 4.3 deals with lithium cobalt and lithium manganese oxides and section 4.4 with the $\text{La}_{1-x}\text{Sr}_x\text{TMO}_3$ perovskites (TM = $3d$ transition metal). In section 4.5 the oxides of vanadium are discussed. The conclusions from the x-ray absorption analysis are used to extend the ideas concerning the electronic structure in section 4.6.

4.1. Introduction

At present the leading model for the interpretation of $3d$ -(transition)-metal compounds is the so-called Zaanen-Sawatzky-Allen (ZSA) model [1]. The ZSA-model is able to explain the metallic or insulating nature of $3d$ -metal compounds. Its central parameters are the charge transfer energy (Δ) and the dd correlation energy (U), which are compared with the bandwidth (W) [1]. The model emerged from the interpretation of x-ray photoemission, Bremsstrahlung Isochromat Spectroscopy (BIS) and x-ray absorption of the nickel and copper halides [2-5]. It is an extension of Anderson's model to explain the magnetic behaviour of $3d$ -metal oxides [6] and the Mott-Hubbard model of metal insulator transitions [7]. The basic idea is that the electronic structure of a $3d$ -metal oxide is dominated by correlation effects of the $3d$ -electrons. The $3d$ -states are considered as localized impurity states which are positioned in between the oxygen $2p$ valence band and the metal $4sp$ conduction band.

Figure 4.1 sketches the electron addition and electron removal states for a $3d$ -metal oxide. From the interpretation of diverse spectroscopies it became clear that the first electron addition state is a $3d^{N+1}$ -state, while the addition of a $4sp$ -electron has a considerable higher energy [9]. The electron removal state with lowest energy is found to be a either $3d^{N-1}$ -state (Mott-Hubbard) or the ejection of an electron from the oxygen $2p$ valence band (charge transfer). From the figure U and Δ can be defined as:

- U is the energy difference between $3d^{N+1}$ and $3d^{N-1}$. Its value is thus defined as $U = E(3d^{N+1}) + E(3d^{N-1}) - 2 \cdot E(3d^N)$.

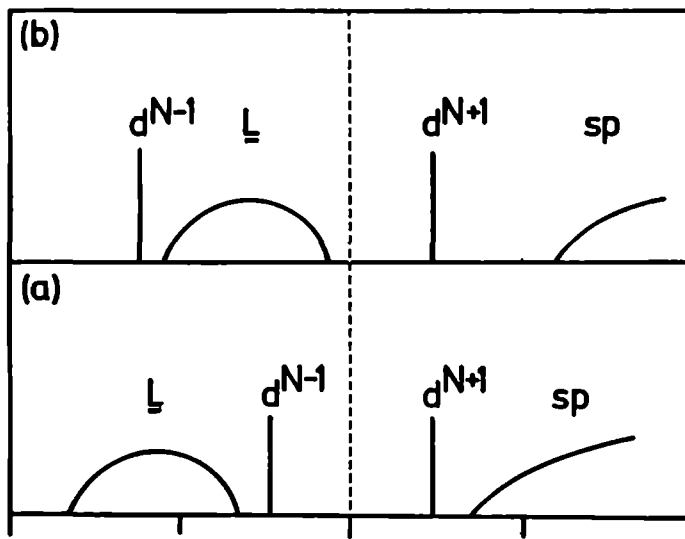


Figure 4.1: Electron addition and removal states of a 3d-metal oxide. (a) Mott-Hubbard, (b) charge transfer.

- Δ is the energy difference between $3d^{N+1}$ and the creation of a hole in the oxygen 2p band (\underline{L}). Its value is defined as $\Delta = E(3d^{N+1}\underline{L}) - E(3d^N)$.

If $U < \Delta$ the energy-gap is determined by U , and the system is a Mott-Hubbard like. A Mott-Hubbard insulator is formed if $U > W$. Alternatively if $U > \Delta$ and $\Delta > W'$ ¹ the system is a charge transfer insulator. If however $\Delta < W'$ the system a metallic state is formed. At the metal insulator transition the value of U and/or Δ generally will collapse to a much smaller value [8]. Figure 4.2 sketches the different regimes: If U or Δ are smaller than the bandwidth a metallic state will form. The insulating oxides can be divided in charge transfer and Mott-Hubbard insulators. If $U \approx \Delta$ an intermediate situation occurs. For the 3d-monoxides TiO, VO and FeO belong to the Mott-Hubbard regime, CuO and NiO to the charge transfer regime and MnO and CoO are intermediate. TiO and VO are (in the model as well in experiment) metals while the other monoxides are insulators [1].

Within the ZSA-model, the following aspects are discussed: what are the influences of multiplets and crystal fields on the values of U and Δ ?; how can theoretical estimates for U and Δ be determined?; how does the trend in the values influence the conductivity?; what exactly means $3d^N$?; and what are the effects if the oxides are doped with holes or electrons? The emphasis will be on the interpretation of oxygen 1s and metal 2p x-ray absorption edges. For the interpretation of other spectroscopies the reader is referred to Refs. 1 and 10 and references therein.

¹In case of a charge transfer system the overall bandwidth W' is a combination of the 3d-bandwidth (W) and the ligand-hole bandwidth (w).

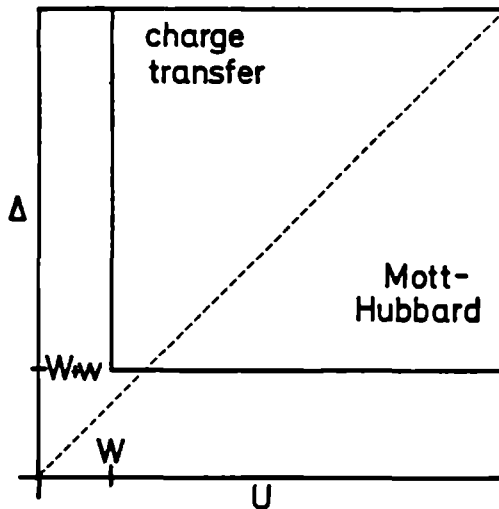


Figure 4.2: The ZSA-diagram for the determination of charge transfer versus Mott-Hubbard behaviour. If $\Delta < W+w$, or if $U < W$, a metallic state is formed.

The influence of multiplets and crystal field effects on U and Δ .

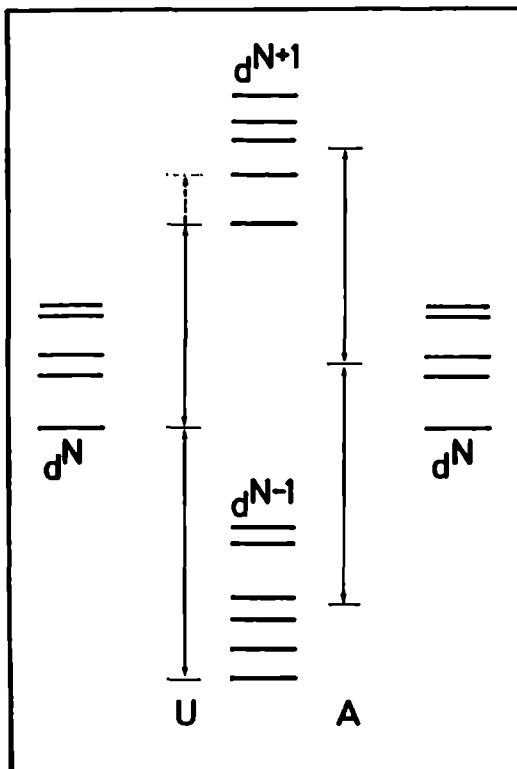


Figure 4.3: Comparison of A with U . The dashed extended line for U indicates a situation for which the lowest state of a $3d^{N+1}$ configuration does not have intensity in the electron addition spectrum.

Configuration	Multiplet	Crystal field
$3d^1 [^2T_2]$	–	$-2/5 \cdot \mathcal{D}$
$3d^2 [^3T_1]^*$	$-5B$	$-4/5 \cdot \mathcal{D}$
$3d^3 [^4A_2]$	$-15B$	$-6/5 \cdot \mathcal{D}$
$3d^4 [^5E]$	$-21B$	$-3/5 \cdot \mathcal{D}$
$3d^5 [^6A_1]$	$-35B$	0
$3d^6 [^5T_2]$	$-35B + 7C$	$-2/5 \cdot \mathcal{D}$
$3d^7 [^4T_1]^*$	$-40B + 14C$	$-4/5 \cdot \mathcal{D}$
$3d^8 [^3A_2]$	$-50B + 21C$	$-6/5 \cdot \mathcal{D}$
$3d^9 [^2E]$	$-56B + 28C$	$-3/5 \cdot \mathcal{D}$
$3d^{10} [^1A_1]$	$-70B + 35C$	0

Table 4.1: Atomic multiplet and crystal field effects ($\mathcal{D} \equiv 10Dq$) on the energy of the ground state of a high-spin $3d^N$ -configuration (modified from Ref.5).

*: The 3T_1 ground state of $3d^2$ and $3d^7$ configurations mixes with an excited state after inclusion of the cubic crystal field which slightly alters the value of $4/5 \cdot \mathcal{D}$; this affects also the magnitude of the atomic multiplet effects, which is $-8B$ (instead of $-5B$) in the atomic case [12].

In the definition for U and Δ as given above, the effects of the multipole interactions as well as the crystal fields effects are included. U measures the energy difference from the ground state in the $3d^N$ -multiplet to the respective ground states in the $3d^{N-1}$ and $3d^{N+1}$ multiplets. Alternatively one can define the value between the energy averages of the respective multiplet states, denoted as A . The difference between U and A is sketched in figure 4.3. In some specific cases the lowest state of $3d^{N+1}$ configuration does not have electron addition spectral weight and in those cases the effective value of U is given by the first state which does have spectral weight. The multipole and crystal field effects on the respective $3d^N$ states are given in table 4.1. From this table the corrections for U and Δ can be obtained directly and they are given in table 4.2.

Theoretical estimates for Δ and U

Theoretical estimates for Δ and U are given by Zaanen [5] and Torrance et al. [11]. In Ref. 5 the ionic estimate for U is based on the atomic U , which can be calculated from the F^0 Slater integrals for the respective Hund's rule ground states of the $N+1$, N and $N-1$ configurations. The values found are renormalized to an empirical value of 6 eV for NiO. In Ref. 11 also the atomic U is determined, but an additional factor is added related to $1/R_{dd}$, with R_{dd} the charge separation which is taken as the nearest neighbour metal metal distance. In the more common assumption of the ZSA-model the charge separation is taken to be infinite from which this extra term vanishes. As no empirical correction is assumed the values from Ref. 11 have an offset of about 6 eV with respect to those of Ref. 5. Figure 4.4 compares the estimates for the monoxides after the results from Ref. 11 have been renormalized to NiO. It should be noticed that these values include the atomic multiplet effects. Thus to find the

Configuration	Corrections on U		Corrections on Δ	
$3d^1 [^2T_2]$ and $3d^6 [^5T_2]$	$-5B$	$2/5 \cdot \mathcal{D}$	$-5B$	$-2/5 \cdot \mathcal{D}$
$3d^2 [^3T_1]$ and $3d^7 [^4T_1]$	$-5B$	0	$-10B$	$-2/5 \cdot \mathcal{D}$
$3d^3 [^4A_2]$ and $3d^8 [^3A_2]$	$+4B$	$5/5 \cdot \mathcal{D}$	$-6B$	$+3/5 \cdot \mathcal{D}$
$3d^4 [^5E]$ and $3d^9 [^2E]$	$-8B$	0	$-14B$	$+3/5 \cdot \mathcal{D}$
$3d^5 [^6A_1]$	$+14B + 7C$	$-5/5 \cdot \mathcal{D}$	$+7C$	$-2/5 \cdot \mathcal{D}$

Table 4.2: Corrections on U and Δ found from the multiplet and crystal field effects as given in table 4.1. For the configurations $3d^6$ to $3d^9$ an extra correction of $+7C$ should be included for Δ . (The corrections for $3d^2$ and $3d^7$ states due to configuration interaction have been neglected).

configuration averaged A -term, the values as given in table 4.2 should be subtracted. The crystal field values (for high spin compounds) are found with the inclusion of the additional energy effects of table 4.2.

Similarly Δ is estimated from the atomic ionization energy plus the variation in the Madelung term. The values found are again renormalized to the NiO value of 6eV. Figure 4.4 gives the two sets of predictions for Δ , which again are similar with the exception of MnO. Also for Δ the multipole effects are included. As the Madelung potential is dependent on the lattice parameter, it is not clear in how far crystal field effects are excluded. Neglecting this effect, the values can be corrected again for crystal field effects with table 4.2. Figures 4.4 and 4.5 give the trend in the values for U and Δ for divalent oxides, with an approximated crystal field splitting of 1.0 eV.

Estimates for higher valencies

Torrance et al. [11] extended the atomic estimations for trivalent and tetravalent transition metal ions in LaTMO_3 and SrTMO_3 perovskites. Figures 4.6 and 4.7 are generated from their results. It is seen that with increasing valency the values for U increase. The calculated values are not considered to be absolute, though the trends are believed to be correct [8]. By contrast the values for Δ decrease with increasing valency. Superimposed on these shifts are the effects of the multiplets and crystal fields, which as discussed determine the strong trends with respect to the number of $3d$ -electrons. Also the crystal field strengths will change as a function of the valency and for trivalent and tetravalent compounds it will be increased to a value of maximally about 2.5 eV for the early, that is $3d^0$ to $3d^3$, tetravalent metal oxides. Thus higher valent oxides will increasingly behave charge transfer like, but especially the tetravalent oxides will tend to be metallic as the values for Δ almost vanish (except for Ti^{4+} -oxides which in general are insulators as the $3d$ -band is empty). Furthermore because the crystal field strengths increase, there is an increasing possibility for low-spin configurations. In the discussions of the x-ray absorption spectra we will come back to these trends.

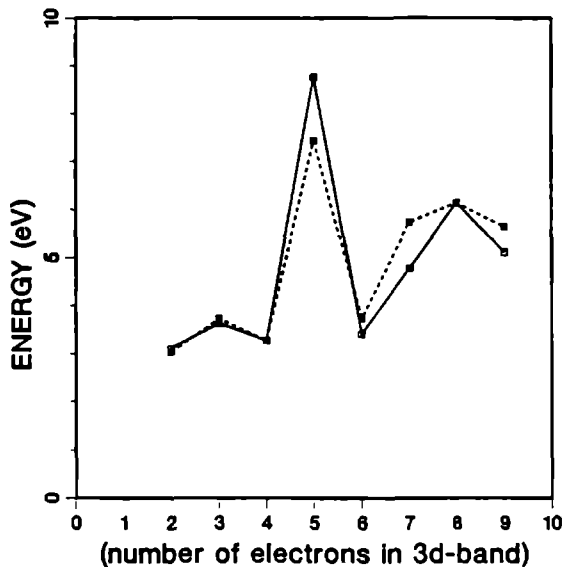


Figure 4.4: Estimates for U based on renormalized atomic values. Solid line gives the values as given in Ref. 5; dashed line Ref. 11.

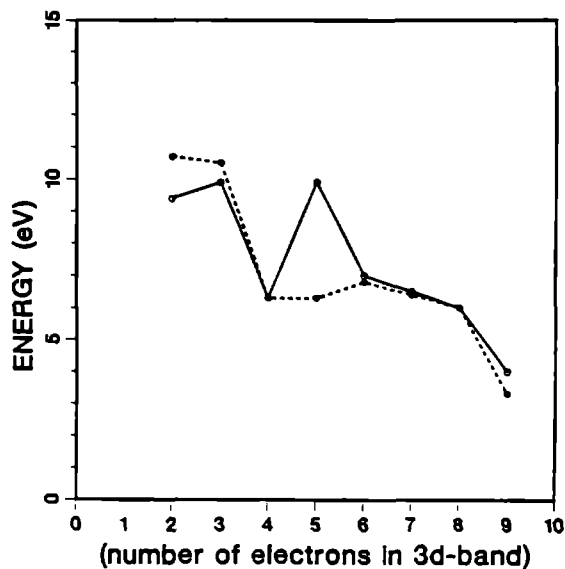


Figure 4.5: Estimates for Δ based on renormalized atomic values. Solid line gives the values as given in Ref. 5; dashed line Ref. 11.

Metals versus insulators

From the trends in U and Δ compared with the bandwidths it has been found that all divalent monoxides, except TiO and VO , are insulators, in agreement with experiment [5]. Also the estimate that trivalent lanthanum-perovskites are insulating while most tetravalent strontium-perovskites are metallic, is in accord with experiment. From the trends in U and

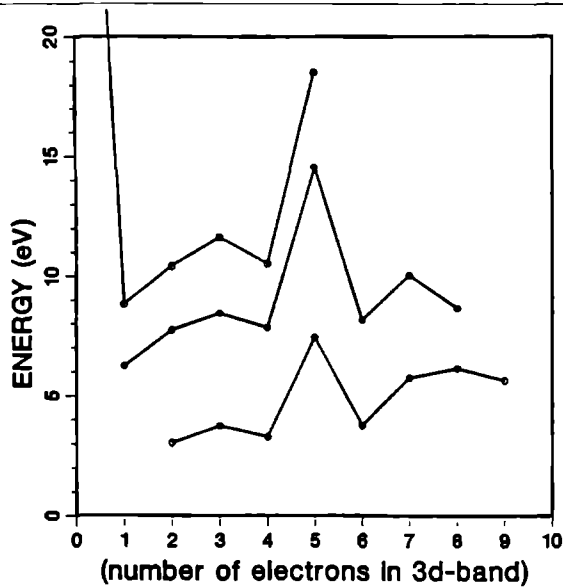


Figure 4.6: Trend of the renormalized values of U for respectively divalent (bottom line), trivalent (middle line) and tetravalent (top) $3d$ -metal ions in oxides.

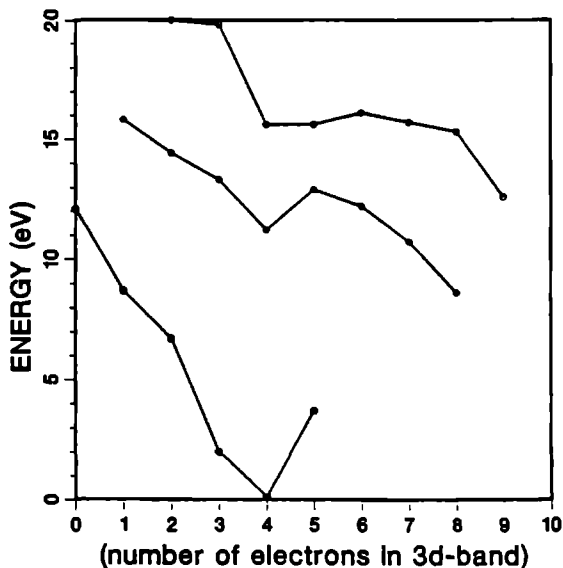


Figure 4.7: Trend of the values of Δ (not renormalized!) for respectively (top line) divalent, (middle) trivalent and (bottom) tetravalent $3d$ -metal ions in oxides.

Δ it was found that especially $3d^5$ is stabilized by exchange, and furthermore $3d^3$ and $3d^8$ configurations are extra stabilized by crystal field effects. Thus these $3d$ -counts, together with $3d^0$ and $3d^{10}$ are expected to have a tendency to be insulating. A closely related additional factor is that these configurations have a closed sub-shell which means that neglecting correlations, as in spin-polarized local density calculations, one can predict these

compounds to be insulating [13], and in these cases the additional correlation effects only increase the magnitude of energy-gap. In those cases with a partly filled sub-band, one-electron models will necessarily predict these compounds to be metallic [13], and only the explicit inclusion of correlation effects will create a band-gap. Recent extensions of local density calculations, including orbital polarization [14, 15] and self-interaction-corrections [16] create band-gaps for FeO. These methods are as yet not fully confirmed. Also it is questionable if the self-interaction-correction results remain within density functional theory as such [17]).

From these considerations concerning the existence of a filled sub-band and additionally the magnitudes of U and Δ , a general trend in the metallic versus insulating behaviour can be given as a function of the $3d$ -band occupancy. Figure 4.8 is reproduced from Wilson [8]; it illustrates the stabilization of the insulating state for compounds with a $3d^0$, $3d^3$, $3d^5$ and $3d^8$ -configuration.

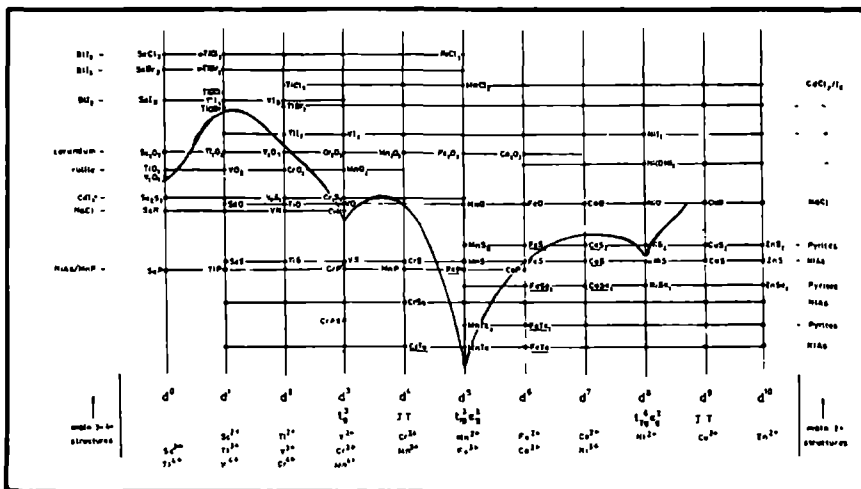


Figure 4.8: The localization/delocalization boundary for $3d$ -compounds as a function of the 'nominal non-bonding d-electron configuration', that is the number of electrons available for the $3d$ -band. The localized, ionic compounds (halides) are placed at the top and the delocalized, covalent compounds (arsenides, tellurides) at the bottom.

High-spin versus low-spin

Related to the division between metals and insulators is the division between high-spin and low-spin compounds. For divalent $3d$ -metal oxides the high-spin state is the rule, but for trivalent and especially tetravalent $3d$ -metal ions the low-spin configuration is more likely

because of an increased covalency and therewith an increased crystal field strength (plus an effective screening of the Slater integrals).

In case of a 3d-metal ion with an octahedral site symmetry, a high-spin versus low-spin state occurs for $3d^4$, $3d^5$, $3d^6$ and $3d^7$ configurations, due to the interplay of the Slater integrals and the cubic crystal field. (For $3d^1$, $3d^2$ and $3d^3$ the ground state contains only electrons in the t_{2g}^+ -state and for $3d^8$ and $3d^9$ the ground state contains only holes in the e_g^- -state). The ground state symmetries for the high-spin and low-spin states were given in table 3.4. For 3d-metal oxides the transition from a high-spin state to a low-spin state is in general accompanied by the transition from an insulator to a metal. This can be understood because for $3d^4$, $3d^5$ and $3d^6$ the low-spin state does not contain any e_g electrons, which results in a contraction of the lattice, increasing the chances for metallic behaviour. For the $3d^7$ -configuration the low-spin state still has an e_g electron and it can be expected that this configuration is unstable. It turns out that in cases where a $3d^7_{LS}$ -configuration is expected like for Ni^{III} , another ground state (best described as $3d^8\bar{L}$) is formed [19].

If a high-spin low-spin transition is induced by temperature, it can give rise to drastic changes to the electronic, magnetic as well as crystallographic structure, such as a transition from 5T_2 -symmetry to 1A_1 -symmetry for a $3d^6$ -configuration. For a $3d^4$ -configuration the high-spin (5E) and low-spin (3T_1) states differ by only one spin-up versus spin-down electron. 3d spin-orbit coupling is able to couple the 5E and 3T_1 states and to generate an intermediate spin configuration. Such an intermediate spin state has been suggested for $SrFeO_3$ [52] and $LiMn_2O_4$ [36]. This suggestion will be supported by the x-ray absorption spectrum of $LiMnO_2$, for which best correspondence is found if the low-spin and high-spin states are close to degenerate, giving rise to an intermediate spin state.

What does $3d^N$ mean ?

In the ZSA-model the ground state is written as $3d^N + 3d^{N+1}\bar{L}$, etc. The usual interpretation of $3d^N$ is a complete ionic picture, in which $3d^N$ stands for N electrons of 3d-character. The mixing of $3d^{N-1}\bar{L}$ -character describes the amount of holes of oxygen 2p-character and thus the amount of covalency.

In case of $SrTiO_3$ it is found from a band structure calculation that the bandgap is placed in between the filled oxygen 2p-band and the empty titanium 3d-band and projected to atomic orbitals the amount of titanium 3d-character in the filled 2p-band is about 1.5 electrons per unit cell. As the 3d-band is empty the ZSA-model starts with a $3d^0$ ground state, and to account for the electrons of oxygen 2p-character in the 3d-band there has to be a large mixing of \bar{L} -character in the ground state. As for a $3d^0$ -compound U is extremely large (as it is impossible to extract a 3d-electron from an empty band), the $3d^2\bar{L}\bar{L}'$ can be excluded. Thus the mixing of \bar{L} -character must be described with $3d^1\bar{L}$ character. However this configuration can never account for the approximately 1.5 electrons of ligand hole character and to solve this discrepancy two approaches can be followed.

1. One can discard the complete ionic identification of $3d^N$ with N electrons of atomic titanium 3d-character and instead interpret $3d^N$ as N 3d-electrons with partial atomic oxygen 2p-character.

2. One can add more configurations to the model. Potentially important configurations are $3d^N \underline{L}4s$ and $3d^{N+1} \underline{L}\underline{L}'4s$.

ad. 1.: In principle one is free to choose any basisset. However with choice of an alternative basisset the values for U and Δ will have to be 'renormalized'. In the ZSA-model U and Δ are determined from XPS and BIS, and it is not a-priori evident that the values found are consistent with the projected atomic orbitals of metal $3d$ and oxygen $2p$ character as determined from local density calculations. Partially this is related to the fact that in local density methods the local l -projected density of states is not uniquely defined; it is dependent on the size of the sphere around the atom and more general on the specific method of calculating the density of states. However it is a definite possibility that the experimentally determined values of U and Δ do not correspond to the ionic limit 'as such' (within the $3d^N + 3d^{N+1} \underline{L}$ basis), because the experimental values include solid state effects and can be considered as effective values only.

Given these considerations one can conclude that $3d^N$ identifies N ' $3d$ -electrons', but not necessarily pure atomic metal $3d$ -orbitals. For metal $2p$ x-ray absorption the most important factor is the symmetry of the ground state, which is determined by $3d^N$ irrespective of its exact interpretation. For example in case of SrTiO_3 the ground state is dominated by $3d^0$ -character, which determines that the ground state has 1S -symmetry, and coupling of $3d^1 \underline{L}$ does not modify the overall symmetry. For oxygen $1s$ x-ray absorption the precise interpretation of $3d^N$ is more crucial. If $3d^N$ is not interpreted in the complete ionic limit, there will be atomic projected oxygen $2p$ -character hybridized in $3d^N$. Consequently it will be possible to make a direct transition from the oxygen $1s$ core state to a 'metal $3d$ '-state. Thus the transition matrix elements $\langle 1s | \hat{e}r | 3d \rangle$ are not zero and have to be added to the $\langle 1s | \hat{e}r | \underline{L} \rangle$ matrix elements. The consequence is that the intensity of the oxygen $1s$ edge does not measure the amount of $3d^{N+1} \underline{L}$ -character directly. This is important for the analysis of the oxygen $1s$ x-ray absorption spectra of the $\text{La}_{1-x}\text{Sr}_x\text{MnO}_3$ -system. The charge transfer will be smaller for the $3d^4$ -configuration of LaMnO_3 . As substitution of strontium for lanthanum decreases the lattice parameter only slightly, the hopping will be of similar magnitude. From these considerations the amount of mixing of $3d^{N+1} \underline{L}$ -character will be larger for LaMnO_3 than for SrMnO_3 . However the spectral weight of oxygen $2p$ -character in the $3d$ -band is much larger for SrMnO_3 , and (within the present set of configurations) the only feasible explanation is to assume a considerable contribution from direct oxygen $1s$ to metal $3d$ transitions.

Mixed valence

Until now the discussion assumed the existence of an integer filling of the $3d$ -band. Notice that as in $3d$ -metal oxides in general the $3d$ -band is separated from both the oxygen $2p$ -band and the metal $4sp$ -band, the total filling of the $3d$ -band is a well defined object, in contrast to case of the pure $3d$ -metals. If two compounds with an equal metal ion but a different $3d$ -count are mixed, a new compound is formed with a total non-integer $3d$ -count. A system which will be studied in detail in the next sections are the mixing of LaTMO_3 with SrTMO_3 , (with $\text{TM} = \text{Ti, Mn, Fe, Co}$) In these compounds, which all have a perovskite

crystal structure, the valency of the metal-ion is defined by the stoichiometry and because by definition the valencies of oxygen, lanthanum and strontium are taken as 2, 2 and 3, the $3d$ -metal ion valence varies between 3 and 4. An important problem is to investigate how these systems cope with mixed valency, that is how the electrons respectively holes will be accommodated and what kind of resulting electronic (and magnetic) behaviour is generated.

Another set of compounds which will be studied are the late monoxides (manganese, cobalt and nickel) doped with lithium. The increase of the divalent state to the trivalent state has surprising effects on the description of the ground state [19, 20]: It is found that the ground state of trivalent nickel is not dominated by $3d^7$ but instead by $3d^8\bar{L}$ character, and in order to account for this $3d^8\bar{L}$ ground state a negative charge transfer energy must be assumed. Before hybridization the lowest state is the $3d^8\bar{L}$ -state (set to zero), the $3d^7$ -state is placed at an energy of $-\Delta$ (~ 4 eV) and the $3d^8\bar{L}L'$ -state is positioned at $\Delta + U$ (~ 6 eV). Consequently the nickel $2p$ edge will be dominated by the transition $3d^8\bar{L} \rightarrow 2p^53d^8\bar{L}$. This spectrum will have a similar shape as the $3d^8 \rightarrow 2p^53d^9$ spectrum, but there is an important difference as for a $3d^8$ ground state the symmetry is confined to the specific symmetry of the (Hund's rule) ground state. In contrast a $3d^8\bar{L}$ -state has a specific overall symmetry, but the contribution to it of the $3d^8$ -part is not apriori determined. Therefore van Elp et al. [10] used a mixture of triplet and singlet $3d^8$ -states to build the $3d^8\bar{L}$ -state of overall 2E -symmetry. This line of reasoning will be used in the discussion of mixed valent oxides in sections 4.3 and 4.4. First the electronic structure of the binary $3d$ -metal oxides is discussed in section 4.2.

4.2. Oxygen 1s x-ray absorption edges of transition metal oxides

Reproduced from *Physical Review B*, volume **40**, page 5715-5723 (1989).

This paper contains an analysis of the oxygen 1s x-ray absorption spectra of a series of binary 3d-metal oxides. The 3d-part of the spectra is analysed qualitatively on the basis of one-electron addition to the ground state symmetry. Use is made of the so-called \mathcal{DK} -model which was discussed in detail in section 3.2. In this model only two interactions are taken into account: the cubic crystal field (\mathcal{D}) and an effective exchange interaction (\mathcal{K}). Apart from the possible reasons for discrepancies between the \mathcal{DK} -model and experimental spectra as discussed in the paper, also 3d correlation effects in the final state are a definite possibility for the discrepancies. These 3d correlation effects were not recognized as important in the paper; they have been discussed theoretically in section 3.2 and also they will be discussed in sections 4.3 and 4.4.

Oxygen 1s x-ray-absorption edges of transition-metal oxides

F M F de Groot, M Groni, and J C Fuggle

Research Institute for Materials, University of Nijmegen, Toernooiveld, NL-6525 ED Nijmegen, The Netherlands

J Ghijsen and G A Sawatzky

Materials Science Centre, University of Groningen, Paddepoel, Nijenborgh 18, NL-9747 AG Groningen, The Netherlands

H Petersen

Berliner Elektronenspeicherung Gesellschaft für Synchrotronstrahlung m b H (BESSY), Lentzeallee 100, D-1000 Berlin 33, Federal Republic of Germany

(Received 17 February 1989, revised manuscript received 8 May 1989)

The oxygen 1s x-ray absorption edges of a series of 3d-transition metal oxides have been measured. The structures at the edge arise from covalent mixing of the metal and oxygen states, which introduces oxygen *p* character in unoccupied states of mainly metal character. The spectra can be divided into two regions. The first is a double-peaked sharp structure near threshold, which can be related to the metal 3d states, the second is a broader structure 5–10 eV above the edge and is related to the metal 4s and 4p bands. We attribute the oxygen *p* character up to 15 eV above threshold to mainly oxygen 2p character. The data are analyzed in terms of ligand-field and exchange splittings. It is shown that the splitting between the two sharp peaks near threshold is related closely to the ligand field splitting, but the relative intensities of the peaks are not fully explained at the present time.

I. INTRODUCTION

In this study we try to learn something about the electronic structure of binary 3d-transition-metal oxides, which still is not well understood despite many past studies^{1–9}. By studying the oxygen 1s (or *K*) absorption edge of binary oxides, we hope to set up a reference for the interpretation of x-ray-absorption edges and the electronic structure of more complex compounds, such as the high- T_c superconducting oxides. The oxygen 1s edge, with an absorption energy of about 530 eV, is situated in the energy range between 300 and 1000 eV, which until recently was technically difficult to reach. The relatively underdeveloped role of this energy region, containing besides the oxygen 1s edge also the 3d-transition-metal 2p (or $L_{2,3}$) edges, compared to, e.g., the transition-metal 1s (or *K*) edges is predominantly caused by poor monochromator resolution. Studies such as ours, with an instrumental resolution of ~500 meV, are now feasible as a result of the development of new and better monochromators for synchrotron radiation in this energy range¹⁰.

X-ray absorption (XAS) is a local process in which an electron is promoted to an excited electronic state, which can be coupled to the original core level with the dipole selection rule stating that the change in the angular momentum quantum number (ΔL) is ± 1 , while the spin is not changed¹¹. For the oxygen 1s edge ($L=0$) this means that only oxygen *p* character ($L=1$) can be reached. The resulting spectrum can be envisaged in a first-order approximation as an image of the oxygen *p* projected unoccupied density of states. For more detailed studies, we note below three problems in relating a calculated DOS to an XAS spectrum.

First, the usual way to calculate the density of states is via the Hohenberg-Kohn density-functional theory within the Kohn-Sham local-density approach¹² (LDA). Using the LDA, the occupied part of the DOS calculation is a routine task for the 3d-transition-metal oxides. For the unoccupied states there are, however, purely technical problems of the requirements for more extended basis sets and avoidance of inappropriate linearization schemes¹³. For instance, the O 3p levels, which begin 10–15 eV above E_F , are not included in density-of-states (DOS) calculations with a basis set limited to one wave function per *L* value. Thus, most published calculations^{6–8} are limited to the first few eV of the unoccupied states. Unfortunately, we know of only one oxide band-structure calculation (for CuO) (Ref. 13) whose basis set is sufficient for a sensible comparison with XAS far above threshold. Calculations also exist within the multiple-scattering formalism which treat the unoccupied density of states (UDOS) up to some 50 eV above threshold¹⁴. However, these calculations, which are used in the description of the transition-metal 1s x-ray-absorption near-edge spectroscopy (XANES) spectra, have not been published for the oxygen 1s edges of many of the oxides we consider here. A second technical problem concerns the single-particle matrix elements for XAS¹⁵. Here we will assume that the oxygen 1s $\rightarrow np$ matrix elements are constant for any given *n* unless otherwise stated.

Finally, there is an important problem of principle. Even if the UDOS was calculated correctly within LDA and corrected for single-particle matrix elements,¹⁵ a comparison to the x-ray-absorption edges is not strictly valid. The excited electron in the final state interacts with its surroundings, modifying the density of states due

to correlation. Moreover, the created core hole affects the final-state DOS, as has, for instance, been shown for the early-transition-metal $2p$ ($L_{2,3}$) (Ref 16) and Al and Si $1s$ (Ref 17) x-ray-absorption spectra. Both effects come under the heading of self energy. For the oxygen $1s$ edges these effects probably are less severe, compared to the transition-metal $2p$ edges, because the core hole now is situated on oxygen while the states in the unoccupied bands just above the Fermi level have most weight on the metal sites. Oxygen $2p$ character hybridizes with these unoccupied metal bands, but the $1s$ hole on oxygen only indirectly influences them.

Because not much high resolution data are available, and even more because of the lack of suitable calculations of the UDOS, we confine ourselves here to a more empirical approach as a starting point. In this paper we study a series of $3d$ -transition-metal oxides, of which all but one (CuO) contain a transition metal which is octahedrally surrounded by oxygen. The major variation is the number of $3d$ electrons, ranging from zero to nine. Also the formal valency varies between 2 and 4, resulting in different crystal structures for each valency: Sc_2O_3 , Ti_2O_3 , V_2O_3 , Cr_2O_3 , and Fe_2O_3 , each with the corundum structure, TiO_2 , VO_2 , and MnO_2 , each with the rutile structure and the complex inverse spinel-structures Fe_3O_4 . We also consider the spectra of the monoxides TiO , MnO , FeO , NiO , and CuO of Nakai *et al*.¹⁸ The first four materials have the rocksalt structure and CuO has its typical structure in which Cu is surrounded by four oxygen atoms. The measurements on NiO and CuO were repeated by us to check the reproducibility of the results under different experimental conditions. We note that especially the monoxides discussed are defect structures,¹⁹ defects can have a considerable influence on XAS spectra as they distort the local symmetry.²⁰ Besides the known defect structures of the monoxides, the samples measured as commercial powders (see Sec II) can be expected to contain a fair amount of defects. As a start we will consider all compounds as stoichiometric, the possible effects of nonstoichiometry are discussed in Sec IV F.

After a short description of the experimental conditions (Sec II), we will present the oxygen $1s$ edges. In their interpretation we will focus on the transition-metal $3d$ -band region (Sec III). In the discussion (Sec IV) a comparison is made with the ligand-field splitting data from the literature and simple models to explain the specific shapes of the $3d$ -band region are discussed.

II. EXPERIMENTAL

The x-ray-absorption measurements were carried out at the Berlin synchrotron-radiation source BESSY, using the SX700 plane grating monochromator.¹⁰ The contribution to the resolution could be reasonably simulated by a Lorentzian of about 0.5 eV full width at half maximum²¹ (FWHM). However, it should be noted that our spectra show as much detail as those of Nakai *et al*,¹⁸ who claims 0.1 eV monochromator resolution. The spectra were recorded in the total electron-yield mode. They were normalized to the beam current, to correct for synchrotron-intensity loss during a measurement. The

samples used were commercial powders (Sc_2O_3 , Ti_2O_3 , VO_2 , V_2O_3 , and Cr_2O_3) and natural minerals (TiO_2 , MnO_2 , MnO , Fe_2O_3 , Fe_3O_4 , and NiO). CuO was obtained as a single crystal from Oxford Laboratories. Solid samples were scraped under vacuum to ensure clean surfaces and were thus preferred to powders. The pressure during measurements was in the 10^{-9} torr range.

The throughput of Cu was measured at the oxygen $1s$ edge to check for oxygen contamination in the monochromator. No contamination was found. The energy calibration of the monochromator was performed by taking pure transition metals (V, Cr, Mn, Fe, and Ni) $2p$ edges and using the energy loss data of Fink *et al*.¹⁶ as a reference. The calibration curve was linear in the energy range probed (400–800 eV). Comparing our numerical results for NiO and CuO with those of Nakai *et al*.¹⁸ showed in both cases that our threshold was shifted 0.3 eV to higher energy, which at this time is an acceptable disagreement for these XAS edges.

III. RESULTS AND INTERPRETATION

Figures 1(a) and 1(b) show the oxygen $1s$ edge x-ray-absorption spectra of a series of $3d$ -transition-metal oxides. The spectra have been approximately normalized to the peak heights, absolute normalization of the intensity scale is not feasible. The spectra have strong structure up to at least 15 eV above threshold and it is this structure we wish to interpret. First, we note that the data presented here are in good agreement with the high-resolution data that exist for TiO_2 (Ref 22) and for NiO and CuO.¹⁸ There is also no disagreement with the available lower-resolution spectra.^{23–25} Besides the oxygen $1s$ edge data there are results on the metal edges of $3d$ transition-metal oxides.^{26,27} These are significant for a complete picture of the electronic structure. However, in this paper we do not include the discussion of the metal edges and consider only the oxygen $1s$ edge.

We divide the spectra into two regions. The first, shaded in the figures, is attributed to oxygen $2p$ weight in states of predominantly transition-metal $3d$ character: the transition-metal $3d$ band. This assignment conforms with that of Fisher²³ and other studies,^{22,28,29} based on a molecular-orbital treatment. Further discussion of this region is given in Sec IV.

The second region, typically 5–10 eV above threshold, is attributed to oxygen p character hybridized with metal $4s$ and $4p$ states.³⁰ Detailed calculations on CuO with an extended basis set (with the inclusion of both oxygen $2p$ and $3p$ character) show this to have principally oxygen $2p$ (not $3p$) character, with the $2p$ count reaching ~6 at about 15 eV above E_F .¹³ We proceed under the assumption that the peaks up to about 15 eV in the other transition-metal oxides are also due to oxygen $2p$ character in the unoccupied states. This high-energy range of spread for oxygen $2p$ character is an indication of strong covalency in these materials and is not in disagreement with traditional chemical ideas.³¹ From Fig 1 and Table I a common structure of the $4sp$ band, consisting of a main peak (E_{p2}) and a low-energy shoulder (E_{p1}) at approximately 3.2 eV ($=\Delta p$), appears throughout the series.

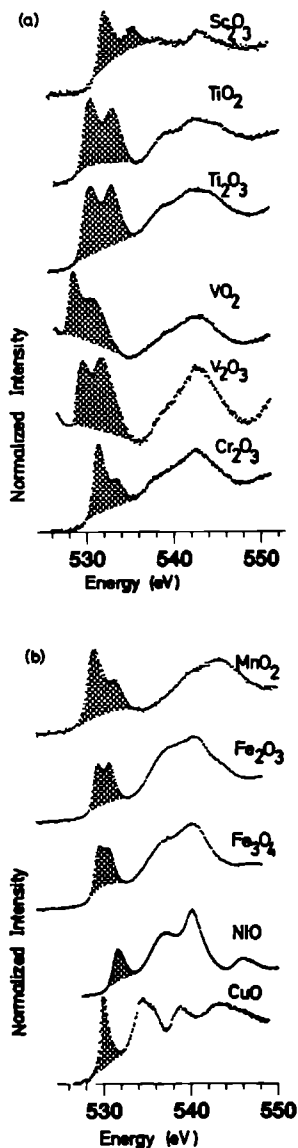


FIG 1 (a) and (b) Oxygen 1s x ray absorption spectra the shaded area is assigned to oxygen p character in the transition-metal 3d band The broader structure above is assigned to oxygen p character in the metal 4s and 4p bands The vanadium edges are distorted by the tail of the vanadium L_2 edge

This structure can be related to the O_H symmetry set up by the nearest (oxygen) neighbors, which octahedrally surround the 3d-transition-metal atoms It shows no strong dependence on the specific crystal structure This structure is absent in the nonoctahedral CuO

A salient point is the decrease in intensity of the 3d band, relative to the 4sp band across the transition-metal series (see Fig 2) As noted above, the dominant reason for this is the decrease in the number of unoccupied 3d states available for mixing with O 2p states, this means that the intensity of the XAS spectra should be linear with the number of holes as is indicated by the line in Fig 2 However, there is a substantial lower intensity of the 3d-band region, especially for the d^5 and d^6 oxides This additional loss of intensity can be explained by the diminished hybridization of the metal 3d orbitals with the oxygen 2p orbitals due to shrinking of the metal 3d orbitals in the late-transition-metal oxides Note that we have plotted the relative intensity of the 3d region with respect to the 4sp region The intensity of this latter region also will be influenced by hybridization We can say something more about the changes in hybridization in the 3d and 4s bands with the use of the hybridization strengths (Δ values) from Andersen *et al*¹² For all transition metals they give tables of the Δ values of each individual l band ($l=0,1,2,3$) This Δ value, a potential parameter in the linear muffin-tin orbital (LMTO) calculation, is proportional to the amplitude of the corresponding radial wave function at the average Wigner-Seitz radius of the lattice The hybridization is equal to $\Delta^{1/2}$, which gives a direct relation between Δ and the intensity of the 3d and 4s bands The values for the pure metals give a clear and—except for titanium—monotone trend to smaller 3d versus 4s hybridization with a higher atomic number Using these (metal) values for the oxides, we have to multiply the number of holes (the straight line in Fig 2) by Δ_{3d}/Δ_{4s} and renormalize the plot We find that the experimental points are scattered around the resulting curve This indicates strongly that the additional

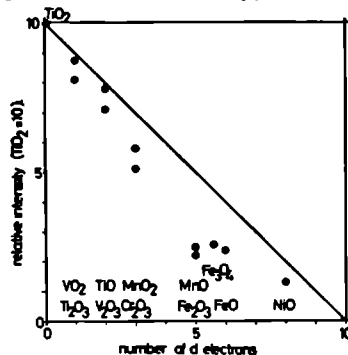


FIG 2 The intensity of the 3d-band region with respect to the 4sp region is plotted against the number of 3d electrons in the ground state The intensity of TiO₂ is set to 10 The line gives the expected intensity ratio, assuming this is proportional to the number of holes

loss of intensity can be explained by taking into account hybridization of both the $3d$ and $4s$ bands. (The curve itself is not included in order not to mislead the reader; a complete treatment would involve calculation of the Δ 's for the oxides.)

IV. DISCUSSION

A. Implication of the O 1s XAS for ideas on covalency

In a purely ionic model, oxygen would have the configuration $O 1s^2 2s^2 2p^6$ and the $1s \rightarrow 2p$ channel would be closed in XAS. Covalency reduces the number of filled states with O $2p$ character, so that the strength of

the O 1s signal at threshold is related to the degree of covalency.³³ It is well known that the transition-metal oxides are not ionic, but have a considerable covalent contribution. There is much evidence for this from pure computations as well as from comparison of computed and experimental magnetic or ligand-field effects.^{5,34,35} It is of particular interest that the ligand-field splittings calculated for early-transition-metal oxides in an ionic model (the crystal field) are about a factor of 3 smaller than those found by optical measurements, but come out correctly when covalency is taken into account.³⁴ The discrepancies are smaller in the late-transition-metal oxides, which is extra evidence that the (oxygen $2p$ -metal $3d$) hybridization is smaller in the late-transition-metal

TABLE I. (a) The crystal structures, formal valencies, and number of d electrons are given. From the spectra in Fig. 1 and from Ref. 19 the first (E_{d1}) and second (E_{d2}) peak positions of the $3d$ band (shaded area) and the first (E_{p1}) and second (E_{p2}) peak positions of the $4sp$ band are measured. (b) The peak splittings and widths of the oxygen 1s XAS spectra. The separation of E_{d1} and E_{d2} is identified with the ligand-field splitting (Δd). The characteristic 3.2-eV distance between E_{p1} and E_{p2} in the sp band is given as Δp . The left-side HWHM(l) of the first peak (Γ_d), the FWHM of the total $3d$ band (Γ_D), and the FWHM of the $4sp$ band (Γ_p) are given. The O 1s edges in VO_x are distorted by the tailing effect of the vanadium L edges. We estimate the uncertainty in Γ_D as ± 0.3 eV. All energies are in eV.

(a)							
Compound	Crystal structure	Valency	d count	E_{d1}	E_{d2}	E_{p1}	E_{p2}
Sc ₂ O ₃	corundum	3+	0	532.4	535.7		543.1
TiO ₂	rutile	4+	0	530.7	533.3	539.4	542.7
Ti ₂ O ₃	corundum	3+	1	530.8	533.2	539.0	542.2
TiO*	rocksalt	2+	2	530.2	533.0	539.5	542.5
VO ₂	rutile	4+	1	528.8	531.0	540.4	543.1
V ₂ O ₃	corundum	3+	2	529.8	531.9	539.2	542.8
Cr ₂ O ₃	corundum	3+	3	531.4	533.7	538.4	542.7
MnO ₂	rutile	4+	3	528.9	531.4	540.5	543.4
MnO*	rocksalt	2+	5	529.6	530.9	538.4	542.5
Fe ₂ O ₃	corundum	3+	5	529.4	530.7	537.4	540.6
Fe ₃ O ₄	inverse spinel	2+ and 3+	5 and 6	528.9	530.5	537.1	540.2
FeO*	rocksalt	2+	6	529.8	531.0	536.3	540.2
NiO	rocksalt	2+	8		531.7	537.0	540.2
NiO*	rocksalt	2+	8		531.4	536.7	540.0
CuO	CuO	2+	9		530.1	534.6	535.9
CuO*	CuO	2+	9		529.8	534.3	535.6

(b)					
Compound	Γ_d HWHM(l)	Γ_D FWHM	Γ_p FWHM	Δd	Δp
Sc ₂ O ₃	0.8	6.0		3.3	
TiO ₂	1.0	4.8	9.5	2.6	3.3
Ti ₂ O ₃	1.2	5.3	9.1	2.4	3.2
TiO*	0.6	5.3	9.1	2.8	3.0
VO ₂	0.9	4.9	7.6	2.2	2.7
V ₂ O ₃	1.0	4.9	6.5	2.2	3.6
Cr ₂ O ₃	0.9	3.6	7.3	2.3	4.3
MnO ₂	0.9	4.2	8.5	2.5	2.9
MnO*	0.6	3.7	7.8	1.3	4.1
Fe ₂ O ₃	0.7	3.3	8.4	1.3	3.2
Fe ₃ O ₄	0.8	3.0	7.1	0.9	3.1
FeO*		3.8	6.8	1.2	3.3
NiO	0.7	2.3	6.7		3.2
NiO*	0.6	2.0	5.6		3.3
CuO	0.6	1.4	3.2		1.3
CuO*	0.45	1.1	3.3		1.3

*Data taken from Reference 19.

oxides, as we already suggested in the discussion of the intensities of the 3d band throughout the series

Because of the technical problems in computing the unoccupied DOS over some energy range, it is not always realized that there is considerable weight of O 2p character in states 10–15 eV above E_F . The evidence from the LASW calculation of CuO is that most O p character up to 15 eV above E_F is in fact O 2p.¹³ The O 1s XAS spectra of the transition-metal oxides show similar broad peaks, which we have attributed to O 2p character in bands with predominantly transition-metal 4sp character. We note that the integrated intensity of the broad 4sp band is comparable to that of the 3d band. In the very reasonable first approximation of constant O 1s → 2p matrix elements, the XAS intensity is proportional to the weight of O 2p character in a band. Thus, in chemical language, the observed intensity ratios in the two spectral regions is evidence that, besides the metal 3d states, also the metal 4sp states are important for the covalency of transition-metal oxides.

B. Ligand-field splittings

We now examine more closely the first structure, the 3d band, which is shaded in Fig 1. This structure consists of two (often similar) peaks. In a first approximation these two peaks can be identified as the t_{2g} - and e_g -symmetry bands separated by a ligand-field splitting, we shall use the term "ligand-field splitting" to denote the "bare" (ionic) crystal-field splitting plus hybridization.¹⁶

To check the validity of the assignment of the two sharp peaks as being related to the t_{2g} and e_g symmetry, with the peak separation mirroring the ligand-field splitting, we first compare our splittings, Δd , with optical data of octahedrally hydrated transition-metal ions, which have been related to the ligand-field splitting.^{5,37} In this comparison some precautions must be taken. Obviously the materials compared are not identical, though in both cases the transition metal is octahedrally surrounded by oxygen ions. Bearing this in mind we compare the results for the ligand-field splitting which are tabulated in Table II. Considering the precision in the determination of our Δd value, good agreement is found for all five transition-metal oxides.

In contrast to the "general rule" that the ligand-field splitting of trivalent ions is around 2.5 eV and the divalent-ion ligand-field splitting is approximately half that value,⁵ we come to the generalization of the division of early- and late-transition-metal oxides, the early-transition-metal oxides with a splitting around 2.5 eV and the late-transition-metal oxides with a splitting around 1.2 eV, as can be checked in Table I. The dividing line between early- and late-transition-metal oxides is the presence of a filled e_g orbital in the ground state. Up to d^3 compounds only t_{2g} states are filled. From d^5 compounds the filled e_g states increase the lattice parameter with respect to the orbital radii, which decrease throughout the 3d-transition-metal series. The consequence for the 3d orbitals is a decrease of hybridization as we discussed in Sec III. The d^4 compounds fall in between the early- and late-transition-metal compounds.

TABLE II Comparison of the splitting between the t_{2g} and e_g peak in XAS (Δd), with optical data of the ligand-field splitting (LFS) in hydrated transition metal ions (Ref 6)

Compound	Δd	LFS
Ti ₂ O ₃	2.4	2.5
V ₂ O ₃	2.2	2.2
Cr ₂ O ₃	2.3	2.1
MnO	1.3	1.5
Fe ₂ O ₃	1.3	1.6

Despite the "disagreement" in the generalizations made, the good individual correspondences of Δd with the optical ligand-field-splitting data give us confidence that the splitting between the two peaks in the 3d band is the same as that attributed to the ligand-field splitting in optical spectra.

C. The intensities of the so-called t_{2g} and e_g peaks

XAS data on peak splittings are analogous to those given by optical-absorption spectroscopy, except that XAS can more easily be used for d^0 materials. However, oxygen 1s XAS spectra also contain information on the peak intensity ratios, which have no analogy in optical data, and in fact our analysis of these intensities will indicate a serious problem, and possibly the need to revise the assignment somewhat. We will develop the ideas of the peak intensities step by step.

The simplest and first effect to be taken into account is the electron counting. The t_{2g} orbitals (xy , xz , and yz) can take six electrons and the e_g orbitals ($x^2 - y^2$, z^2) can take four. Thus the ratio of empty orbitals $t_{2g} : e_g$ is 6:4 for d^0 compounds and decreases to zero in low-spin compounds as the electron count is increased to d^6 . This is shown by the dashed line in Fig 3. However, note that for high-spin materials the exchange splitting may lead to filling of the majority-spin e_g states before the minority-spin t_{2g} states. Thus for high-spin compounds the ratio of $t_{2g} : e_g$ holes rises from 3:4 at d^3 to 3:2 at d^5 , before dropping to 0:2 at d^8 , as is shown by the upper dashed line in Fig 3. The curves based on electron counting in Fig 3 may be compared with the experimental ratio of the first to second peaks. Although the separation of the two peak areas is only approximate, we immediately see some serious discrepancies. There is considerable scatter of the experimental points, which may be an indication of the accuracy of the separation, but for the d^3 materials Cr₂O₃ and MnO₂ the ratio of the low-energy to the high-energy peak is much too high to be explained by ideas based on electron counting.

D. Orbital hybridization

We note that even where the peak intensity ratio is in reasonable agreement with the electron-count curve, this creates a problem because of the role of orbital hybridization. In octahedral complexes the metal e_g orbitals are directed towards the oxygen atoms and have a stronger overlap with the oxygen 2p orbitals. In general it is assumed¹ (following calculations^{6,38,39}) that the hybridiza-

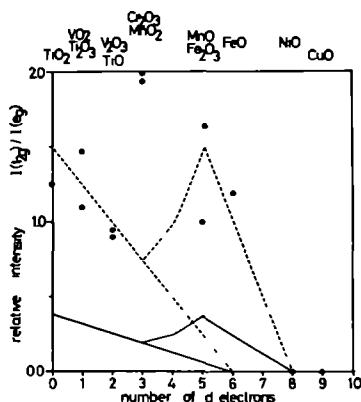


FIG 3 The relative intensity of the t_{2g} vs the e_g peak is given. The theoretical assumption that the t_{2g} hybridization is half that of e_g hybridization is given as the solid line, the dashed line gives just the electron counting (equal or no hybridization). For the late-transition metal oxides two lines are given: high-spin states are given with the upper lines, low-spin states with the lower lines. The points are the experimental values (Sc_2O_3 is omitted), which cannot be determined very precisely. For further details, see text.

tion of t_{2g} orbitals (forming π bonds) is about half that of e_g orbitals (forming σ bonds). The ground state of the early-3d-transition-metal compounds can be described by $|t_{2g}^N\rangle + (n_i)^{1/2}\alpha_i |t_{2g}^{N+1}L\rangle + (n_e)^{1/2}\alpha_e |t_{2g}^N e_g L\rangle$, with N ranging from 0 to 3. In the presence of the dominating octahedral surrounding the two distinct states, $|t_{2g}^{N+1}L\rangle$ and $|t_{2g}^N e_g L\rangle$ have to be considered. This implies that due to covalency the d^N state mixed with states in which an electron has jumped from the ligand (in this case a hole of oxygen 2p character is formed) to a transition-metal 3d orbital. This means that as the mixing coefficients α_i and α_e account for the amounts of hybridization with, respectively, t_{2g} and e_g character, $\alpha_i = \frac{1}{2}\alpha_e$.

In oxygen 1s absorption, an electron is excited from the oxygen 1s core state to states with some oxygen p character, i.e., $|t_{2g}^N e_g L\rangle$. Thus we can now relate the intensities to the covalency $n_i \alpha_i^2$ gives the amount of $|t_{2g}^{N+1}L\rangle$ character in the ground state and it is this character which is probed in the oxygen 1s absorption process. From this it is clear that the intensity ratio I_i/I_e should be equivalent to the amount of covalent mixing $n_i \alpha_i^2 / n_e \alpha_e^2 = n_i / 4n_e$. In Fig 3 we have compared this ratio (solid line) to the experimental values. It is directly evident that the theoretical lines strongly underestimate the experimental ratio, i.e., the relative t_{2g} intensity. At this moment we cannot explain the relative intensities generally observed, despite consideration of several subsidiary effects described below.

E. Exchange splitting

The whole concept of high-spin and low-spin configurations for 3d-transition-metal oxides implies that

we must consider exchange effects, which split the two groups of bands, t_{2g} and e_g , into four spin-up t_{2g} , spin-up e_g , spin-down t_{2g} , and spin-down e_g . Consider, for example, the d^3 compounds Cr_2O_3 and MnO_2 , which show a sharp peak near threshold followed by a weak shoulder at 2.4 eV. This result can only be explained if exchange is included. The exchange splitting is proportional to the number of unpaired spins, being three in d^3 compounds. For Cr^{3+} the tabulated exchange splitting per spin is about 0.9 eV⁴⁰. The total splitting becomes 2.7 eV, which is about the same value as the ligand-field splitting ($=2.3$ eV). Including this exchange splitting makes the approach to the spectrum quite different. Looking at the spectrum (see also Fig 4), the first peak can be assigned to a superposition of the spin-down t_{2g} state and the spin-up e_g state with a total number of five electrons. The second peak (shoulder) relates to the remaining two spin-down e_g electrons. This superposition is thus a consequence of the equivalent values of exchange and ligand-field splitting.

The result of including exchange effects here is that the electron-counting method increases the peak ratio to $5(3+2)/2$. If hybridization is included with a factor of 2, as in Sec IV D, this value is still only decreased to $(\frac{1}{2}+2)/2 = 1.7$. It is clear that a value of the t_{2g} e_g hybridization ratio could be chosen so as to fit the experimentally observed peak ratio. We conclude on the basis of this analysis for d^3 compounds that exchange effects should not be ignored. However, there are other compounds with other numbers of d electrons for which exchange splittings cannot explain the discrepancies in Fig 3. An example are the high-spin d^5 compounds MnO and Fe_2O_3 .

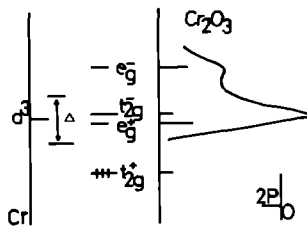


FIG 4 The line spectrum for $d^3 \text{Cr}_2\text{O}_3$ is given. First, a single energy level is given. This level is split by the crystal-field splitting ($\Delta = 2.3$ eV) into a t_{2g} (six electrons) and an e_g (four electrons) level. Then the exchange splitting of about 2.7 eV is considered. The result is that the e_g spin-up and t_{2g} spin-down levels almost coincide. The t_{2g} spin-up level is filled with three electrons, this leaves the other three levels empty, and thus they are candidates for absorption. The fourth series of lines gives the amount of oxygen 2p character which is hybridized with the metal 3d states (in fact, the square is given). The assumption that e_g hybridizes twice as much as t_{2g} (and consequently that the intensity is 4 times as much) is used. The heights of these lines should be reflected in the XAS spectra. In Fig 5 we will use the same way of presenting the energy levels.

for which the energy levels are illustrated in Fig 5 The exchange splitting is much larger than the crystal-field splitting, so that spin-up t_{2g} and e_g states are filled and the spin-down ones are empty As a consequence, the exchange splitting does not change the ratio of the two peaks and the intensity ratio $t_{2g} e_g$ should be $\frac{1}{2} 2=0.38$ when the different hybridization is taken into account This is far lower than the values measured (1.0 and 1.6)

F. Possible reasons for the discrepancies

In the solid, bond formation leads to broadening of the t_{2g} and e_g levels It is probable that the t_{2g} and e_g descriptions are only approximately applicable to the two peaks observed and to some extent t_{2g} and e_g character is spread throughout the whole region of the unoccupied $3d$ levels⁴¹ This will modify the spectra distributions directly In addition, it opens the possibility for the core-hole potential to shift weight towards the threshold We have argued earlier that the influence of the core hole on the oxygen 1s site is small because the unoccupied states have principally metal $3d$ character However, this does not mean it can be ignored completely in the context of intensity distributions within the rather narrow, empty $3d$ region There may be other reasons for the anomalous intensity ratios we find, but we feel that these two effects of band formation cannot be dismissed without further quantitative investigation

A further reason of discrepancies might be found in the nonstoichiometry of some samples, defects distort the local symmetry and lead to some variation in the interatomic distances This results in a variation in the amount of hybridization,⁴² which in principle can influence the t_{2g} versus e_g intensity distribution and also the ligand-field splitting We note that although computed charges of the vanadium 1s XAS spectra from $VO_0.8$ to $VO_{1.25}$ are quite large,²⁰ published vanadium 1s spectra show a smaller sensitivity, which, if reproduced at the oxygen 1s edges, would not be large enough to explain the discrepancies we observe Although we have not considered defects in detail here, we have measured NiO in

its black (defect-rich) and green form⁴³ Their oxygen 1s XAS spectra were identical, which suggests that defects are not too critical for the shape of the spectra A study of Li-doped NiO (or $Ni_{1-x}Li_xO$) which results in oxygen 2p holes,⁴⁴ revealed that besides the extra peak at the edge (2p hole states) the rest of the spectrum did not change much, except for an increasing width of the peaks This may not be true for highly defective oxides, like VO and TiO, and the question of the influence of defects deserves much more detailed study However, the results discussed in this paragraph suggest that defects cannot explain the discrepancies we discuss

V. CONCLUDING REMARKS

All oxygen 1s absorption edges of the transition-metal oxides can be divided into two regions In the first, near threshold, the oxygen 2p character is hybridized with the sharp structured transition-metal $3d$ band In the second region, O 2p character is hybridized with the weakly structured $4sp$ band The integrated intensity of the $4sp$ region is at least equal to the $3d$ -band region, which indicates that the metal $4sp$ states are important for the covalency of the transition-metal oxides The metal $4sp$ hybridization gives a more or less constant bonding effect above which the metal $3d$ hybridization accounts for the specific, material-dependent, effects

The $3d$ band consists of two peaks, which we believe are mainly related to, respectively, t_{2g} and e_g symmetry, despite the observation of anomalous intensity ratios For all oxides considered, the ligand-field-splitting parameter, from optical spectroscopy, is well reproduced by the separation of the first two sharp XAS peaks for Cr_2O_3 and MnO_2 , the description of the combined effect of ligand-field and exchange splitting leads to the conclusion that the first peak is an "accidental" superposition of t_{2g} spin-down and e_g spin-up states, while the second peak relates to the remaining e_g spin-down states

The intensities of t_{2g} and e_g do not conform with the rule that e_g hybridization is twice as big at t_{2g} hybridization¹⁶ Across the series the intensity of the t_{2g} peak is underestimated The reason is not clear to us, but we believe that band formation in the solid, with all its consequences, may explain at least some of the discrepancies

Our analysis showed that an important factor determining the shape and magnitude of the $3d$ region in the oxygen 1s XAS spectra of the $3d$ -transition-metal oxides is the presence of a filled e_g orbital in the ground state This criterion splits the $3d$ -transition-metal oxides into two main groups the early- (or light) $3d$ -transition-metal oxides with zero to three d electrons, and the late- (or heavy) $3d$ -transition-metal oxides with five or more d electrons, which are more localized

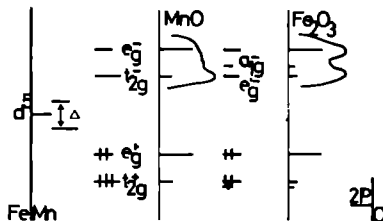


FIG 5 The line spectra for d^5 MnO and d^5 Fe_2O_3 are given The exchange splitting of five electrons is much larger than the ligand field effects This leaves only the spin-down levels empty The symmetry of Fe_2O_3 is broken and as a consequence the t_{2g} level is split The given splitting is not quantitative The decrease of the Fe_2O_3 t_{2g} peak (compared to MnO) can be related to this broken symmetry

ACKNOWLEDGMENTS

We thank S Hufner for constructive discussions, W Braun for his efforts in coordinating our experiments, and B E Watts for provision of a single crystal of CuO We are grateful to the staff of the Berliner Elektronen Speicherring-Gesellschaft für Synchrotronstrahlung

(BESSY) for their support. This work was supported, in part, by the Dutch Foundation for Chemical Research [Stichting Scheikundig Onderzoek Nederland (SON)] with financial assistance of the Netherlands Organization

for Scientific Research [Nederlandse Organisatie voor Wetenschappelijk Onderzoek (NWO)] and by the Committee for the European Development of Science and Technology (CODEST) program

- ¹G A Sawatzky, in *Narrow Band Phenomena*, edited by J C Fuggle, G A Sawatzky, and J W Allen (Plenum, New York, 1988)
- ²J B Goodenough, *Phys Rev* **117**, 1442 (1960), *Prog Solid State Chem* **5**, 145 (1972)
- ³J B Goodenough, in *Magnetism and the Chemical Bond* (Wiley-Interscience, New York, 1963)
- ⁴P W Anderson, *Phys Rev* **115**, 2 (1959)
- ⁵S Sugano, Y Tanabe, and H Kitamura, in *Multiplets of Transition Metal Ions in Crystals* (Academic, New York, 1970)
- ⁶L F Mattheiss, *Phys Rev* **5**, 290 (1972), **5**, 306 (1972)
- ⁷J-L Calais, *Adv Phys* **26**, 847 (1977)
- ⁸A Neckel, P Rastl, R Eibler, P Weinberger, and K Schwarz, *J Phys* **C9**, 579 (1976)
- ⁹K Terakura, T Oguchi, A R Williams, and J Kubler, *Phys Rev* **B30**, 4734 (1984)
- ¹⁰Examples of high resolution monochromators for the oxygen 1s edge (500 eV) are the SX700 at BESSY, Berlin, H Petersen, *Nucl Instrum Methods A* **246**, 260 (1986), the 10-m grazing-incidence monochromator at the Photon Factory, H Maezawa, S Nakai, S Mitani, A Mikuni, T Namioka, and T Sasaki, *Nucl Instrum Methods A* **246**, 310 (1986), and the Dragon monochromator at Brookhaven National Laboratory, C T Chen, *Nucl Instrum Methods A* **256**, 595 (1987). The pace of development in this area is so high that within the last year 500 meV resolution can be significantly bettered in some instruments
- ¹¹For example, R D Cowan, in *The Theory of Atomic Structure and Spectra* (University of California Press, Berkeley, 1981)
- ¹²For example, L Hedin, *Phys Rev* **139**, A796 (1965)
- ¹³We know of only one oxide band structure calculation (for CuO), whose basis set includes also the metal 4s and 4p and the oxygen 3s and 3p states and thus is more appropriate for a comparison with oxygen 1s XAS. A detailed comparison for CuO is given by M Grioni, M T Czyzyk, F M F de Groot, J C Fuggle, and B E Watts, *Phys Rev B* **39**, 4886 (1989). The theoretical and mathematical details concerning this extended basis set are discussed by M T Czyzyk and R A de Groot (unpublished)
- ¹⁴D Norman, K B Garg, and P J Durham, *Solid State Commun* **56**, 895 (1985)
- ¹⁵H Winter, P J Durham, and G M Stocks, *J Phys F* **14**, 1047 (1984)
- ¹⁶Zaanen, G A Sawatzky, J Fink, W Speier, and J C Fuggle, *Phys Rev* **32**, 4905 (1985), J Fink, Th Muller Heinzerling, B Scheerer, W Speier, F U Hillebrecht, J C Fuggle, J Zaanen, and G A Sawatzky, *ibid* **32**, 4899 (1985)
- ¹⁷S W Kortboyer, M Grioni, W Speier, R Zeller, L M Watson, M T Gibson, F Schäfers, and J C Fuggle, *J Phys C* (to be published)
- ¹⁸S Nakai, T Mitsuishi, H Sugawara, H Maezawa, T Matsukawa, S Mitani, K Yamasaki, and T Fujikawa, *Phys Rev B* **36**, 9241 (1987)
- ¹⁹A F Wells, in *Structural Inorganic Chemistry*, 3rd ed (Clarendon, Oxford, 1962), p 475
- ²⁰F W Kutzler and D E Ellis, *Phys Rev B* **29**, 6890 (1984)
- ²¹S W Kortboyer, J B Goedkoop, F M F de Groot, M Grioni, J C Fuggle, and H Petersen, *Nucl Instrum Methods A* **275**, 435 (1989)
- ²²R Brydson, B G Williams, W Engel, H Sauer, E Zettler, and J M Thomas, *Solid State Commun* **64**, 609 (1987)
- ²³L A Grunes, R D Leapman, C N Wilker, R Hoffman, and A B Kunz, *Phys Rev B* **25**, 7157 (1982)
- ²⁴D W Fisher, *J Phys Chem Solids* **32**, 2455 (1971)
- ²⁵I Davoli, A Macelli, A Bianconi, M Tomellini, and M Fanfani, *Phys Rev B* **33**, 2979 (1986), G E Brown, Jr, G A Waychunas, J Stohr, and F Sette, *J Phys (Paris) Colloq* **47**, C8-685 (1986)
- ²⁶A discussion on TM oxide metal K edges is given in A Balzarotti, F Comin, L Incoccia, M Piacenti, S Mobilio, and A Savoia, *Solid State Commun* **35**, 145 (1980) (on TiO₂), M Belli, A Scafati, A Bianconi, S Mobilio, L Palladino, A Reale, and E Burratini, *ibid* **35**, 355 (1980) (on manganese), A Bianconi, *Phys Rev B* **26**, 2741 (1982) (on VO₂), G S Knapp, B W Veal, H K Pan, and T Klippert, *Solid State Commun* **44**, 1343 (1982), L A Grunes, *Phys Rev B* **27**, 2111 (1983), J Wong, F W Lytle, R P Messmer, and D H Maylotte, *ibid* **30**, 5596 (1984) (on vanadium), Th Lindner, H Sauer, W Engel, and K Kambe, *ibid* **33**, 22 (1986) (on MgO), S-H Chou, J Guo, and D E Ellis, *ibid* **34**, 12 (1986) (on FeO)
- ²⁷Results on the TM oxide metal L_{2,3} edges can be found in R D Leapman, L A Grunes, and P L Fejes, *Phys Rev B* **26**, 614 (1982), S L Hulbert, B A Bunker, F C Brown, and P Pianetta, *ibid* **30**, 2120 (1984) (on Cu₂O)
- ²⁸K Tsutsumi, O Aita, and K Ichikawa, *Phys Rev B* **15**, 4638 (1977)
- ²⁹C Sugiura, M Kitamura, and S Muramatsu, *J Chem Phys* **84**, 4824 (1986), C Sugiura, M Kitamura, and S Muramatsu, *ibid* **85**, 5269 (1986), C Sugiura, M Kitamura, and S Muramatsu, *Phys Status Solidi B* **135**, K57 (1986), C Sugiura, M Kitamura, and S Muramatsu, *ibid* **141**, K173 (1987), M Kitamura, S Muramatsu, and C Sugiura, *Phys Rev B* **33**, 5294 (1986), Y Ohno, K Hiram, S Nakai, C Sugiura, and S Okada, *ibid* **27**, 3811 (1983), Y Ohno and S Nakai, *J Phys Soc Jpn* **54**, 3591 (1985), S Nakai, K Ogata, M Ohashi, C Sugiura, T Mitsuishi, and H Maezawa, *ibid* **54**, 4034 (1985), S Nakai, A Kawata, M Ohashi, M Kitamura, C Sugiura, T Mitsuishi, and H Maezawa, *Phys Rev B* **37**, 10895 (1988)
- ³⁰This assignment does agree with, e.g. P R Sarode, *J Phys F* **17**, 1605 (1987)
- ³¹K Fajans and G Joos, *Z Phys* **23**, 1 (1923), K Fajans, *Naturwissenschaften* **11**, 165 (1923), *Z Kristallogr* **61**, 18 (1924)
- ³²O K Andersen, O Jepsen, and D Glötzel, in *Highlights in Condensed Matter Theory*, edited by F Bassani, F Fumi, and M P Tosi (North-Holland, Amsterdam, 1985), pp 82 and 113

- M P Tosi (North Holland, Amsterdam, 1985), pp 82 and 113
- ³³M Pedio, J C Fuggle, J Somers, E Umbach, J Haase, Th Lindner, U Höfer, M Grioni, F M F de Groot, B Hillert, L Becker, and A Robinson, *Phys Rev B* (unpublished)
- ³⁴J Owens and J H M Thornley, *Rep Prog Phys* **29**, 675 (1966), K W H Stevens and C A Bates, in *Magnetic Oxides*, edited by D J Craik (Wiley, London, 1975), pp 141ff, A S Chakravarty, *Introduction to the Magnetic Properties of Solids* (Wiley, New York, 1980), pp 271ff, and references therein
- ³⁵See, e.g., M Tsukada, *J Phys Soc Jpn* **49**, 1183 (1980), M Tsukada, H Adachi, and C Satoko, *Prog Surf Sci* **14**, 113 (1983)
- ³⁶C J Ballhausen, in *An Introduction to Ligand Field Theory* (McGraw-Hill, New York, 1962)
- ³⁷O W Holmes and D S McClure, *J Chem Phys* **26**, 1686 (1957)
- ³⁸W Harrison, in *Electronic Structure and Properties of Solids* (Freeman, San Francisco, 1980)
- ³⁹O Gunnarsson, O K Andersen, O Jepsen, and J Zaanen, *Phys Rev B* **39**, 1708 (1989)
- ⁴⁰C E Moore, *Atomic Energy Levels*, Nat Bur Stand (US) Circ No 467 (US GPO, Washington, DC, 1958), Pis 1-III
- ⁴¹This is reflected in a band structure calculation of TiO₂, as given by S Munnix and M Schmeits, *Phys Rev B* **30**, 2202 (1984)
- ⁴²K E Smith and V E Henrich, *Phys Rev B* **38**, 5965 (1988)
- ⁴³See, e.g., P A Cox, in *The Electronic Structure and Chemistry of Solids* (Oxford University Press, London, 1987), pp 215ff
- ⁴⁴P Kuiper, G Kruizinga, J Ghijsen, G A Sawatzky, and H Verweij, *Phys Rev Lett* **62**, 221 (1989)

4.3. Metal 2p and oxygen 1s x-ray absorption of lithium-cobalt and lithium-manganese oxides

4.3.1. Introduction

In this section the electronic structure of a series of lithium-cobalt and lithium-manganese oxides will be analysed by means of metal 2p and oxygen 1s x-ray absorption. For the lithium-cobalt oxides emphasis is given to the effects of doping of CoO. In case of the lithium-manganese a series of oxides with different manganese valencies are measured.

For the metal 2p x-ray absorption spectra it has been shown in section 3.2 to 3.7 that in many cases the experimental spectrum is reproduced in great detail by a crystal field multiplet model [25]. In this crystal field multiplet model only a single ground state configuration is assumed. Because of the large amount of details in the metal 2p edges, the spectral analysis could be made in a rather detailed fashion. Not only the main effects such as the valency of the metal, its symmetry and the cubic crystal field strengths are determined, but also the more subtle effects of covalency and 3d spin-orbit coupling can be analysed. The effects of covalency include the potential presence of 'satellite' structures due to charge transfer and the simulation of the covalency by means of the reduction of the Slater integrals. The 3d spin-orbit coupling causes splittings in the ground state of CoO and it will be shown that it also causes the admixture of high-spin and low-spin configurations in case of trivalent manganese. The emphasis in this section will be on the electronic structure and for a more detailed discussion of the aspects of the x-ray absorption process is referred to chapter 3. Section 3.5. discusses the effects of 3d spin-orbit coupling and section 3.7. deals with the inclusion of hybridizational effects.

For the oxygen 1s x-ray absorption spectra the situation is different, mainly because the 1s core hole does not give rise to multipole effects. The starting point for the analysis are one-electron models. The oxygen p projected density of states is calculated by means of ground state density functional theory, as has been discussed in detail in section 3.8. In case of LiCoO₂ the core hole potential is taken into account. For strongly correlated systems, which the 3d-metal oxides are, it is expected that the one-electron models are not the full story. Specifically the dd correlation effects are known to be important for the analysis of not only the metal 2p x-ray absorption spectra, but also for experiments like XPS and BIS. In case of the oxygen 1s x-ray absorption spectra it is not straightforward to take the correlation effects into account correctly. As yet efforts to do so have been done by means of a cluster calculation of the one electron addition states, in close analogy to the BIS spectra [10]. In this paper these effects of dd-correlation are kept in mind, but the starting point of the analysis is based on the one-electron models.

Properties of the materials

In table 4.3 the symmetries and the unit cell parameters of the discussed lithium cobalt and lithium manganese oxides are given. CoO is an anti-ferromagnetic insulator. The band gap, determined from XPS-BIS, is 2.4 eV [10]. The traditional density functional results always predicted CoO to be a metal [13]. Recently efforts have been taken to calculate

CoO with more elaborate models, which still are based on density functional but which included orbital polarization [14] or a self-interaction correction [16]. Orbital polarization is an effective treatment of the multipole $3d3d$ interactions U_M , in which an effective solid state Racah-parameter is determined self-consistently. If the orbital polarization effects are taken into account for CoO, the results reached as yet still predict only a pseudo-gap [15]. The self-interaction corrected (SIC) density functional results from Svane and Gunnarsson predict a band gap of 2.81 eV close to the experimental value. In these SIC calculations a local solution at the cobalt site is found to be more stable than a delocalized state. The ZSA-model (see section 4.1) takes into account U and Δ explicitly and treats the hybridization in an approximate tight-binding scheme. It finds a cobalt ground state of 80% $3d^7$ character and 20% $3d^8\bar{L}$ character [10]. It is possible to replace cobalt by lithium to form $\text{Li}_x\text{Co}_{1-x}\text{O}$ up to $x = 0.2$. The cell parameter decreases linearly with the doping concentration [10]. The lithium doped CoO materials are unstable for doping concentrations over 20%, but LiCoO_2 is again a stable compound. Its electronic structure is clearly defined as a 1A_1 -symmetry $3d^6$ ground state, which is a stable configuration with all t_{2g} levels filled and all e_g levels empty.

MnO is an anti-ferromagnetic insulator with a band-gap of 3.9 eV. Its ground state has a 6A_1 -symmetry. Its valence band photoemission, BIS and $2p$ XPS spectrum have been studied in great detail by van Elp et al. [46] and by Fujimori et al. [47], both by making use of configuration interaction calculations based on the ZSA-model. In these calculations the ground state was found to be completely dominated by $3d^5$ character (85% in Ref. 46).

Compound	Symmetry	Unit cell parameters(Å)	Ref.
CoO	O_h^1	a=4.26	[10]
$\text{Li}_{0.2}\text{Co}_{0.8}\text{O}$	O_h^1	a=4.20	[37]
LiCoO_2	D_{3d} ($R\bar{3}m$)	a=2.82 c=14.05	[10]
MnO	O_h^1	a=4.44	[34]
LiMnO_2	D_{2h}^{13} (P_{mnm})	a=2.80 b=5.75 c=4.58	[38]
LiMn_2O_4	O_h	a=8.24	[35]
Li_2MnO_3	C_{2h}^6 (C_2/c)	a=4.92 b=8.53 c=9.60 $\beta = 99.5^\circ$	[32]

Table 4.3: Compounds: Unit cell parameters and symmetry.

Sample preparation

The $\text{Li}_{0.1}\text{Co}_{0.9}\text{O}$ and $\text{Li}_{0.2}\text{Co}_{0.8}\text{O}$ samples are prepared by grinding together the proper amounts of Li_2CO_3 and CoO. The pressed powders are kept at 950°C under a dry oxygen flow for 16 hours, reground and kept at 1050°C in argon atmosphere for 24 hours. By fast cooling the meta-stable high-temperature phases are preserved. X-ray diffraction showed a homogeneous phase with less than 1% of LiCoO_2 . The Li-content found from the lattice parameter was consistent with a wet chemical analysis [10]. The LiCoO_2 sample was

prepared from Li_2CO_3 and CoO by keeping the pressed powders at 950°C in dry oxygen for 16 hours. X-ray diffraction showed homogeneous single phase samples.

Li_2MnO_3 was prepared by mixing Li_2CO_3 with MnO . The powders were mixed and pressed to 15 mm diameter pellets. They were heated for 24 hours at 1050°C in an alumina basket under oxygen flow. After pulverization the procedure was repeated. During the last stage the pellets were reduced under argon flow at 1050°C . Instead of MnO also MnO_2 or Mn_3O_4 were used with equivalent results [32]. The x-ray diffraction results agreed well with the calculated results for the given Li_2MnO_3 structure [33]. Some weak reflexions, not resolved previously, were seen but some other weak reflexions were missing. The MnO sample with 1% Li was prepared by mixing Li_2MnO_3 with MnO . The pressed powder was kept at 900°C at a pressure of 0.15 Pa. To prevent the lithium reacting, the sample was kept in Ag-foil capsules within a quartz tube. The weighted quantity of Li was 1.08% and the quantity determined from the cell-parameter (after heat treatment) was 0.95%. LiMnO_2 was prepared similarly; the x-ray diffraction results confirmed the results in Ref. 34. LiMn_2O_4 was prepared by mixing Li_2CO_3 with Mn_3O_4 and sintering the pressed powders for 24 hours at 850°C under oxygen flow (in alumina). The x-ray diffraction results correspond to a spinel structure with $a = 8.239 \text{ \AA}$, equivalent to the result found in Refs. 35 and 36. The (220) and (224) reflexions, related to the tetrahedral sites, were absent. This confirms that the lithium occupies the tetrahedral sites and all manganese is positioned in the octahedral sites.

Experimental

The x-ray absorption spectra were measured with the DRAGON monochromator [30] at the National Synchrotron Light Source (NSLS) of Brookhaven National Laboratory (BNL). The monochromator resolution was about 0.1 eV (fwhm) for the oxygen 1s edge. The energy calibration of the monochromator was set by measuring the titanium 2p and oxygen 1s spectra of SrTiO_3 and alignment with spectra published previously [25, 31]. The spectra were recorded in total electron yield mode. They were corrected for intensity loss of the beam during measurement. The samples, sintered pellets, were scraped with a ruby file to ensure surface cleanliness. The reproducibility of the results was checked by multiple scraping and measurements at different sample positions.

4.3.2. The cobalt 2p edges of the lithium cobalt oxides

Figure 4.9 shows the cobalt 2p x-ray absorption spectra of the lithium cobalt oxides. The spectra are divided in two parts, denoted as L_3 and L_2 because they are dominated by respectively $2p_{3/2}$ and $2p_{1/2}$ character of the core hole. It is seen that the spectra show a large amount of fine structure. The bottom three spectra are found to be close to identical which suggests that the doping with lithium does not affect the situation of the metal sites too much. In contrast the spectral shape of LiCoO_2 is completely different which indicates a different symmetry state, while the shift to higher energy is a mark of the higher valency of LiCoO_2 .

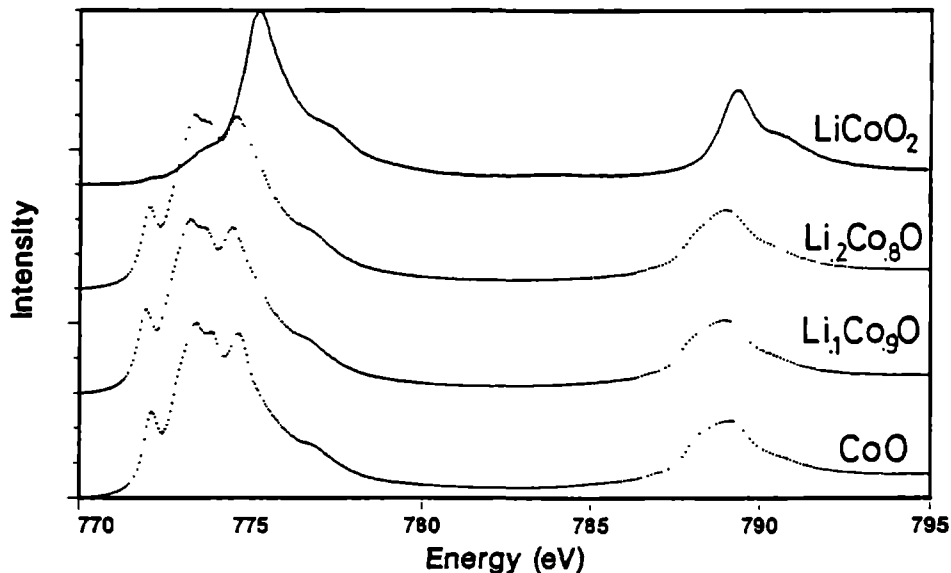


Figure 4.9: The cobalt $2p$ x-ray absorption spectra of CoO (bottom), $\text{Li}_{0.1}\text{Co}_{0.9}\text{O}$, $\text{Li}_{0.2}\text{Co}_{0.8}\text{O}$ and LiCoO_2 (top).

The cobalt $2p$ x-ray absorption spectrum of CoO is discussed first. The ground state is described as a state with a single configuration of $3d^7$ character and with high-spin 4T_1 -symmetry. The influence of $3d^8\bar{L}$ character is neglected. From the optimisation of the spectral shape of the $3d^7 [{}^4T_1] \rightarrow 2p^5 3d^8$ transition, an effective cubic crystal field strength of 1.05 eV (± 0.05) is found. The theoretical spectrum is given in figure 4.10 at the bottom. Especially in the L_2 region the agreement with the spectral shape is not good, and as has been discussed in section 3.5 the agreement is improved considerably if the $3d$ spin-orbit coupling is taken into account. The middle solid line in figure 4.10 refers to the calculated spectrum for the E_2 (overall spin plus orbital symmetry) ground state. The splittings induced by the $3d$ spin-orbit coupling are in the order of 100 meV (see section 3.5 for more details). The spectrum for 300 Kelvin, given as the top solid line, shows a further improvement of the agreement. The remaining discrepancy is believed to be related to the crude estimates of the Slater integrals for which the atomic values were used.

Upon doping with lithium, a first observation is that the cobalt $2p$ x-ray absorption spectra hardly change and the spectrum is still dominated by the $3d^7 \rightarrow 2p^5 3d^8$ transition of CoO. Figure 4.11 gives a closer comparison of the $\text{Li}_{0.2}\text{Co}_{0.8}\text{O}$ spectrum with the CoO spectrum, which reveals the existence of extra intensity at about 776 eV. The difference spectrum shows a peak at exactly the position of the the LiCoO_2 spectrum, which suggests a similar nature. In the next section it is shown that the ground state in LiCoO_2 has $3d^9[{}^1A_1]$ -symmetry, but the assignment of this low-spin character to the lithium doping induced Co^{III} ions in CoO is in contrast to conclusions which were drawn from XPS and

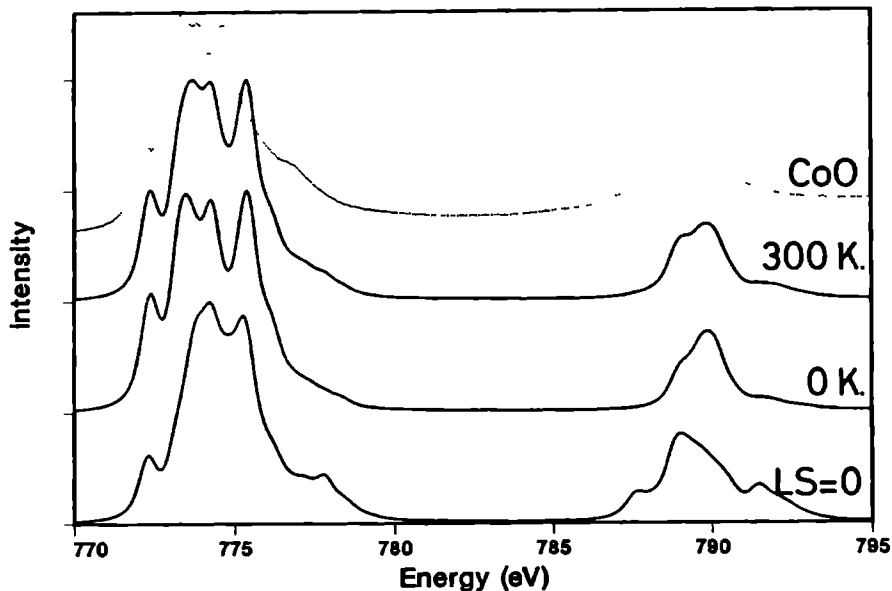


Figure 4.10: Crystal field multiplet spectra for Co^{II} . The crystal field strength is 1.05 eV. Bottom: $3d$ spin-orbit coupling is zero; Middle: atomic value of $3d$ spin-orbit coupling, ground state; Top: Boltzmann distribution for 300 Kelvin. Experimental spectrum (dots): CoO .

BIS measurements where a 3T_1 -symmetry state was found [10]. To clarify this discrepancy the doping induced states are discussed in more detail.

In the impurity model results of Ref. 10, it was found that for CoO $U \approx \Delta$, thus in the case of doping with holes the first state will be of strongly mixed $3d^7\bar{L}$ and $3d^6$ character. To find a rough estimate of the energy positions of the $3d^6$ states, a Hartree-Fock calculation is performed for a cubic crystal field value of 1.2 eV, from which it is found that the 4 lowest states have respectively of 5T_2 , 5E , 3T_1 and 1A_1 symmetry with relative energies of 0, 1.4 eV, 1.7 eV and 1.9 eV. The energy of the respective $3d^7\bar{L}$ states can be found from the addition of a ligand hole of respectively t^{2g} -symmetry (t) or e_g -symmetry (\bar{e}) to the $3d^7$ -states of high-spin 4T_1 -symmetry and (at slightly higher energy) of low-spin 2E symmetry. Addition of \bar{e} lowers the energy more due to its stronger covalent interaction. In this manner four different $3d^7\bar{L}$ -states are formed. Figure 4.12 sketches the consequences of the configuration interaction of the $3d^6$ states with the $3d^7\bar{L}$ states. The 5T_2 ground state of the crystal field multiplet of the $3d^6$ -configuration couples with ${}^4T_1\bar{t}$ -state. The 3T_1 -state couples with the ${}^4T_1\bar{e}$ -state.

It is seen that for the used positioning of the energy-levels a ground state of 3T_1 -symmetry can be formed because of its stronger coupling. Extending this model to higher lithium concentrations leads to the following observations: If the lithium concentration is increased, the

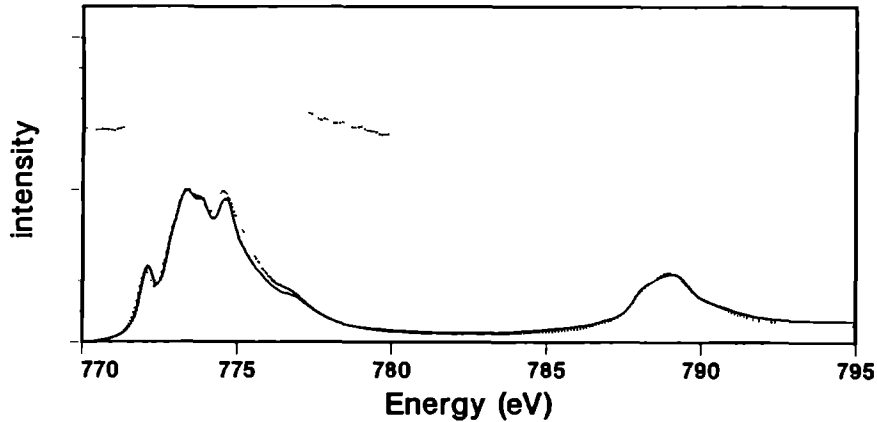


Figure 4.11: Difference spectrum of the cobalt $2p$ x-ray absorption spectra of CoO (solid line) and $\text{Li}_{0.2}\text{Co}_{0.8}\text{O}$ (dots). The top spectrum is the difference between both. The difference spectrum is smoothed and only half its points are plotted.

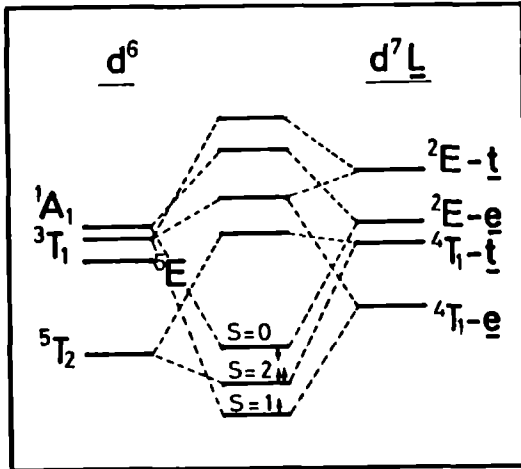


Figure 4.12: Energy diagram for the ground state of the lithium doped states.

cell parameter is decreased which in turn increases the effective cubic crystal field strength. The effect of an increased crystal field is that the energy of the 1A_1 -state is lowered (indicated with the arrows in figure 4.12). Whether in the actual situation the ground state is 3T_1 or 1A_1 can not be resolved by this model. It should be noticed that an additional complication is that the 3T_1 and 1A_1 symmetries can be mixed by $3d$ spin-orbit coupling. Hence, the possibility of an intermediate spin-state between triplet and singlet is possible. The differences between 3T_1 -symmetry to 1A_1 -symmetry are large: because the 1A_1 state does not contain e_g electrons, its cation size is considerably smaller than in the case of a 3T_1 -symmetry state of the Co^{III} ion, which has a similar cation-size than the 4T_1 ground state of Co^{II} . An additional important difference between Co^{III} ions of 3T_1 -symmetry and 1A_1 -symmetry, is that the latter does not couple to the Co^{II} ions in CoO, which are of 4T_1 -

symmetry. Thus impurity Co^{III} states of 3T_1 -symmetry can move through the material by electron hopping, whereas impurity Co^{III} states of 1A_1 -symmetry can not. The observation that the compound is not stable for $x > 0.2$ might suggest that at this doping concentration, the ground state is changed from 3T_1 -symmetry (or mixed symmetry) to pure 1A_1 -symmetry. Because of the small cation size the 1A_1 -symmetry state causes structural 'stress' on the doped CoO crystal which for $x > 0.2$ phase segregation to LiCoO_2 and CoO (+ Li) is to be expected. Alternatively it is possible that the Co^{III} -ions are of low-spin symmetry at all doping concentrations, but at 20% doping the caused structural stress becomes too large and phase segregation occurs.

In conclusion it is found that the cobalt $2p$ x-ray absorption results suggest a 1A_1 -symmetry of the doping induced impurities. This suggestion contradicts the conclusion of the XPS/BIS analysis, but this contradiction can as yet not be resolved.

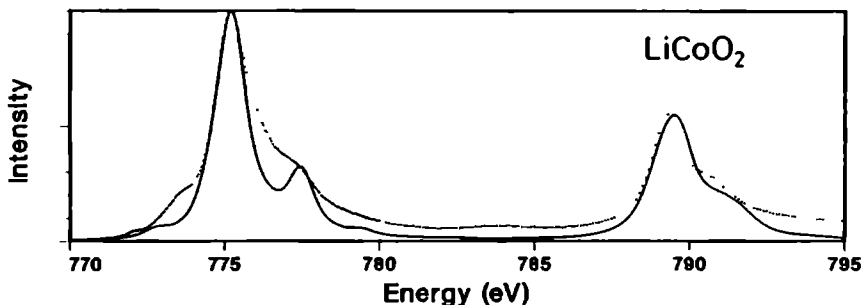


Figure 4.13: Cobalt $2p$ x-ray absorption spectrum of LiCoO_2 (dotted) compared with a crystal field multiplet calculation of the $3d^6[{}^1A_1] \rightarrow 2p^53d^7$ transition (solid line).

Figure 4.13 compares the spectrum of LiCoO_2 with a crystal field multiplet calculation of the $3d^6[{}^1A_1] \rightarrow 2p^53d^7$ transition. The main features are reproduced but it is clearly visible that the experimental spectrum shows additional structure on the low-energy side of the L_3 -edge. This structure might be related to $\text{Co}^{II} [{}^4T_1]$ -impurities, but an alternative interpretation is that this intensity is caused by mixing of $3d^7\bar{L}$ character in the ground state. An impurity calculation gives a ground state which is of strongly mixed $3d^6 + 3d^7\bar{L}$ -character [10], but to resolve this question a more detailed analysis must be performed.

4.3.3. The manganese $2p$ edges of the lithium manganese oxides

Figure 4.14 gives the manganese $2p$ x-ray absorption spectra of the lithium manganese oxides. Similar to the lithium-cobalt oxides a large amount of fine structure is visible. All spectra are clearly different which indicates the effects of the specific crystal field multiplets of the subsequent manganese valencies. Also it is seen that the spectra shift to higher energy as a function of the valency: MnO (bottom) is divalent and Li_2MnO_3 (top) is tetravalent.

The manganese $2p$ x-ray absorption spectrum of MnO relates to the $3d^5[{}^6A_1] \rightarrow 2p^53d^6$ transition. Figure 4.15 gives the comparison with a crystal field multiplet calculation with a cubic crystal field strength of 0.8 eV. The overall agreement is good; the main peak of

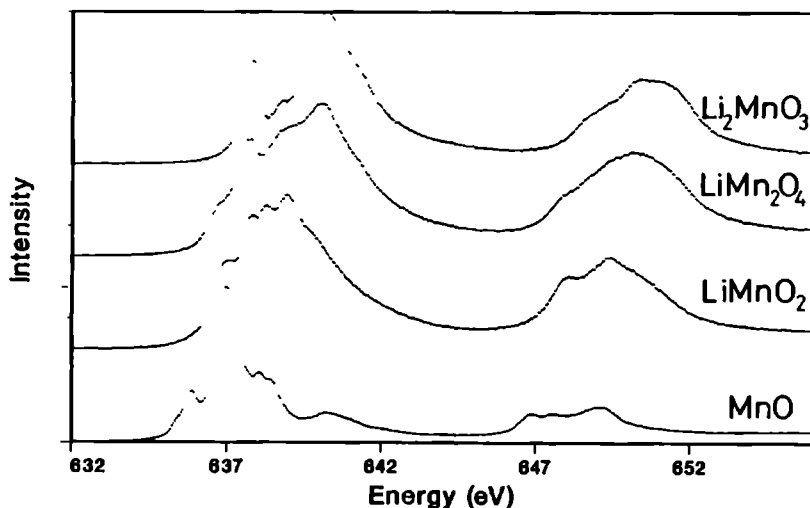


Figure 4.14: The manganese $2p$ x-ray absorption spectra of MnO (bottom), LiMnO₂, LiMn₂O₄ and Li₂MnO₃ (top).

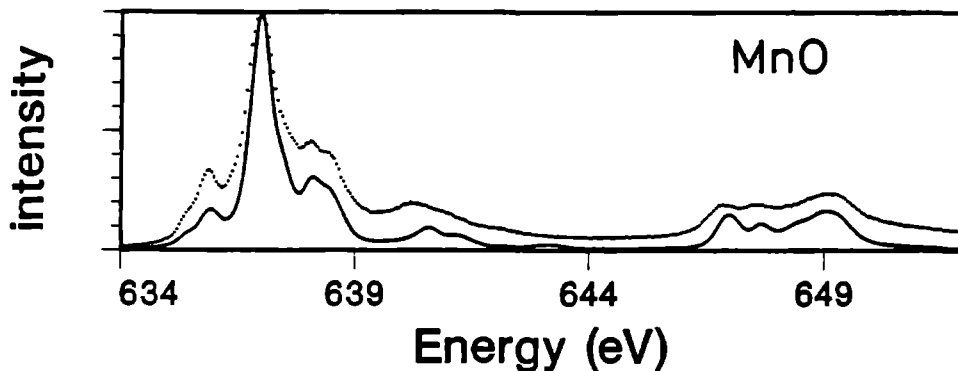


Figure 4.15: Manganese $2p$ x-ray absorption spectrum of MnO (dotted) compared with a crystal field multiplet calculation (solid line). The cubic crystal field strength ($10Dq$) was taken as 0.8 eV.

the L_3 edge is lower in the experimental spectrum than in the calculation. Also the small shoulder at the high energy side is slightly misplaced in the theoretical curve, which is most probably due to the rough treatment of the Slater integrals. It should be stressed that the good agreement between theory and experiment indicates that even for MnO one can use the atomic values of the Slater integrals.

Li₂MnO₃ (top spectrum in figure 4.14) contains Mn^{IV} ions in approximately octahedral sites. It forms the stable 4A_2 ground state of the $3d^3$ configuration. The t_{2g} spin-up band is

filled and all other $3d$ subbands are empty. The manganese $2p$ x-ray absorption spectrum is compared with a crystal field multiplet calculation in figure 4.16. As for tetravalent metal ions the hybridization is strong, the Slater integrals have been reduced from their atomic values. In figure 4.16 the spectrum using atomic Slater integrals is included as the dashed line. The Slater integrals were that reduced to 75% for the dd interactions and to 88% for the pd interactions. It should be noted that a detailed study for the optimisation of these reductions has not yet been performed. The correct approach would be to search for a theoretical justification for a specific reduction of (some of) the Slater integrals. Notice in total there are seven Slater integrals: in the initial state F_{dd}^2 and F_{dd}^4 and in the final state F_{dd}^2 , F_{dd}^4 , F_{pd}^2 , G_{pd}^1 and G_{pd}^3 . The different reduction of dd and pd Slater integrals is justified because the hybridization effects will expand the wavefunction of the $3d$ -electrons (and not affect the $2p$ core hole), hence the interaction between the $3d$ -electrons will decrease more rapidly.

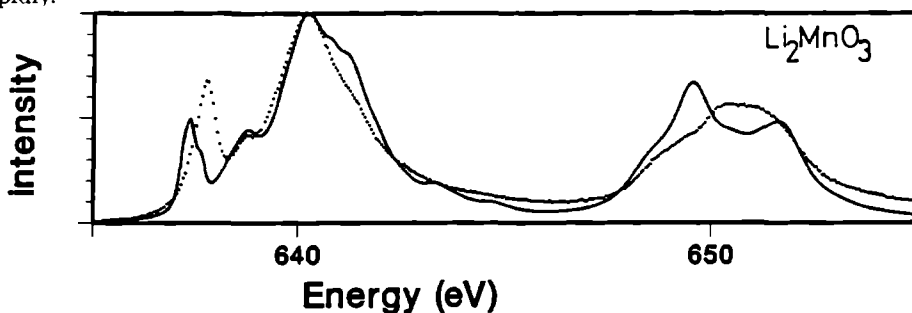


Figure 4.16: Manganese $2p$ x-ray absorption spectrum of Li_2MnO_3 (dotted) compared with a crystal field multiplet calculation (solid line). The Slater integrals were reduced from their atomic values.

LiMnO_2 contains trivalent manganese ions with four electrons in the $3d$ -band. It is known that the $3d^4$ -configurations give rise to a large variety of ground state symmetries: SrFeO_3 is believed to be a low-spin (3T_1) or intermediate spin conductor [51,52]. LaMnO_3 is a high-spin (5E) insulator [50], and also CaFeO_3 has a high-spin configuration, but it is most likely subject to partial charge disproportionation below $T = 290\text{K}$ [52]. The examples given illustrate that if the covalent bonding between the $3d^4$ -metal ion and oxygen is strong, a tendency to low-spin configurations is found. It is clear that the tetravalent iron compounds are highly covalent, whereas the covalency for LaMnO_3 is less due to its trivalent manganese ions and also due to the competition with the relatively covalent lanthanum ion. Lithium is more ionic than lanthanum and an increased covalency between oxygen and manganese is to be expected for LiMnO_2 . This might result in close to degenerate high-spin and low-spin states and due to the $3d$ spin-orbit coupling an intermediate spin state will form. Also the trivalent manganese ions in LiMn_2O_4 are expected to be in an intermediate spin state, as has been suggested from magnetization measurements [36]. Given these considerations it was checked in detail in what manner the spectral shape in the crystal field multiplet calculations behaves close to the high-spin low-spin transition in Mn^{III} . To simplify the problem the crystal

field multiplet calculations are performed in octahedral symmetry and possible effects of the Jahn-Teller distortion on the high-spin 5E -configuration are neglected. The Slater integrals are reduced to 75% for dd -interactions and to 88% for pd interactions and the atomic $3d$ spin-orbit coupling is used. Figure 4.17 gives the energy levels of the $3d^4$ ground state for four different values of the cubic crystal field close to the transition point. The high-spin 5E -configuration splits after inclusion of the $3d$ spin-orbit coupling into 5 states of respectively A_1 , A_2 , T_1 , T_2 and E symmetry. Likewise the 3T_1 -configuration splits into 4 states of A_1 , T_1 , T_2 and E symmetry.

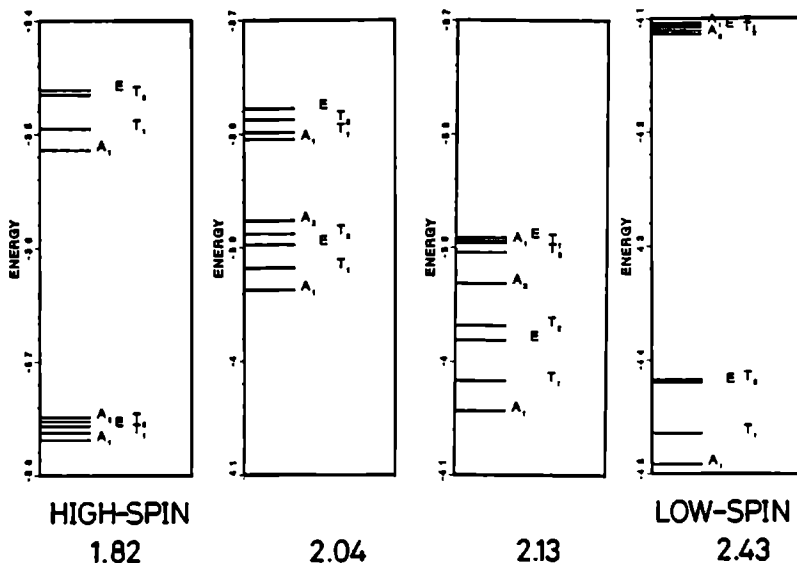


Figure 4.17: Distribution of multiplet split states in the $3d^4$ initial state of trivalent manganese. The symmetries of the total J moment (after $3d$ spin-orbit coupling) are given. From left to right the cubic crystal field values are 1.82 eV (high-spin), 2.04 eV, 2.13 eV and 2.43 eV (low spin). In all four diagrams the overall energyrange of the vertical axis is 0.4 eV.

For a cubic crystal field of 1.82 eV, the ground state has high-spin 5E symmetry. $3d$ spin-orbit coupling is only a second order effect for states of E -symmetry, hence the splittings are small (of the order of 0.02 eV) as can be checked in the figure. At room temperature (0.025 eV) the ground state is given as (close to) a statistical distribution of the five spin-orbit split states. If the cubic crystal field is increased to 2.04 eV the lowest five states do still relate to the high-spin configuration, but the splittings between the states are enlarged due to considerable admixture of 3T_1 character. It is noted that the state of A_2 symmetry is contained in the 5E -state only, hence it is not subject to admixture with the low-spin states and it can be used as an indication of the position of the high-spin configuration without interaction with the low-spin configuration.

For a cubic crystal field of 2.13 eV the A_2 state is shifted upward and is positioned in between the bonding and anti-bonding combinations of the other symmetries. From the fact that the splittings between the four bonding combinations are larger than for the anti-bonding combinations it can be concluded that the symmetry of the ground state has become to be dominated by the low-spin configuration. For a cubic crystal field of 2.43 eV the ground state is low-spin. The splittings due to $3d$ spin-orbit coupling are of the order of 0.1 eV which means that at room temperature the ground state is not a statistical distribution over the four symmetries, but instead it is dominated by the lowest state of A_1 -symmetry.

Figure 4.18 give the spectral shapes found from the crystal field multiplet calculations for, from bottom to top, the low-spin 3T_1 -configuration (cubic crystal field is 2.43 eV), the high-spin 5E -configuration (1.82 eV) and the mixed spin state (2.13 eV). The experimental spectrum of LiMnO_2 with dots and it shows most similarity to the mixed spin state.

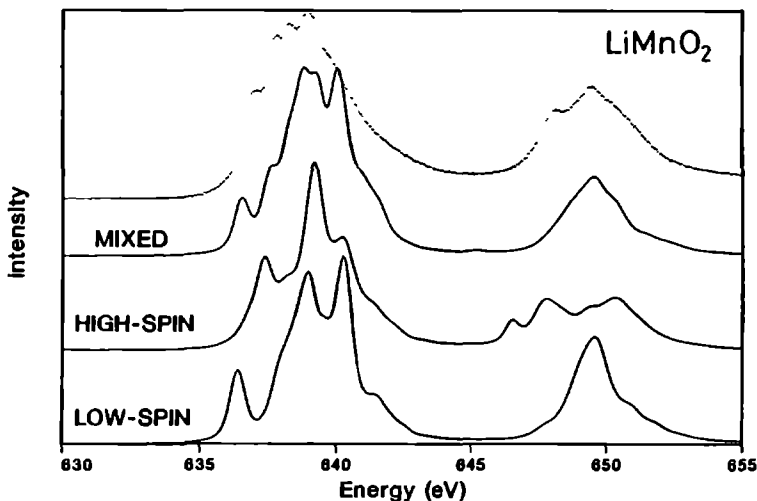


Figure 4.18: Crystal field multiplet calculation for the $2p$ x-ray absorption spectrum of the low-spin, high-spin and mixed (or intermediate) spin ground state for trivalent ($3d^4$) manganese atoms. The top spectrum is the $2p$ x-ray absorption spectrum of LiMnO_2 .

With regard to the optimisation of the spectral shape there are several complicating factors: the Slater integrals were set roughly to slightly reduced values and the symmetry distortion related to the Jahn-Teller effect is neglected. Figure 4.19 sketches the consequences of a small tetragonal distortion on the mixed spin configuration for a cubic crystal field of 2.13 eV. The lowest state of A_1 symmetry is not split; the first excited (T_1 -symmetry) state splits into two and the energy difference between the A_2 state and the A_1 ground state decreases. Details concerning the magnitude and the specific choice of parameters for a tetragonal distortion are as yet not known, hence no attempt was made to optimize the

spectral shape as found from the calculations in tetragonal symmetry. For the moment it is concluded only that in the region of the high-spin low-spin transition the $3d$ spin-orbit coupling gives a mixed spin state and the resulting spectral shape is similar to the experimental spectrum of LiMnO_2 .

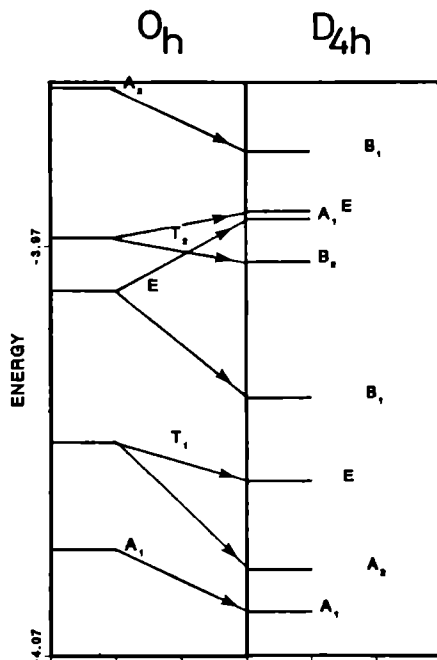


Figure 4.19: Effect of a small tetragonal distortion on the distribution of states for the mixed spin situation. The cubic crystal field is 2.13 eV; the tetragonal X_{220} parameter [53] is set to 0.2 eV; the other tetragonal parameter is kept zero.

The manganese $2p$ x-ray absorption spectrum of the spinel LiMn_2O_4 , which contains 50% trivalent and 50% tetravalent manganese atoms, looks similar to a 1 to 1 admixture of the spectra of trivalent LiMnO_2 and tetravalent Li_2MnO_3 . Therefore it is concluded that the trivalent manganese atoms in this spinel will be in the mixed spin regime too. It was found from experimental data on the magnetic moment that the trivalent manganese atoms of this compound were partly of high spin and partly of low-spin character [36]. This finding can be explained naturally from the mixed spin ground state.

4.3.4. The oxygen $1s$ edges of the lithium cobalt oxides

Figure 4.20 shows the oxygen $1s$ x-ray absorption spectra of the lithium cobalt oxides. The structures at threshold relate to the transitions of oxygen p -character in the metal $3d$ -band and above 533 eV the metal $4sp$ -band is visible, as has been discussed in detail in Ref. 48. In contrast to the metal $2p$ edges the effects of lithium-doping are directly visible in the growth of the peak at threshold. Again the LiCoO_2 spectrum is distinct from the other spectra.

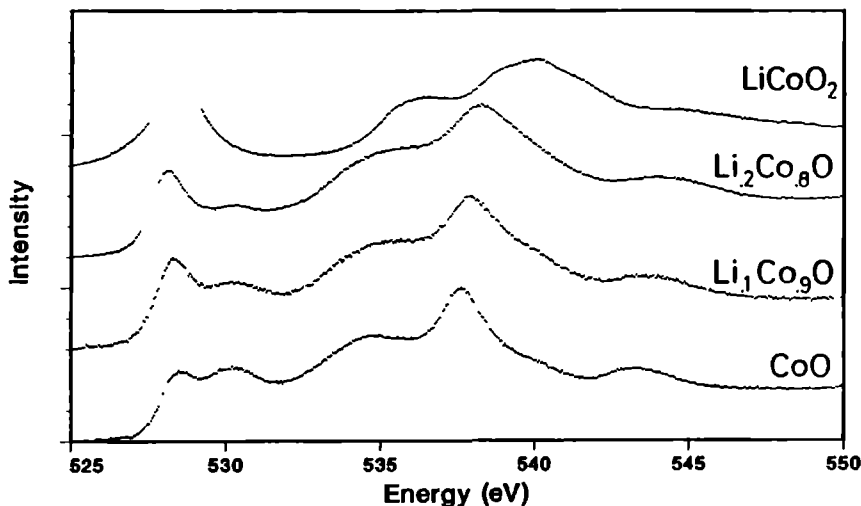


Figure 4.20: The oxygen 1s x-ray absorption spectra of CoO (bottom), $\text{Li}_{0.1}\text{Co}_{0.9}\text{O}$, $\text{Li}_{0.2}\text{Co}_{0.8}\text{O}$ and LiCoO_2 (top).

The oxygen 1s x-ray absorption spectrum of CoO (bottom) shows a two-peaked structure in the 3d-band region. This structure can in a one-electron model be assigned to states related to addition of respectively a t_{2g} and an e_g electron, split by the cubic crystal field (see section 3.2). If 3d-correlation effects are included in the final state it is necessary to calculate the crystal field multiplet for the $3d^8$ -final state. A cluster calculation, in which the crystal field multiplet as well as the charge transfer to the $3d^9\bar{L}$ -state are included, shows that due to the multipole interactions weight is transferred to states which can only be reached with two-electron transitions [10]. The charge transfer satellites are positioned at higher energy and have negligible intensity. The spectral shape of the crystal field multiplet shows with respect to the \mathcal{DK} -model an additional peak related to a final state with two t_{2g} holes, however this extra peak is not observed experimentally. Unfortunately most density functional calculations focus on the proper description of for example the band gap and the magnetic moment [15,16], and they do not contain an accurate description of the first 20 eV of the unoccupied states necessary for a sensible comparison with the oxygen 1s x-ray absorption spectrum. Consequently the oxygen 1s x-ray absorption result of CoO can not be checked against density functional results.

Upon doping with lithium the oxygen spectra are broadened slightly in the 4sp-region, but the most remarkable feature is the increase of intensity at the position of the first peak. In contrast to the $\text{Li}_x\text{Ni}_{1-x}\text{O}$ -system the peak related to doping, the 'impurity state', is not build in the gap [19] but instead close to the lowest unoccupied state in CoO.

The expected transition is: $3d^7\bar{L} + 3d^8 \rightarrow 3d^7 + 3d^8\bar{L}$ (neglecting the oxygen 1s core hole). As can be checked in figure 4.11 the peak which grows with doping has an energy close to the peak of the LiCoO_2 spectrum. This is a similar result as found from metal 2p

x-ray absorption, and its implication was discussed in the foregoing section. Unfortunately the amount of structure in the oxygen $1s$ spectrum (and the complications in the analysis of the different symmetries), makes a closer analysis difficult.

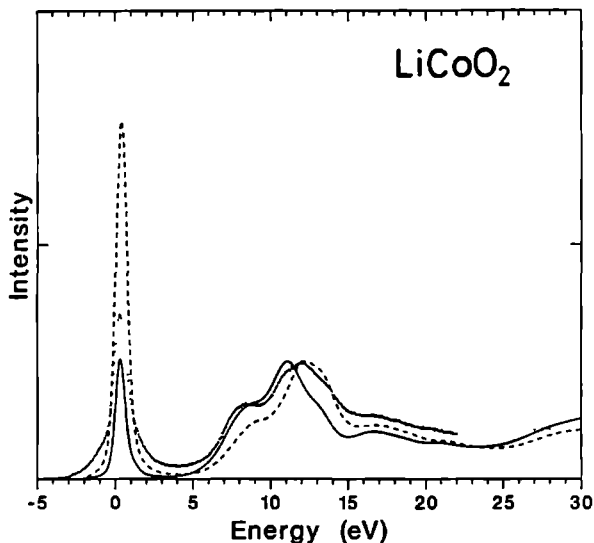


Figure 4.21: Oxygen $1s$ x-ray absorption spectrum of LiCoO_2 (dotted) compared with an LSW band structure calculation. The solid line gives the ground state N -particle density of states; the dashed line relates to density of states after inclusion of the core hole (reproduced from Ref. 43).

The oxygen $1s$ x-ray absorption spectrum of LiCoO_2 shows a sharp single peak at threshold. It is clearly separated from the other structures. For LiCoO_2 an accurate density functional calculation has been performed [43] and figure 4.21 shows a comparison with it. The ground state calculation of the oxygen p -projected density of states overestimates the intensity of the leading peak. The final state calculation, described in section 3.8, reduces the intensity of the first peak. In fact the intensity of the first peak is reduced too much. Also in the structure at 6 to 12 eV intensity is shifted downward. It can be concluded that the overall agreement between the $1s$ x-ray absorption spectrum and the band structure calculation is good, taking into account the fact that $3d$ -correlations have been neglected. It must be remarked that the 1A_1 -symmetry $3d^6$ state is special in that there is no spin-polarization and also there is a clear gap between the t_{2g} and the e_g bands, which are fortunate circumstances for one electron models to work.

It is noted that if the crystal field multiplet model is applied to LiCoO_2 it will predict nine possible transitions to states within the final state $3d^7$ -multiplet. The fact that only one distinct peak is visible in the experiment indicates that the effective Slater integrals are too small to transfer a considerable amount of intensity to any other of these nine states of the crystal field multiplet (or to the charge transfer states). Close examination of the experimental spectrum in comparison with the density of states indicates extra intensity at the low-energy side (between -3 and -1 eV in figure 4.21), which might be related to the multiplet effects though this remains to be checked.

4.3.5. The oxygen 1s edges of the lithium manganese oxides

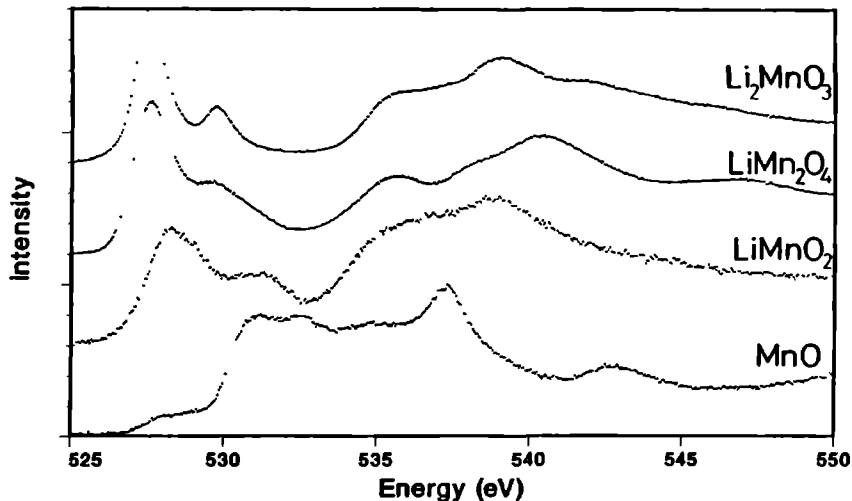


Figure 4.22: The oxygen 1s x-ray absorption spectra of MnO (bottom), LiMnO₂, LiMn₂O₄ and Li₂MnO₃ (top).

Figure 4.22 gives the oxygen 1s x-ray absorption spectra of the lithium manganese oxides. The spectra are clearly different from each other and specifically the variations in the 3d-part are large. The oxygen 1s x-ray absorption spectrum of MnO relates to the $3d^5 + 3d^6 \bar{L} \rightarrow 3d^6$ transition. In the DK -model two final states can be reached as the electron can be added to the empty t_{2g} or e_g band, both spin-down. All spin-up states are full in the ground state. In this case the crystal field multiplet model gives an identical result as the ($S=2$) final states contain only a single spin-down electron. The splitting of the final state is related to the cubic crystal field which is about 1 eV. As the MnO sample was doped with 1% lithium, some impurity states related to $3d^4 + 3d^5 \bar{L} \rightarrow 3d^5$ transitions are expected in the bandgap. They are indeed observed in the experiment as the low-intensity leading (double) peak. From the cluster analysis it is found that both U and Δ are about 8 eV [10]. This places MnO in the intermediate regime in between charge transfer and Mott-Hubbard insulators in the ZSA-model. From this it is expected that the first states related to lithium doping have a strongly mixed $3d^4 + 3d^5 \bar{L}$ character. The states induced by the lithium doping appear in the gap as has been found for NiO [19] but in contrast to CoO for which the peaks related to doping appear at a similar energy as the original peaks.

The oxygen 1s x-ray absorption spectrum of Li₂MnO₃ can be separated into a two-peaked 3d-part and at considerably higher energy the 4sp-bands plus bands related to lithium. The 3d-part of the spectrum bears close resemblance to the oxygen 1s x-ray absorption spectrum of MnO₂, which also has manganese in the 4A_2 ground state of the $3d^3$ configuration. Within the DK -model an oxygen 1s electron is excited to an empty e_g^+ , e_g^- or t_{2g}^- sub-band. As there

are only two separate structures visible the t_{2g}^- and e_g^+ bands are expected to overlap. This overlap is a uniform feature of $3d^3$ compounds [48] and in Li_2MnO_3 , MnO_2 and also Cr_2O_3 a similar two-peaked structure is found with an energy splitting of about 2.4 eV. Thus the cubic crystal field as well as the effective exchange splitting are in the order of 2.4 eV. It should be noted that the $(t_{2g}^+)^3e_g^+$ and $(t_{2g}^+)^3t_{2g}^-$ final states can be mixed by $3d$ spin-orbit coupling to form a combined final state, which consequently shows up in the oxygen $1s$ x-ray absorption spectrum as a single feature.

An additional justification of this assignment is given by the manganese oxides with a $3d^4$ -configuration which are found to be close to the low-spin high-spin transition: The $3d$ -part of the oxygen $1s$ x-ray absorption spectrum of LiMnO_2 shows a broad peak and a shoulder at the high-energy side. The peak is assigned to the empty states of the t_{2g}^- -band and the e_g^+ -band. As it was found from the analysis of the manganese $2p$ spectrum that the ground state is formed as a mixture of high-spin and low-spin, these bands overlap. The high-energy shoulder relates to the e_g^- -band. The Jahn-Teller lattice distortion will cause additional (non-resolved) splittings and consequently a broad spectral shape. The $3d$ -part of the spinel LiMn_2O_4 is described as a 1 to 1 superposition of the spectra of trivalent LiMnO_2 and tetravalent Li_2MnO_3 , though the limited amount of structure makes an accurate analysis impossible. The remainder of the LiMn_2O_4 spectrum is related to the manganese $4sp$ -band; this band is completely delocalized and its shape will be determined mainly by the spinel crystal structure. It is noticed that the shape of the structure in between 534 eV and 545 eV bears close resemblance to the structure of the oxygen $1s$ x-ray absorption spectra of the $\text{Zn}_{1-x}\text{Li}_x\text{V}_2\text{O}_4$ - spinel system which will be discussed in section 4.5.2.

4.3.6. Conclusions

It is shown that the metal $2p$ x-ray absorption spectra of the lithium cobalt and lithium manganese oxides are described well by the crystal field multiplet model. However if the hybridization increases it is necessary to reduce the Slater integrals from their atomic values (in the present approach).

The dominating symmetries and $3d$ -counts of the ground state are given in table 4.4, in accord with determinations from XPS/BIS [10]. The binary oxides CoO and MnO are completely dominated by respectively $3d^7$ and $3d^5$ ground states, both high-spin. The lithium doped CoO states have strongly mixed $3d^6 + 3d^7\bar{L}$ character. The assignment to 3T_1 character follows from other experiments. From the x-ray absorption spectra alone the assignment to overall 1A_1 symmetry is more obvious, as this would explain directly the spectral changes of the oxygen $1s$ edge (and not disagree with the cobalt $2p$ edge). However it cannot be concluded that the observed spectral shapes exclude 3T_1 -symmetry. As the 3T_1 and 1A_1 can be mixed by $3d$ spin-orbit coupling it is possible that the overall symmetry is a mixture of triplet and singlet character. With increased doping the singlet state will tend to dominate more and more as the cubic crystal field increases. It is likely that at 20% doping the 1A_1 -state dominates so much that the crystal structure collapses and segregation to LiCoO_2 and CoO (+Li) takes place. LiCoO_2 has a low-spin $3d^6$ ground state; the amount of $3d^7\bar{L}$ character will be considerable which can explain the low-energy satellites absent

Compound	3d-count	Symmetry
CoO	$3d^7$	${}^4T_1^*$
$\text{Li}_{0.2}\text{Co}_{0.8}\text{O}^{**}$	$3d^6 + 3d^7\bar{L}$	3T_1 (or 1A_1 ?)
LiCoO_2	$3d^6 (+ 3d^7\bar{L})$	1A_1
MnO	$3d^5$	6A_1
LiMnO_2	$3d^4$	mixed ${}^5E + {}^3T_1$
LiMn_2O_4		
. . . site 1:	$3d^4$	mixed ${}^5E + {}^3T_1$
. . . site 2:	$3d^3$	4A_2
Li_2MnO_3	$3d^3$	4A_2

Table 4.4: Symmetries of the lithium cobalt oxides and lithium manganese oxides.

** The symmetry of the doped state is given. The majority of states is still as for CoO (see text). * Split by 3d spin-orbit coupling.

in the calculated $3d^6$ multiplet. Trivalent manganese is found to be best described by a mixed spin ground state, in agreement with other experiments. It is noted that in contrast to tetravalent iron, trivalent manganese is dominated by $3d^4$ character and the admixture of $3d^5\bar{L}$ character is below the 'detection limit'. The $3d^4$ state in LiMnO_2 and LiMn_2O_4 is found to be simulated best if the symmetry of the ground state is described as a mixture of high-spin 5E and low-spin 3T_1 symmetry. This mixing is caused by the 3d spin-orbit coupling and it is effective close to the high-spin low-spin transition. A Jahn-Teller distortion of the high-spin configuration affects the spectral shape only slightly.

For the oxygen 1s x-ray absorption spectra it is concluded that the most direct way to explain the spectrum is the qualitative DK-model in which an electron is added to the respective 3d sub-bands of a ground state calculation. In most cases the best quantitative method available is a core-hole density of states calculation, despite the fact that it is a one-electron method and correlation effects are treated incorrectly. The cluster calculations with the crystal field multiplet model (performed as yet) result in spectra with distinct peaks related to multi-electron transitions. These peaks are not observed experimentally and hence it is concluded that the multipole dd-interactions as well as the effects of charge transfer are not large enough to give rise to separate structures in the experimental spectrum. However as it is known from other spectroscopies that correlation effects are important for a correct description of the ground state of 3d-metal oxides, these correlation effects will have to be incorporated in future efforts to improve the models to explain the oxygen 1s x-ray absorption experiments.

Acknowledgements

The x-ray absorption measurements were performed in close collaboration with Miguel Abate, with the assistance of Yan-jun Ma, Chien-te Chen and Francesco Sette (AT&T Murray Hill). The lithium-cobalt and lithium-manganese samples were prepared by Leo Wieland,

Rudolf Potze and Jan van Elp. The crystal field multiplet program was developed by Theo Thole (University of Groningen). The LSW band structure calculation of LiCoO_2 has been performed by Marek Czyżyk (Universities of Nijmegen and Groningen).

4.4. The metal 2p and oxygen 1s x-ray absorption spectra of the $\text{La}_{1-x}\text{Sr}_x\text{TMO}_3$ perovskites

This section deals with the electronic structure of the perovskites $\text{La}_{1-x}\text{Sr}_x\text{TMO}_3$ for the 3d-metals titanium, manganese, iron and cobalt. In LaTMO_3 the transition metal ion is in a formally trivalent state and in SrTMO_3 in a tetravalent state. Mainly due to the increased valency the strontium perovskites have a more covalent bonding of the 3d-metal with oxygen. However the major variation in the electronic properties is related to the number of 3d electrons present. In this section emphasis is given to a detailed analysis of the endmembers of the series. The goal is to determine the dominating ground state configuration and its symmetry of all the LaTMO_3 and SrTMO_3 perovskites with the final goal to systemize the main configurations and main symmetries of all transition metal ions (octahedrally surrounded by oxygen).

From the foregoing sections it has been concluded that the oxygen 1s x-ray absorption spectra do not show much evidence for distinct spectral features related to 3d-correlation effects in the final state. In other words the interactions determining the oxygen 1s x-ray absorption spectra cause it to be relatively well described in the weakly correlated limit, which justifies the use of one-electron models as the basic starting point. Hence the analysis of the oxygen 1s spectra will be based on band structure calculations (discussed in section 3.8), though the possible influences of correlation effects in the 3d-band are kept in mind. In contrast the metal 2p x-ray absorption spectra are described with the crystal field multiplet model (discussed in sections 3.2 to 3.7).

The x-ray absorption spectra were measured with the SX700 (II) monochromator [49] at the Berliner Elektronenspeicherring Gesellschaft für synchrotronstrahlung (BESSY). The monochromator resolution was about 0.1 eV (hwhm) for the oxygen 1s edge at about 530 eV. The spectra were recorded in total electron yield mode and were corrected for intensity loss of the beam during measurement. The samples, sintered pellets, were scraped with a diamond file to ensure surface cleanliness. The samples have been prepared by M. Takano, Y. Takeda, H. Eisaki, S. Uchida, Y. Fujishima and Y. Tokura.

4.4.1. The metal 2p x-ray absorption spectra

The titanium 2p edges of $\text{La}_{1-x}\text{Sr}_x\text{TiO}_3$

Figure 4.23 shows the 2p x-ray absorption spectra of the $\text{La}_{1-x}\text{Sr}_x\text{TiO}_3$ -perovskites. The spectrum of SrTiO_3 (given at the top) shows four sharp peaks and two small leading structures. The solid line given underneath is the result of a $3d^0 \rightarrow 2p^5 3d^1$ crystal field multiplet calculation with atomic Slater integrals and a cubic crystal field of 1.5 eV. The details concerning this crystal field multiplet calculations were given in chapter 3. The agreement is excellent and it can be concluded that ground state is described as $3d^0$. There are no clear signs of the admixture of $3d^1\bar{L}$ character in the ground state. For clarity it is repeated that the admixture of $3d^1\bar{L}$ -character might affect the spectral shape in at least three ways:

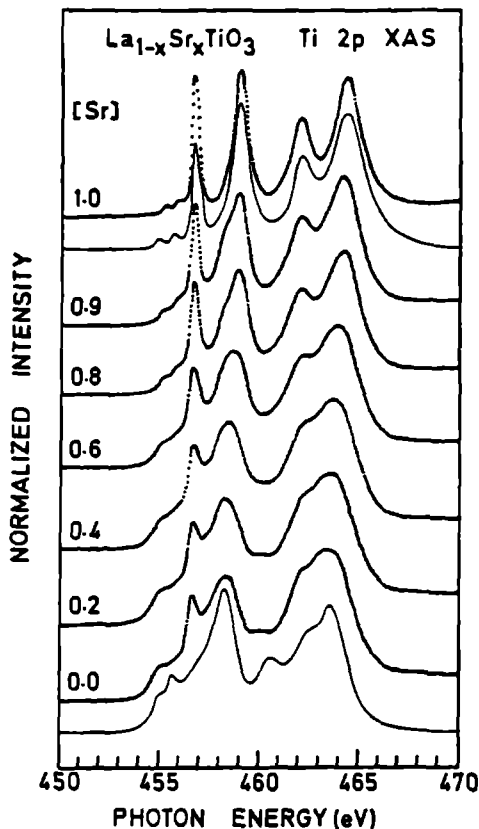


Figure 4.23: The $2p$ x-ray absorption spectra of the $\text{La}_{1-x}\text{Sr}_x\text{TiO}_3$ -system. The solids lines are the results of crystal field multiplet calculations; At the bottom the $3d^1 [^2T_2] \rightarrow 2p^5 3d^2$ transition is given and the solid line simulating the SrTiO_3 spectrum relates to the $3d^0 [^1A_1] \rightarrow 2p^5 3d^1$.

- A satellite structure can appear at the position of the anti-bonding combination of the $2p^5 3d^1$ and $2p^5 3d^2 \underline{L}$ final states.
- Due the partial occupancy of $3d^1 \underline{L}$ -character in the ground state, transitions from this state to the bonding combination of the $2p^5 3d^1$ and $2p^5 3d^2 \underline{L}$ final states occurs. Neglecting interference effects this can be described as the superposition of the $3d^1 \underline{L} \rightarrow 2p^5 3d^2 \underline{L}$ transition and the original $3d^0 \rightarrow 2p^5 3d^1$ transition. (For the actual calculation of the crystal field multiplet, it is as yet not possible to include the potential effects of the ligand hole).
- An additional effect of the covalency is the possibility that apart from the $3d^0 + 3d^1 \underline{L}$ basis, additional configurations have a considerable ground state occupation. As argued in section 3.7, instead of the actual inclusion of these states their influence can be simulated via the reduction of the Slater integrals.

In case of SrTiO_3 no significant feature which can be related to these effects is observed. The spectrum of LaTiO_3 is simulated with a $3d^1 [^2T_2] \rightarrow 2p^5 3d^2$ crystal field multiplet

calculation with a cubic crystal field of 1.8 eV. With respect to SrTiO₃ a slightly increased broadening has been applied. The main features in the spectrum are reproduced, though the agreement is less than for SrTiO₃. Partially this is due to the existence of 10% of TiO₂ impurities, which were found as impurity phases by x-ray diffraction. Specifically the sharp peak at 457 eV is a consequence the TiO₂ impurities.

The compounds in the La_{1-x}Sr_xTiO₃-series contain titanium in a mixed valent state. Because a quantum state with non-integer valency is unlikely due to the 3*d* correlation effects, a titanium ion will be in either a 3*d*¹ or a 3*d*⁰ state. In a metallic phase the valency fluctuates between 3*d*¹ and 3*d*⁰. This fluctuation is in general too fast to be followed by lattice readjustments. Hence there are two electronically different titanium states, but only one crystallographically different titanium site. The x-ray absorption process has a timescale shorter than the electron hopping, thus it will not notice that a specific titanium atom has a fluctuating valency, but instead it will see only static titanium atoms with either a 3*d*⁰ or a 3*d*¹ configuration. Hence, the metal 2*p* x-ray absorption spectra of the La_{1-x}Sr_xTiO₃-series are described as a superposition of *x* times the spectrum of SrTiO₃ plus 1 - *x* times the spectrum of LaTiO₃. There can be small modifications to the spectra of SrTiO₃ and LaTiO₃ due to a slightly different cubic crystal field strengths, due to the equivalence of the crystallographic sites of the 3*d*¹ and 3*d*⁰ configurations. (The lattice parameter is almost identical in LaTiO₃ and SrTiO₃ thus this effect will be small) The spectral shapes of metal 2*p* x-ray absorption of La_{1-x}Sr_xTiO₃ (figure 4.23) show a smooth spectral variation with increasing *x*, in full agreement with the described superposition model.

The manganese 2*p* edges of La_{1-x}Sr_xMnO₃

Figure 4.24 shows the 2*p* x-ray absorption spectra of the La_{1-x}Sr_xMnO₃-perovskites. SrMnO₃ is an insulator, in contrast to SrVO₃, SrCrO₃, SrFeO₃ and SrCoO₃, which all are metallic. The reason for the insulating behaviour of SrMnO₃ is the half-filled *t*_{2*g*}-band, thus the bandgap is a result of the gap between the *t*_{2*g*}⁺-band and the *e*_g⁺-band as calculated with one electron methods. The gap will be increased by correlation effects, but from the observation that SrVO₃, etc are metallic it can be concluded that correlation effects alone (that is if not assisted by a filled band situation) are not capable of opening a gap, which is due to the large covalency of the bonds between the 3*d*-metal and oxygen.

The 2*p* x-ray absorption of SrMnO₃ is similar to the spectrum of Li₂MnO₃ given in section 4.3. The Li₂MnO₃ spectrum has been compared with a crystal field multiplet calculation with reduced Slater integrals in figure 4.16. The agreement is not perfect, mainly due to uncertainties in the values for the Slater integrals. The SrMnO₃ spectrum is considerably broader than the Li₂MnO₃ spectrum, which makes it not sensible to further optimize the crystal field multiplet calculations to this spectrum. The reason for the considerably broader spectrum for SrMnO₃ as compared with Li₂MnO₃ can not be found in covalency effects, because strontium is more covalent than lithium, which in principle will decrease the covalency of the bonds between oxygen and manganese. Thus covalency effects (such as the mixing of 3*d*⁴*L*-character) are expected to be smaller for SrMnO₃. Possibly a reason for the extra broadening can be found in distortions from the octahedral surrounding of the

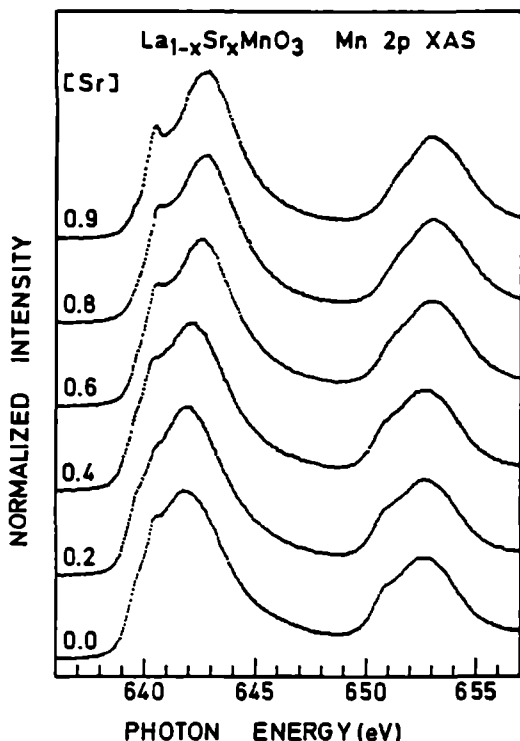


Figure 4.24: The $2p$ x-ray absorption spectra of the $\text{La}_{1-x}\text{Sr}_x\text{MnO}_3$ -system.

manganese atoms in the perovskites, which are known to be subject to large site distortions. An additional, closely related, reason are the relatively large vibrational effects.

LaMnO_3 has a high-spin (5E) ground state. It is semiconducting and at room temperature it shows a clear Jahn-Teller distortion [50]. Its manganese $2p$ x-ray absorption spectrum shows a correspondence to the spectrum of LiMnO_2 (see section 4.3), but similarly to SrMnO_3 it is considerably broader. LiMnO_2 was found to have a ground state which is formed from an admixture of both the high-spin and low-spin configuration, due to the effects of $3d$ spin-orbit coupling. Probably LaMnO_3 is still on the high-spin side, but due to the $3d$ spin-orbit coupling the ground state will be dominated by a state with a total symmetry of A_1 (check with figure 4.17). Due the larger broadening the amount of structure is not enough to perform a detailed simulation in which the effects of the $3d$ spin-orbit coupling and the Jahn-Teller effect are varied. Also the effects due to the admixture of $3d^5L$ -character can not be tested. Thus it can only be concluded that the spectral shape resembles a $3d^4$ ground state with 5E -symmetry (with the possible admixture of some low-spin character due to $3d$ spin-orbit coupling).

The spectral variations in the $\text{La}_{1-x}\text{Sr}_x\text{MnO}_3$ series agree with the superposition of the spectra of LaMnO_3 and SrMnO_3 . The fact SrMnO_3 is insulating and becomes metallic upon doping with lanthanum will not alter the description of the manganese $2p$ edges as the time

scale of the valence fluctuations (creating the metallic state) is too long to affect the x-ray absorption process.

The iron 2p edges of $\text{La}_{1-x}\text{Sr}_x\text{FeO}_3$

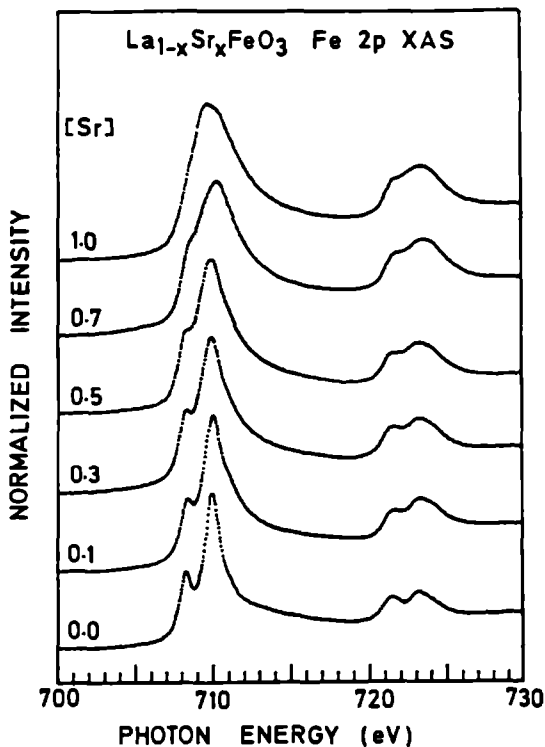


Figure 4.25: The 2p x-ray absorption spectra of the $\text{La}_{1-x}\text{Sr}_x\text{FeO}_3$ -system.

Figure 4.25 shows the iron 2p x-ray absorption spectra of the $\text{La}_{1-x}\text{Sr}_x\text{FeO}_3$ -perovskites. LaFeO_3 is a high-spin insulator, in which the Fe^{III} has a $3d^5$ -configuration with 6A_1 -symmetry. The spectral shape is in close agreement with the $3d^5 [{}^6A_1] \rightarrow 2p^5 3d^6$ transition which has been given in figure 4.26.

SrFeO_3 is metallic and contains Fe^{IV} ions, which have a $3d^4$ -configuration. The magnetic data on SrFeO_3 is contradictory: The magnetic moment found for stoichiometric SrFeO_3 is $2.7 \mu_B$ at 77 K, but is reduced to $1.6 \mu_B$ for $\text{SrFeO}_{2.9}$ [54]; in contrast in Ref. 55 a magnetic moment of $3.7 \mu_B$ has been found, which is close to the high-spin value of $4 \mu_B$. This suggests that the Fe^{IV} ion has a high-spin 5E -symmetry, but strangely enough no Jahn-Teller distortion is found [52].

In the ZSA-model the ground state of Fe^{IV} is expected to be dominated by $3d^5 \underline{L}$ -character, similar to Cu^{III} and Ni^{III} states, because for Fe^{III} $U \gg \Delta$. Thus LaFeO_3 (and also for example Fe_2O_3) is a pure charge transfer insulator, and if this trivalent iron-oxide is

doped with holes, a state dominated by ligand hole character will be formed, similar to the cases of divalent nickel and copper. If the ground state is dominated by $3d^5\bar{L}$ -character, the $2p$ x-ray absorption spectrum will resemble a combination of the $3d^5[\Gamma_1] \rightarrow 2p^53d^6$ multiplets instead of the $3d^4[{}^5E] \rightarrow 2p^53d^5$ multiplet. The symmetry of the $3d^5$

The difference with a normal $3d^5$ ground state is that for a $3d^5\bar{L}$ -state the symmetry is not confined to the single ground state configuration, but will be build from a linear combination of specific symmetries. In case of $3d^5$ there are three symmetries which can be important: the high-spin $(t_{2g}^+)^3(e_g^+)^2 [{}^6A_1]$ -state, the low-spin $(t_{2g}^+)^3(t_{2g}^-)^2 [{}^2T_2]$ -state and the intermediate spin $(t_{2g}^+)^3(t_g^-)^1(e_g^+)[{}^4T_1]$ -state. With the addition ligand hole of a t_{2g} or an e_g symmetry, these symmetries, combined with $3d^4$ -configuration(s), form the overall ground state. Assuming the symmetry of the overall ground state to be 5E , in accord with the magnetic moment of about $4 \mu_B$, the $3d^5\bar{L}$ states which can contribute must have either 6A_1 or 4T_1 symmetry. The low-spin state of 2T_2 -symmetry does not couple.

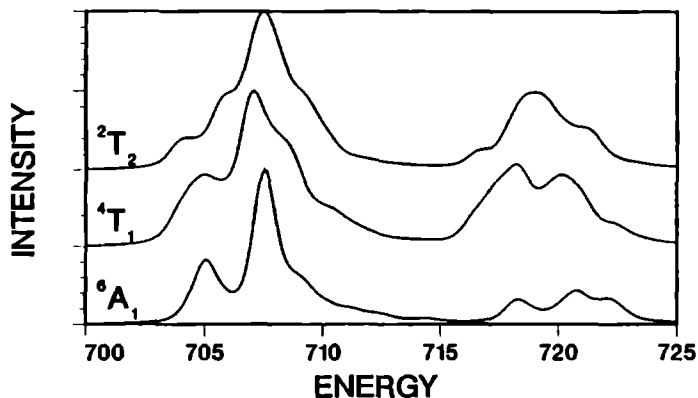


Figure 4.26: The $3d^5 \rightarrow 2p^53d^6$ spectral shapes for, from top to bottom the $(t_{2g}^+)^3(t_{2g}^-)^2 [{}^2T_2]$ -state, the $(t_{2g}^+)^3(t_g^-)^1(e_g^+)[{}^4T_1]$ -state and the $(t_{2g}^+)^3(e_g^+)^2 [{}^6A_1]$ -state.

Figure 4.26 gives the calculated spectral shapes of the respective symmetries of the $3d^5$ -configuration. The spectral shape of $SrFeO_3$ is difficult to simulate exactly, but from the comparison with the theoretical curves in figure 4.26 it is concluded that the spectrum is dominated by $3d^5\bar{L}$ -configurations build from 4T_1 and 6A_1 $3d^5$ -like states.

In conclusion it can be stated that the ground state of $SrFeO_3$ is dominated by $3d^5\bar{L}$ -character of partial symmetries 6A_1 and 4T_1 . Both symmetries can couple to the $3d^4$ -configuration of 5E -symmetry. This assignment can explain the spectral shape of the $2p$ x-ray absorption spectrum, and it is also in full accord with the predictions from the ZSA-model as well as with the magnetization measurements. Because the admixture of 6A_1 -symmetry and 4T_1 -symmetry states is not necessarily equal, the magnetic moment can (slightly) differ from 4.

In the $\text{La}_{1-x}\text{Sr}_x\text{FeO}_3$ -series a transition is made from a $3d^5$ -state with 6A_1 -symmetry for LaFeO_3 to a $3d^5\bar{L} + 3d^4$ state with 5E -symmetry for SrFeO_3 . Starting from LaFeO_3 the doping with strontium will create $3d^5\bar{L}$ -like Fe^{IV} impurities, which can couple strongly to the Fe^{III} configurations. From Mössbauer spectroscopy it can be concluded that the electron transfer is fast enough to produce an average isomer shift [52, 56]. The x-ray absorption process will however still be of a shorter timescale and consequently the trend in the spectra can again be explained as a linear combination of the spectra of LaFeO_3 and SrFeO_3 . This is shown in detail in figure 4.27 which compares the spectrum of $\text{La}_{0.5}\text{Sr}_{0.5}\text{FeO}_3$ with a one-to-one addition of the spectra of LaFeO_3 and SrFeO_3 .

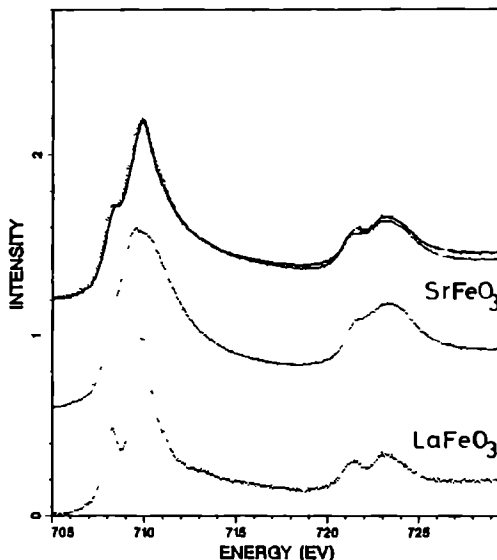


Figure 4.27: Top spectrum: One-to-one addition of the experimental spectra of LaFeO_3 and SrFeO_3 (solid line), compared with the spectrum for $\text{La}_{0.5}\text{Sr}_{0.5}\text{FeO}_3$ (dotted). For comparison the spectra of the pure LaFeO_3 and SrFeO_3 samples are also given.

The cobalt 2p edges of $\text{La}_{1-x}\text{Sr}_x\text{CoO}_3$

Figure 4.28 shows the 2p x-ray absorption spectra of the $\text{La}_{1-x}\text{Sr}_x\text{CoO}_3$ -perovskites. It is known that LaCoO_3 is at room temperature a low-spin insulator ($3d^6[{}^1A_1]$ -state), with the existence of some disordered high-spin impurities [50]. The 2p x-ray absorption spectral shape clearly shows correspondence to the $3d^6[{}^1A_1] \rightarrow 2p^53d^7$ transition. In section 4.3 this crystal field multiplet spectrum has been given in comparison with the cobalt 2p x-ray absorption spectrum of LiCoO_2 (figure 4.13).

Figure 4.29 shows the correspondence to a $3d^5[{}^2T_2] \rightarrow 2p^53d^6$ crystal field multiplet calculation. The Slater integrals are reduced to 75% for the $3d3d$ -interactions and to 88% for the $2p3d$ -interactions. The overall shape of the SrCoO_3 spectrum is reproduced, though there are some discrepancies left. A significant difference is the high-energy shoulder which is not reproduced correctly. Possibly the Slater integrals are not reduced correctly, but a more probable explanation is that for SrCoO_3 the admixture of $3d^6\bar{L}$ -character is considerable. The high-energy shoulder would then relate to a 'charge transfer satellite', due to the antibonding combination of the $2p^53d^6$ and $2p^53d^7\bar{L}$ final states. It is concluded that SrCoO_3 is

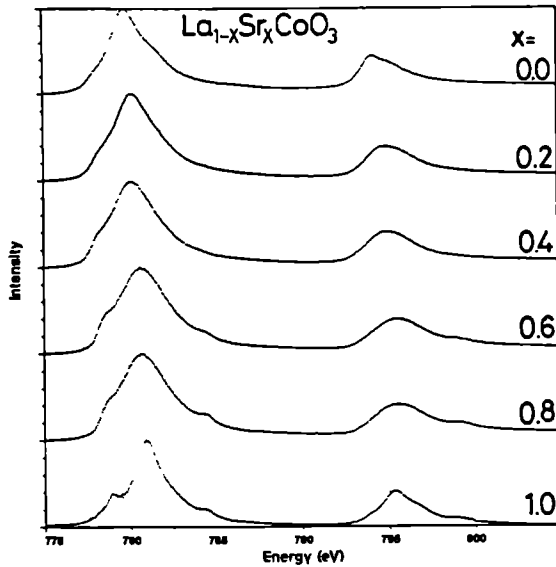


Figure 4.28: The 2p x-ray absorption spectra of the $\text{La}_{1-x}\text{Sr}_x\text{CoO}_3$ -system.

dominated by a low-spin $3d^5$ -configuration (with considerable admixture of $3d^6\bar{L}$ -character). Notice that the existence of a low-spin configurations means that the cubic crystal field, in other words the covalency, is strong enough to overcome the exchange energy of the five aligned spins of the high-spin configuration. The variations with x in $\text{La}_{1-x}\text{Sr}_x\text{CoO}_3$ do not show any deviation from the linear interpolation scheme, as explained for the other perovskite systems.

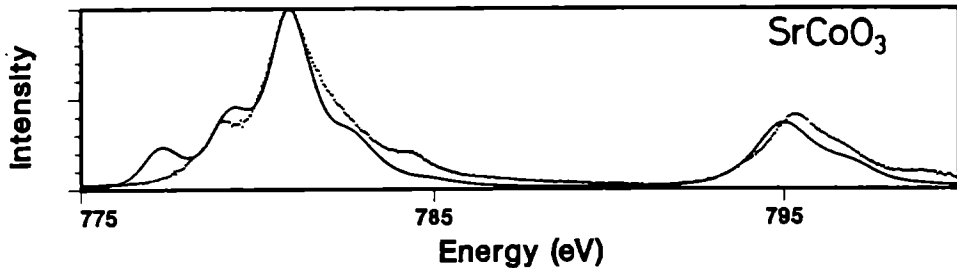


Figure 4.29: Comparison of the 2p x-ray absorption spectrum of SrCoO_3 (dotted) with a crystal field multiplet calculation for a $3d^5 [^2T_2]$ ground state (solid line).

4.4.2. The oxygen 1s x-ray absorption spectra

In this section the oxygen 1s x-ray absorption spectra are analysed. The analysis consists of a comparison with density functional calculations of the N-particle density of states with the purpose to reveal the major changes in the density of states as a result of the interchange

of lanthanum for strontium. A second purpose of the density of states calculations is the possibility to isolate the metal $3d$ -part of the spectrum. This metal $3d$ -part might be subject to $3d$ -correlation effects which modify the spectral shape.

The oxygen $1s$ edges of $\text{La}_{1-x}\text{Sr}_x\text{TiO}_3$

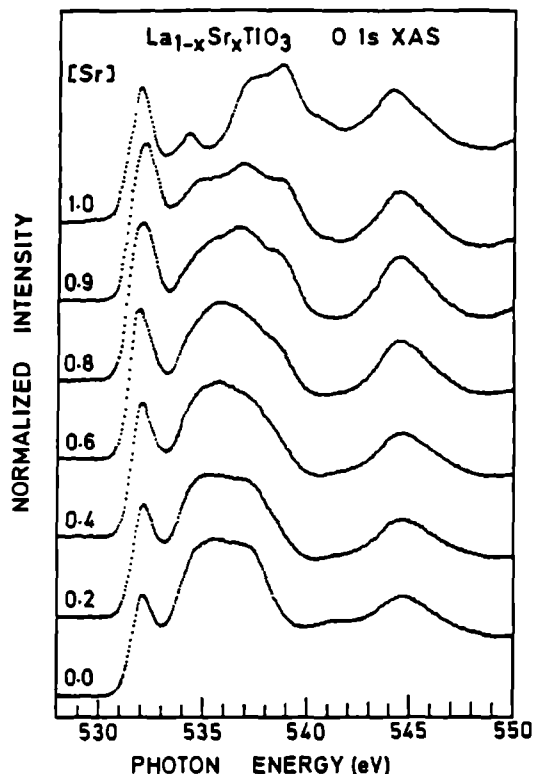


Figure 4.30: The oxygen $1s$ x-ray absorption spectra of the $\text{La}_{1-x}\text{Sr}_x\text{TiO}_3$ -system.

Figure 4.30 shows the $1s$ x-ray absorption spectra of the $\text{La}_{1-x}\text{Sr}_x\text{TiO}_3$ -perovskites. They are compared with the density functional calculations with the localized spherical wave (LSW) method. In section 3.8 the LSW-calculation of SrTiO_3 has been discussed in detail. A similar calculation for LaTiO_3 has been performed in a cubic perovskite crystal structure (O_h^1) with a lattice parameter $a = 3.92 \text{ \AA}$ [57]. The calculation is completely equivalent to that of SrTiO_3 with the exchange of lanthanum for strontium. The lanthanum $4f$ states are not included in the Hamiltonian (they are included in the expansion) to avoid problems with this narrow band.

Figure 4.32 shows the total density of states and the density of states projected to the lanthanum, titanium and oxygen sites for LaTiO_3 which is found to be a metal. The energy zero refers to the Fermi level. Compared to the LSW-result of SrTiO_3 , for clarity reproduced in figure 4.31, the oxygen $2p$ band and the titanium t_{2g} band are shifted to lower energy

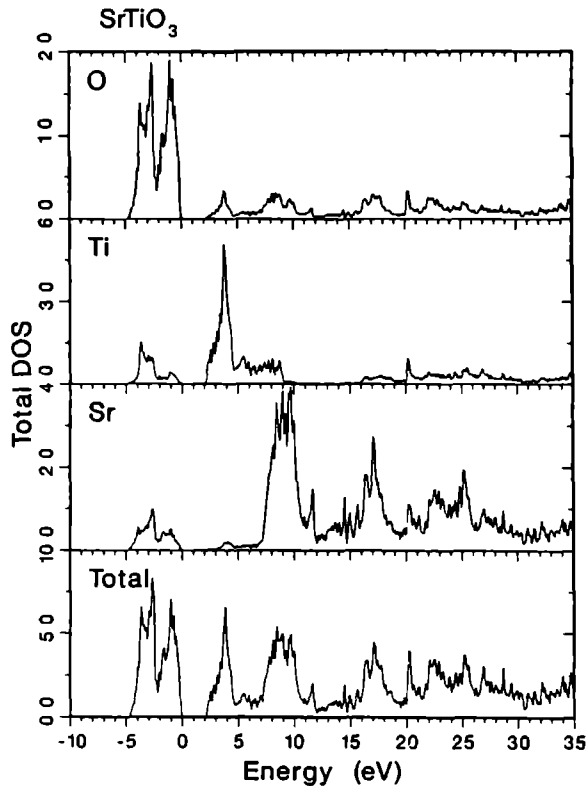


Figure 4.31 SrTiO_3 density of states. The total density of states (bottom) is split in the partial strontium, titanium and oxygen density of states.

due to the extra valence electron. An important effect of the exchange of strontium for lanthanum is that the lanthanum $5d$ is placed much closer to the Fermi level (between 2 and 4 eV) and in fact it completely overlaps with the titanium e_g -band.

Figure 4.33 and figure 4.34 show the comparison with the oxygen p projected density of states. The calculated oxygen p -projected density of states of SrTiO_3 is aligned at the first sharp peak which relates to the titanium t_{2g} -band. The structure between about 7 and 10 eV in the oxygen p -projected density of states relates to the strontium $4d$ -band and the shoulder at about 12 eV to the strontium $6s$ -band. These structures are in the experimental spectrum found at slightly higher energy. The structures in the density of states at about 17 eV and between 21 and 25 eV relate to the $4s$ and $4p$ -band of titanium and in the experimental spectrum these structures are found at slightly lower energy. The sharp peak in the experimental spectrum at about 6 eV is related to the e_g band. In the calculation only a weak shoulder is visible but as discussed in section 3.8 the sharp peak is a consequence of the oxygen $1s$ core hole which is neglected in the present calculations. In case of LaTiO_3 the major differences with SrTiO_3 are that the lanthanum $5d$ -band is positioned closer to the $3d$ -band and in fact it overlaps with the e_g peak which as a consequence is blurred in this

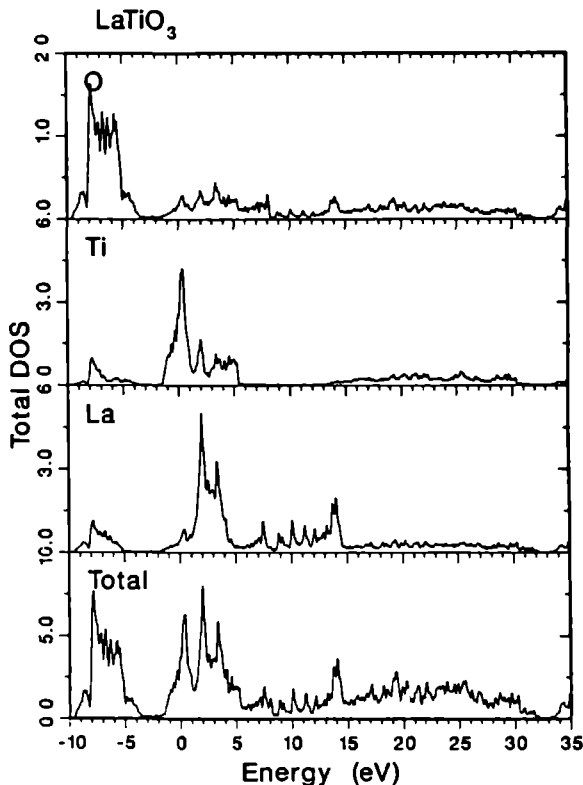


Figure 4.32: LaTiO_3 density of states. The total density of states (bottom) is split in the partial lanthanum, titanium and oxygen density of states.

structure. The first peak in the spectrum again relates to oxygen $2p$ -character hybridized in the titanium $3d$ -band of t_{2g} -character (the spectra again are aligned at this peak). As LaTiO_3 is calculated as a metal the theoretical spectrum is cut at the Fermi level which is placed at zero. Notice that for SrTiO_3 the zero is placed at the top of the valence band and the absolute energy scales do not have an identical meaning in the two figures. The peak at about 14 eV is the titanium $4sp$ -band. In both oxides the strontium (lanthanum) structures are found at slightly higher energies in the experiment and the titanium $4sp$ -band is found at slightly lower energies. It can be concluded that on overall the main features are reproduced in the calculation, but the precise spectral shapes do not match exactly. Important causes for the observed discrepancies are the neglect of the core hole (in section 3.8 it was shown that the inclusion of the core hole potential enhances the agreement considerably) and the incomplete treatment of the electron correlations.

With use of these comparisons with the densities of states the main features in the series of oxides as given in figure 4.30 can be identified. The first sharp peak related to the titanium t_{2g} -band is positioned at a (close to) constant energy of 532.5 eV. It is seen that already with 10% lanthanum ($x=0.9$) the intensity at about 535 eV rises and at 20% the e_g -

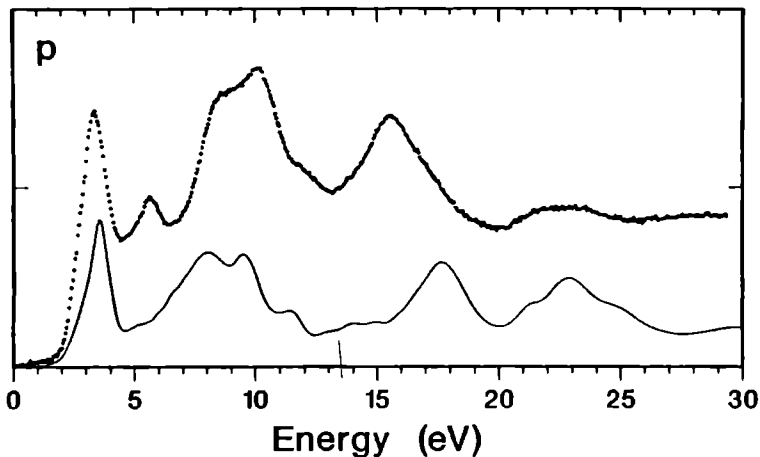
Oxygen k edge of SrTiO_3 

Figure 4.33: The comparison of the N-particle oxygen p projected density of states with the oxygen $1s$ x-ray absorption spectrum for SrTiO_3 .

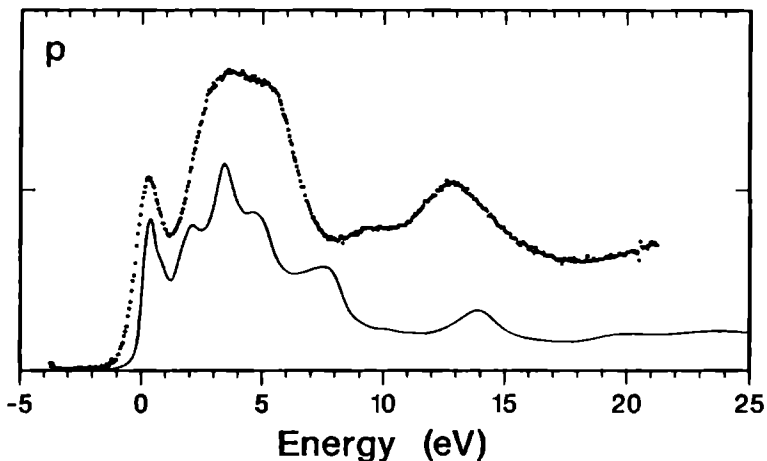
Oxygen k edge of LaTiO_3 

Figure 4.34: The comparison of the N-particle oxygen p projected density of states with the oxygen $1s$ x-ray absorption spectrum for LaTiO_3 .

peak, which is observed for SrTiO_3 is obscured by the oxygen p -states which are hybridized with the lanthanum $5d$ -band. This lanthanum $5d$ band gains intensity while the strontium $4d$ -band loses intensity in going from the top to the bottom. The peak at about 545 eV relates to the titanium $4sp$ -band and its energy position is close to constant. It should be noted that for the LaTiO_3 -sample an impurity phase related to ($\approx 10\%$) unreacted TiO_2

has been detected by x-ray diffraction.

The oxygen 1s edges of $\text{La}_{1-x}\text{Sr}_x\text{MnO}_3$

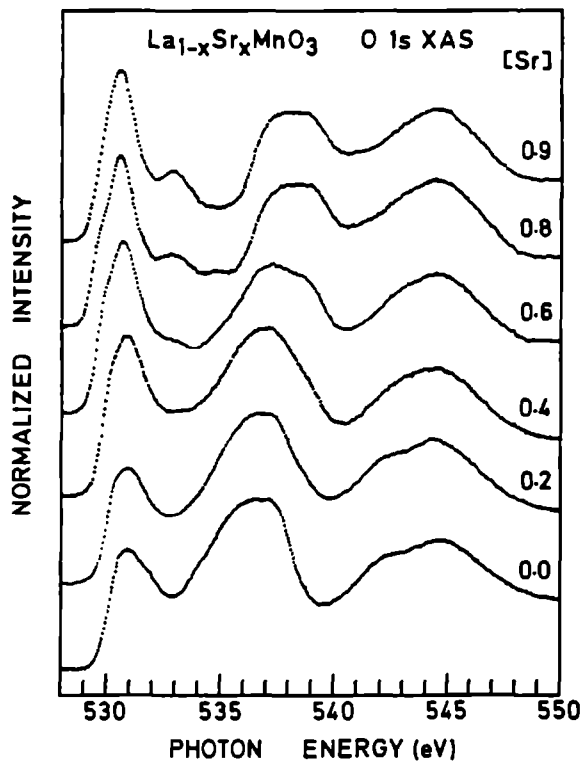


Figure 4.35: The oxygen 1s x-ray absorption spectra of the $\text{La}_{1-x}\text{Sr}_x\text{MnO}_3$ -system.

Figure 4.35 shows the 1s x-ray absorption spectra of the $\text{La}_{1-x}\text{Sr}_x\text{MnO}_3$ -perovskites. The SrMnO_3 spectrum (with 10% La) shows a spectrum which is in some aspects similar to SrTiO_3 . The oxygen p -character of the strontium $4d$ -band is positioned in between about 537 and 539 eV. The $3d$ -band region relates to the empty states of Mn^{IV} . Only the t_{2g}^+ -subband is filled and there are 3 empty subbands. As discussed in section 3.5 the e_g^+ - and the t_{2g}^- -bands will be close to degenerate and the first peak is assigned to these two bands. The second smaller peak relates to the e_g^- band. It is noticed that the $3d$ -band of the spectrum is similar to that of other tetravalent manganese oxides such as MnO_2 (section 4.2) and Li_2MnO_3 (section 4.3). Effects from dd -correlations can modify the detailed spectral shape of the $3d$ -band region, but as yet no calculations are available to check this in detail.

In LaMnO_3 the lanthanum $5d$ -band again is positioned closer to the $3d$ -band. The $3d$ -band of LaMnO_3 has a high-spin $3d^4$ configuration, but from the analysis of the metal $2p$ edge it has been concluded that the compound will have close to degenerate high-spin and low-spin configurations, with some admixture due to $3d$ spin-orbit coupling. Therefore

the first peak is assigned to the remaining e_g^+ -band overlapping with the t_{2g}^- band. From the analogy with the oxygen 1s spectrum of LiMnO_2 (also Mn^{IV}), it is expected that there exists a second broad peak (or shoulder) at about 533 eV, though in the case of LaMnO_3 this peak is obscured by the lanthanum 5d-band.

The overall intensity of to the 3d-band is considerably larger for SrMnO_3 than for LaMnO_3 . This is caused by an increased covalency of the tetravalent manganese ions in SrMnO_3 . This covalency effect can be described as the mixing of $3d^{N+1}\underline{L}$ -character in the $3d^N$ ground state. According to the trends in the 3d-series in the ZSA-model, a $3d^3$ -configuration (like SrMnO_3) should have a considerably larger charge transfer energy than a $3d^4$ -configuration (LaMnO_3). (The hopping will be similar of magnitude as the lattice constants are close to equal). This indicates that within the ZSA-model the mixing of $3d^{N+1}\underline{L}$ -character is expected to be larger in case of LaMnO_3 , in conflict with experiment. The most probable solution to this discrepancy is to assume that the amount of admixture of $3d^{N+1}\underline{L}$ -character does not agree exactly with the amount of covalency. As has been discussed in section 4.1, a $3d^N$ -configuration does not necessarily relate to atomic states of projected 3d-character. The direct consequence is that in principle there can be direct transitions from the oxygen 1s core state to metal 3d-states and these transitions can explain the extra intensity of the compounds with a higher valency like SrMnO_3 .

The oxygen 1s edges of $\text{La}_{1-x}\text{Sr}_x\text{FeO}_3$

Figure 4.36 shows the 1s x-ray absorption spectra of the $\text{La}_{1-x}\text{Sr}_x\text{FeO}_3$ -perovskites. In the oxygen 1s spectrum of LaFeO_3 the 3d-band shows a sharp two-peaked structure. Because the iron atom is in a high spin 6A_1 configuration, all spin-up states are filled and all spin-down states are empty. Assuming the one-electron addition states to dominate, the two sharp peaks relate to the spin-down t_{2g} and spin-down e_g states, and consequently the splitting relates to the cubic crystal field splitting (with a small correction due to slightly different exchange effects for t_{2g} respectively e_g electrons as discussed in chapter 3). It should be noticed that the 3d-part of the LaFeO_3 spectrum is similar to that of Fe_2O_3 (section 4.2) and also MnO (section 4.3), which both also have a 6A_1 ground state.

The SrFeO_3 spectrum shows an intense two-peaked structure in the 3d-part, at considerably lower energy than the two LaFeO_3 -peaks. Because the ground state is dominated by $3d^5\underline{L}$ with some $3d^4$ admixture, the shape of the one-electron addition spectra is difficult to predict. In principle the first peak will be related mostly to the oxygen p character of the t_{2g}^- -band (but partly of the e_g^+ -band) the second peak relates to the e_g^- band. In the crystal field multiplet model the final state, a transition is made from $3d^5\underline{L} \rightarrow 3d^5$ for both the 6A_1 and the 4T_1 symmetry.

If LaFeO_3 is doped with only 10% strontium the SrFeO_3 -related peaks appear in the gap, which is in complete analogy to NiO doped with lithium [19]. The only difference is that for LaFeO_3 both the original as well as the impurity states are split by the cubic crystal field. Thus the oxygen 1s x-ray absorption spectra confirm that LaFeO_3 is indeed a pure charge transfer insulator and if doped with holes, the holes will go mainly to the oxygen sites. With increasing x in the $\text{La}_{1-x}\text{Sr}_x\text{FeO}_3$ -system the 'impurity states', related

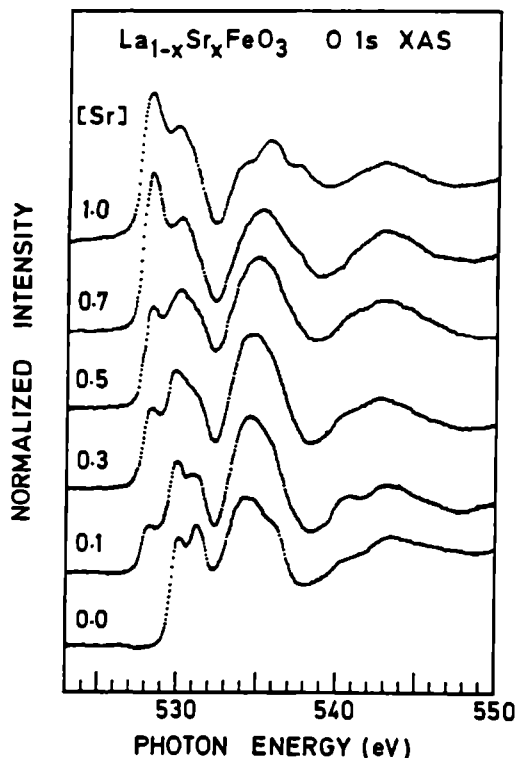


Figure 4.36: The $1s$ x-ray absorption spectra of the $\text{La}_{1-x}\text{Sr}_x\text{FeO}_3$ -system.

to LaFeO_3 gain intensity and start to dominate the spectral shape.

4.4.3. Conclusions

Most structures in the metal $2p$ x-ray absorption spectra can be explained with the crystal field multiplet model. From this analysis the dominating configuration as well as its (dominating) symmetry can be determined. Table 4.5 gives these configurations and symmetries for the end-members of the measured perovskites. The symmetries found are in agreement with the available experiments of the magnetic structure [50, 52].

The SrFeO_3 ground state is found to be dominated by $3d^5 \underline{L}$ -character, which places it in the class of oxides (with for example LiNiO_2 [19] and NaCuO_2 [58]) which are dominated by a ligand hole ground state. These compounds, if placed in the Zaanen-Sawatzky-Allen (ZSA) diagram [1], are described with a negative charge transfer (negative Δ). If the absolute value of this negative Δ is larger than the bandwidth an insulator is formed, as is the case for LiNiO_2 and NaCuO_2 . The metallic behaviour of SrFeO_3 indicates that ($|\Delta|$) is smaller than the bandwidth. Thus the oxides with Ni^{II} , Cu^{II} and Fe^{III} ions are pure charge transfer insulators with a large value for U and a considerably smaller value for Δ . The charge transfer insulators are characterized by a relatively large bandgap due to a closed

compound	main configuration	main symmetry
SrTiO_3	$3d^0$	1A_1
LaTiO_3	$3d^1$	2T_2
SrMnO_3	$3d^3$	4A_2
LaMnO_3	$3d^4$	${}^5E^*$
SrFeO_3	$3d^5\bar{L}$	${}^5E^{**}$
LaFeO_3	$3d^5$	6A_1
SrCoO_3	$3d^5$	2T_2
LaCoO_3	$3d^6$	1A_1

Table 4.5: Symmetries of the parent compounds as found from metal $2p$ x-ray absorption. Specifically SrCoO_3 shows signs of a considerable admixture of $3d^{N+1}\bar{L}$ -character. *: Due to effects of $3d$ spin-orbit coupling there will be some admixture of 3T_1 -character. **: The approximate overall symmetry is given. The dominating symmetries are the contributing $3d^5\bar{L}$ -configurations with partial 6A_1 and 4T_1 symmetry.

subshell system and/or large correlation effects. If mixed valence systems are studied, for example $\text{La}_{1-x}\text{Sr}_x\text{FeO}_3$ or $\text{Li}_x\text{Ni}_{1-x}\text{O}$, the states related to the valency with the negative charge transfer (Ni^{III} ; Fe^{IV}) are placed in the bandgap of the charge transfer insulators.

In contrast to SrFeO_3 , LaMnO_3 is not dominated by $3d^5\bar{L}$ -character, but instead it has clear $3d^4$ -behaviour including the Jahn-Teller distortion. Though there will be considerable admixture of $3d^5\bar{L}$ -character, the ground state is dominated by $3d^4$ -character. This can be related to the fact that Mn^{II} forms in contrast to the iso-electronic Fe^{III} ion not pure charge transfer insulating oxides, because not only U but also Δ is large (as discussed in section 4.1 U increases whereas Δ decreases with increasing valency).

Acknowledgements

The x-ray absorption measurements were performed in close collaboration with Miguel Abate, with assistance of Leonardo Soriano, Francesca Lopez and Oliver Streb. The LSW band structure calculations of SrTiO_3 and LaTiO_3 were performed with the assistance of Marek Czyżyk. We would like to thank A. Fujimori, M. Takano, Y. Takeda, H. Eisaki, S. Uchida, Y. Fujishima and Y. Tokura for providing the samples.

4.5. Vanadium 2p and oxygen 1s x-ray absorption of vanadium oxides

In this section the vanadium 2p and oxygen 1s x-ray absorption spectra of vanadium oxides are discussed. Section 4.5.1. deals with the binary vanadium oxides V_2O_3 , VO_2 and V_2O_5 . In section 4.5.2. the results on the spinel system $Zn_{1-z}Li_zV_2O_4$ are discussed and section 4.5.3. focuses on the electronic phase transition in VO_2 .

Vanadium oxides attract much attention due to their complicated electronic and structural phase transitions, occurring in for example $V_2O_3(+Cr)$, VO_2 and $LiVO_2$ [50, 59, 60]. The main reason for the complicated electronic and structural behaviour is that for the $3d^1$ and $3d^2$ configurations the $3d$ electrons are correlated, but as compared with the late transition-metal oxides this correlation is less strong: In the late transition metal oxides, like for instance NiO the correlation effects are so strong that they completely dominate the electronic behaviour.

The $3d^0$ compounds (TiO_2 or V_2O_5) are insulators with a band gap which is positioned in between the filled oxygen 2p band and the empty $3d$ band. The $3d^3$ compounds have a filled t_{2g}^+ band, which also will tend to give an insulating state as in Cr_2O_3 and $SrMnO_3$. If the number of $3d$ electrons is 4 or more, correlation effects will become more dominant as is clear from the examples given in the foregoing sections. The $3d^1$ (Ti^{III} , V^{IV}) and $3d^2$ (V^{III} , Cr^{IV}) configurations have a partly filled t_{2g}^+ -band. The electrons in this band behave in a less correlated manner as they are more extended in character. The consequences are a large metal-metal interaction. VO_2 forms dimers below 350 Kelvin and $LiVO_2$ forms trimers; also other vanadium oxides tend to form metal-metal bonds. The effects of metal-metal interactions will drive the crystal-structure to distort and complicated temperature dependent structural changes can occur.

The driving force for the metal-metal bonding effects is the stabilization of the partly filled t_{2g}^+ band by for example a dimerization, with the corresponding crystallographic distortion. The main difference between the $3d^1$ and the $3d^2$ configurations is the larger effective exchange splitting (\mathcal{K}) for the latter. The effective exchange splitting is about twice as large for $3d^2$ and whereas a $3d^1$ system like VO_2 can distort by the formation of singlet vanadium dimers, $3d^2$ systems will only split the t_{2g}^+ band by a lattice distortion. A similar splitting will occur for the t_{2g}^- band but this band has a higher energy due to the effective exchange splitting. Given these relatively strong metal-metal interactions, the vanadium 2p x-ray absorption spectra will appear difficult to describe with the crystal field multiplet model. The local geometry of the vanadium atoms will relate to low-symmetry point groups with large distortions from a pure octahedral surrounding and furthermore the multiplet structure will be blurred. With this in mind the x-ray absorption spectra of some vanadium oxides are analysed in the following sections.

4.5.1. The binary vanadium oxides

The ground state configurations of the binary vanadium oxides are respectively $3d^0[1A_1]$ for V_2O_5 , $3d^1[2T_2]$ for VO_2 and $3d^2[3T_1]$ for V_2O_3 . Their vanadium 2p and oxygen 1s x-ray

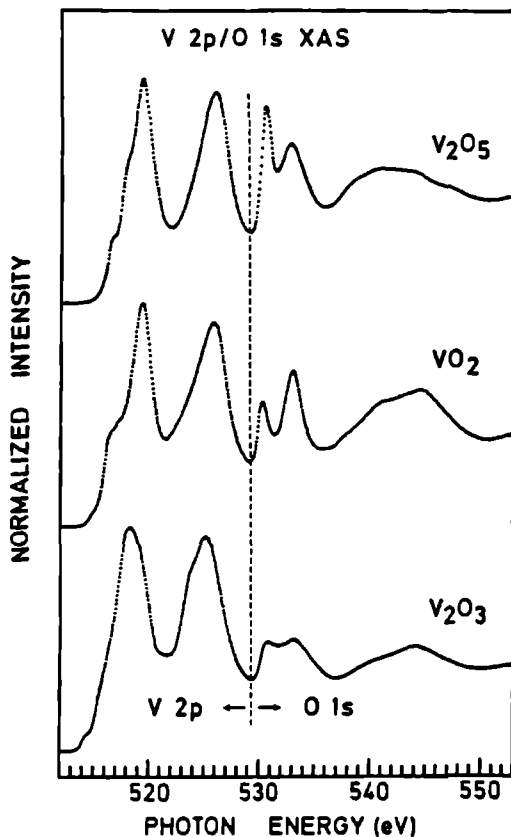


Figure 4.37: The overlapping vanadium 2*p* and oxygen 1*s* x-ray absorption spectra of the binary vanadium oxides.

absorption spectra have been measured at the DRAGON monochromator [30] at the National Synchrotron Light Source at Brookhaven National Laboratory. The monochromator resolution was better than 100 meV at 500 eV photon energy. The binary vanadium oxides were obtained from A. Fujimori; more information concerning their preparation are given in Ref. 61. A complicating factor is that the core level binding energies of a vanadium 2*p* state and an oxygen 1*s* state are almost equal. Figure 4.37 gives the spectral shape in the energy region between 510 and 550 eV. In between the vanadium 2*p* part and an oxygen 1*s* part a rather artificial borderline is drawn. Although the vanadium 2*p* edges and the oxygen 1*s* edges partly overlap, they still can be analysed. The vanadium edge will not show any effect of oxygen until about 527 eV. Because the metal 2*p* edges are known to have little structure behind the strong transitions to the 3*d*-band, also the oxygen spectra are only slightly distorted.

Figure 4.38 shows the vanadium 2*p* x-ray region of the absorption spectra of V₂O₃, VO₂ and V₂O₅. The V₂O₃ spectrum can be explained from a 3*d*² [³T₁] → 2*p*⁵3*d*³ crystal field multiplet calculation as given in section 3.4. The experimental spectrum is broad which complicates a detailed analysis. However the small 'pre-edge' structure and the bump in

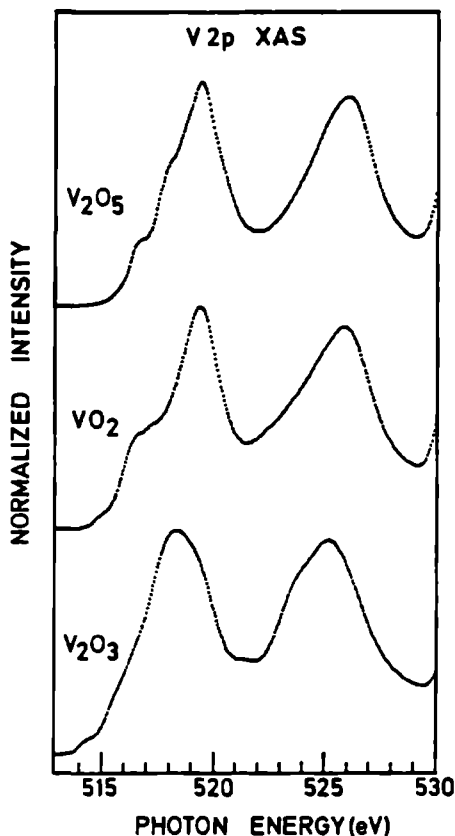


Figure 4.38: The vanadium $2p$ x-ray absorption spectra of the binary vanadium oxides.

between the L_3 and L_2 edge are a clear indication of a $3d^2[{}^3T_1]$ ground state. The broadness of the structure is related to the lattice distortion. The VO_2 spectrum is given for the cubic high temperature phase (the effects of the phase transition are given in section 4.5.3). The correspondence to the crystal field multiplet calculation for the $3d^1[{}^2T_2]$ -state is not good and to optimize the calculations possibly the Slater integrals have to be decreased. The spectrum of VO_2 is also broad, which is due to large vibrational effects and the existence of quite strong lattice distortions. Because of the broadness of the spectrum it is not easy to optimize the crystal field multiplet calculation. The shape of the V_2O_5 spectrum does not show well resolved peaks, in contrast to other $3d^0$ oxides such as Sc_2O_3 and TiO_2 . The most probable explanation is that the complicated surrounding of the vanadium ions in V_2O_5 complicates the crystal field multiplet spectrum, whereas the large vibrational effects obscure a detailed structure. It can be concluded that the spectral shapes of the vanadium oxides are broad, due to the relatively large distortions from octahedral surroundings and large vibrational effects, which complicates their analysis.

Figure 4.39 gives the oxygen $1s$ x-ray absorption spectra of V_2O_3 , VO_2 and V_2O_5 . As discussed in section 4.2 the spectra contain a double peak related to the $3d$ -band and at

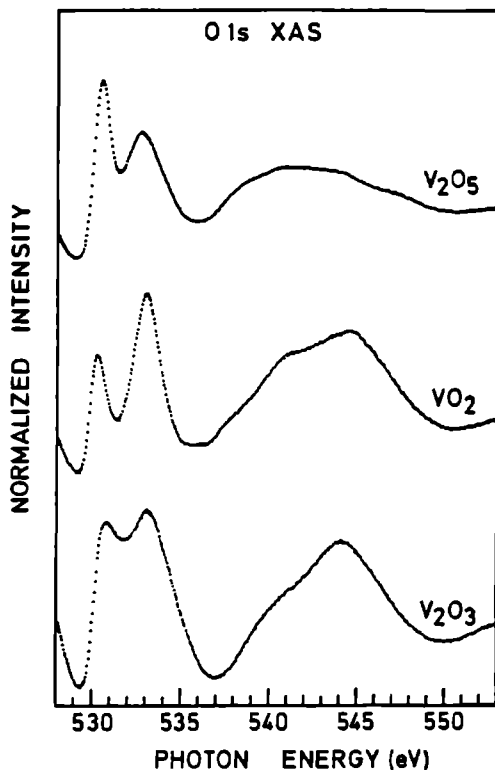


Figure 4.39: The oxygen $1s$ x-ray absorption spectra of the binary vanadium oxides.

higher energy a structure related to the $4sp$ -band. Using a one-electron approach the double peak of the $3d$ -band is ascribed to respectively the t_{2g} and the e_g subband split by the cubic crystal field. V_2O_5 shows a sharp t_{2g} peak and a considerably broader e_g peak, in accord with the larger dispersion of the e_g states. For VO_2 an electron is present in the t_{2g}^+ band and this electron will cause an effective exchange splitting in both the t_{2g} and e_g band. The first peak relates again to t_{2g} -symmetry and the second peak to the e_g states. In principle both will be split by the exchange splitting of about 0.6 eV, but the dispersional (plus life-time) broadening will obscure this splitting. In V_2O_3 both the t_{2g} and the e_g band are split by an exchange splitting of the order of 1.2 eV and the t_{2g}^+ and t_{2g}^- sub-bands are split by the lattice distortions. Thus a whole series of slightly displaced bands are present. However in the oxygen $1s$ x-ray absorption spectrum these small splittings will not be visible and only the main cubic crystal field splitting of the order of 2.5 eV is seen. The fact that the crystal field split peaks are not as well resolved as for VO_2 is a further indication that the spectrum consists of a series of slightly displaced overlapping bands. A more detailed comparison with theory needs the calculation of the oxygen p projected density of states, preferably with the inclusion of the core hole. As discussed before the one-electron analysis is an approximation in its incorrect treatment of correlation effects, which affect specifically the $3d$ -part of the spectrum.

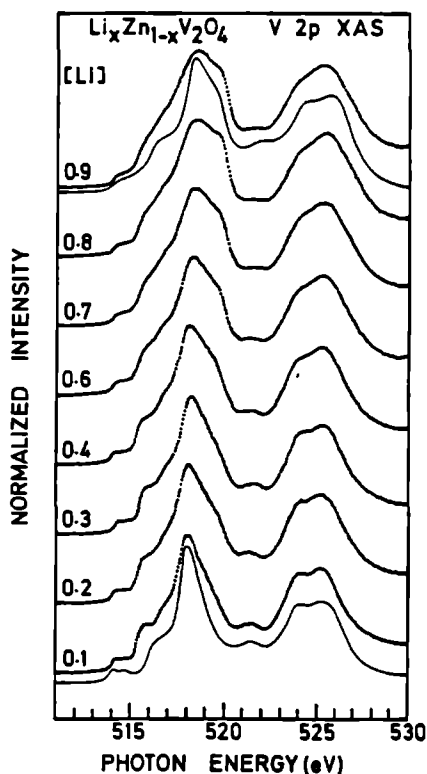
4.5.2. The $\text{Zn}_{1-x}\text{Li}_x\text{V}_2\text{O}_4$ spinel system

Figure 4.40: The vanadium 2p x-ray absorption spectra of the $\text{Zn}_{1-x}\text{Li}_x\text{V}_2\text{O}_4$ spinel system.

The $\text{Zn}_{1-x}\text{Li}_x\text{V}_2\text{O}_4$ oxides have been much studied [50, 62, 63]. ZnV_2O_4 is an insulator in which the trivalent vanadium ions of $3d^2$ [3T_1]-character occupy octahedral sites in the spinel structure. LiV_2O_4 is metallic and contains 50% trivalent and 50% tetravalent vanadium ions. The conductivity is caused by metal-metal hopping from the $3d^1$ to the $3d^2$ configuration. In the mixed $\text{Zn}_{1-x}\text{Li}_x\text{V}_2\text{O}_4$ system the replacement of lithium for zinc increases the amount of tetravalent vanadium, due to which an insulator to metal transition occurs at $x \approx 0.35$. As noticed by Goodenough et al. [60] this relates to a percolation threshold for the metallic pathway, associated with V^{III} - V^{IV} neighbours.

The x-ray absorption spectra were measured with the SX700 (II) monochromator [49] at the Berliner Elektronenspeicherring Gesellschaft für synchrotronstrahlung (BESSY). The monochromator resolution was about 0.1 eV (fwhm). The spectra were recorded in total electron yield mode and were corrected for intensity loss of the beam during measurement. The samples, sintered pellets, were scraped with a diamond file to ensure surface cleanliness.

Figure 4.40 shows the vanadium 2p x-ray absorption spectra of the mixed spinel system $\text{Zn}_{1-x}\text{Li}_x\text{V}_2\text{O}_4$. The bottom spectrum contains only 10% lithium, thus only 5% tetravalent

vanadium, and the spectrum is compared with a crystal field multiplet calculation of the $3d^2 [^3T_1] \rightarrow 2p^5 3d^3$ transition. From the good agreement it is concluded that the trivalent vanadium ions are indeed in a 3T_1 configuration. Because the x-ray absorption process has a smaller time scale than the electron hopping, the vanadium $2p$ x-ray absorption spectra can be described as an superposition of the trivalent and tetravalent vanadium spectra. Thus the spectrum of LiV_2O_4 (with 10% Zn) is simulated with a one-to-one addition of the multiplet structures for $3d^2 [^3T_1]$ and $3d^1 [^2T_2]$. The agreement with the experimental spectral is good. The series of spectra shown in figure 4.40 show a gradual change, in agreement with the linear interpolation scheme of the addition of the multiplet spectra of the two distinct valencies according to their occupancy.

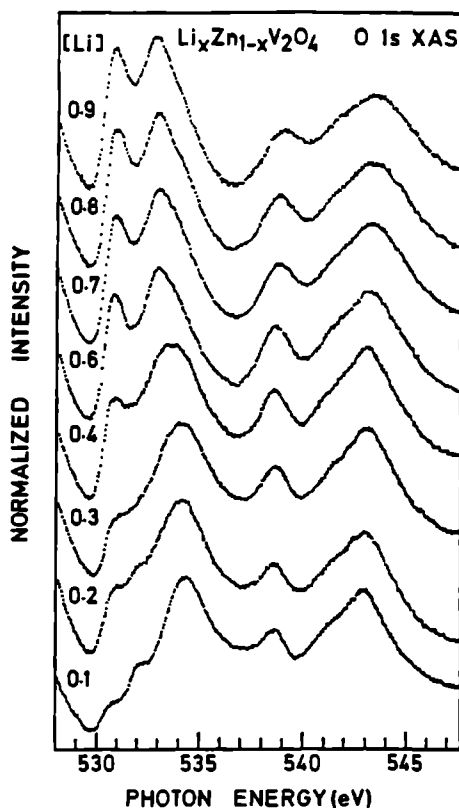


Figure 4.41: The oxygen $1s$ x-ray absorption spectra of the $\text{Zn}_{1-x}\text{Li}_x\text{V}_2\text{O}_4$ spinel system.

Figure 4.41 shows the oxygen $1s$ x-ray absorption spectra of the mixed spinel-system $\text{Zn}_{1-x}\text{Li}_x\text{V}_2\text{O}_4$. The $\text{Zn}_{0.9}\text{Li}_{0.1}\text{V}_2\text{O}_4$ shows a first structure at 535 eV with two shoulders on its low energy side, and at higher energy a sharp peak at about 539 eV and a peak at 543 eV. Following the assignments as discussed in the comparison with band structure calculations in section 4.4, the structures at 539 and 543 eV are assigned to oxygen p character hybridized with vanadium $4sp$ -bands. This structure is insensitive to the lithium concentration. The

structures at the edge are assigned to the $3d$ -band, but as in this case the oxides contain zinc, it is possible that the zinc $4s$ -band hybridizes strongly with the oxygen $2p$ states and generates a distinct peak relatively close to threshold. Because vanadium in ZnV_2O_4 is trivalent and surrounded octahedrally, the $3d$ -part of the spectrum is expected to resemble the spectrum of V_2O_3 as given in section 4.2. However the spectral shape is different and this supports the hypothesis that the main peak at 535 eV in fact relates to the zinc $4s$ -band. The shoulder at 532 eV is assigned to the t_{2g} peak of trivalent vanadium and there will be a second peak at about 534.5 eV, which is obscured by the zinc-peak. The small peak at about 530.5 eV is assigned to the tetravalent vanadium states due to the 10% lithium doping. Unfortunately pure ZnV_2O_4 has not been measured, but as this peak gains intensity for the sample with 20% lithium the assignment is justified.

The oxygen $1s$ x-ray absorption spectrum of $\text{Zn}_{0.1}\text{Li}_{0.9}\text{V}_2\text{O}_4$ is dominated by two strong peaks which are assigned to the t_{2g} and e_g bands. The V^{III} - V^{IV} hopping will be of a shorter timescale than the reaction of the crystal lattice, thus the vanadium to oxygen distances will be in between those of V^{III} and V^{IV} and is only one crystallographic site, which contains two electronically different (fluctuating) vanadium ions.

Going from the ZnV_2O_4 to LiV_2O_4 the peak related to zinc should disappear, the peaks related to trivalent vanadium should diminish to half its intensity and the peaks related to tetravalent vanadium will appear (and are much more intense due to increased covalence). The peak at threshold increases intensity as a function of the lithium doping, and the peak at 532 eV, visible at 10% and 20% lithium-concentration, disappears. From this observation it is concluded that the peak at 532 eV relates to the t_{2g} peak of trivalent vanadium which becomes blurred in the spectrum due to the increase of the e_g peak of the tetravalent vanadium. In the insulating phase there are crystallographically distinct V^{III} and V^{IV} sites, whereas in the metallic phase there still will be electronically distinct vanadium sites, but as it is expected that the crystallographic rearrangements cannot adjust to the hopping, there will exist an effective vanadium-oxygen distance. To clarify this point it is noted that the assumption of two electronically distinct sites implicates that the system is considered as a heterogeneous mixed valence system. The alternative is a homogenous mixed valence system, which contains only one kind of vanadium sites, which are a quantum-mechanical mixture of the $3d^1$ and $3d^2$ configurations. A heterogeneous mixed valence system can be metallic even if both U and Δ are larger than the bandwidth, because the hopping from a specific $3d^1$ site to a $3d^2$ site does not cost energy apart from an activation energy.

The metal insulator transition is not visible in the x-ray absorption spectra. The vanadium $2p$ x-ray absorption spectra do not distinguish metals² from insulators because the absorption process has a shorter timescale than the electron hopping. The indirect effects (on the cubic crystal field strength) due to the existence of crystallographic equivalent V^{III} and V^{IV} sites in the metallic phase will be too small to be detected with the amount of structure present. Also in the oxygen $1s$ edges the transition is not directly evident; the close similarity of the spectra in the metallic region (for $x_{\text{Li}} \geq 0.6$) is possibly related to the fact that in this regime the V^{III} and V^{IV} sites are crystallographically equivalent (but still there should be the additional effect of zinc $4s$ states). The $x_{\text{Li}} = 0.4$ spectrum (at the

²That is metallic behaviour as a result of electron hopping.

metal insulator transition point) is clearly different from the higher lithium concentrations, which most probably is related to the existence of two different crystallographic site in the insulating phase.

4.5.3. The phase transition of VO₂

Reproduced from *Physical Review B*. **43**, 7263 (1991).

This paper focuses on the phase transition occurring in VO₂. The purpose is to show the effects of the phase transition on the oxygen 1s x-ray absorption spectrum, in order to show that oxygen 1s x-ray absorption is a sensitive probe to changes in the electronic structure. For the case of VO₂ it is concluded that in the insulating phase below 67° Celsius, the *t*_{2g}-band is split due to vanadium-vanadium interactions. in agreement with the qualitative molecular orbital model.

Soft-x-ray-absorption studies of the electronic-structure changes through the VO₂ phase transition

M Abbate, F M F de Groot, and J C Fuggle

Research Institute of Materials, University of Nijmegen, Toernooiveld 1, 6525 ED Nijmegen, The Netherlands

Y J Ma, C T Chen, and F Sette

AT&T Bell Laboratories, Murray Hill, New Jersey 07974

A Fujimori

Department of Physics, University of Tokyo, 7-3-1 Hongo, Bunkyo-ku, Tokyo 113, Japan

Y Ueda

Institute for Solid State Physics University of Tokyo, Roppongi, Tokyo 106, Japan

K Kosuge

Department of Chemistry, University of Kyoto, Sakyo-ku, Kyoto 606, Japan

(Received 9 November 1990)

We present the O 1s and V 2p absorption edges of VO₂ at room temperature and at $T = 120^\circ\text{C}$, i.e., below and above the metal-insulator transition temperature $T_c \approx 67^\circ\text{C}$. The O 1s spectra show a clear splitting of 1 eV in the unoccupied $d_{||}$ band below T_c . Because the V 2p absorption edges are dominated by the V 2p-3d interaction in the final state, these spectra show minor changes that cannot be easily correlated with the changes in the unoccupied density of states.

I. INTRODUCTION

The site and symmetry selectivity of x-ray absorption has always been a major potential source of information. However the deep core levels probed by hard x rays are broad and only the recent improvements in the energy resolution of the soft-x-ray monochromators¹⁻³ and the development of powerful theoretical techniques to analyze the experimental results⁴⁻¹⁰ has allowed a boom in the field of soft-x-ray-absorption spectroscopy (XAS). In an effort to explore the limits of soft-XAS we are using it to study the unoccupied states in very interesting and sometimes difficult materials. In this case we present data on VO₂ which undergoes a first-order structural phase transition at $T_c \approx 67^\circ\text{C}$ which is accompanied by an abrupt change in the electric conductivity. In addition the optical properties of this material also change dramatically, even in the visible, which promises to make VO₂ a very useful component in future optical switching devices.

Here we present the O 1s and V 2p absorption edges of VO₂ at room temperature and at $T = 120^\circ\text{C}$ (i.e., below and above the transition temperature T_c , respectively). The O 1s spectrum proves to be very useful in the study of the metal-insulator transition because it maps the unoccupied states on the V 3d band due to O 2p-V 3d covalent mixing. The fact that we are not dealing with joint density of states usually makes the interpretation of the spectra much easier in comparison with the analysis of optical properties. In particular we will show that the O 1s spectrum gives directly the splitting of the unoccupied $d_{||}$ band, and that the changes across the phase tran-

sition are larger than those indicated for other states by other investigations.

The paramagnetic metallic phase of VO₂ has the tetragonal rutile (TiO₂) structure. Below T_c it undergoes a structural transition to a nonmagnetic monoclinic phase in which pairs of V atoms are brought closer to each other.¹¹ This material has been studied by means of many spectroscopic techniques such as photoemission,¹²⁻¹⁵ reflectance, and hard-x-ray absorption,¹⁶ and especially photoemission spectra showed the disappearance of the states at the Fermi level when going from the high-temperature to the low-temperature phase.¹⁵ The electronic structure of VO₂ was calculated using the band-structure approach in the metallic phase and cluster calculations in both phases.¹⁷⁻¹⁹

II. EXPERIMENTAL DETAILS

The experiments reported here were performed at the National Synchrotron Light Source in Brookhaven using the Dragon monochromator.³ The energy resolution of the monochromator in the energy range of interest (~ 500 eV) was better than 100 meV. Note that the O 1s linewidth is about 100-200 meV,²⁰ which is narrower than the energy resolution of any monochromator in this energy range up to 1988. The sample was a VO₂ single crystal grown by the chemical vapor transport method and cleaved parallel to the (110)_c plane of the rutile phase. The spectra were collected in the total electron yield mode with the polarization vector of the photons parallel to the c axis of the rutile phase.

III. RESULTS AND DISCUSSION

Figure 1 shows the O 1s absorption spectra of VO₂ taken at room temperature and $T=120^\circ\text{C}$. The sharp peaks near threshold are attributed to transition to states with mainly V 3d character which are hybridized with O 2p states. This is in agreement with the assignment of this structure in previous studies of transition-metal oxides.²¹ To understand the origin of the different peaks in the spectra we will resort to the widely used classification scheme based largely on molecular-orbital (MO) and crystal-field ideas.²²

The top panel of Fig. 2 shows schematically how the VO₆ octahedra share edges in the undistorted rutile structure and the coordinate system used in the present analysis. The V $3d_{3z^2-r^2}$ and $3d_{x^2-y^2}$ orbitals point towards the ligands and form the σ and σ^* bands with the O 2p orbitals. On the other hand, the V $3d_{xz}$ and $3d_{yz}$ orbitals point in between the ligands and form the π and π^* bands. Finally the relatively nonbonding V $3d_{xy}$ orbital points in between the ligands and towards the next-nearest-neighbor V site and form the $d_{||}$ band. Figure 2(a) shows the electronic structure of metallic VO₂ based on this MO analysis.^{22,23} In particular we note the formation of the partially filled $d_{||}$ band overlapping the π^* band. The complicated distortion below T_c destroys completely the symmetry of the VO₆ octahedra and forms pairs of V atoms. Figure 2(b) shows the splitting of the $d_{||}$ band due to the formation of the V-V dimers. The band splitting is partly originated by pairing effects, however, electron repulsion yields an important contribution to the splitting.^{18,24,25} The filling of the lower energy band, which corresponds to singlet pairing within the dimers, explains both the abrupt drop in the electric conductivity and the absence of magnetic order below T_c .

With this classification in mind we can now assign the

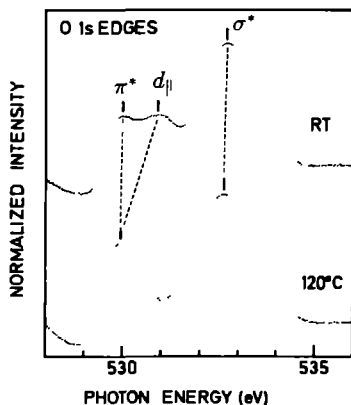


FIG. 1 O 1s absorption spectra of VO₂ taken at room temperature and $T=120^\circ\text{C}$.

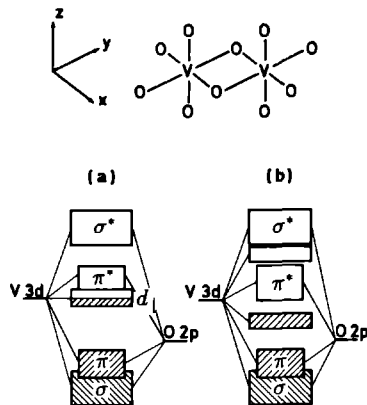


FIG. 2 Top panel schematic representation of the VO₆ octahedra in the undistorted rutile structure. Lower panel MO approach to the electronic structure in VO₂, (a) undistorted and (b) distorted.

peaks in the O 1s spectra. In particular we note that the localized pairing interactions, which result from the V-V dimerization below T_c , are strong enough to push the unoccupied part of the $d_{||}$ band more than 1 eV above the π^* band edge. By contrast, the weak shift of the σ^* band towards higher energies (~ 0.2 eV) reflects smaller changes in bonding and the π^* band hardly shifts at all due to its even weaker bonding properties. As optical data and photoemission spectra indicate that the gap between the occupied $d_{||}$ and the unoccupied π^* edges is ~ 0.7 eV (Ref. 15) we arrive at a splitting of more than 2 eV between the occupied and the unoccupied $d_{||}$ band edges. Thus it is worth stressing again that the main changes occur in the $d_{||}$ band and that the π^* band hardly changes.

Within the framework of the model discussed above the intensity of the different peaks in the O 1s spectra should be related to the degree of hybridization in each MO-derived band. Using this criterion one could explain the larger intensity of the σ^* band peak with respect to the weakly bonding π^* and $d_{||}$ band peaks. However, it is particularly puzzling that the relatively nonbonding $d_{||}$ band peak in the distorted phase is almost as intense as the π^* band peak. This discrepancy between simple MO theory and experiment was already noticed in the study of the O 1s spectra of transition-metal oxides²¹ and indicates the importance of solid-state effects beyond this approximation. A full qualitative discussion of the O 1s spectra would require a symmetry-projected band-structure calculation, like the one presented in the study of the O 1s spectra of CuO,⁸ the computation of independent particle matrix elements and the inclusion of core-hole effects. Unfortunately, not even a band-structure calculation of VO₂ in the distorted phase is available at the present time.

Figure 3 shows the V $2p$ absorption edge of VO_2 taken at room temperature and $T = 120^\circ\text{C}$. We observe the presence of minor changes between the spectra which are not commensurate with those observed in the O $1s$ spectra and cannot be explained by an increase in the phonon contribution to the broadening either. However, the spectra have some common features whose discussion is a good starting point to understand the origin of the changes between the spectra. These features are the transfer of spectral weight away from threshold, the deviation of the intensity ratio between the spin-orbit-split $2p_{3/2}$ and $2p_{1/2}$ doublet from the ideal 2/1 ratio, and the decrease in the apparent spin-orbit splitting of the $2p$ level in the absorption spectra ($\sim 6.6\text{ eV}$) as compared with the splitting observed in XPS ($\sim 7.4\text{ eV}$).¹⁴ Zaanen *et al* demonstrated that all these effects are the natural consequence of the strong interaction between the $2p$ core hole and the $3d$ electrons in the final state.⁶ These interactions are of the same order of magnitude of the V $2p$ spin-orbit splitting which causes a large redistribution of the intensity throughout the entire spectra.⁶

We also note that the structure of the V $2p$ edges does not match the density of states inferred from the O $1s$ spectra or given by *ab initio* calculations.^{17,19} We attribute this discrepancy to the strong influence of the V $2p$ - $3d$ interactions in the final state. Taking these points into account we conclude that the changes in the V $2p$ absorption spectra above and below T_c are mainly due to changes in the V $3d$ band structure, but since the atomic correlations dominate the spectra these changes are washed out.

Finally we discuss the question of whether the transition is of a Mott (electron-electron correlation) or a Peierls (electron-lattice interaction) type. This question was the subject of intense theoretical efforts based on sophisticated computation techniques.²⁶⁻²⁹ We believe that no clear-cut answer is possible because *both* effects contribute to the transition. In particular electron correlation contributes to the splitting of the d band^{18,24,25} and the observation of an anomalously large Debye-Waller factor in x-ray-diffraction studies of VO_2 just above the transition indicates the importance of electron-phonon interactions.³⁰ However, we want to make a few remarks. The absence of magnetic order below T_c indicates that the transition cannot be formally considered of the Mott type and suggests the formation of a singlet within each dimer. The large splitting of the $d_{||}$ band inferred from the O $1s$ spectra, in contrast with the weak changes observed in the π^* and σ^* bands, shows clearly the importance of *localized pairing interactions* within the V-V dimer. Therefore, we think that the transition in VO_2 is basically driven by the lowering in energy of the occupied $d_{||}$ band associated with the distortion of the crystal symmetry and the concomitant enhancement of electron-electron correlation effects. We also note that if pairing

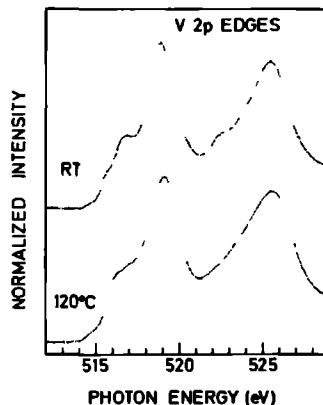


FIG 3 V $2p$ absorption spectra of VO_2 taken at room temperature and $T = 120^\circ\text{C}$

is necessary for the formation of a given bond then each extra bond makes more likely the formation of the next bond since the hopping which stabilizes the metallic phase is made less probable, this provides the basis of the cooperative effect necessary to explain the origin of the phase transition itself.

IV. SUMMARY AND CONCLUSIONS

In summary, we have shown that XAS yields very interesting information on the metal-insulator phase transition in VO_2 . In particular the O $1s$ spectrum maps the mainly V $3d$ band character and shows directly the splitting of the unoccupied $d_{||}$ band. This observation gives further support to the theories which explain the transition in terms of *localized pairing interactions* within the V-V dimer. We think that the potential of XAS in the study of phase transitions is not limited to this particular case and deserves to be fully investigated.

ACKNOWLEDGMENTS

This work was partially supported by Fundamental Onderzoek der Materie (FOM) and Scheikundig Onderzoek Nederland (SON). The research was carried out in part at the National Synchrotron Light Source, Brookhaven National Laboratory, which is supported by the U.S. Department of Energy. We want to thank Professor G. A. Sawatzky, Professor P. F. Bongers for illuminating comments and support to the project, and Professor S. Shin for his cooperation.

- ¹H Petersen, *Nucl Instrum Methods A* **246**, 260 (1986)
- ²H Maezawa, S Nakai, S Mitami, A Mikumi, T Namioka, and I Sasaki, *Nucl Instrum Methods A* **246**, 310 (1986)
- ³C T Chen, *Nucl Instrum Methods A* **256**, 595 (1987), C T Chen and F Sette, *Rev Sci Instrum* **60**, 1616 (1989)
- ⁴O Gunnarsson and K Schonhammer, *Phys Rev B* **28**, 4315 (1983)
- ⁵B T Thole, R D Cowan, G A Sawatzky, J Fink, and J C Fuggle, *Phys Rev B* **31**, 6856 (1985)
- ⁶J Zaanen, G A Sawatzky, J Fink, W Speier, and J C Fuggle, *Phys Rev B* **32**, 4905 (1985)
- ⁷B T Thole, G van der Laan, J C Fuggle, G A Sawatzky, R C Karnatak and J M Esteve, *Phys Rev B* **32**, 5107 (1985)
- ⁸M Grioni, M T Czyzyk, F M F de Groot, J C Fuggle, and B L Wats, *Phys Rev B* **39**, 4886 (1989)
- ⁹F M F de Groot, J C Fuggle B T Thole, and G A Sawatzky, *Phys Rev B* **41**, 928 (1990)
- ¹⁰W Speier, J F van Acker, and R Zeller, *Phys Rev B* **41**, 2753 (1990) P J W Weijs *et al*, *ibid* **41**, 11 899 (1990)
- ¹¹A F Wells, *Structural Inorganic Chemistry* (Clarendon, Oxford, 1975), p 448
- ¹²C Blaaw, F Leenhouts, F van der Woude, and G A Sawatzky, *J Phys C* **8**, 459 (1975)
- ¹³S Vasudevam M S Hedge, and N R Rao, *Solid State Commun* **27**, 131 (1978)
- ¹⁴G A Sawatzky and D Post, *Phys Rev B* **20**, 1546 (1979)
- ¹⁵S Shin, S Suga, M Taniguchi, M Iijisawa, H Kanzaki, A Fujimori, H Daimon Y Ueda, K Kosuge, and S Kachi, *Phys Rev B* **41**, 4993 (1990)
- ¹⁶A Bianconi, *Phys Rev B* **26**, 2741 (1982)
- ¹⁷E Caruthers, L Kleinman, and H I Zhang, *Phys Rev B* **7**, 3753 (1973), E Caruthers and L Kleinman, *ibid* **7**, 3760 (1973)
- ¹⁸C Sommers, R de Groot, D Kaplan, and A Zylbersztejn, *J. Phys (Paris)* **36**, L157 (1975)
- ¹⁹M Gupta and D E Ellis, *Phys Rev B* **13**, 3405 (1976), M Gupta, A J Freeman, and D E Ellis, *ibid* **16**, 3338 (1977)
- ²⁰M O Krause and J H Oliver, *J Phys Chem Ref Data* **8**, 329 (1979), see also *Unoccupied Electronic States*, edited by J C Fuggle and J E Inglesfield (Springer, Berlin, 1991)
- ²¹F M F de Groot, M Grioni, J C Fuggle, J Ghysen, G A Sawatzky, and H Petersen, *Phys Rev B* **40**, 5715 (1989)
- ²²J B Goodenough, *J Solid State Chem* **3**, 490 (1971)
- ²³N Beatham and A F Orchard, *J Electron Spectrosc Relat Phenom* **16**, 77 (1979)
- ²⁴N F Mott and L Friedman, *Philos Mag* **30**, 389 (1975)
- ²⁵C Sommers and S Domach, *Solid State Commun* **28**, 133 (1978)
- ²⁶A Zylbersztejn and N F Mott, *Phys Rev B* **11**, 4383 (1975)
- ²⁷A Holz, K A Penson, and K H Bennemann, *Phys Rev B* **16**, 3999 (1977)
- ²⁸D Paquet and P Leroux Hugon, *Phys Rev B* **22**, 5284 (1980)
- ²⁹F Gervais and W Kress, *Phys Rev B* **31**, 4809 (1985)
- ³⁰D B McWhan, M Marezio, J P Remeika, and P D Dernier, *Phys Rev B* **10**, 490 (1974)

4.5.4. Conclusions for the vanadium oxides

The binary vanadium oxides have, in comparison with the late transition metal oxides, broad metal $2p$ x-ray absorption spectra. This large broadening is related to the relatively extended $3d$ -electrons. This gives rise to extra broadening due to dispersion, vibrations and lattice distortions. The $2p$ x-ray absorption spectrum of ZnV_2O_4 is considerably sharper in accord with the lack of (strong) vanadium-vanadium interactions. The relatively extended $3d$ wavefunctions give rise to metal-metal bonding effects. As discussed in section 4.5.3 VO_2 forms a singlet bond between the two $3d^1[{}^2T_2]$ -states of neighbouring vanadium sites and this bond-formation is accompanied by a lattice distortion and a metal insulator transition. In case of V_2O_3 the effective exchange of the $3d^2[{}^3T_1]$ configuration is too large to allow the formation of singlet states and the lattice distortion which takes place splits the t_{2g}^+ -band. The t_{2g}^- -band is positioned at higher energy.

In its metallic phase the $\text{Zn}_{1-x}\text{Li}_x\text{V}_2\text{O}_4$ system the electronic hopping is faster than the crystallographic reaction to it and the result is that there are two electronically different vanadium states that occupy identical crystallographical sites. In contrast in the insulating phase there are two distinct crystallographic (and electronic) sites. For the vanadium $2p$ x-ray absorption spectra this implicates that in the insulating phase the total spectrum is an addition of the two valencies with their specific cubic crystal field strength. In the metallic phase the spectrum is also an addition of the two valencies but because there is only one crystallographic site the cubic crystal field strengths are slightly modified.

A similar line of reasoning should apply to the oxygen $1s$ x-ray absorption spectra and in the insulating phase indeed two different valencies can be identified. In the metallic phase however only one set of crystal field split peaks is seen. In principle there should be two electronically distinct final states, but as they have an identical cubic crystal field they possibly overlap. The influence of the zinc $4s$ -band should be clarified with a density of states calculation.

Acknowledgements

The experimental data were taken in close cooperation with Miguel Abbate. The assistance of Yan-Jun Ma (Brookhaven) and Oliver Strebler and Francesca Lopez (Berlin) is kindly acknowledged. We would like to thank Prof. A. Fujimori for providing the vanadium oxide samples.

4.6. Conclusions concerning the electronic structure

In the foregoing sections different groups of transition metal oxides have been discussed. In this concluding section the results concerning the configurations and the symmetries of the $3d$ -metal ions. In table 4.6 the dominating configuration and its (dominating) symmetry are given. It must be kept in mind that in general a strong mixing between $3d^N$ and $3d^{N+1}\underline{L}$ can occur. For example Mn^{III} , Co^{III} and Co^{IV} will contain a considerable amount of ligand hole character.

Compound	Valency		
	2	3	4
Sc	-	$3d^0$	-
Ti	-	$3d^1 \bowtie$	$3d^0$
V	-	$3d^2 \bowtie$	$3d^1 \bowtie$
Cr	-	$3d^3$	$(3d^3 \underline{L}) ?$
Mn	$3d^5_{HS}$	$3d^4_{IS}$	$3d^3$
Fe	$3d^6_{HS}$	$3d^5_{HS}$	$3d^5 \underline{L}$
Co	$3d^7_{HS}$	$3d^6_{LS}$	$3d^5_{LS}$
Ni	$3d^8$	$3d^8 \underline{L}$	-
Cu	$3d^9$	$3d^9 \underline{L}$	-

Table 4.6: The dominating configuration of the ground states of the 3d-metal ions in (stoichiometric) oxides where they occur in (distorted) octahedral sites. The symmetry of the state is denoted with *LS*, low-spin and *HS*, high-spin. *IS* denotes an intermediate (or mixed) spin state. \bowtie indicates strong lattice distortions in the binary oxides due to metal-metal bonding effects.

Divalent oxides

It can be seen in the table that all divalent 3d-metal oxides occur in the high-spin configuration. This is caused by the relatively small covalent bonding of the metal 3d-electrons with the oxygen 2p-electrons and correspondingly the relatively small cubic crystal field strengths of about 1 eV. An additional consequence of the small covalency are small 3d bandwidths, which means that U and Δ are larger than the bandwidths and hence all (late) divalent 3d-metal oxides are insulators. For NiO and CuO $U > \Delta$ and according to the ZSA-diagram a pure charge transfer state is formed. For MnO, FeO and CoO $U \approx \Delta$ and an intermediate charge transfer/Mott-Hubbard state is formed. (For a more quantitative interpretation see for example Refs. 5 and 10).

Charge transfer insulators

Apart from Ni^{II} and Cu^{II} also Fe^{III}-ions form pure charge transfer insulators. If a pure charge transfer insulator is doped with holes these holes are accommodated at the oxygen sites. A direct consequence is that the stoichiometric oxides with a higher valency, thus Ni^{III} in LiNiO₂, Cu^{III} in NaCuO₂ and Fe^{IV} in SrFeO₃, are also dominated by $3d^{N+1} \underline{L}$ -character. If these oxides are placed in the ZSA-diagram they have to be described with a negative charge transfer energy, that is the system gains energy if an electron is transferred from the oxygen-ligands to the metal site.

Tetravalent oxides

The tetravalent oxides are dominated by strong covalency effects which will cause large cubic crystal field strengths and consequently low-spin states as for example for Co^{IV} , which has a low-spin ground state despite the fact that the large effective exchange of the five spin-up electrons favours a high-spin configuration. Notice the trends in the spin-state: divalent iron has a high-spin $3d^6$ -configuration, but trivalent cobalt is low-spin. Likewise divalent manganese and trivalent iron are high-spin, but tetravalent cobalt is low-spin. The large covalency will also favour a metallic state as the resulting bandwidth will tend to dominate over correlation effects. The SrTMO_3 perovskites discussed in section 4.4 indeed are metallic in case of vanadium, chromium, iron and cobalt. However there are a range possible alternatives to the metallic phase. SrTiO_3 is not metallic (at room temperature) because a bandgap is formed between the filled oxygen $2p$ -band and the empty titanium $3d$ -band. SrMnO_3 is also not metallic as a small bandgap is formed in between the filled t_{2g}^+ sub-band and the other sub-bands. Also VO_2 is not a metal at room temperature and as has been discussed in section 4.5 this is caused by metal-metal bonding which forms vanadium dimers.

Trivalent oxides

The covalency of the trivalent oxides is intermediate between the divalent and the tetravalent oxides. The spin state, which is formed as a result of the competition between the covalency (cubic crystal field) and the effective exchange, is low-spin for $3d^6\text{-Co}^{III}$ and high-spin for $3d^5\text{-Fe}^{III}$. The reason is that a $3d_{HS}^5$ -configuration is stabilized by the 5 unpaired spins, while the $3d_{LS}^6$ -configuration is stabilized by the fact that its t_{2g} sub-band is completely filled. For the $3d^4$ -state of trivalent manganese oxides the low-spin and high-spin configurations are close to degenerate and furthermore they are mixed by $3d$ spin-orbit coupling. The actual ground state is sensitive to the structure of a specific oxide and in general the description must use a combination of high-spin (5E) and low-spin (3T_1) configurations. A further complication is that the high-spin configuration will be affected by a Jahn-Teller distortion. The analysis of the manganese $2p$ x-ray absorption spectrum of LiMnO_2 (given in section 4.3.) showed that in this compound the spin state must be described as a mixture of 3T_1 and 5E symmetries.

References

- [1] J. Zaanen, G.A. Sawatzky and J.W. Allen, *Phys. Rev. Lett.* **55**, 418 (1985).
- [2] G. van der Laan, C. Westra, C. Haas and G.A. Sawatzky, *Phys. Rev. B.* **23**, 4369 (1981).
- [3] J. Zaanen, C. Westra and G.A. Sawatzky, *Phys. Rev. B.* **33**, 8060 (1986).
- [4] G. van der Laan, J. Zaanen, G.A. Sawatzky, R. Karnatak and J.-M. Esteve, *Phys. Rev. B.* **33**, 4253 (1986).
- [5] J. Zaanen, PhD. thesis: *The electronic structure of transition metal compounds in the impurity model* (University of Groningen, 1986).
- [6] P.W. Anderson, *Phys. Rev. B.* **115**, 2 (1959).

- [7] J. Hubbard, *Proc. R. Soc. A.* **276**, 238 (1963); *ibid.* **277**, 237 (1964); *ibid.* **281**, 401 (1967).
- [8] J. A. Wilson, *Adv. in Physics* **21**, 143 (1972).
- [9] Ref. 5; page 155.
- [10] J. van Elp, PhD-thesis: "The electronic structure of doped late transition metal monoxides" (University of Groningen, 1991).
- [11] J.B. Torrance, P. Lacorro, C. Asavaroengchai and R.M. Metzger, *J. Sol. State Chem.* **90**, 168 (1991).
- [12] J.S. Griffith, *The Theory of Transition Metal Ions* (Univ. Press, Cambridge, 1964); chapter 9.
- [13] K. Terakura, T. Oguchi, A.R. Williams and J. Kübler, *Phys. Rev. B.* **30**, 4734 (1984).
- [14] O. Eriksson, L. Nordström, A. Pohl, L. Severin, A.M. Boring and Börje Johansson, *Phys. Rev. B.* **41**, 11807 (1990); O. Eriksson, Börje Johansson, R.C. Albers, A.M. Boring and M.S.S. Brooks, *Phys. Rev. B.* **42**, 2707 (1990).
- [15] M.R. Norman, *Phys. Rev. Lett.* **64**, 1162 (1990); *ibid.* **64**, 2466 (1990) (E).
- [16] A. Svane and O. Gunnarsson, *Phys. Rev. B.* **37**, 9919 (1988). A. Svane and O. Gunnarsson, *Phys. Rev. Lett.* **65**, 1148 (1990).
- [17] Y. Ishii and K. Terakura, *Phys. Rev. B.* **42**, 10924 (1990).
- [18] S. Nakai, A. Kawata, M. Ohashi, M. Kitamura, C. Sugiura, T. Mitsuishi and H. Maezawa, *Phys. Rev. B.* **37**, 10895 (1988).
- [19] P. Kuiper, *Phys. Rev. Lett.* **62**, 221 (1989).
- [20] P. Kuiper, PhD-thesis *Where are the holes in doped transition metal oxides?* (University of Groningen, 1990).
- [21] P.C. Hohenberg and W. Kohn, *Phys. Rev.* **136**, 864 (1964).
- [22] W.Kohn and L.J. Sham, *Phys. Rev.* **140**, 1133 (1965).
- [23] P.W. Anderson *Phys. Rev.* **115**, 2 (1959).
- [24] O. Gunnarsson and K. Schönhammer, *Phys. Rev. B.* **28**, 4315 (1983); O. Gunnarsson and K. Schönhammer, *Phys. Rev. B.* **31**, 4815 (1985).
- [25] F.M.F. de Groot, J.C. Fuggle, B.T. Thole and G.A. Sawatzky, *Phys. Rev. B.* **41**, 928 (1990).
- [26] C.K. Jorgensen, *Absorption Spectra and Chemical Bonding in Complexes*, (Pergamon Press, Oxford, 1962); C.K. Jorgensen, *Modern Aspects of Ligand Field Theory*, (North Holland, Amsterdam, 1971).
- [27] D.W. Lynch and R.D. Cowan, *Phys. Rev. B.* **36**, 9228 (1987).
- [28] M.T. Czyżyk and R.A. de Groot, *Conference Proceedings of the 2nd European Conference on Progress in X-ray Synchrotron Radiation Research*, Eds. A. Balerna, E. Bernieri and S. Mobilio (SIF, Bologna, 1990), page 47.
- [29] Result from the LSW calculation discussed in section 3.8.
- [30] C.T. Chen, *Nucl. Instrum. Meth. A.* **256**, 595 (1987); C.T. Chen and F. Sette, *Rev. Sci. Instrum.* **60**, 1616 (1989).
- [31] F.M.F. de Groot, M.O. Figueiredo, M.J. Basto, M. Abbate, H. Petersen and J.C. Fuggle, *Phys. and Chem. of Min.*, submitted.
- [32] M. Jansen and R. Hoppe, *Z. Anorg. Allg. Chem.* **397**, 279 (1973).
- [33] R. Potze, private comm.
- [34] W.D. Johnston and R.R. Heikes, *J. Am. Chem. Soc.* **78**, 3255 (1960).
- [35] D.G. Wickham and W.J. Croft, *J. Phys. Chem. Solids* **7**, 351 (1958).
- [36] L. Schutte, G. Colmsan and B. Reuter, *J. Sol. State Chem.* **27**, 227 (1979).
- [37] W.D. Johnston, R.R. Heikes and D. Sestrich, *J. Phys. Chem. Solids* **7**, 1 (1958).

- [38] R. Hoppe, G. Brachtel and M. Jansen, *Z. Anorg. Allg. Chem.* **417**, 1 (1975).
- [39] S. Sugano, Y. Tanabe and H. Kitamura, *Multiplets of Transition Metal Ions* (Academic Press, New York, 1970).
- [40] T. Yamaguchi, S. Shibuya, S. Sugano, *J. Phys. C* **15**, 2625 (1982).
- [41] T. Yamaguchi, S. Shibuya, S. Suga, S. Shin, *J. Phys. C* **15**, 2641 (1982).
- [42] R.D. Cowan, *The Theory of Atomic Structure and Spectra* (Univ. of California Press, Berkeley, 1981).
- [43] M.T. Czyżyk and G.A. Sawatzky, *Phys. Rev. B.*, submitted.
- [44] P.J.W. Weijs, M.T. Czyżyk, J.F. van Acker, W. Speier, J.B. Goedkoop, H. van Leuken, H.J.M. Hendriks, R.A. de Groot. G. van der Laan, K.H.J. Buschow, G. Wiech and J.C. Fuggle *Phys. Rev. B* **41**, 11899 (1990).
- [45] M. Grioni, M.T. Czyżyk, F.M.F. de Groot, J.C. Fuggle, B.E. Watts, *Phys. Rev. B* **39**, 4886 (1989).
- [46] J. van Elp, PhD. thesis: *The electronic structure of doped late transition metal monoxides* (University of Groningen, 1991); chapter 4.
- [47] A. Fujimori, N. Kimizuka, T. Akahane, T. Chiba, S. Kimura, F. Minami, K. Siratori, M. Taniguchi, S. Ogawa and S. Suga, *Phys. Rev. B* **42**, 7580 (1990).
- [48] F.M.F. de Groot, M. Grioni, J.C. Fuggle, J. Ghijsen, G.A. Sawatzky and H. Petersen, *Phys. Rev. B* **40**, 5715 (1989).
- [49] H. Petersen, *Opt. Comm.* **40**, 402 (1982); H. Petersen, *Nucl. Instrum. Meth. A* **246**, 260 (1986); M. Domke, C. Xue, A. Puschman, T. Mandel, E. Hudson, D. Shirley and G. Kaindl, *Chem. Phys. Lett.* **173**, 122 (1990).
- [50] J.B. Goodenough, *Progress in Solid State Chemistry*, Ed. H. Reiss (Pergamon Press, Oxford, 1971); J.B. Goodenough, *Magnetism and the Chemical Bond* (Interscience and Wiley, New York, 1963).
- [51] J.B. McChesney, R.C. Sherwood, J.F. Potter, *J. Chem. Phys.* **43**, 1907 (1965).
- [52] C. Gleitzer and J.B. Goodenough, *Mixed valence iron oxides*, in: *Structure and Bonding*, **61**, 1 (1985).
- [53] P.H. Butler, *Point Group Symmetry Applications: Methods and Tables*, (Plenum Press, New York, 1981).
- [54] H. Oda, Y. Yamaguchi, H. Watanabe, *J. Phys. (Paris). Coll-2.* **40**, 331 (1979).
- [55] T. Takeda, S. Komura and H. Fugii, *J. Magn. Magn. Mat* **31-34**, 797 (1983).
- [56] M. Takano, J. Kawachi, N. Nakanichi and Y. Takeda, *J. Solid State Chem.* **39**, 75 (1981).
- [57] R.W.G. Wyckoff, *Crystal Structures II* (Interscience, New York, 1964).
- [58] K. Okada, A. Kotani, B.T. Thole and G.A. Sawatzky, *Sol. State Comm.* **77**, 835 (1991).
- [59] P.F. Bongers, PhD Thesis (University of Leiden, 1957); P.F. Bongers, in: *Crystal Structure and Chemical Bonding in Inorganic Chemistry*, Eds. C.J.M. Rooymans and A. Rabenau (Elsevier, Amsterdam, 1975); chapter 4.
- [60] J.B. Goodenough, G. Dutta and A. Manthiram, *Phys. Rev. B* **43**, 10170 (1991).
- [61] S. Shin, S. Suga, M. Taniguchi, M. Fujisawa, H. Kanzaki, A. Fujimori, H. Daimon, Y. Ueda, K. Kosuge and S. Kachi *Phys. Rev. B* **41**, 4993 (1990).
- [62] A. Fujimori, K. Kawakami and N. Tsuo, *Phys. Rev. B* **38**, 7889 (1988).
- [63] K. Kawakami, Y. Sakai and N. Tsuda, *J. Phys. Soc. Jap.* **55**, 3174 (1986); F. Takagi, K. Kawakami, I. Maezawa, Y. Sakai and N. Tsuda, *J. Phys. Soc. Jap.* **56**, 444 (1987); F. Takagi, K. Kawakami and N. Tsuda, *J. Phys. Soc. Jap.* **57**, 3119 (1988).

REFERENCES

- [64] M. Abbate, F.M.F. de Groot, J.C. Fuggle, Y.J. Ma, C.T. Chen, F. Sette, A. Fujimori, Y. Ueda, K. Kosuge *Phys. Rev. B.* **43**, 7263 (1991).

5. APPLICATIONS

As intimated earlier in this thesis the potential of (soft) x-ray absorption spectroscopy has developed from a rather uninteresting and experimentally difficult technique to a technique with high sensitivity, very high resolution and backed by a considerable degree of theoretical understanding. This development makes (soft) x-ray absorption spectroscopy a potentially useful tool for the study of a wide variety of fields. For this reason cooperations have been started with a number of well-known groups to demonstrate the possible applications of (soft) x-ray absorption. In this chapter a number of these applications are illustrated.

Fields of potential interest include the study of the metal-centers in for example enzymes and other bioinorganic materials. A preliminary study is discussed in section 5.1. Section 5.2 deals with the superconducting oxides, specifically the lead/bismuth perovskites. In section 5.3 the use of x-ray absorption for mineralogy is discussed: In the study of minerals an important question is the determination of the (distribution of the) crystallographic sites of the constituents and its relation to the local electronic structure. Section 5.4 combines polarization dependent measurements with ion yield detection for the study of surfaces and interfaces.

5.1. Bioinorganics

Bioinorganics is concerned with the role of metal ions in living systems. Metal ions, in particular iron, copper and manganese, play an important role in metalloproteins like haemoglobin and the photo-redox system [1]. An important aspect of the $3d$ -metal ions is their ability to change their valency with all the consequences for its magnetic, electronic and structural behaviour.

Because the $3d$ -metal ions are embedded in large organic complexes, with concentrations which are typically of the order of $1 : 10^6$, x-ray absorption is a valuable technique due to its site selectivity. At present the EXAFS signal of the metal K edges is a successfully applied experimental technique for the determination of the local site geometry of the metal-centers [2, 3]. The great promise of (soft) x-ray absorption of the metal $2p$ edges is the possibility to analyse the electronic structure in great detail and in this manner to unravel the intimate connections between structural and electronic (plus magnetic) aspects of the metal-centers in organic complexes.

The structures in the metal $2p$ edges are as sharp as 0.1 eV (hwhm), and these edges have a great potential to derive more detailed electronic structure information. Furthermore the $2p$ edges are sensitive to the valency, the symmetry of the ground state, the ligand field strength and in specific cases the $3d$ spin-orbit coupling and site distortions from cubic symmetry. A typical example of a $3d$ -metal complex in bioinorganics is photo-system II, which contains an active site with four manganese ions. The valency is changed in steps from (four) trivalent to tetravalent manganese ions. Though EXAFS of the metal K edges has been able to determine accurately the nearest neighbour distances [4, 5], the electronic as well magnetic changes still remain largely unsolved.

The main problem in metal $2p$ x-ray absorption spectroscopy has been the detection of the low concentrations of metal ions, but with the development of sensitive fluorescence detectors this problem is largely solved now [6]. As yet, some preliminary studies on rubredoxin and copper (II) complexes have been performed [7]. The next section contains a study to verify the possibility to determine the cubic crystal field and the valency of manganese in a series of inorganic compounds as well as organic complexes. The experiments were performed by Steve Cramer et al., using the DRAGON monochromator at NSLS, Brookhaven.

5.1.1. Ligand field strengths and oxidation states from manganese L-edges

This section has been accepted in the Journal of the American Chemical Society and will be published September 1991.

S.P. Cramer^{1,8}, F. M. F. deGroot⁴, Y. Ma², C.T. Chen², F. Sette²,
C. A. Kipke⁶, D. M. Eichhorn⁶, M. K. Chan⁶, W. H. Armstrong⁶,
E. Libby³, G. Christou³, S. Brooker⁷, V. McKee⁷, O. C. Mullins⁵, and J. C. Fuggle⁴

- | | |
|--|---|
| 1 Department of Applied Science
University of California
Davis, CA 95616 | 5 Schlumberger-Doll Research
Old Quarry Road
Ridgefield, CT 06877 |
| 2 AT&T Bell Laboratories
Murray Hill, NJ 07974 | 6 Department of Chemistry
University of California
Berkeley, CA 94720 |
| 3 Department of Chemistry
Indiana University
Bloomington, IN 4740 | 7 Department of Chemistry
Canterbury University
Christchurch, New Zealand |
| 4 Research Institute for Materials
University of Nijmegen
Toernooiveld, NL-6525 ED Nijmegen
The Netherlands | 8 Division of Applied Science
Lawrence Berkeley Laboratory
Berkeley, CA 94720 |

ABSTRACT

L_{2,3} x-ray absorption spectra have been recorded for Mn^{II}, Mn^{III}, and Mn^{IV} samples with a variety of ligands. For high-spin Mn^{II} complexes, a systematic variation in spectra is observed as the ligand field is increased. A dramatically different spectrum is observed for Mn(CN)₆⁴⁻, consistent with the presence of a low spin complex. Progressing in oxidation state from Mn^{II} to Mn^{III} through Mn^{IV} complexes, the primary peak position shifts first 1.5-2 eV and then 1-2 eV to higher energy, and the ratio of L₃ to L₂ intensity decreases. The spectra have been quantitatively simulated using an atomic multiplet program with an octahedral crystal field superimposed. The high resolution, strong sensitivity to chemical environment and amenability to quantitative spectral shape analysis indicate that L-edges of the first transition series metals are a potentially useful probe for bioinorganic studies.

Introduction

This paper presents new data on the chemical sensitivity of manganese $L_{2,3}$ x-ray absorption edges and discusses the potential bioinorganic applications of soft x-ray L-edge spectroscopy. Transition metal complex $L_{2,3}$ -edge spectra involve $2p \rightarrow 3d$ transitions, and hence are sensitive to factors which change $3d$ orbital splittings and populations [8]. Improved synchrotron radiation beam lines allow these $3d$ -metal L-edge spectra to be probed with high resolution [9], and soft x-ray array detectors permit analysis of dilute metalloproteins [6]. In this communication, we illustrate the sensitivity of manganese L-edges to ligand field, spin state, and oxidation state, and we interpret the effects by performing atomic multiplet calculations including the cubic crystal field.

Experimental

L-edge spectra were recorded in electron yield mode using beam line U4-B [9] at the National Synchrotron Light Source. Finely powdered compounds were spread across the adhesive side of aluminium tape and placed with the sample normal at 45 degrees to both the incoming beam and the vertical chamber axis. The sample chamber vacuum of better than 10^{-5} torr was separated from the upstream vacuum of 10^{-10} torr by a 1000 Å aluminium foil. A Galileo 4716 channeltron electron multiplier measured the electron yield from the sample as the monochromator swept the incident energy. The spectra were calibrated arbitrarily using 640 eV for the absorption maximum in MnF_2 ; the true value may be 1-2 eV lower.

MnF_2 , MnO_2 , $MnCl_2$ and $MnSO_4$ were used as received from Alfa Products. MnS was a kind gift from Dr. Russel Chiannelli, Exxon Research. $(NEt_4)_2MnCl_4$ [10], $K_4Mn(CN)_6$ [11], $[HB(3,5-Me)_2pz_3]_2 \cdot Mn^{IV}(ClO_4)_2$ [12], $[HB(3,5-Me)_2pz_3]_2 \cdot Mn^{III}(ClO_4)$ [13], $[HB(3,5-Me)_2pz_3]_2 \cdot Mn^{II}$ [13] and $[Mn(acen)(NO_2)]$ [14] were prepared in the Armstrong laboratory by the cited literature methods. $[Mn_2(H_2L)(Cl)_2]_2 \cdot (ClO_4)_2 \cdot 2dmf \cdot H_2O$ [15] was prepared in the McKee laboratory, and $Mn_2O_2(pic)_4$ [16] was prepared in the Christou laboratory.

Results and Discussion

The profound differences between $3d$ -metal K and L-edges are illustrated for $MnCl_2$ in Figure 5.1. A $1s \rightarrow 3d$ transition is dipole-forbidden, and the weak doublet found at the foot of the K-edge is thought to occur both as a $1s \rightarrow 3d$ quadrupole transition and by mixing of $4p$ character into the $3d$ -band, by vibrations or other means. [17, 18]. The splitting of 1.0 eV resolved in the second derivative spectrum is close to optical values of 0.93-1.03 eV reported for 10Dq [19, 20]. In contrast with the simple and weak K-edge doublet, numerous strong features are observed at the L-edge.

The additional structure has been interpreted as the combination of crystal field effects with splittings due to multipole pd and dd interactions. For the Mn^{II} ion the $3d^5[{}^6S]$ atomic ground state is determined by the multipole dd interactions, either factorized in Slater integrals (F^2, F^4) or alternatively in Racah parameters (B, C). The 6S atomic ground state does not split; in cubic symmetry the fully symmetric state is renamed to 6A_1 . From this ${}^6A_1(2p^6 3d^5[(t_{2g}^+)^3(e_g^+)^2])$ ground state, transitions are possible to a series of $2p^5 3d^6$ final states

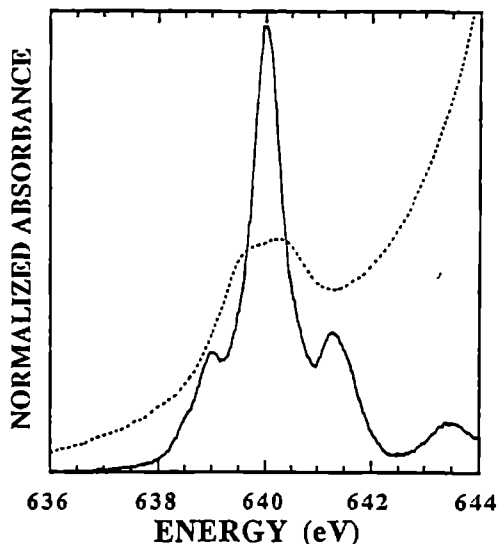


Figure 5.1: Comparison of K (- -) and L_3 (—) edges for $MnCl_2$. The spectra have been arbitrarily aligned and only the $1s \rightarrow 3d$ region of the K-edge is shown.

of symmetries which couple to the ground state. The final states are, like the ground state, determined by the dd multipole interactions. Important additional interactions are caused by the core hole: the $2p$ core hole spin-orbit coupling splits the absorption spectrum into an L_3 and an L_2 part, and the pd multipole Coulomb and exchange interactions (F^2 , G^1 , G^3), which are in the order of 5 eV also modify the spectrum considerably. This gives rise to hundreds of lines with distinct envelopes [21].

An important factor for the broadening of the line spectrum is the lifetime of the final state. Depending on the specific symmetry of the final state, the possible (Auger) decay channels have different transition probabilities and lifetimes. As these symmetry-dependent relaxation rates are unknown, for the simulations all lines are broadened equivalently with a Lorentzian of 0.1 eV for the L_3 edge and 0.3 eV for the L_2 edge.

Mn^{II} Complex	Optical 10Dq (eV)	X-Ray 10Dq (eV)	Ref.
$(Et_4N)_2[MnCl_4]$	-0.41	-0.3	[27]
MnS	.88	0.6	[28]
$MnCl_2$	0.93	0.75	[19]
MnF_2	0.97	0.75	[29]
$MnSO_4$	~ 1.0	0.75	[30]
$[HB(3,5-Me_2pz)_3]_2Mn$	~ 1.3	1.05	[30]
$K_4Mn(CN)_6$	~ 3.7	3.9	[32]

Table 5.1: Comparison of the cubic crystal field strengths as derived from optical spectroscopy and manganese $2p$ x-ray absorption.

Experimental L-edge spectra for a series of octahedral Mn^{II} complexes are compared

with atomic multiplet calculations in Figure 5.2. For these calculations, atomic values for the Slater integrals were used [22]. The values of $10Dq$ which gave the best simulations are compared with parameters derived from UV-visible spectroscopy in the Table. It reveals that there is a deviation between the UV-visible and x-ray results. The $10Dq$ values from x-ray absorption, which in fact are final state values, are approximately 25% smaller than the UV-visible results. This relation is valid for all high-spin Mn^{II} complexes. The decrease of the cubic crystal field strength in the final state may be due to an increased localisation of the $3d$ -states in the presence of the core-hole [23]. A similar argument would appear to hold for the K-edge splittings; yet these appear comparable to the optical values. Further study of the relationship between x-ray and optical splittings is clearly needed.

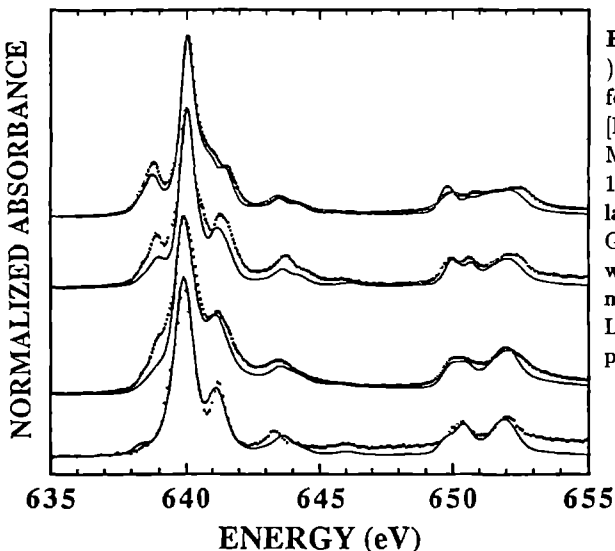


Figure 5.2: Experimental (---) and theoretical (—) $L_{2,3}$ edges for (top to bottom) $[HB((3,5Me)_2pz)_3]_2Mn$, MnF_2 , MnS , and $[NEt_4]_2MnCl_4$. The $10Dq$ values used for the simulations are given in the table. A Gaussian broadening of 0.1 eV was applied to correct for instrumental broadening. Additional Lorentzian linewidths were applied to best simulate the data.

The branching ratio of L_3 intensity to total line strength, $I(L_3)/I(L_3 + L_2)$, decreases significantly for low-spin Mn^{II} , as illustrated by the spectrum of $Mn(CN)_6^{4-}$ in figure 5.3. Such changes have been theoretically analysed by Thole and van der Laan [24]. For Mn^{II} the theoretical branching ratio is 0.75 for high-spin and 0.59 for low-spin. A crystal field multiplet calculation with an octahedral crystal field strength of 3.9 eV results in a ${}^2T_2(3d^5[(t_{2g}^+)^3(t_{2g}^-)^2])$ ground state. From this ground state, transitions are possible to the $2p^53d^0$ final state where the six $3d$ -electrons have ${}^1A_1[(t_{2g}^+)^3(t_{2g}^-)^3]$ symmetry. For the L_3 region, this state is separated by about 2 eV from the other $2p^53d^0$ multiplet lines. Examination of the low energy side of this band reveals a line width of about 0.35 eV.

Significant changes in L-edge structure and position occur upon oxidation from Mn^{II} to Mn^{III} or Mn^{IV} , as shown in Figure 5.4. For complexes with the same ligands, the average shift in main peak position is on the order of 1.5-2 eV for Mn^{II} to Mn^{III} , and about 1-2 eV

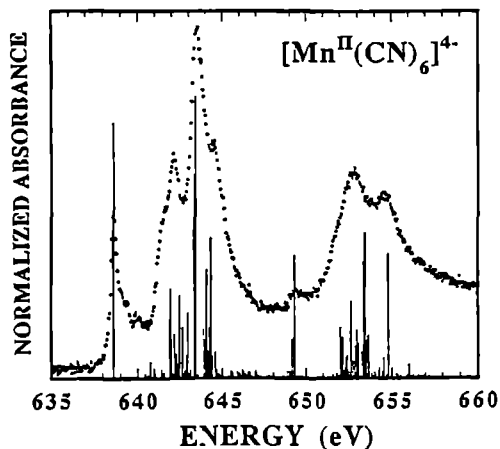


Figure 5.3: Experimental $L_{2,3}$ spectrum for $\text{K}_4\text{Mn}(\text{CN})_6$ compared with stick diagram showing relative oscillator strengths of individual transitions before instrumental and linewidth broadening, calculated using $10Dq = 3.9$ eV.

for Mn^{III} to Mn^{IV} . For comparison, manganese K-edges shift on the order of 3-4 eV for similar oxidation state changes [25]. Since the reported natural line widths for K and L-edges are 1.12 and 0.32 eV respectively [26], it appears that the ratio of edge shift to resolution is higher for the L-edges. This should make L-edges more favourable for deciphering mixtures of oxidation states.

In the present simulations it is assumed that the Mn^{II} ion exists as a pure $3d^5$ ground state. For a higher oxidation state such as Mn^{IV} , assumption of the corresponding $3d^3$ ground state is less justified. Due to increased covalency, mixing of $3d^4\bar{\text{L}}$ character, where $\bar{\text{L}}$ means a hole on the ligand, is more important. In the present calculations the role of covalency is not considered explicitly, but the effects are effectively included by reducing the Slater integrals.

An additional complicating factor for the Mn^{III} spectra is that the ${}^5E - 3d^4[(t_{2g}^+)^3(e_g^+)^1]$ ground state in octahedral symmetry is not stable because of the half-filled e_g level. This degeneracy is lifted by a Jahn-Teller distortion which reduces the symmetry to tetragonal. Preliminary investigation reveals lower symmetry can have a considerable effect on the spectra. In summary, although the simulations of ionic Mn^{II} complexes were successful, additional work is needed to assess the utility of the atomic multiplet model for lower symmetry and more covalent Mn^{III} and Mn^{IV} complexes.

Conclusions and Prognosis

Since K level near edge and EXAFS spectroscopies are now popular tools for bioinorganic studies, it is worth noting the potential of $L_{2,3}$ edges for first transition metal characterization in biological samples [35]. A dominant experimental factor is the short penetration length of L-edge x-rays. In the 500-1000 eV range where vanadium through zinc L-edges occur, many absorption coefficients are 2-3 orders of magnitude higher than at the corresponding K-edges. Thus, for example, the $1/e$ transmission length in aqueous media is 7800 Å at the manganese L-edge, compared to 0.4 mm at 6 keV near the manganese K-edge. This

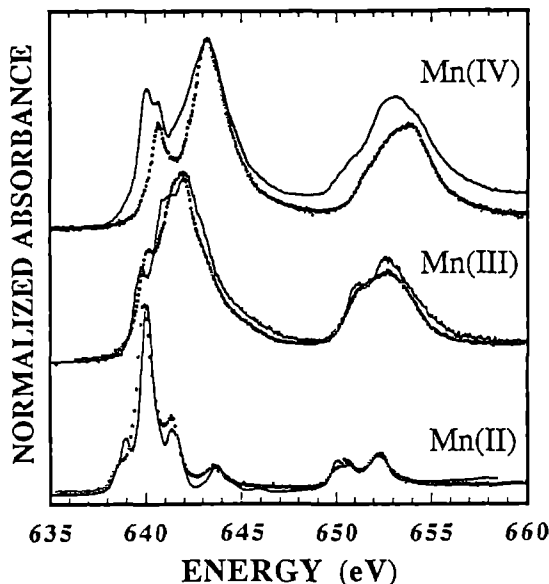


Figure 5.4: Oxidation state dependence of L-edge position and shape. Top to bottom: $[\text{HB}(3,5\text{Me})_2\text{pz}]_3\text{Mn}^{\text{IV}}(\text{ClO}_4)_2$ (—) and $\text{Mn}_2^{\text{IV}}\text{O}_2(\text{pic})_4$ (- - -), where ‘pic’ = picolinate anion;

piemontite - $\text{Ca}_2(\text{Mn}^{\text{III}},\text{Fe}(\text{III}),\text{Al})_2\text{AlO}\cdot\text{OH}[\text{Si}_2\text{O}_7][\text{SiO}_4]$ (—) and $\text{Mn}^{\text{III}}(\text{acen})(\text{NO}_2)$ (- - -), where ‘acen’ = N,N’-ethylenebis(acetylacetonate imine);

$\text{Mn}^{\text{II}}\text{F}_2$ (—) and $[\text{Mn}_2^{\text{II}}(\text{HL})(\text{Cl})_2]_2(\text{ClO}_4)_2\cdot 2\text{dmf}\cdot \text{H}_2\text{O}$ (- - -), where ‘HL’ = 1,7,14,20-tetramethyl-2,6,15,19-tetra-aza[7,7] (2,6)pyridinophane-4,17-diol.

The spectrum of the former Mn^{IV} complex appears to be contaminated by a small amount of its Mn^{II} precursor complex. Energy calibration arbitrarily used MnF_2 maximum as 640 eV.

requires dramatic changes sample handling, window technology, and detectors. Also, the $\text{L}_{2,3}$ fluorescence yields are 0.3 to 1% [36], 50-100 times lower than the K-edge yields. Fortunately, the background signal from Compton scattering is small at L-edge energies. Although the overall experimental sensitivity may be lower, the signal-to-noise requirements for edge-analysis are less stringent than for EXAFS, and as the technology improves, obtaining these spectra will no doubt eventually become routine.

Compared to the broad K-edge features, the sharper and richer $\text{L}_{2,3}$ -edge multiplet structure appears more amenable to resolving the presence of mixtures of oxidation states, although this remains to be proven. For spectroscopic determination of interatomic distances, K-edge EXAFS is not challenged by 3d-metal L-edge EXAFS, because several hundred volts of uninterrupted oscillations are generally required, and too many overlapping and interfering edges occur in the soft x-ray region. However for detecting small changes in the

transition metal site symmetries, the sharper $L_{2,3}$ edge spectra may be more sensitive and more quantitatively interpretable than the K edge data. The confluence of better sources, monochromators, detectors, and theoretical procedures makes soft x-ray spectroscopy a promising new tool for bioinorganic problems.

Acknowledgements

We thank Dr. Theo Thole and Prof. George Sawatzky for helpful discussions and for making their simulation software available. Dr. Andrew Campbell and Prof. Roger Burns of MIT are gratefully acknowledged for the piemontite sample. This work was partially supported by the National Institutes of Health, Grants GM-44380 (to SPC) and GM-38275-01 (to WHH). WHH also acknowledges funding from the Searle Scholars and the National Science Foundation Presidential Young Investigators Programs. The National Synchrotron Light Source is funded by the Department of Energy, Office of Basic Energy Sciences.

5.2. Superconducting oxides

The discovery of oxides which are superconducting at temperatures of the order of 100 Kelvin, stimulated much research to determine the electronic structure of these materials [38]. The common object of all oxides with a superconducting transition temperature above 30 Kelvin is the existence of non-stoichiometric copper-oxygen layers embedded in layers with heavy ions. The superconducting behaviour is a result of the extra holes (or electrons) in the copper-oxygen layers.

The oxygen $1s$ x-ray absorption spectra of the copper oxides, for example La_2CuO_4 , show apart from the structure related to the strontium and lanthanum bands a sharp peak at threshold related to the empty state in the $3d$ -band of the divalent $3d^9$ copper-ion. Cu^{II} is a charge transfer insulator with $U \gg \Delta$ and consequently Cu^{II} contains a ground state dominated by $3d^9\bar{L}$ character. If an oxide which contains Cu^{II} is doped with holes by partial replacement of strontium for lanthanum, Cu^{III} impurities are formed. They are marked by a sharp peak at about 1.5 eV below the Cu^{II} -peak and this Cu^{III} -peak is related to transitions from the $3d^9\bar{L}$ ground state. Experimental oxygen $1s$ x-ray absorption (respectively EELS) spectra of the layered copper-oxides were first given for the $\text{YBa}_2\text{Cu}_3\text{O}_{7-\delta}$ by the Karlsruhe group [39]. Similar results have been found for the other layered copper-oxides in Refs. 38, 40, 45 and references therein. Because these copper-oxides are layered materials a strong linear dichroism is expected (see section 3.6), and it indeed has been found that the doping-related holes are strongly polarized and largely confined to the copper-oxide plane [41–44].

Apart from the layered copper-oxides a number of other oxides show superconductivity. Among them are the perovskites SrTiO_3 , $\text{BaPb}_{0.75}\text{Bi}_{0.25}\text{O}_3$ and related oxides. In the next section the oxygen $1s$ x-ray absorption spectra of the perovskite system $\text{BaPb}_{1-x}\text{Bi}_x\text{O}_3$ is investigated.

5.2.1. Oxygen 1s x-ray absorption of $\text{BaPb}_{1-x}\text{Bi}_x\text{O}_3$

This section has been accepted in Physical Review B. and will be published September 1991.

F.M.F. de Groot¹, J.C. Fuggle¹ and J.M. van Ruitenbeek².

- 1 Spectroscopy of Solids and Surfaces, University of Nijmegen
Toernooiveld, 6525 ED Nijmegen, The Netherlands
- 2 Kamerlingh Onnes Laboratory, Leiden University
PO Box 9506, 2300 RA Leiden, The Netherlands

ABSTRACT

Oxygen 1s x-ray absorption spectra of the $\text{BaPb}_{1-x}\text{Bi}_x\text{O}_3$ - system have been measured. The spectra do not show the pre-peak structures as common in the doped copper-oxide superconductors. The observed shift of the first peak is much smaller than predicted by single particle density-of-states calculations.

Introduction

The $\text{BaPb}_{1-x}\text{Bi}_x\text{O}_3$ -compounds are perovskites. Their electronic properties vary considerably as a function of x and because for $x = 0.25$ a superconducting state was found up to 13 K [46], this system was much studied in the last decade [47]. Although originally overshadowed by the development of the high T_c copper oxide based superconductors, the $\text{BaPb}_{1-x}\text{Bi}_x\text{O}_3$ -compounds are still of interest and their study received new impetus from the discovery of T_c up to 30 K in the related $\text{Ba}_{1-x}\text{K}_x\text{BiO}_3$ -materials [48]. It is known that the group of $(\text{Ba},\text{K})(\text{Pb},\text{Bi})\text{O}_3$ perovskite compounds have some properties, like an exceptionally high ratio of T_c to the linear specific heat coefficient, in common with the copper-oxide based superconductors [49]. This of course opens the question of possible similarities in the mechanism causing superconductivity.

One of the important diagnostic techniques for the determination of the electronic structure of the copper-oxide based superconductors was x-ray absorption, and more specifically oxygen 1s edge. [40,38] and the related electron-energy-loss technique (EELS) [50]. Because of its site and symmetry selectivity it was possible to show the nature of the states responsible for superconductivity. The results showed the growth of a pre-peak as a function of the doping concentration, which indicates the introduction of hole states, with predominantly oxygen 2p character, in the gap as the insulating parent compounds, like La_2CuO_4 and $\text{YBa}_2\text{Cu}_3\text{O}_6$, are doped with holes. One of the objectives here will be to see whether similar pre-peaks exist in the $\text{BaPb}_{1-x}\text{Bi}_x\text{O}_3$ -compounds.

The question of 'gap states' relates also to the origin of the band gap in the parent compounds. For the copper-oxide based superconductors it is now clear that the bandgap is caused by Mott-Hubbard correlation, but spectroscopic studies and cluster calculations showed that the lowest energy excitations across the gap actually have predominantly charge transfer character [51]. Following the Zaanen-Sawatzky-Allen model this means that the Mott-Hubbard correlation in the copper 3d-band (U) is much larger than the charge transfer to the oxygen (Δ), indicating that if holes are created they will have mainly oxygen 2p character [52]. Oxygen 1s x-ray absorption does not give direct evidence on such gaps, but it can be used to see if the spectral function is similar to the predictions from single particle density-of-states calculations or if correlation effects have to be taken into account explicitly (as for the copper-oxide based superconductors).

A final question which we believe may be partly answered by oxygen 1s x-ray absorption relates to the possible models to describe the influence of substitution of lead by bismuth. Here one can imagine models as a combined rigid band shift or the formation of superstructures due to (partial) ordering of lead and bismuth.

Density-of-states from electronic structure calculations

To understand the questions addressed here it is necessary to consider the results of single particle density-of-states calculations from the literature [47, 53–57]. For the purpose of this paper the density-of-states-calculation of Takegahara and Kasuyo [54], reproduced in figure 5.5 may be considered representative [58]. These calculations show that the occupied states around the Fermi energy are dominated by oxygen 2p character, while the unoccupied

states have mostly lead/bismuth and barium character. The main structure of the lead and bismuth compounds is rather similar but the Fermi level appears at higher energy with respect to these structures in the bismuth compound because bismuth has one more electron. BaPbO₃ is calculated to be metallic in accord with experiment; the number of charge carriers is of the order of $1 \cdot 10^{20} \text{cm}^{-3}$ [59]. For the bismuth compound experiment finds a bandgap of 0.3 eV (activation energy) [60] in contrast to the metallic result of the calculation. This discrepancy is attributed to a charge density fluctuation, with a tendency towards disproportionation of the bismuth-sites into Bi^V and Bi^{III} [47]. The existence of two different bismuth sites is confirmed by bismuth K edge extended x-ray absorption fine structure (EXAFS) [61, 62], but in bismuth 4f x-ray photoemission spectroscopy (XPS) [63–65] no clear indication for charge disproportionation is found.

Considerable effort has been put into trying to find suitable schemes to interpolate between the BaPbO₃ and BaBiO₃ limits and in order to explain the changes in superconductivity as a function of composition. Spectral studies of the occupied levels have also been made by photo-emission and they show negligible shift of the oxygen 2p levels as a function of composition [63, 66–70] in contrast to the calculated density-of-states results (see figure 5.5). In this paper we will follow the trends of the unoccupied states in the oxygen 1s x-ray absorption spectra, which should closely reflect the partial density of oxygen 2p states (which in turn reflect the peaks in the total density-of-states) as shown in figure 5.5. Our results will in fact show that there is as little agreement between theory and experiment for the unoccupied states as for the occupied states and that in both cases the problem lies in a much smaller experimental shift than predicted between the observed structures in BaPbO₃ and BaBiO₃.

Experimental

The x-ray absorption measurements were carried out at the Berliner Elektronen-Speicherung Gesellschaft für Synchrotronstrahlung (BESSY), using the SX700(I) plane grating monochromator [71]. The experimental resolution was 0.5 eV half-width half-maximum (hwhm). The spectra were recorded in total electron yield mode and were normalized to the beam current. The pressure during measurements was in the 10^{-10} torr range. To calibrate the energy we measured TiO₂, and vanadium-metal, using the EELS data of Fink et al. [72] as reference.

The samples were prepared in air by solid state reaction of BaCO₃, PbO₂ and Bi₂O₃ powders with two intermittent regrindings. For the final heat treatment the powders were pressed into pellets. Each heat treatment lasted 24 hours. For samples up to $x = 0.5$ a temperature of 880 degrees Celsius was used in the final sintering, for the higher bismuth concentrations a slightly lower temperature of 830 degrees Celsius was used. X-ray diffraction confirmed the lattice structure and no evidence for impurity phases was observed. The pellets were mounted with conducting paste to a grounded sample-holder and placed in the UHV system. At a pressure of about 10^{-9} torr the samples were scraped with a ruby file. The reproducibility was tested by re-scraping.

To compare the calculated oxygen *p* projected density-of-states to experiment, the density-

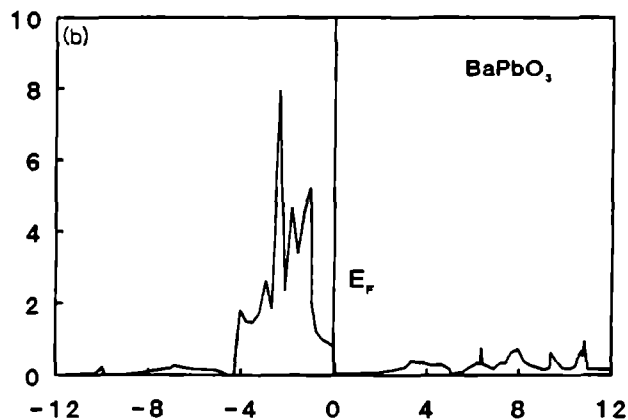
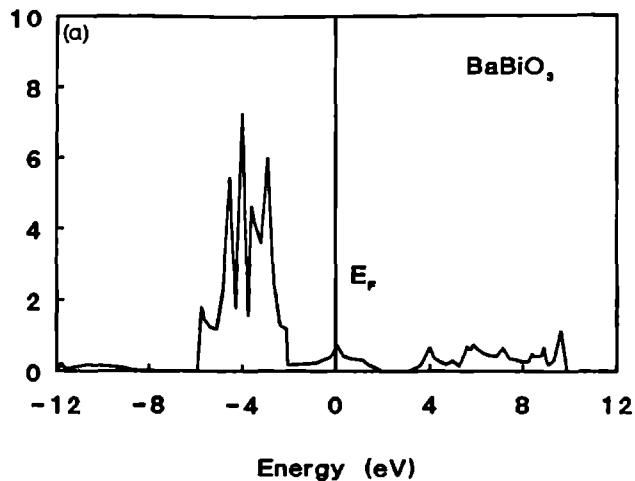


Figure 5.5: The oxygen p -projected density of states for (a) BaBiO_3 and (b) BaPbO_3 , as calculated in Ref. 54.

of-states is broadened with a Lorentzian of 0.3 eV to simulate the core-hole lifetime and convoluted with a Gaussian of 0.5 eV to simulate the experimental resolution of the SX700(I) monochromator. As threshold we used the oxygen $1s$ x-ray photo-emission peak position, which was found to be at a constant value of 529.1 eV throughout the series [73].

Results and interpretation

The oxygen $1s$ x-ray absorption spectra of ten $\text{BaPb}_{1-x}\text{Bi}_x\text{O}_3$ compounds are shown in figure 5.6. The overall shape of the spectra is similar and shows three distinct features

in the first 15 eV above the edge. Unambiguous assignment of these peaks to features in the partial density-of-states of figure 5.5 is difficult, partly because the density-of-states calculation is unreliable at higher energies (because the energy-window of linearization is insufficient) and partly because of the absence of x-ray absorption matrix elements and possibly the neglect of the core hole effects [74].

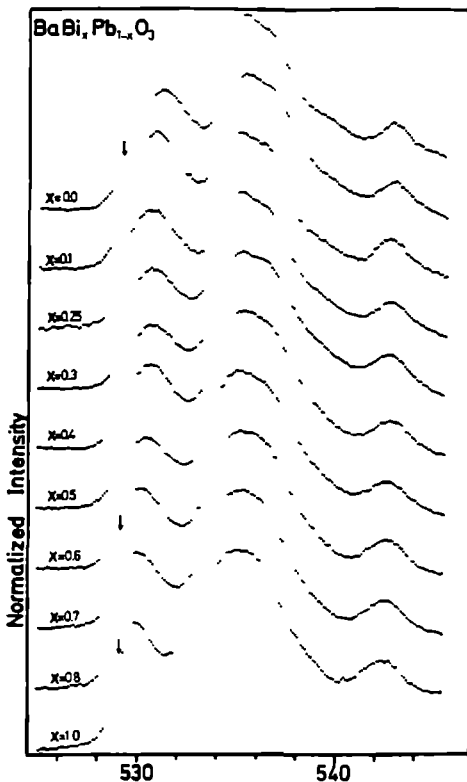


Figure 5.6: Oxygen 1s x-ray absorption spectra of a series of ten $\text{BaPb}_{1-x}\text{Bi}_x\text{O}_3$ compounds, measured with the SX700(I) monochromator at BESSY.

In figure 5.7 we compare x-ray absorption and oxygen p projected density-of-states for BaPbO_3 and BaBiO_3 . We tentatively assign the peak at about 536 eV, approximately 7 eV above threshold to the major peak seen in the calculated density-of-states about 9 eV above the Fermi level in BaPbO_3 and about 6 eV above the Fermi level in BaBiO_3 . This major feature changes shape somewhat as a function of composition but shifts considerably less than in the calculation.

The most interesting peak in the spectra of figure 5.6 is that nearest threshold which shifts gradually from from 529.8 eV for BaBiO_3 to 531.1 eV for BaPbO_3 . This shift is again much smaller than the shift predicted by the density-of-states calculation where a shift of about 3 eV is seen, together with some modifications of the shape. Neither can we see any pre-peak structure growing as a function of composition as was the case in copper oxide

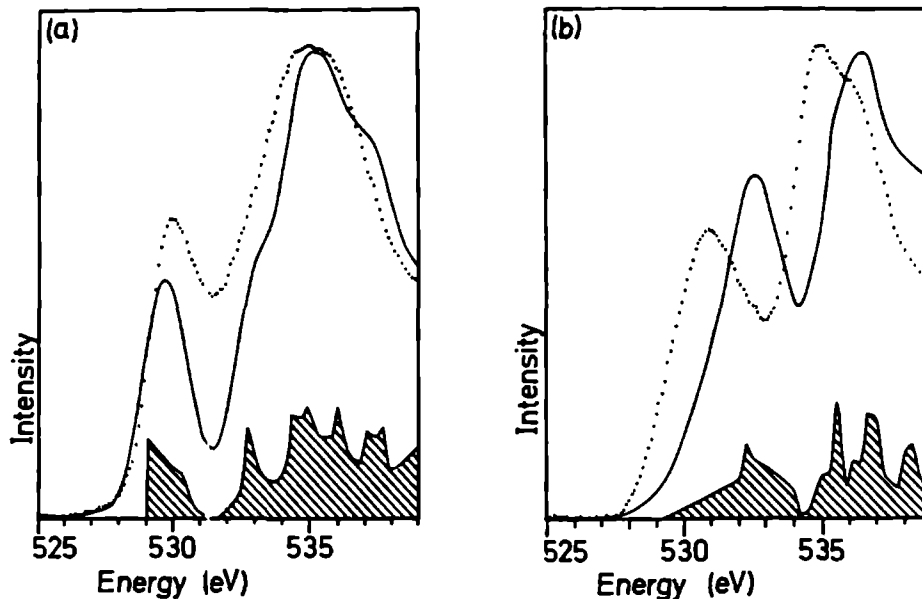


Figure 5.7: Comparison of the SX700(I) results with the broadened oxygen p density-of-states from Ref. 54. Comparisons are made for (a) BaBiO₃ and (b) BaPbO₃. The oxygen p density-of-states is given by the hatched area. The solid line gives the density-of-states broadened with a Lorentzian of 0.3 eV (fwhm), to simulate intrinsic broadenings, and a Gaussian of 0.5 eV (fwhm) to simulate the experimental resolution.

based superconductors like YBa₂Cu₃O_{7- δ} and La_{2- x} Sr _{x} CuO₄. In this our results disagree with the previously published oxygen 1s x-ray absorption data [75], where the authors claim the appearance of an extra feature at threshold as a result of doping with bismuth. The total absence of this pre-peak structure was confirmed by measurements taken with higher monochromator resolution [76, 77]. We stress that this marks a clear distinction with the copper oxide based superconductors, where the pre-peaks due to doping-induced gap states are the most important.

Discussion

For us the central discrepancy is that found for BaPbO₃ between the density-of-states and the oxygen 1s x-ray absorption peak positions (see figure 5.7). The following points will be discussed:

- The influence on the spectral function of the core hole

- Limitations of the single particle approach
- Stoichiometry effects
- Modifications in the density-of-states due to a calculation in the real crystal structure and to relativistic effects

Core hole effect

An effect which can play a role is the influence of the core hole. The spectral function of x-ray absorption relates, according to the final state rule, to the final state density-of-states. In general it can be stated that the core hole will cause a shift of spectral weight to lower energies due to the attractive core hole potential [78]. However we know of no case where oxygen $1s$ peaks are shifted by as much as 2 eV, which would be necessary to explain the present results [74].

Limitations in the single particle approach

A second reason for the discrepancy are modifications induced by the single particle approximation: Strictly speaking Eigenenergies in a density-of-states should not be equated with ionization energies and electron affinities. Ground state self energy shifts can have large effect on the gaps calculated for insulators but generally have small effect for states near the Fermi level in metals [79, 74].

Stoichiometry effects

According to Takegahara and Kasuyo [54], the discrepancy of the energy positions for BaPbO_3 can be due to extra oxygen vacancies which will shift the Fermi level. Because of the low density-of-states just above the Fermi level this effect can be considerable. For the related $\text{BaSn}_{1-x}\text{Sb}_x\text{O}_{3-\delta}$ -system, samples which were prepared differently showed differences in resistivity measurements, but from accurate weight measurements it was found that δ was maximally 0.01 [80]. To test this option for BaPbO_3 we repeated the x-ray absorption experiments for 6 samples prepared at different temperatures to influence the vacancy concentrations. They again had different resistivities and Hall-coefficients [81], but all oxygen $1s$ x-ray absorption spectra were found to be identical and no shift was observed. From this we conclude that the option of non-stoichiometry effects to explain the found discrepancy is unlikely.

Crystal Structure and Relativistic effects

Another factor which can play a role is that the calculations are performed in an ideal cubic structure. Mattheiss and Hamann [47] have repeated the calculations for BaBiO_3 and $\text{BaPb}_{0.7}\text{Bi}_{0.3}\text{O}_3$ for the real orthorhombic and tetragonal crystal structures and the differences are found to be small. Comparison of the oxygen p projected density-of-states of $\text{BaPb}_{0.7}\text{Bi}_{0.3}\text{O}_3$ in both crystal structures, results in a shift of the peak position, after

broadening, of only about 0.2 eV. From these results it can be expected that also for BaPbO_3 only minor effects are to be expected. A further approximation in the calculations is the treatment of the relativistic effects. Mattheiss and Hamann say that the spin-orbit coupling, neglected in their calculations, should only shift the Fermi level over about 0.1 eV, but we are measuring peaks with more lead character which are predicted some eV away from the Fermi level. We cannot tell if the approximations are less valid for such peaks, but suggest that this is one line of questioning that should be followed up.

Concentration dependence

A final problem relates to the electronic structure model for mixed $\text{BaPb}_{1-x}\text{Bi}_x\text{O}_3$. In figure 5.8 we plot the position of the first peak as a function of the bismuth concentration. A monotonic shift is observed. The discrepancy between calculation and experiment for BaPbO_3 robs us of a suitable reference point and we cannot fully judge the utility of the different models for treating this problem. Three prominent models are the combined rigid band model [57], the virtual crystal approximation [47] and a superlattice calculation [54]. The combined rigid band model uses the bandstructure results for BaBiO_3 and BaPbO_3 as input and the density-of-states of a mixed material is obtained by adding up the density-of-states of the pure materials with the Fermi energy shifted to adjust the number of introduced holes respectively electrons. As the density-of-states of BaPbO_3 is unreliable it is not possible to test this model in detail.

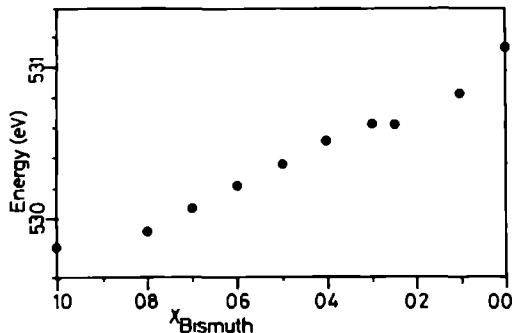


Figure 5.8: Maxima of the first peak in the oxygen 1s x-ray absorption spectra as a function of the bismuth concentration (x_{Bi}).

Another approach is the calculation of a NaCl superstructure of the lead and bismuth positions for $\text{BaPb}_{0.5}\text{Bi}_{0.5}\text{O}_3$. This approach can be excluded because the resulting density-of-states clearly shows a spurious double peak close to the Fermi level [54], whereas in the experiment there is only one peak, intermediate between the BaBiO_3 and BaPbO_3 cases.

A third model is the virtual crystal approximation [82]. In this model it is assumed that the combination of lead and bismuth atoms can be approximated with an artificial atom with an intermediate nuclear charge. Using this model a calculation is performed for $\text{BaPb}_{0.7}\text{Bi}_{0.3}\text{O}_3$ [47]. Figure 5.9 compares the broadened oxygen 2p density-of-states

with the experimental curve. The agreement in shape and position of the first peak is good. Thus like for BaBiO_3 ($x_{\text{Bi}} = 1$) also for $\text{BaPb}_{0.7}\text{Bi}_{0.3}\text{O}_3$ ($x_{\text{Bi}} = 0.3$) there is good agreement in peak position, in contrast to the situation for BaPbO_3 . Yet, in view of the gross oversimplifications of this model it is not clear what can be concluded from this agreement.

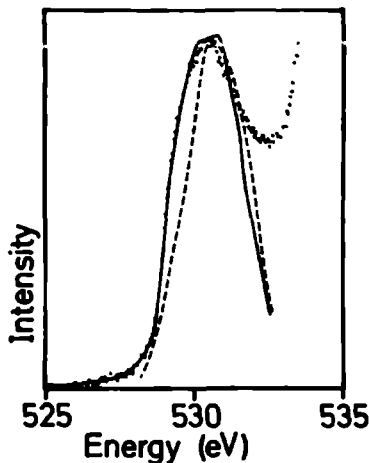


Figure 5.9: Comparison of the $\text{BaPb}_{0.7}\text{Bi}_{0.3}\text{O}_3$ x-ray absorption result with the broadened oxygen p density-of-states from Ref. 47 calculated in the virtual crystal approximation for cubic (dashed line) and tetragonal (solid line) crystal structures. The same broadening as in figure 5.7 is applied.

Concluding Remarks

We have presented an experimental study of the oxygen 1s x-ray absorption spectra of $\text{BaPb}_{1-x}\text{Bi}_x\text{O}_3$ oxides and have found that:

- No pre-edge peaks as in the copper oxide base superconductors exist and hence there is no evidence for gap states.
- We have found the shifts in the x-ray absorption spectra to be smaller than predicted by density-of-states calculations. This is a similar result to that found for the *occupied* states by photoemission studies [63,66–70]. We consider the discrepancies for BaPbO_3 crucial and they must certainly be cleared up before a proper theoretical understanding of the electronic structure of these materials can be achieved. We suggest that lines of investigation would be to include, one at a time, relativistic effects and core hole potentials in band structure calculations in the real crystal structure with a larger energy window in the unoccupied part of the density-of-states.
- This discrepancy obstructs detailed analysis of the mixing of BaBiO_3 and BaPbO_3 . The experiment shows a smooth trend in the position of the first maximum and a comparison with a virtual crystal calculation at $x_{\text{Bi}} = 0.3$ gives good agreement, suggesting that the discrepancy mainly occurs at the lead-rich side.

Acknowledgements

We are grateful to the staff of the Berliner Elektronen-Speicherring Gesellschaft für Synchrotronstrahlung (BESSY) for their support; we especially want to thank H. Petersen and W. Braun. This work was supported, in part, by the Committee for the European Development of Science and Technology (CODEST) program and by the European Community Large-Scale-Installation (EG-LSI) program. We thank I. van Vijfeijken for his support in the sample preparation.

5.3. Minerals

In mineralogy most questions are related to the determination of the crystallographic structures of the minerals, for example the determination of the distribution of sites for a specific metal ion. In contrast to fundamental science in which materials generally are purified to such extent that the idealized models concerning their crystallographic and electronic structure can be tested, the study of natural minerals additionally deals with the determination of the, for example geographical, varieties of a given species.

Section 5.3.1 deals with the role of titanium in minerals. As yet total electron yield is used as detection technique. In future it would be desirable to use fluorescence yield as a standard for the analysis of minerals in order to eliminate surface effects.

5.3.1. 2p x-ray absorption of titanium in minerals

This section has been submitted to Physics and Chemistry of Minerals.

F.M.F. de Groot¹, M.O. Figueiredo², M.J. Basto³, M. Abbate¹, H. Petersen⁴,
and J.C. Fuggle¹.

- 1 Spectroscopy of Solids and Surfaces, University of Nijmegen
Toernooiveld, 6525 ED Nijmegen, The Netherlands
Fax number: ++31-80-652604.
- 2 Centro de Cristalografia e Mineralogia,
Instituto de Investigação Científica Tropical
H Al.Afonso Henriques 41 – 4^oe, 1000 Lisboa, Portugal
- 3 Laboratória de Mineralogia e Petrologia
Instituto Superior Técnico
Av. Rovisco Pais 1, 1096 Lisboa, Portugal
- 4 Berliner Elektronenspeicherring- Gesellschaft
für Synchrotronstrahlung (BESSY)
Lentzeallee 100, 1000 Berlin 33, Germany

ABSTRACT

Titanium 2p x-ray absorption spectra for a series of minerals have been measured. Crystal field multiplet calculations can explain the spectral shape in detail. The asymmetry of the e_g peak is shown to be related to distortions of the Ti^{IV} octahedron. It is found, theoretically as well as experimentally, that the absorption spectra are more sensitive to tetragonal distortions than to trigonal distortions. A number of silicate minerals and metamict minerals containing titanium are measured and no Ti^{III} has not been observed in any of these minerals. A comparison is made to the 1s x-ray absorption, and the potential of both for the study of minerals is discussed.

Introduction

The use of x-ray absorption spectroscopy in mineralogy has until now largely been limited to the metal K edges, but there is a real need to investigate the potential of the $L_{2,3}$ edges. We choose an example from titanium mineralogy where the main questions are the valency of titanium and the geometry of its surroundings. Questions to be answered concern the possibility of tetrahedral site occupation, the existence of Ti^{III} and the site preference among the possible octahedral sites. titanium $1s$ (near edge) x-ray absorption spectra can give information on these matters, but it is mostly qualitative in nature [83]. In this study we measured the titanium $2p$ x-ray absorption edges, which can add extra information because of a more detailed theoretical understanding combined with considerably sharper structures due to better monochromator resolution and smaller intrinsic broadening.

In oxide minerals titanium has a strong tendency to be tetravalent and to be coordinated by six oxygens in an octahedral, or distorted octahedral site [84]. This situation occurs in binary and ternary oxide minerals, like anatase, rutile, brookite (all TiO_2) and ilmenite ($FeTiO_3$), where Ti^{IV} occupies distorted octahedral sites. In extreme cases titanium is forced to an alternative situation and it may become 5-coordinated as in the mineral fersnoite, $Ba_2TiO[Si_2O_3]$ or it may become tetrahedrally coordinated as in the compound Ba_2TiO_4 [85] or it can occur as Ti^{III} . For clarity we state that with the Ti^{IV} -notation we mean a formal valency of 4, like in $SrTiO_3$. The oxygen $2p$ -band, that is the band formed from the bonding combinations of oxygen $2p$ states and metal states (plus non-bonding oxygen $2p$ states), is completely filled for all transition metal oxides. Therefore the formal valency is directly related to the total occupancy of the transition metal $3d$ -band. As for $LaTiO_3$ the formal valency of titanium is 3, its titanium $3d$ -band will effectively contain one electron, whose character will be mainly titanium $3d$ but partly oxygen $2p$. In some minerals titanium occurs only as a minor constituent c.q. as an impurity. If for a titanium impurity the anti-bonding titanium $3d$ - oxygen $2p$ states (in other words the $3d$ -band) are empty the titanium is tetravalent, but if locally one extra electron is present, filling an anti-bonding state, this can be denoted as Ti^{III} .

The presence of Ti^{III} can be determined with optical spectroscopy, because of the strong transitions within the $3d$ -band. However in almost all natural minerals the presence of titanium is accompanied by the presence of iron and due to the partly filled iron $3d$ -band the analysis of the optical spectrum is complicated and the possibility to prove the existence of Ti^{III} difficult. Also the quantitative determination of the percentage of Ti^{III} from wet chemical analysis is not unquestioned [86]. If titanium occurs only a minor constituent, it is often tacitly assumed that for example in pyroxenes or amphiboles, titanium will fill the tetrahedral sites in cases where the amount of silicon (and aluminium) is insufficient. This assumption is heavily debated [83] and it is as yet not resolved because of the difficulty to attain conclusive information on this problem.

In this paper we will address the questions regarding the site-preference, site geometry and valency from the viewpoint of the electronic structure, by making use of the titanium $2p$ x-ray absorption edges. The advent of synchrotron radiation sources and high-resolution soft x-ray monochromators created a novel experimental set-up for detailed x-ray absorption

studies, ideally suited for the study of the electronic structure. The use of x-ray absorption in mineralogy has until now largely been limited to the hard x-ray metal K edges [83]. Analysis of the x-ray absorption near edge structure (XANES) revealed correlations between the positions of the multiple scattering peaks and the mean oxygen-titanium distance. Also correlations have been found between the ($1s \rightarrow 3d$) prepeak intensity and the octahedral site distortions and it was found that Ti^{III} has a main edge shift of approximately 2 eV with respect to tetravalent titanium [83,87]. Analysis of the extended x-ray absorption fine structure (EXAFS) spectrum can reveal the nearest neighbour distances [88], being particularly useful for non-crystalline specimens.

However the soft x-ray metal $2p$ or $L_{2,3}$ edges, and the equivalent electron energy loss (EELS) spectra [89,90], deserve attention too: The progress in soft x-ray monochromators have made it possible to measure the titanium $2p$ x-ray absorption edges at about 450 eV with a resolution better than 0.1 eV half width half maximum [91,92], far better than the resolution obtainable at the titanium K ($1s$) edge. The $2p$ spectra of $3d$ -metal compounds are completely dominated by the strong $2p \rightarrow 3d$ dipole transitions and the spectra show fine details as shown in figure 5.10. In the $1s$ x-ray absorption spectra the $3d$ -states are only visible as the small 'pre-edge' structures and the main edge relates to the $4p$ -band. The possibility to measure structures with a sharpness up to 0.1 eV creates a powerful tool to study the electronic structure of solids in more detail. With the results of these high resolution data the theoretical methods to establish the electronic structure in minerals can be made more accurate, creating a more complete picture of the chemical bonding. Before presenting the experiments we will shortly discuss the theoretical background for the analysis of the titanium $2p$ x-ray absorption spectra.

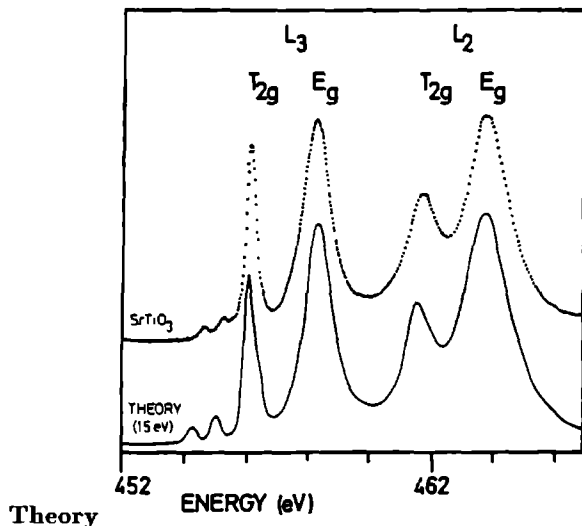


Figure 5.10: Titanium $2p$ x-ray absorption spectrum of $SrTiO_3$ taken with the SX700(II) monochromator, compared with the theoretical atomic multiplet calculation (bottom) and the cubic crystal field calculation with a strength ($10Dq$) of 1.5 eV.

Theory

The x-ray absorption spectral function is described according to Fermi's Golden rule:

$$\sigma(E_{h\nu}) \sim \sum |\langle \phi_i | \mathcal{H} | \phi_f \rangle|^2 \cdot \delta(E_i + E_{h\nu} - E_f)$$

E_i , $E_{h\nu}$ and E_f are respectively the energy of the initial state, the x-ray and the final state. \mathcal{H} is the Hamiltonian describing the interaction of x-rays with matter for which the dipole approximation is used [93]. To calculate the spectral function it is thus necessary to find the initial and final state energies and wave functions. A central criterion for treatment of this problem for a specific x-ray absorption edge is the influence of the core hole on the final state wave functions [94]. For the metal K edge the $1s$ core hole does not usually dominate the spectral shape, although its attractive potential can distort the spectra. Therefore the theoretical models to determine the spectral shape are based on finding the projected density of states by an electronic structure calculation. Alternatively a multiple scattering calculation can be performed; both methods are proven to give equivalent results, provided they are applied without further approximations [95]. However the computational problems are still too complicated to calculate the x-ray absorption spectral function without a series of approximations. The multiple scattering results for rutile and anatase show that one still has to improve upon these approximations considerably [90]. In contrast to the $1s$ edges the titanium $2p$ edges are dominated by the coupling of the $3d$ electron with the $2p$ core hole. This problem has until now only been solved by a crystal field multiplet model; the atomic multiplet spectrum is calculated [96] and the wavefunctions are projected to cubic symmetry. The cubic crystal field strength is fitted to experiment [97].

As an example to explain the general spectral features we show in figure 5.10 the titanium $2p$ x-ray absorption spectrum of SrTiO_3 [98]. The experimental spectrum is compared with the crystal field multiplet spectrum for the $3d^0 \rightarrow 2p^5 3d^1$ transition of Ti^{IV} , with a cubic crystal field strength of 1.5 eV. As reference also the atomic multiplet spectrum is given. With this approach all six peaks can be explained in a uniform way: The first two small peaks are related to a transition which is forbidden in LS-coupling, but which becomes allowed because of the multipole pd interactions. The third and fourth peaks can be related to respectively the t_{2g} and the e_g symmetries of the L_3 edge. They are repeated for the fifth and sixth peak for the L_2 edge. The splitting between the third and fourth peak relates closely to the cubic crystal field strength¹. All details of the L_2 edge are blurred, because the intrinsic broadening is considerably larger than for the L_3 edge, due to an extra Auger decay channel.

SrTiO_3 is cubic. For compounds in which the titanium octahedron is distorted, like for rutile, it is necessary to project the cubic symmetry further to the D_{2h} point group symmetry of the titanium atom. Distortions from cubic symmetry will give rise to modifications in the spectrum. Calculations in which the symmetry was lowered to tetragonal and trigonal symmetry revealed that the e_g part² of the spectrum is more strongly modified by these distortions. Figure 5.11 illustrates this with some representative examples. It can be seen that a tetragonal distortion has a considerably larger effect on the spectrum than a trigonal distortion. The calculation for a tetrahedral surrounding is clearly different from the octahedral one, which in fact will identify titanium in tetrahedral surroundings. The calculation for Ti^{III} shows more structure because of the increased number of final states of the $2p^5 3d^2$ -multiplet [99].

¹However the splitting is not generally *equal* to the cubic crystal field, see [97].

²Strictly speaking the description e_g is not longer appropriate for lower symmetries

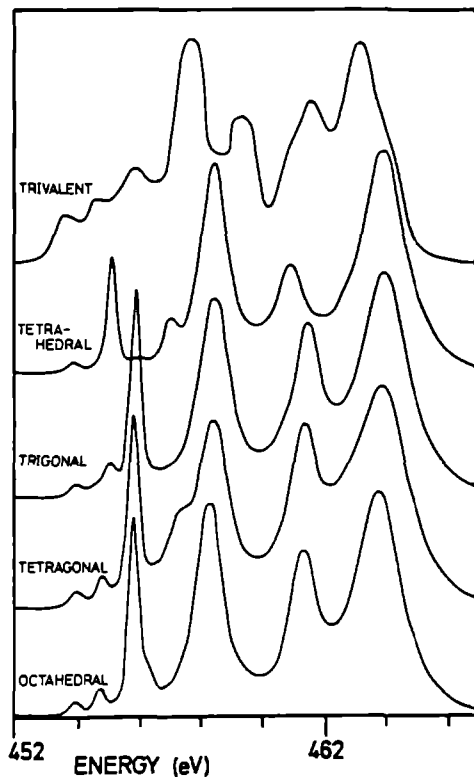


Figure 5.11: Crystal field multiplet calculations. In all spectra the cubic crystal field strength ($10Dq$) is 2.1 eV. From top to bottom: a calculation in octahedral symmetry, tetragonal (D_{4h}) symmetry, trigonal (D_{3d}) symmetry, tetrahedral symmetry ($10Dq = -2.1$ eV) and a calculation for Ti^{III} ($3d^1 \rightarrow 2p^5 3d^2$).

Experimental

The x-ray absorption spectra were measured with the SX700(I) monochromator [91] at the Berliner Elektronenspeicherring-Gesellschaft für Synchrotronstrahlung (BESSY). The monochromator resolution was about 0.5 eV (hwhm) for the titanium 2*p* edge at 450 eV. The energy calibration of the monochromator was set by comparing the titanium 2*p* and oxygen 1*s* spectra of rutile to spectra published previously [100]. The spectra were recorded in total electron yield mode (see discussion). They have been corrected for intensity loss of the beam during measurement. All samples, with the exception of the metamict minerals, were scraped with a ruby file to ensure surface cleanliness. The measured minerals are listed in table 5.2.

Results and Interpretation

Figure 5.12 shows the titanium 2*p* x-ray absorption spectra of $FeTiO_3$ (ilmenite) and of TiO_2 in three different crystal structures. The spectra are normalized to the peak height and for minerals with only minor titanium content an extra, linear, background correction had to be performed to correct for the sloping background. In these binary and ternary

Material	Source	Formula	Ref.
Anatase	Blue Piz Switzerland	TiO ₂	[101]*
Rutile	Saint Yrieix Limoges, France	TiO ₂	[101]**
Brookite	Crystal fragment (location unknown)	TiO ₂	[101]*
Ilmenite	Blåfjell Norway	FeTiO ₃	[102]
titanite	Renfrew, Canada	CaTiSiO ₅	[101]**
Ti-Augite	Santiago Island Capo Verde	(Ca,Na)(Mg _{0.82} Fe _{0.22} Al _{0.02} Ti _{0.04})- -(Si _{1.8} Al ₂) ₂ O ₆	[103]
kaersutite	Fogo Island Capo Verde	Ca ₂ Na(Mg,Fe) ₄ Ti- -(Si _{1.6} Al ₂) ₂ O ₂₂ (OH) ₂	[104]
Melanite- Schorlomite	North Santiago Island Capo Verde	Ca ₃ (Fe,Ti) ₂ (Si,Ti) ₃ O ₁₂	[105]

Table 5.2: Minerals: Origin and chemical formula.

*Samples from the international collection of the late Mineralogical and Geological Museum, Lisbon University [106].

**Samples from the mineralogical collection of the Bensaude Museum, IST, Technical University of Lisbon.

oxide minerals the local titanium geometries are known accurately: In rutile and anatase the main distortion is the elongation of one axis to form a tetragonal surrounding. There are additional distortions (on the angles) to lower the symmetry as indicated in table 5.3. Because of this distortion the e_g peak is split in agreement with the calculations in figure 5.11 which indeed found the e_g -peak splitting to be most sensitive to tetragonal symmetry-lowering. Ilmenite does not show any significant splitting of the e_g peak, which reflects the predicted insensitivity of the spectral shape to trigonal distortions. In figure 5.12 the two prepeaks are barely visible because the resolution (~ 0.5 eV) is not as good as that of the SrTiO₃ spectrum in figure 5.10.

Figure 5.13 shows the spectra of four silicate minerals containing titanium. In silicate minerals oxygen is bonded to a great variety of cations, with the consequence of another type of behaviour as compared to the binary oxides.

- kaersutite contains three possible octahedral sites for titanium, labelled M1, M2 and M3 in the usual site nomenclature for amphibole minerals. A number of neutron scattering structural refinement studies have been performed on several amphiboles [112–114]. The results are not uniform and titanium is assigned to different sites in different studies. The observed spectrum for kaersutite consists of four structureless peaks, from which it is difficult to extract any clear information. From the absence of the asymmetry in the e_g peak it can

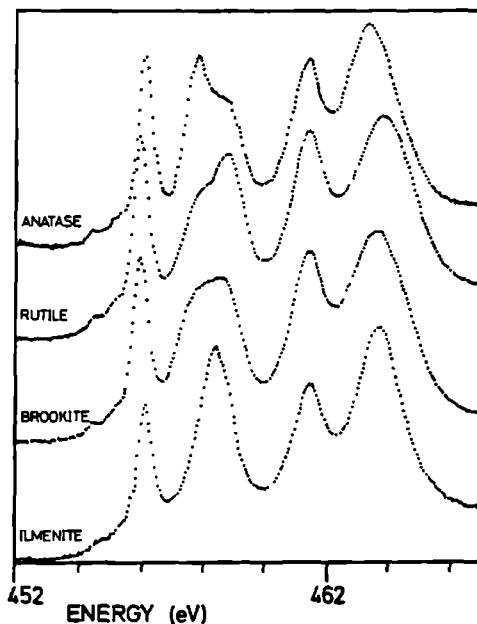


Figure 5.12: 2p x-ray absorption spectra of the minerals rutile, anatase, brookite and ilmenite.

Sample	Symmetry	Metal-oxygen bond length (Å)	Mean (Å)	Ref.
Anatase	D_{2d} ($42m$)	1.937 (4) 1.983 (2)	1.952	[107]
Rutile	D_{2h} (mmm)	1.946 (4) 1.984 (2)	1.959	[108]
Brookite	C_1 (1)	1.87 1.92 1.94 1.99 2.00 2.04	1.96	[109]
Ilmenite	C_3 (3)	1.874 (3) 2.088 (3)	1.981	[110]
titanite	C_1 (1)	1.76 1.97 1.98 2.00 2.01 2.02	1.96	[111]

Table 5.3: Minerals: metal-oxygen bond lengths and site symmetry.

be concluded that the titanium sites are not be (tetragonally) distorted.

• Ti-augite shows a unique feature in the extremely broad t_{2g} peak; this suggests that titanium occupies different sites. A partial occupation of higher coordination sites (M2) or tetrahedral sites will broaden the t_{2g} peak as the sharp t_{2g} -peaks of the subsequent sites are replaced from each other. The broadening cannot be related to the site-distortion of a single site due to the insensitivity of the t_{2g} -peak to distortions.

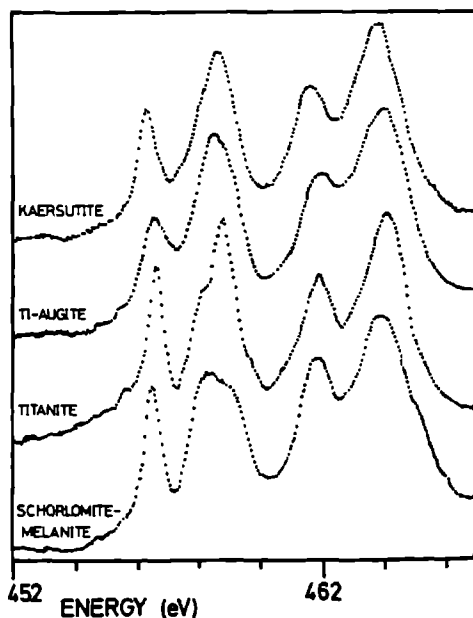


Figure 5.13: 2*p* x-ray absorption spectra of the minerals titanite, Ti-augite, kaersutite and melanite-schorlomite.

- titanite is a well studied mineral; its most interesting feature is the existence of an extremely short titanium-oxygen distance of 1.76 Å. The titanium is furthermore surrounded by 5 more or less equidistant oxygens (see table 5.3). The titanium 2*p* x-ray absorption spectrum of titanite is rather sharp. The e_g peak clearly has a shoulder on the low energy site, which can be related to the energy-difference between the $d_{x^2-y^2}$ and the d_{z^2} orbitals due to the interaction with the closeby oxygen.

- The melanite-schorlomite garnet should contain titanium in octahedra [115]. The spectrum surprisingly shows a broad e_g peak, which as discussed is a signature of a clear (tetragonal) symmetry distortion. As yet this discrepancy is unresolved and a more detailed study of garnets must give an answer to this problem.

In summary we conclude that the complications of the silicate minerals are too large to relate the 2*p* x-ray absorption spectra unambiguously to a specific phenomenon. Nevertheless as indicated the spectra can add important information as to limit the range of possibilities. In combination with other available techniques a more definitive answer regarding the site distortions and admixtures will have to be formulated.

Figure 5.14 contains the titanium 2*p* x-ray absorption spectra of perierite from four different localities (Mozambique, India, Japan and Madagascar). In table 5.4 the chemical composition of these metamict³ minerals is summarized [116]. The four spectra are rather similar and consist of four peaks. The e_g peak is unstructured which indicates that the Ti-octahedra are not strongly distorted. There is some variation in the sharpness of the t_{2g}

³Metamict minerals are minerals which contain radioactive constituents, which in the course of time have destroyed the long range crystal structure

peak; perrierite from Mozambique has a considerable sharper t_{2g} peak and this is therefore expected to contain a more uniform distribution of titanium sites. However these samples could not be scraped because of which the small differences could be due to surface contamination and further study on other samples and preferably with fluorescence yield is clearly necessary.

Constituent	Ifasina	Bangalore	Bingre	Kobe
	%	%	%	%
TiO ₂	16	17	16	16
ThO ₂	1	2	0	2
RE ₂ O ₃	21	20	27	26
CeO ₂	22	19	19	19
Fe ₂ O ₃ *	11	9	9	9
CaO**	2	8	4	4
Nb ₂ O ₅	1	0	1	1
SiO ₂	26	25	24	23

Table 5.4: Metamict Minerals: Approximate contents. For a full account of the contents see [116]. RE means yttrium plus the rare earths La, Pr, Nd, Sm, Gd, Dy, Er and Yb.

*Including minor contents of MnO₂.

**Including minor contents of PbO and SrO.

Discussion

Electronic structure and site geometry

From comparison to calculations conclusions regarding the site geometry and the valency can be drawn. However the combined possibilities of trivalent titanium, site distortions and multiple site occupation generates a complicated problem. For silicate minerals, with in general only minor titanium contents, no definitive results can be obtained from titanium $2p$ x-ray absorption alone. In future studies the variations of the titanium $2p$ x-ray absorption spectra within a mineral-group of for example garnets will be checked in detail. The spectra contain enough features sensitive to small variations in site symmetry and given the detailed theoretical simulations these variations can be related to the effects discussed.

Even more important will be to relate the titanium $2p$ x-ray absorption spectrum to other x-ray absorption edges of the same compound. The titanium $1s$ edge (see below), the oxygen $1s$ edge and for most compounds also the iron $1s$ and $2p$ edges contain additional information and a combination of all these spectra will create a more complete picture of the electronic structure. In this respect especially the oxygen $1s$ edge can prove to be important. The oxygen $1s$ x-ray absorption spectra reflect closely the energy distribution of unoccupied oxygen p -states [117,100]. For $3d$ transition metal ions the first empty states will have a combined metal $3d$ -oxygen $2p$ character and these states will appear clearly

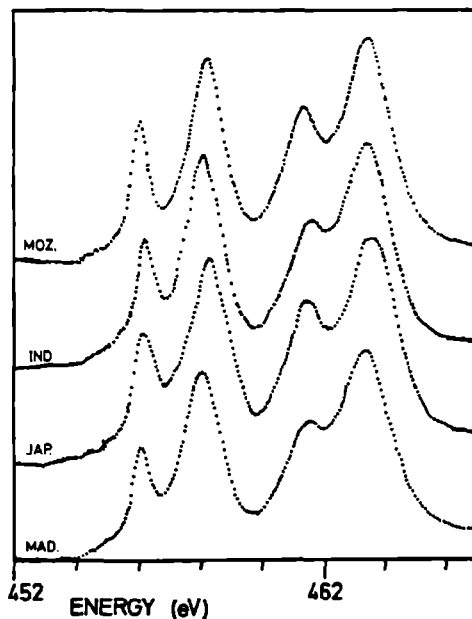


Figure 5.14: 2*p* x-ray absorption spectra of four metamict minerals.

before the anti-bonding oxygen-silicon states. Therefore the states at the oxygen 1*s* edge will contain information about the bonding to the metal 3*d* states. For example preliminary results for kaersutite indicate that the 3*d*-part of the oxygen 1*s* spectrum is dominated by oxygen 2*p*-iron 3*d* states.

Comparison of the titanium 2*p* and 1*s* x-ray absorption spectra

Comparing the titanium 1*s* [83] with the titanium 2*p* x-ray absorption spectra one can conclude that both edges are sensitive to the site symmetry. The 2*p* edge is dominated by the 2*p* → 3*d* transitions, whereas the 1*s* edge is dominated by 1*s* → *p* transition with the 3*d*-band region as small 'pre-edges' only. Therefore the theoretical approaches are quite different: The crystal-field multiplet model accounts well for the 2*p*-edge and the 1*s* edge should in principle be largely explained by a band structure (or multiple scattering) calculation [90]. Due to its relatively straightforward calculational method it is possible to relate the crystal-field multiplet results closely to the site geometry as discussed before. Such a detailed interpretation of the spectra is not yet possible for the 1*s* edge. Furthermore the sharpness of the spectral features, due to intrinsic as well as experimental broadening effects is considerably smaller for the 2*p* edges. The sharpest features seen for oxides are the first peak of the 2*p* edge of titanium in SrTiO₃, given in figure 5.10, with a half-width half-maximum of 0.2 eV; for the 1*s*-edges the first pre-peak of titanium in TiO₂ has a half-width

half-maximum of about 0.6 eV [118,119] Because of this difference in obtainable resolution, the $2p$ edges are to be preferred for considerations concerning the electronic structure. However an important feature of the $1s$ edges is that the delocalized p states and especially the EXAFS region can be measured. For the $2p$ edges this is virtually impossible because of overlapping L_3 and L_2 spectra and the presence of the oxygen $1s$ edge at approximately 530 eV.

The conclusions of both the $1s$ edges and the $2p$ edges with respect to the valency determination are similar. Ti^{III} gives a completely different $2p$ spectrum and for the $1s$ edge the main edge is shifted by about 2 eV, making the identification of trivalent titanium in principle straightforward. However the existence of small amounts of Ti^{III} are difficult to detect in both methods if the spectrum is dominated by the signal from Ti^{IV} . These difficulties can be overcome if one measures standards of similar structure. For the $2p$ edge this has been shown for the $La_xSr_{1-x}TiO_3$ system [98].

The average Ti-O distance will be related to the cubic crystal field parameter [120]. This will be reflected in the t_{2g} - e_g splitting, and intensity ratio, of the $2p$ spectrum [97]. This can be checked in the spectra: rutile and anatase have considerably larger splittings and t_{2g} intensities. As it is difficult to find a simple quantitative measure from the spectra, because of the splitting of the e_g peak and the variations in the broadenings, we did not try to determine a quantitative measure. As far as the $1s$ spectra are concerned we believe that the t_{2g} - e_g splitting is reflected in the distance between the first two small leading peaks, in contrast with the more general assignment which relates the second and third peak to respectively the t_{2g} and e_g peak with a so-called 'excitonic feature' in front [83,89]. In figure 3. of Ref. 83 a clear reciprocal relation of this splitting with the nearest neighbour distance can be seen. As discussed it would be advantageous to combine both methods. For the oxide minerals with titanium this has been done by Brydson et al. [90]. However especially for the silicate minerals, where the titanium sites are not *a priori* known, a combination of titanium $1s$ and $2p$ x-ray absorption would be of great interest.

Experimental aspects

Until now $2p$ x-ray absorption studies have been performed mostly on ordered solids. For these materials the crystal structures are generally known in detail and the main objective is to elucidate the electronic structure of the $3d$ -states in detail by comparison to the crystal field multiplet calculations. Mostly the oxygen $1s$ edge is measured additionally and compared to electronic structure calculations. In mineralogy the situation is different. As the materials are in general much more complex and no detailed electronic structure calculations can be performed, the analysis of the spectra must be done by comparison to known standards. Furthermore there are variations from one sample to the other and sometimes also within a sample and the determination of these variations is an important goal in mineralogy.

An important experimental aspect is the probing depth of x-ray absorption. In the total electron yield mode the probing depth is, in case of oxides, in the order of 50 Å [121]. Though this will be in general deep enough to ensure a bulk-measurement, it will be advantageous

to measure minerals with fluorescence yield [122,123], with a probing depth in the order of 1000 Å. Fluorescence yield is also the preferred mode for dilute samples.

A potential future development can be found in the angular dependent detection of the 'x-ray absorption' spectrum. Taftø and Krivanek [124] used the diffractive variation of the electron energy loss spectrum, which is identical to the x-ray absorption spectrum [89], to determine the valency of iron in a site selective manner: They measured the iron $L_{2,3}$ edge at two diffraction spots which had different contributions from respectively octahedral and tetrahedral sites. The obtained spectra are clearly different and though the original interpretation of the spectral shapes is in contradiction with present models [99], the most important conclusion is that it is actually possible to measure these effects. Therefore we expect that future developments in detection techniques will make possible measurements of the spectral shapes at different diffraction positions with EELS, x-ray Raman [125] and possibly x-ray absorption, though technically more difficult due to a relatively large variation in energy (thus direction of diffraction).

Concluding remarks

We have shown that the $2p$ x-ray absorption spectra can be explained in detail by crystal field multiplet calculations. The asymmetry of the e_g peak is shown to be related to distortions of the Ti^{IV} octahedron. It is found theoretically that the absorption spectrum is more sensitive to tetragonal distortions than to trigonal distortions. This is confirmed experimentally: The spectra of anatase and rutile show a clear asymmetry whereas ilmenite has a symmetric e_g peak.

The $2p$ x-ray absorption edges of silicate minerals are quite distinct from each other, which offers the possibility to use the spectra as a fingerprint. The possible variations in the spectra within a class of minerals remain to be checked. Ti^{III} was not observed in any of the minerals, though minor concentrations will not be detected easily.

We have shown that titanium $2p$ x-ray absorption spectra are sensitive to details of the local chemical environment and can play an important role in the determination of the electronic structure and the site geometry of titanium in minerals. A combination with other x-ray absorption edges, specifically the titanium $1s$ and the oxygen $1s$ edge, will reveal significantly new information regarding the electronic structure and chemical bonding in minerals.

Acknowledgements

We are grateful to the staff of the Berliner Elektronen-Speicherring Gesellschaft für Synchrotronstrahlung (BESSY) for their support; we especially want to thank Dr. W. Braun. We thank Prof. G.A. Sawatzky and Dr. B.T. Thole for discussions and for the development of the crystal field multiplet program. This work was supported by the European Community Large Scale Installation (EG-LSI) program and the Dutch foundation for Chemical Research (SON) with financial support from the Dutch Foundation for Science (NWO), and the Dutch Foundation for Fundamental Research into Materials (FOM).

5.4. Surfaces

In this section the use of x-ray absorption for the study of surfaces is discussed. With ion-yield detection the probing depth of x-ray absorption is limited to only one atomic layer, which makes it an ideal tool for the study of clean surfaces. Furthermore because the surface breaks the three-dimensional symmetry, the use of polarization dependent measurements can reveal directional information of the surface states.

5.4.1. Fine structure of the calcium 2p x-ray absorption edge for bulk compounds, surfaces and interfaces

Reproduced from *Physical Review B.*, volume **43**, page 6899 - 6907 (1991).

ABSTRACT

In this study the possibility to determine non-cubic crystal field parameters is studied. A detailed comparison is made between the (polarization dependent) crystal field multiplet calculations in O_h as well as C_{3v} symmetry, with the polarization dependent calcium 2p x-ray absorption spectra of the $\text{CaF}_2/\text{Si}(111)$ -system. A series of other calcium compounds are measured as reference. The final goal of the study is to elucidate the electronic structure of the CaF_2 -surface and the $\text{CaF}_2/\text{Si}(111)$ interface.

Fine structure of the Ca 2p x-ray-absorption edge for bulk compounds, surfaces, and interfaces

F J Himpsel, U O Karlsson,* A B McLean,[†] and L J Terminello

IBM Research Division, Thomas J Watson Research Center, P O Box 218, Yorktown Heights, New York 10598

F M F de Groot, M Abbate, and J C Fuggle

Research Institute for Materials, University of Nijmegen, Toernooiveld, 6525 ED Nijmegen, The Netherlands

J A Yarmoff

Department of Physics, University of California, Riverside, California 92521

B T Thole and G A Sawatzky

Materials Science Centre, University of Groningen, Nijenborgh 18, Paddepoel, 9747 AG Groningen, The Netherlands

(Received 15 October 1990)

The fine structure of the Ca 2p soft-x-ray-absorption edge is studied for a variety of bulk compounds (Ca metal, CaSi₃, CaO, and CaF₂), for surfaces and interfaces (CaF₂(111), BaF₂ on CaF₂(111), Ca and CaF₂ on Si(111)), and for defects (*F* centers in CaF₂). The observed multiplet structure is explained by atomic calculations in a crystal field [cubic *O_h* for the bulk and threefold *C_{3v}* for the (111) surfaces and interfaces]. While the bulk spectra are isotropic, the surface and interface spectra exhibit a pronounced polarization dependence, which is borne out by the calculations. This effect can be used to become surface and/or interface selective via polarization-modulation experiments, even for buried interfaces. A change in valence from Ca²⁺ to Ca¹⁺ causes a downwards energy shift and extra multiplet lines according to the calculation. The energy shift is observed for *F* centers at the CaF₂ surface and for the CaF₂/Si(111) interface.

I. INTRODUCTION

The fine structure of x-ray-absorption edges is a useful probe for the structural environment of atoms and their chemical state.¹⁻³ For example, there is a relationship between the fine structure of the absorption edge and the oxidation state, or valence, of the absorbing atom. A program correlating the multiplet structure of an absorption edge with the valence has been successfully carried out for the rare earths.^{2,1} Similar attempts are beginning to take hold for transition metals.⁴⁻¹⁴ The task is more difficult for the latter, since the atomic multiplet splittings are smaller. Consequently, they are affected by the crystal field and broadened by band formation. Despite these difficulties, it has been possible in some cases to identify the valence and even the spin alignment¹¹ from the multiplet structure. The knowledge of the valence is important for materials as diverse as high-temperature superconductors¹⁶⁻¹⁹ and metalorganic compounds¹⁰ (phthalocyanines, hemoglobin, chlorophyll).

A second avenue is just opening up, i.e., the spectroscopy of buried interfaces. The main difficulty is to penetrate the overlayer, and still be sensitive to a monolayer at the interface. It has been pointed out that the core level and Auger shifts at the interface can be used to become interface selective.²⁰ In addition, the lower symmetry of the interface causes anisotropy, which distinguishes interface transitions from bulk transitions by their polarization dependence. The same arguments apply to surfaces. Polarization-modulation spectroscopy at core-level absorption edges could become a viable tool

when using the high brilliance of undulator-based synchrotron radiation sources. This method would pick out the interface (surface) contribution in a clean way, even for buried interfaces, where very few techniques are available.

The Ca 2p edge is a prime candidate for testing the feasibility of these concepts. The fine structure is very sharp, since it is mainly due to localized Ca 2p-to-3d transitions.^{21,22} Therefore an atomic picture is a good starting point. Ca has been the subject of widespread interest, ranging from biology to semiconductor physics. For example, microscopy of Ca-containing bone tissue has been performed with x rays at the Ca 2p absorption edge.²³ The CaF₂/Si(111) interface has been studied extensively,^{20,24-30} because of its high structural quality, and interface-related structures have been observed at the Ca 2p absorption edge.^{20,25,27} Here we aim at an in-depth understanding of the fine structure for various model compounds, surfaces, interfaces, and defects. For this purpose we correlate the experimental spectra with calculations of the atomic multiplet structure that include the effect of the crystal field, valence changes, and the lowering of the symmetry at surfaces and interfaces.

II. EXPERIMENT

The experiments were carried out with a 10-m toroidal grating monochromator¹¹ (TGM), combined with a display spectrometer³² at the National Synchrotron Light Source at Brookhaven. Core-level absorption was measured by detecting Auger electrons, which are proportional to the number of core holes created in the absorber.

tion process. In some instances we also collected secondary electrons and photoadsorbed positive ions. The latter were used to obtain a signal from the immediate surface region. Auger and secondary electrons gave similar results,³³ as long as the energy detection window for Auger electrons was kept sufficiently wide (9 eV in our case) to cover the main part of the Auger multiplet structure.^{20, 27, 34-36} By selecting portions of the Auger spectrum it was possible to enhance certain members of the absorption edge multiplet (see Fig. 4). Similarly, the energy shift between bulk and interface Auger peaks^{20, 27} could be used to selectively enhance bulk or interface features, depending on the placement of the energy window. It should be noted that the cross section in the main Ca 2*p* absorption lines of CaF₂ is so large that saturation effects are encountered, particularly when the incident light is close to grazing. In this case the escape depth of the Auger (secondary) electrons becomes larger than the absorption depth of the light, and all core holes contribute to the electron yield, independent of the absorption coefficient. As noted early on,³⁷ this violates the principal premise of absorption spectroscopy in the partial-yield mode, which requires that the electron escape depth is small compared to the photon absorption depth. The polarization was varied from *s* polarization, with light incident normal to the sample surface, to *p* polarization with light incident about 60° from normal.

The samples were prepared as follows. CaF₂ was grown epitaxially^{20, 24, 40} on a clean Si(111)7×7 surface at about 700°C, with postanneals in the 800°C–850°C range, depending on thickness. Cleaved single crystals were also used, but they gave broader structures, since heating was required to avoid charging. CaO single crystals³⁸ were cleaved and heated. Ca was evaporated CaSi₂ was prepared by evaporating Ca onto Si and annealing.³¹ For thin epitaxial CaF₂ films on Si(111) the thickness could be monitored by observing the Ca 2*p* and Ca 3*d* core level intensities of the shifted interface peak²⁴⁻²⁸. It should be noted that the ionic Ca compounds are very sensitive to radiation damage⁴⁰⁻⁴² (see also Sec. VI). However, the dose to collect an absorption spectrum with the efficient display spectrometer¹² was about 10³ times less than that required for radiation damage to occur.

III. CALCULATION METHOD

The Ca 2*p* electron has dipole-allowed transitions into *s*- and *d*-like final states, the lowest being Ca 4*s* and Ca 3*d*. The 3*d* channel is by far stronger than the other channels since the 3*d* wave functions collapse in the presence of the Ca 2*p* core hole, and thus dramatically increase their overlap with the Ca 2*p*.^{21, 22} This makes the problem of calculating the Ca 2*p* absorption edge amenable to an atomic multiplet approach, i.e., the calculation of the Ca²⁺ 2*p*⁶3*d*⁰-to-2*p*⁵3*d*¹ dipole transition. Thereby one starts from the premise that the interaction of the core hole with the excited electron dominates over the interactions with neighboring atoms. The local environment in the solid is then taken into account as the adaptation of the spherically symmetric, atomic field to the crystal symmetry. The first step is the inclusion of a cu-

bic (octahedral) crystal field, representing the *O_h* symmetry in the bulk Ca compounds studied here. It is represented by a single parameter X^{400} . Then the symmetry is reduced to *C_{3v}*, representing the threefold CaF₂(111) surface or interface. In this case one has two extra parameters,⁴³ i.e., X^{410} and X^{210} . The total crystal-field Hamiltonian in *C_{3v}* symmetry is

$$H_{\text{CF}} = X^{400}U^{400} + X^{410}U^{410} + X^{210}U^{210}$$

The U^{λ} are unitary transformations, which relate to scaling factors of 0.304, 0.530, and 0.358, respectively. The $X^{400}U^{400}$ term, also denoted by $10Dq$, splits the *d* orbitals into a triply degenerate t_{2g} (Γ_{2g}) and a double degenerate e_g (Γ_{1g}) manifold, excluding spin degeneracy. The X^{410} and X^{210} terms split the t_{2g} manifold into a doublet (A_1) and a singlet (A_1). The e_g manifold turns into a Λ_1 doublet in the *C_{3v}* symmetry, and mixes with the A_3 doublet derived from the t_{2g} manifold. The crystal-field parameters are fitted to the experimental multiplet structure. Since the X^{410} and X^{210} terms do not modify the average cubic crystal-field splitting, one can use the bulk X^{400} term as a starting point for calculating a surface multiplet. Details concerning the group theory and the calculation methods can be found in the book by Butler⁴³ and in Ref. 44.

IV. BULK COMPOUNDS

X-ray absorption spectra of Ca²⁺ are shown on the bottom of Fig. 1 for octahedral, sixfold coordination in CaO and for cubic, eightfold coordination in CaF₂. They are reproduced by our multiplet calculations using crystal-field parameters $10Dq$ of +1.2 and -0.75 eV, respectively (Fig. 1, top). The theoretical CaO spectrum consists of seven allowed transitions, which are broadened by a combination of a Gaussian and a Lorentzian to simulate broadening mechanisms originating from band dispersion, vibrations, and (autoionization) decay. These broadening mechanisms are found to result in different values for every of the four main peaks.¹² As the main interactions are the core-hole spin-orbit splitting and the crystal field, the four main peaks can be loosely assigned as $2p_{1/2}\text{-}t_{2g}$, $2p_{1/2}\text{-}e_g$, $2p_{1/2}\text{-}t_{2g}$, $2p_{1/2}\text{-}e_g$, in order of increasing energy. The small leading peaks originate from the mixing of states due to the multipole interaction of the core hole with the valence electron, combined with the 3*d* spin-orbit splitting. The absolute energy scale is off by about 2 eV. This originates mainly from the neglect of screening. The interpretation of the CaF₂ spectrum is similar, but due to the eightfold surrounding one has a negative $10Dq$, and the order of the t_{2g} and e_g orbitals is reversed. The intensity of the e_g peaks is low, which prohibits a simple assignment of the $2p_{1/2}$ (L_1) part.

The Ca 2*p* absorption spectra of Ca in metallic environments, such as Ca metal and CaSi₂, show two broad peaks with a weak, sharper structure at the onset (Fig. 2, bottom). Note that the core-level binding energies relative to the Fermi level (vertical bars in Fig. 2) coincide with the onset of the absorption. This triplet structure is

similar to a broadened version of the calculated atomic multiplet (Fig 2, top), which agrees well with the atomic spectrum of Ca reported in the literature.²¹ This indicates a weak crystal field, which is consistent with the more homogeneous, jelliumlike charge distribution in a metal, as opposed to the strong point charges in an ionic insulator. Though it is possible to simulate the spectra with the multiplet approach, the information that can be gained is limited because of the large broadenings and possible modifications due to band dispersion effects. However, we note that the agreement that can be reached from this approach is at least similar to the results for Ca obtained by Zaanen *et al*.⁹

We note that the spectrum of a submonolayer of Ca on Si(111) in Fig 2 also bears clear resemblance to the atomic spectrum, with less broadening than in Ca metal and CaSi₂. This indicates that the Ca atom is bonded weakly to the Si(111) surface, in other words, that the bonding length is rather long. To optimize the resemblance to experiment, the theoretical spectrum in Fig 2 is broadened with a Fano line shape. The strong Fano asymmetry ($q = 6$) indicates strong autoionization.⁴⁵

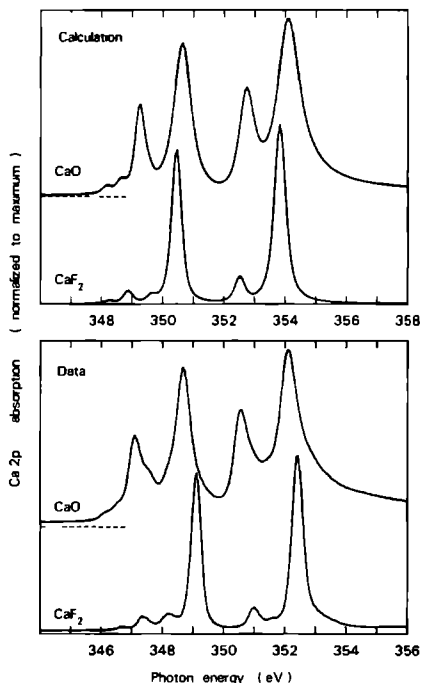


FIG 1 Calculated and experimental Ca 2p absorption edges for Ca²⁺ in CaF₂ and CaO. The sign of the crystal field parameter $10Dq$ reverses when going from the fluorite to the rocksalt structure ($10Dq = -0.75$ eV for CaF₂, and $10Dq = +1.2$ eV for CaO).

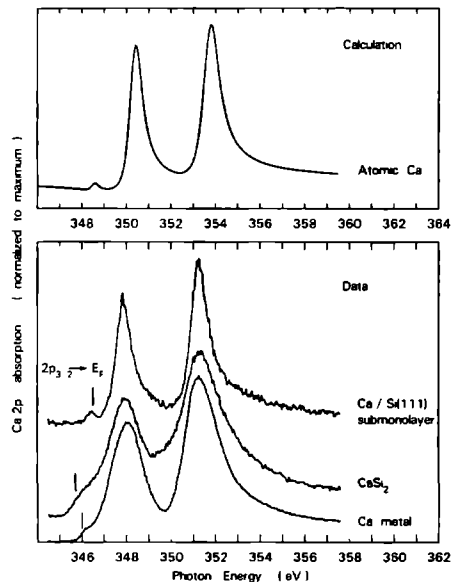


FIG 2 Ca 2p absorption edges of Ca in metallic environments i.e. Ca metal, CaSi₂, and a submonolayer of Ca on Si(111). The calculation represents a free atom without crystal field, with the broadening matched to the submonolayer case. The absorption edges in Ca metal and CaSi₂ exhibit the same three atomic lines, except broadened by band formation.

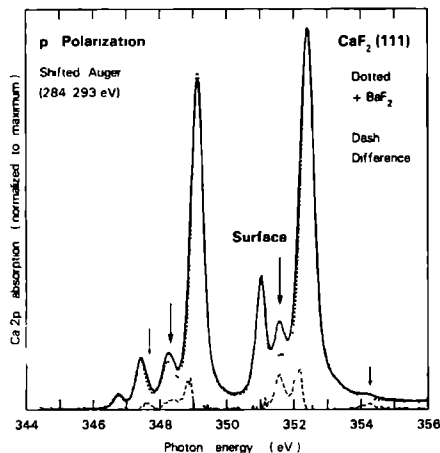


FIG 3 Surface effects at the Ca 2p edge for clean CaF₂(111). Surface-related features (arrows) are quenched by covering the surface with BaF₂, thereby creating a bulklike environment of the surface Ca atoms.

V. SURFACES AND INTERFACES

First, we will discuss surface effects, since they can be detected rather well. Interface features always show up together with surface features on thin film samples. To isolate them requires a good understanding of the surface contribution. The clean $\text{CaF}_2(111)$ surface exhibits several characteristic surface contributions to the Ca $2p$ edge, as indicated by arrows in Fig 3 and in the experimental part of Fig 4. Similar surface excitons have been observed for ionic⁴⁶⁻⁴⁹ and rare gas^{50,51} solids. The surface features on $\text{CaF}_2(111)$ are revealed by suppressing them with a few layers of adsorbed BaF_2 (overlapping dotted and solid curves in Figs 3 and 4). BaF_2 exhibits the same ionic lattice as CaF_2 and thus provides a bulk-like environment for Ca surface atoms. The spectra in

Fig 3 are taken in the Auger detection mode with a probing depth of typically 20 Å, according to universal escape depth curves³³. By moving the Auger detection window off the bulk Auger peak we have suppressed the two large bulk peaks in Fig 3. The surface sensitivity can be further enhanced by detecting ions, emitted from the surface as decay product of the Ca $2p$ core holes. Low-energy ions do not penetrate more than one or two atomic layers^{41,52}. Such spectra are shown in the experimental part of Fig 4. As expected, the surface peaks are even stronger.

It is important to observe that the surface features depend on the polarization of the incident light (Fig 4). Most of them are excited by the component of the electric-field vector perpendicular to the surface, which is present in p polarization only. In s polarization, on the

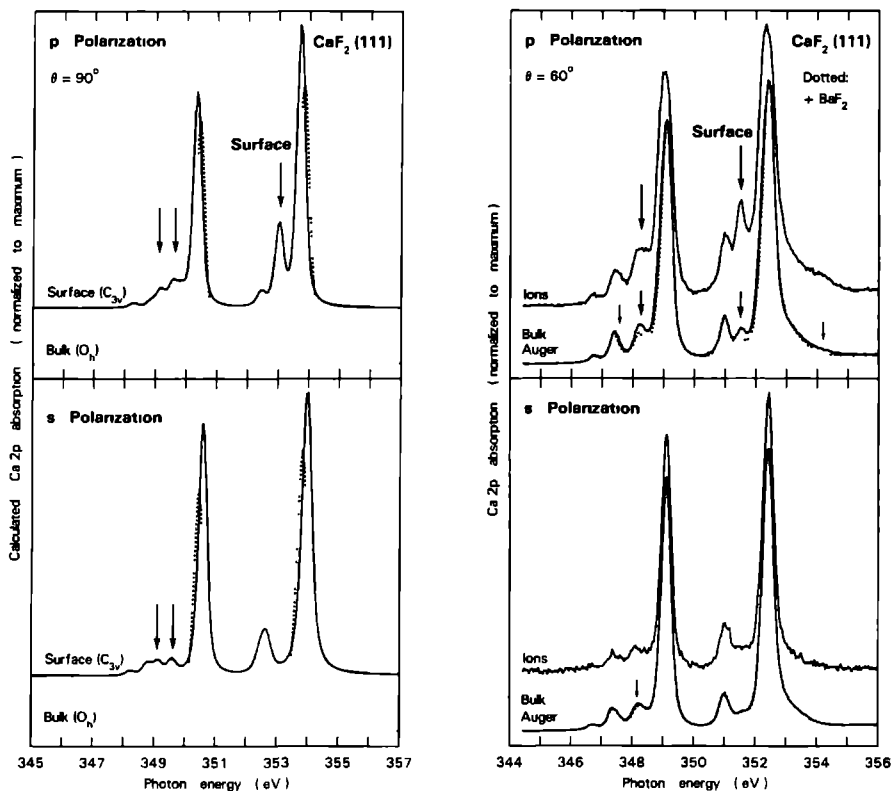


FIG 4 Polarization dependence of surface features at the Ca $2p$ absorption edge of clean $\text{CaF}_2(111)$ (Calculated spectra on the left, experiment on the right). The surface selectivity is enhanced experimentally by detecting photodesorbed (positive) ions instead of Auger electrons. Surface effects are quenched by covering the surface with BaF_2 , as in Fig 3. The most prominent surface feature at 351.5 eV is excited by the component of the electric field vector perpendicular to the surface. The calculations explain the polarization dependence by the lower symmetry of the surface (C_{3v}) as opposed to the isotropic bulk (O_h).

other hand, the solid and dotted lines for the clean and BaF₂-covered surface nearly completely overlap each other, except for a region around 348 eV (bottom of the experimental part of Fig 4). This strong polarization dependence of the surface features is in contrast to isotropic behavior of the bulk spectra, as represented by the BaF₂ covered surface.⁵³ No polarization dependence is expected from an isotropic bulk lattice, such as the cubic CaF₂ structure. The (111) surface, on the other hand, has a lower symmetry, giving rise to an anisotropy of the optical absorption. The F atom above the outermost Ca atom is missing, thereby lowering the symmetry to three-fold C_{3v}. Consequently, the orbitals oriented perpendicular to the surface are not equivalent to orbitals oriented parallel to the surface. By using optical selection rules for the perpendicular component of the angular momentum m_j , one can select orbitals of various orientations by using the orientation of the electric field vector. This prototype case shows that anisotropy could be useful for future, polarization-modulation experiments that separate surface and interface contributions from the bulk.

The extra peaks in the surface absorption spectrum and their polarization dependence can be calculated by taking into account the lowering of the symmetry from O_h for bulk Ca atoms to C_{3v} for surface Ca atoms, as shown in the theoretical part of Fig 4. The parameters for the calculation are $10Dq = X^{400}U^{400} = -0.75$ eV, as in bulk CaF₂, $X^{410} = -1.0$ eV, and $X^{210} = +1.0$ eV. The extra surface features essentially originate from transitions that were symmetry forbidden in the bulk, but become allowed in the lower symmetry of the surface. The main surface feature at 351.5 eV is clearly accounted for, including its polarization dependence. Note that the experimental, *p*-polarized spectra include components of the electric-field vector parallel and perpendicular to the surface, since they are taken at angle of incidence of 60° from normal.⁵⁴ The other pair of extra surface features at lower energy (see arrows in the theoretical part of Fig 4) has a counterpart in the difference spectra of Fig 3 too, although less pronounced. Additional peaks in the difference spectra on the low-energy tail of the two big bulk lines are due to a narrowing of those lines upon BaF₂ adsorption. This may indicate an energy shift of the two principal lines from the bulk to the surface, as expected from the calculations. The pair of low-energy features is calculated to appear in *s* polarization as well as in *p* polarization. Comparing the clean and BaF₂-covered spectra for *s* polarization in Fig 4 a slight, though inconclusive difference is seen near the calculated energy in *s* polarization (see fine arrow). Minor differences between calculation and experiment, e.g., a weak extra surface feature above 354 eV, could be due to the choice of the parameters for the surface crystal field, or due to the neglect of 4s final states.

An interface contribution to the Ca 2p absorption spectrum can be found at the CaF₂/Si(111) interface.^{20, 25, 27} Figure 5 shows data for epitaxially grown CaF₂ films, normalized to the incident photon flux. Interface contributions can be identified by observing their attenuation

when the film thickness is increased beyond a monolayer. Surface contributions, on the other hand, remain independent of thickness, while bulk contributions increase with thickness. Looking in Fig 5 for spectral regions where the intensity (per incident photon) decreases with thickness, one finds two peaks at energies 0.6 eV below the two main bulk features. They are best seen in spectrum for two layers (solid line). For the five-layer film the interface peaks are attenuated, and a pair of surface features starts to dominate at an energy 0.3 eV below the interface structures (compare Figs 3 and 4). In order to obtain the proper line shape for the interface layer we have tried to subtract the contribution of the outer layer from the two-layer spectrum by using the surface spectra from Fig 4. This turned out to be difficult since small modifications of the sharp bulk lines have a large effect on the difference spectra. We have found that the best estimate of the interface spectrum is the monolayer spectrum, shown on a larger scale in Fig 6. It is known from previous work^{24, 29} that both the Ca core-level shifts and the energy of the Ca-related interface state near the top of the valence band do not change when the first layer is covered by further layers. We can expect that the Ca 2p absorption spectra of the monolayer and the interface layer are similar, too. The monolayer spectrum in Fig 6 depends on the polarization, reflecting a lowering of the

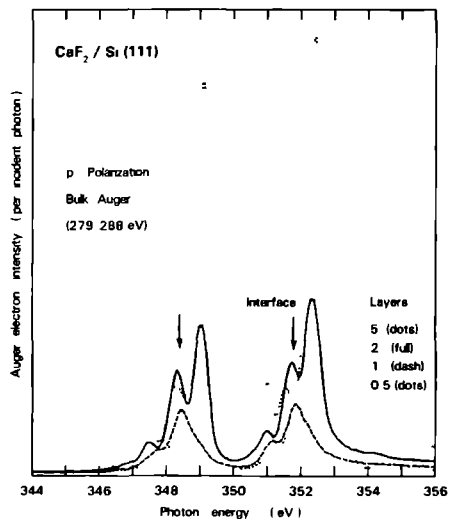


FIG 5 Thickness dependence of the Ca 2p edge for CaF₂ grown epitaxially on Si(111). There is evidence for interface features from their attenuation with increasing film thickness (arrows). The interface signal is similar to that from the monolayer (dashed, for a closeup view see Fig 6). Its two principal peaks are shifted down by 0.6 eV from the bulk.

symmetry to C_{3v} , analogous to that of the surface. This result suggests that polarization modulation techniques will be a useful tool for picking up the signal from buried interfaces.

For a theoretical analysis of the interface absorption we use the monolayer spectrum, as shown in Fig 6. From its polarization dependence it is clear that the lowering of the symmetry to C_{3v} has to be taken into account. In addition, we will have to consider a possible valence change from Ca^{2+} to Ca^{1+} , as suggested previously.²⁰ The unpaired electron from the dangling bond at the Si(111) surface forces Ca into the $1+$ oxidation state, such that it can form a bond using its unpaired $4s$ electron. In Fig 7 we show the influence of a valence change on the theoretical spectrum (compare also the discussion in Sec VI). The main effect is a shift to lower energy. This is also seen for the experimental spectra of the interface and the monolayer, supporting the view of a valence change from Ca^{2+} to Ca^{1+} at the $CaF_2/Si(111)$ interface. Another effect is the generation of more lines. Whereas the $2p^63d^0(J=0)$ to $2p^53d^1(J=1)$ atomic multiplet has only three lines, the transition from $2p^63d^04s^1$ to $2p^53d^14s^1$ has eleven lines in the atomic case. The ground state now has $J = \frac{1}{2}$, because of the spin of the $4s$ electron. With the dipole selection rules the $J = \frac{1}{2}$ and $\frac{3}{2}$ final states can be reached, which are, respectively, fourfold and sevenfold degenerate. Projection to O_h symmetry causes a mixing of states and produces a total of 29 allowed transitions for a $J = \frac{1}{2}$ ground state, as can be inferred from the branching tables in Ref 43. However, in Fig 7 it can be seen that the effect on the spectral shape

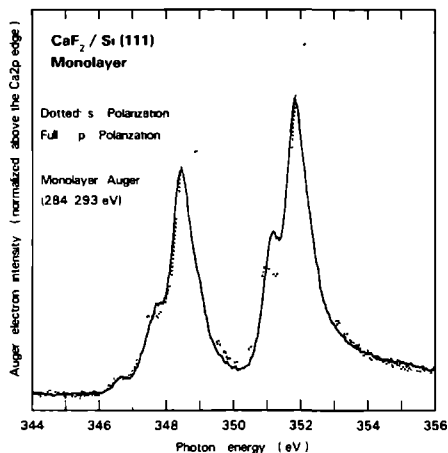


FIG 6 Polarization-dependent Ca $2p$ absorption edges for a monolayer of CaF_2 on Si(111). These spectra are representative of the $CaF_2/Si(111)$ interface as well. Figure 7 gives an approximate calculation, based on a valence change from Ca^{2+} to Ca^{1+} and a reversal of the crystal-field parameter $10Dq$.

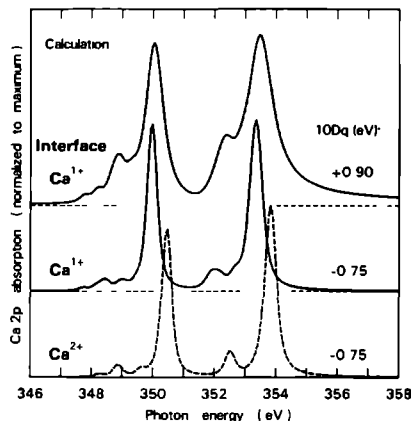


FIG 7 Calculated Ca $2p$ edge fine structure for Ca^{2+} and Ca^{1+} , showing the effect of a valence change. The two bottom curves have a crystal field $10Dq$ corresponding to bulk CaF_2 , the top curve has a crystal field with reverse sign, corresponding to the $CaF_2/Si(111)$ interface. The multiplet structure of Ca^0 is similar to that of Ca^{2+} since the two configurations differ only by the filled Ca $4s$ shell.

is minimal if the crystal field $10Dq$ is maintained at the bulk, CaF_2 value of -0.75 eV. Comparing the experimental spectrum of Fig 6 with the calculations of Fig 7, it is evident that the spectral shape is reproduced much better with a positive value of $10Dq$, which is related to octahedral surroundings. This can be seen directly from the rather strong intensity of the extra peaks induced on the low-energy tails of the main doublet. They resemble those of CaO , which also has positive $10Dq$ (compare Fig 1). The top spectrum in Fig 7 gives the result for the $Ca^{1+} 3d^04s^1$ state with $10Dq = +0.9$ eV. From the shift to lower energy and the close similarity to this octahedral simulation, we conclude that the interface spectrum is consistent with Ca^{1+} in a quasioctahedral surrounding. The polarization dependence shows that the symmetry is not exactly octahedral. This is because of the inequivalence of the surrounding Si and F atoms and their displacements from octahedral positions.

VI. VALENCE DETERMINATION

In order to assess the effect of a valence change on the Ca $2p$ absorption spectrum experimentally, it is necessary to have reference compounds. Metallic Ca^0 and ionic Ca^{2+} compounds are readily available (see Sec IV). They can be described by the same atomic multiplet structure (neglecting the perturbation by the crystal field), since they only differ by the filled Ca $4s$ shell. The Ca^{1+} configuration is unstable. The only reference that we have been able to find is provided by the F centers (Ca^{1+} ions next to an F vacancy) that are induced in Ca

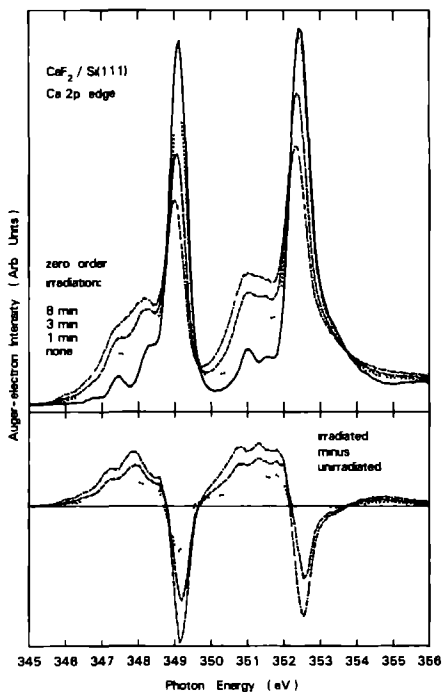


FIG 8 Effect of soft x ray irradiation on the Ca 2p edge of CaF_2 . F centers are created at the surface (Ref 40), which are used as representative of the Ca^{1+} valence state. The radiation dose is in the order of 10^{17} photons/cm².

halides by irradiation with electrons or photons. For the $\text{CaF}_2(111)$ surface it has been found that an ordered monolayer of surface F centers can be formed.⁴⁰ Figure 8 shows Ca 2p absorption spectra for radiation doses in the appropriate range.⁵⁵ The main effect of irradiation is a shift of spectral weight from the main two peaks down to a broad feature at about 1.2 eV lower energy. Some fine structure appearing in the difference spectra is caused by a broadening of the spectral features of CaF_2 . The downwards shift can be rationalized by noticing that the extra Ca 4s electron induces a Ca 2p core-level shift towards lower binding energy (about 3.8 eV). Note that the core-level shift is smaller than that of the absorption edge. This is also true for the $\text{CaF}_2/\text{Si}(111)$ interface where the shift is 2.1 eV for the Ca 2p core level²⁷ and 0.6 eV for the Ca 2p absorption peaks. The difference between the core-level and the absorption edge shifts is due to the fact

that the excited Ca 3d electron in the Ca 2p-to-3d absorption process resides partly inside the charge distribution of the Ca 4s electron, i.e., the 2p and the 3d states both experience a shift in the same direction. Therefore the shifts of the upper and lower state partially compensate each other in the absorption process. The theoretical prediction for the effect of a valence change from Ca^{2+} to Ca^{1+} has already been discussed with Fig 7. The main feature is a shift towards lower energy, as observed experimentally.

VII. SUMMARY

The Ca 2p-to-3d absorption edge is found to exhibit a variety of multiplet structures for bulk compounds, surfaces, and interfaces. In the bulk, the fine structure develops from an atomiclike triplet for metallic compounds to a seven line multiplet for ionic compounds. The latter is produced by the splitting of the 3d orbitals in a strong crystal field. The sign of the crystal field can be reversed by varying the crystal structure from rocksalt (with octahedral coordination) to fluorite (with cubic coordination). At surfaces, extra multiplet lines show up due to the lower symmetry. They become polarization dependent, as opposed to the isotropic bulk lines. The same phenomena are observed at interfaces, thereby opening up the possibility of applying polarization modulation techniques in order to selectively observe surface or interface absorption. A change of valence from Ca^{2+} to Ca^{1+} is calculated to shift the main absorption lines down in energy, in agreement with results from F centers in CaF_2 . Such a shift is also observed at the $\text{CaF}_2/\text{Si}(111)$ interface, indicating a valence change from Ca^{2+} to Ca^{1+} .

This type of analysis can be extended to a variety of other materials, i.e., using atomic-multiplet plus crystal-field effects to distinguish the atomic environment. In general, one needs an absorption edge with sufficiently localized character. While it is too early to say definitively for how many elements the present approach would be appropriate, it certainly is appropriate for K, Ca, and the 3d transition metal series, using the 2p absorption edge. In addition, there are strong indications that a similar approach, combined with the use of polarized light and single-crystal samples, will be a source of information for the lanthanides, using the 3d and 4d edges. We also have some indication that the approach may work for the 2p edges of the 4d transition metal series, but here, and for other elements like the 3d and 4d edges of actinides, more work is needed to define the situation clearly.

ACKNOWLEDGMENTS

This research was carried out (in part) at the National Synchrotron Light Source, Brookhaven National Laboratory, which is supported by the U.S. Department of Energy, Division of Materials Sciences and Division of Chemical Sciences.

- *Present address Max-Lab, University of Lund, Box 118, S-22100, Lund, Sweden
- ¹Present address Department of Physics, Queen's University, Kingston, Ontario, Canada K7L 3N6
- ¹J Stohr and D A Outka, *J Vac Sci Technol A* **5**, 919 (1987)
- ²G Kaindl, G Kalkowski, W D Brewer, B Perscheid, and F Holtzberg, *J Appl Phys* **55**, 1910 (1984)
- ³B T Thole, G van der Laan, J C Fuggle, G A Sawatzky, R C Karnatak, and M M Esteve, *Phys Rev B* **32**, 5107 (1985)
- ⁴R D Leapman, L A Grunes, and P L Fejes, *Phys Rev B* **26**, 614 (1982)
- ⁵J E Muller, O Jepsen, and J W Wilkins, *Solid State Commun* **42**, 365 (1982)
- ⁶T Yamaguchi, S Shitbuya, S Suga, and S Shin, *J Phys C* **15**, 2641 (1982)
- ⁷J Barih, F Gerken, and C Kunz, *Phys Rev B* **28**, 3608 (1983)
- ⁸J Fink, Th Muller-Heinzerling, B Scheerer, W Speier, F U Hillebrecht, J C Fuggle, J Zaenen, and G A Sawatzky, *Phys Rev B* **32**, 4899 (1985)
- ⁹J Zaenen, G A Sawatzky, J Fink, W Speier, and J C Fuggle, *Phys Rev B* **32**, 4905 (1985)
- ¹⁰E E Koch, Y Jugnet, and F J Himpsel, *Chem Phys Lett* **116**, 7 (1985)
- ¹¹G van der Laan, B T Thole, G A Sawatzky, and M Verdaguier, *Phys Rev B* **37**, 6587 (1988)
- ¹²F M F de Groot, J C Fuggle, B T Thole, and G A Sawatzky, *Phys Rev B* **41**, 928 (1990)
- ¹³F Sette, B Sinkovic, Y J Ma, and C T Chen, *Phys Rev B* **39**, 11125 (1989)
- ¹⁴C T Chen and F Sette, *Phys Scr* **T31**, 119 (1990)
- ¹⁵F M F de Groot, J C Fuggle, B T Thole, and G A Sawatzky, *Phys Rev B* **42**, 5459 (1990)
- ¹⁶D D Sarma, O Strebel, C T Simmons, U Neukirch, G Kaindl, R Hoppe, and H P Muller, *Phys Rev B* **37**, 9784 (1988)
- ¹⁷A Bianconi, M De Santis, A DiCicco, A M Flank, A Fontaine, P Lagarde, H Katayama-Yoshida, A Kotani, and Marcelli, *Phys Rev B* **38**, 7196 (1988)
- ¹⁸M Grioni, J B Goedkoop R Schoorl, F M F de Groot, J C Fuggle, F Schafers, E C Koch, G Rossi, J-M Esteve, and R C Karnatak, *Phys Rev B* **39**, 1541 (1989)
- ¹⁹K Okada and A Kotani, *J Phys Soc Jpn* **58**, 1095 (1989)
- ²⁰F J Himpsel, U O Karlsson, J F Morar, D Rieger, and J A Yarmoff, *Phys Rev Lett* **56**, 1497 (1986), see also C T Chen and F Sette, *ibid* **60**, 160 (1988), and F J Himpsel, U O Karlsson, J F Morar, D Rieger, and J A Yarmoff, *ibid* **60**, 161 (1988)
- ²¹M W D Mansfield, *Proc R Soc London Ser A* **348**, 143 (1976)
- ²²A A Maiste, R E Ruus, and M A Elango, *Zh Eksp Teor Fiz* **79**, 1671 (1980) [*Sov Phys —JETP* **52**, 844 (1980)]
- ²³J M Kenney, C Jacobsen, J Kirz, H Rarback, F Cnotti, W Thomlinson, R Rosser, and G Schidlowsky, *J Microscopy* **138**, 321 (1985)
- ²⁴F J Himpsel, F U Hillebrecht, G Hughes, J L Jordan, U O Karlsson, F R McFeely, J F Morar, and D Rieger, *Appl Phys Lett* **48**, 596 (1986)
- ²⁵U O Karlsson, F J Himpsel, J F Morar, D Rieger, and J A Yarmoff, *J Vac Sci Technol B* **4**, 1117 (1986)
- ²⁶M A Olmstead, R I G Uhrberg, R D Bringans, and R Z Bachrach, *J Vac Sci Technol B* **4**, 1123 (1986)
- ²⁷D Rieger, F J Himpsel, U O Karlsson, F R McFeely, J F Morar, and J A Yarmoff, *Phys Rev B* **34**, 7295 (1986)
- ²⁸M A Olmstead, R I G Uhrberg, R D Bringans, and R Z Bachrach, *Phys Rev B* **35**, 7526 (1987)
- ²⁹A B McLean and F J Himpsel, *Phys Rev B* **39**, 1457 (1989)
- ³⁰T F Heinz, F J Himpsel, E Palange, and E Burstein, *Phys Rev Lett* **63**, 644 (1989)
- ³¹F J Himpsel, Y Jugnet, D E Eastman, J J Donelon, D Grimm, G Landgren, A Marx, J F Morar, C Oden, R A Pollak, J Schreier, and C A Crider, *Nucl Instrum Methods* **222**, 107 (1984)
- ³²D E Eastman, J J Donelon, N C Hien, and F J Himpsel, *Nucl Instrum Methods* **172**, 327 (1980)
- ³³We also used secondary electron detection (not shown) and obtained results similar to the Auger detection mode, nearly independent of the kinetic energy of the secondary electrons. The surface sensitivity did not increase significantly near the escape depth minimum of the secondary electrons. This is probably due to the fact that most of the secondary electrons originate from Ca 2p Auger electrons near the Ca 2p threshold, and therefore have an escape depth equal to that of the Auger electrons plus that of the secondary electrons
- ³⁴M Meyer, E v Raven, M Richter, B Sonntag, R D Cowan, and J E Hansen, *Phys Rev A* **39**, 4319 (1989)
- ³⁵T Tiedje, K M Colbow, D Rogers, and W Eberhardt, *Phys Rev Lett* **65**, 1243 (1990)
- ³⁶F M F De Groot *et al* (unpublished)
- ³⁷W Gudat and C Kunz, *Phys Rev Lett* **29**, 169 (1972)
- ³⁸CaO single crystals were obtained from W C Spicer Ltd., 1276 Vanbrugh Hill, Greenwich, London SE 10, UK
- ³⁹J F Morar and M Wittmer, *J Vac Sci Technol A* **6**, 1340 (1988)
- ⁴⁰U O Karlsson, F J Himpsel, J F Morar, F R McFeely, D Rieger, and J A Yarmoff, *Phys Rev Lett* **57**, 1247 (1986)
- ⁴¹R Souda and M Aono, in *The Structure of Surfaces II*, edited by J F van der Veen and M A van Hove, Springer Series in Surface Science Vol 11 (Springer-Verlag, Berlin, 1987), p 581
- ⁴²F Senf, thesis, Hamburg, 1987 (unpublished)
- ⁴³P H Butler, *Point Group Symmetry Applications, Methods and Tables* (Plenum, New York, 1981)
- ⁴⁴B T Thole (unpublished)
- ⁴⁵U Fano, *Phys Rev* **124**, 1866 (1961)
- ⁴⁶V E Henrich, G Dresselhaus, and H J Zeiger, *Phys Rev Lett* **36**, 158 (1976)
- ⁴⁷Y Rehder, W Gudat, R G Hayes, and C Kunz, in *Proceedings of the Seventh International Vacuum Congress and Third Conference of Solid Surfaces*, edited by R Dobrozemsky, F Rudenauer, F P Viehbock, and A Breth (IVC, ICSS, Wien, 1977), p 453
- ⁴⁸O Aita, K Ichikawa, and K Tsutsumi, *Phys Rev B* **38**, 10079 (1988)
- ⁴⁹K Ichikawa, O Aita, and K Tsutsumi, *Phys Rev B* **39**, 1307 (1989)
- ⁵⁰V Saile, M Skibowski, W Steinmann, P Gurtler, E E Koch, and A Kozevnikov, *Phys Rev Lett* **37**, 305 (1976)
- ⁵¹V Saile and E E Koch, *Phys Rev B* **20**, 784 (1979)
- ⁵²E Taglauer and W Heiland, *Appl Phys* **9**, 261 (1976)
- ⁵³A slight remnant of the upper surface peak is seen in the spectra of the BaF₂-covered surface for p polarization. This could be due to incomplete BaF₂ coverage, e.g., caused by island formation
- ⁵⁴The ion spectrum appears to contain some extra bulk contribution, even taking the mixture of parallel and perpendicular

components in p polarization at $\theta=60^\circ$ into account. This might be explained by the open structure of the CaF₂(111) surface, where F above the second layer Ca can be emitted into vacuum without colliding with other atoms.

⁵⁵For the higher radiation doses a further conversion of Ca¹⁺ to metallic Ca⁰ is beginning to take place. This may explain that the energy shift is larger than at the CaF₂/Si(111) interface.

References

- [1] I.S. Butler and J.F. Harrod, *Inorganic Chemistry*, (Benjamin Cummings Publ., Redwood City, 1989); chapter 24.
- [2] *X-ray Absorption Fine Structure*, Ed. S.S. Hasnain (Ellis Horwood Publ., Chichester, 1991); chapter III: metals in biology.
- [3] *Synchrotron Radiation and Biophysics*, Ed. S.S. Hasnain (Ellis Horwood Publ., Chichester, 1990).
- [4] G.N. George, R.C. Prince and S.P. Cramer, *Science* **243**, 789 (1989).
- [5] M. Kusunoki, T. Ono, Y. Inoue, M. Susuki, A. Uehara, T. Matsushita and H. Oyanagi, *X-ray Absorption Fine Structure*, Ed. S.S. Hasnain (Ellis Horwood Publ., Chichester, 1991); page 174.
- [6] S.P. Cramer, O. Tench, M. Yocum, H. Kraner, L. Rogers, V. Radeka, O. Mullins and S. Rescia, *X-ray Absorption Fine Structure*, Ed. S.S. Hasnain (Ellis Horwood Publ., Chichester, 1991).
- [7] S. George, J. Chien and S.P. Cramer, *NSLS Activity Report* (1990).
- [8] J.C. Fuggle, *Physica Scripta*. **T17**, 64 (1987).
- [9] C.T. Chen, *Nucl. Instr. Meth. A*. **256**, 595 (1987); C.T. Chen and F. Sette, *Rev. Sci. Instr.* **60**, 1616 (1989).
- [10] N.S. Gill and F.B. Taylor, *Inorg. Syn.* **9**, 136 (1967).
- [11] J. Meyer, *Z. Anorg. Chem.* **81**, 385 (1913).
- [12] M.K. Chan and W.H. Armstrong, *Inorg. Chem.* **28**, 3777 (1989).
- [13] M.K. Chan and W.H. Armstrong, manuscript in preparation.
- [14] L.J. Boucher and V.W. Day, *Inorg. Chem.* **16**, 1360 (1977).
- [15] S. Brooker and V. McKee, *J. Chem. Soc. Chem. Comm.* 619 (1989).
- [16] G. Christou, *Acc. Chem. Res.* **22**, 328 (1989).
- [17] J.E. Hahn and K.O. Hodgson, in: *Inorganic Chemistry: Towards the 21st Century*, Ed. M.H. Chisholm, (ACS Symposium Series, **211**, New York, 1983); page 431; J.E. Hahn, R.A. Scott, K.O. Hodgson, S. Doniach, S.R. Desjardins and E.I. Solomon, *Chem. Phys. Lett.* **88**, 595 (1984).
- [18] B. Poumellec, R. Cortes, G. Tourillon and J. Berthon, *Conference Proceedings Vol 25: 2nd European Conference on Progress in X-ray Synchrotron Radiation Research*, Eds. A. Balerna, E. Bernieri and S. Mobilio, (SIF, Bologna, 1990).
- [19] R. Pappalardo, *J. Chem. Phys.* **31**, 1050 (1959).
- [20] J.W. Stout, *J. Chem. Phys.* **33**, 303 (1960).
- [21] F.M.F. de Groot, J.C. Fuggle, B.T. Thole, G.A. Sawatzky, *Phys. Rev. B*. **41**, 928 (1990); F.M.F. de Groot, J.C. Fuggle, B.T. Thole, G.A. Sawatzky, *Phys. Rev. B*. **42**, 5457 (1990).
- [22] The atomic values for the Slater integrals are calculated *ab-initio* within the Hartree-Fock limit using Cowan's RCN program. To account for intra-atomic configuration interaction the Hartree-Fock values are reduced to 80%. See R.D. Cowan in *The Theory of Atomic Structure and Spectra* (University of California Press, Berkeley, 1981); page 464; references therein.
- [23] O. Gunnarsson, O. K. Andersen, O. Jepsen, and J. Zaanen, in *Core-Level Spectroscopy in Condensed Systems*, Eds. J. Kanamori and A. Kotani, (Springer Series in Solid State Science. Vol. 81, Springer-Verlag, Berlin, 1988); page 82.
- [24] B.T. Thole and G. van der Laan, *Phys. Rev. B*. **38**, 3158 (1988).
- [25] J.E. Penner-Hahn, R.M. Fronko, V.L. Pecoraro, C.F. Yocum, S.D. Betts and S.R. Bowlby,

- J. Am. Chem. Soc.* **112**, 2549 (1990).
- [26] M.O. Krause and J.H. Oliver, *J. Chem. Phys. Ref. Data* **8**, 329 (1979).
- [27] M.T. Vala, C.J. Ballhausen, R. Dingle and S.L. Holt, *Mol. Phys.* **23**, 217 (1972).
- [28] C.K. Jorgenson, *Structure and Bonding* **1**, 1 (1966).
- [29] J.W. Stout, *J. Chem. Phys.* **31**, 709 (1959).
- [30] Approximate values for $10Dq$ are estimated using Jorgenson's relation $10Dq \cong f \cdot g \cdot 10^3 \text{ cm}^{-1}$ [31]. For Mn^{II} complexes we used $g \cong 8.0$; for MnSO_4 we assumed $f \cong 1.3$ (based on the value reported for SO_3^{2-}), and for the *tris*-pyrazoylborate complex we used $f \cong 1.43$ (based on the value reported for *o*-phenanthroline [33]).
- [31] C.K. Jorgenson, *Absorption Spectra and Chemical Bonding in Complexes*, (Pergamon Press, Oxford, 1962); C.K. Jorgenson, *Modern Aspects of Ligand Field Theory*, (North Holland, Amsterdam, 1971).
- [32] J.J. Alexander and H.B. Gray, *J. Am. Chem. Soc.* **90**, 4260 (1968).
- [33] B.N. Figgis, *Introduction to Ligand Fields* (John Wiley, New York, 1966), page 244; A.P.B. Lever, *Inorganic Electronic Spectroscopy* (Elsevier, Amsterdam, 1984); page 748.
- [34] B.T. Thole, R.D. Cowan, G.A. Sawatzky, J. Fink and J.C. Fuggle, *Phys. Rev. B.* **31**, 6856 (1985).
- [35] Preliminary spectra for the blue copper protein stellacyanin [6] and the Fe-S protein rubredoxin [7] have already been reported.
- [36] M.O. Krause, *J. Chem. Phys. Ref. Data* **8**, 307 (1979).
- [37] D.W. Lynch and R. Cowan, *Phys. Rev. B.* **36**, 9228 (1987).
- [38] F. Al-Shamma and J.C. Fuggle *Physica C.* **169**, 325 (1990); references therein.
- [39] N. Nücker, J. Fink, B. Renker, D. Ewert, C. Politis, P.J.W. Weijs and J.C. Fuggle, *Z. Phys. B.* **67**, 9 (1987).
- [40] P. Kuiper, G. Kruijzinga, J. Ghijsen, M. Grioni, P.J.W. Weijs, F.M.F. de Groot, G.A. Sawatzky, H. Verwey, L.F. Feiner and H. Petersen, *Phys. Rev. B.* **38**, 6483 (1988).
- [41] N. Nücker, H. Romberg, X.X. Xi, J. Fink, B. Gegenheimer and Z.X. Zhao, *Phys. Rev. B.* **39**, 6619 (1989).
- [42] P. Kuiper, M. Grioni, G.A. Sawatzky, D.B. Mitzi, A. Kapitulnik, A. Santaniello, P. de Padova and P. Thiry, *Physica C.* **88**, 260 (1989).
- [43] P. Kuiper, PhD. thesis: *Where are the holes in doped transition metal oxides?*, (University of Groningen, 1990).
- [44] Y. Seino, K. Okada and A. Kotani, *J. Phys. Soc. Jap.* **59**, 1384 (1990).
- [45] F.J. Himpsel, G.V. Chandrashekar, A.B. McLean and M.W. Schafer, *Phys. Rev. B.* **38**, 11946 (1988).
- [46] A.W. Sleight, J.L. Gilson and P.E. Bierstedt, *Solid State Comm.* **17**, 27 (1975).
- [47] L.F. Mattheiss and D.R. Hamann, *Phys. Rev. B.* **28**, 4227 (1983); references therein.
- [48] L.F. Mattheiss, E.M. Gyorgy and D.W. Johnson Jr., *Phys. Rev. B.* **37**, 3745 (1988).
- [49] B. Batlogg et al., *Physica C* **164-164**, 1393 (1989).
- [50] N. Nücker, H. Romberg, X.X. Xi, J. Fink, B. Gegenheimer and Z.X. Zhao, *Phys. Rev. B.* **39**, 6619 (1989).
- [51] H. Eskes, L.H. Tjeng and G.A. Sawatzky, *Phys. Rev. B.* **41**, 288 (1990); references therein.
- [52] J. Zaanen, G.A. Sawatzky and G. Allen, *Phys. Rev. Lett.* **55**, 418 (1985).
- [53] L.F. Mattheiss and D.R. Hamann, *Phys. Rev. Lett.* **60**, 2681 (1988).
- [54] Katsuhiko Takegahara and Tadao Kasuya, *J. Phys. Soc. Jap.* **56**, 1478 (1987).
- [55] A.M. Bratkovsky and S.N. Rashkeev, *Phys. Lett. A.* **142**, 172 (1989).

- [56] Noriaki Hamada, Sandro Massida, Arthur J. Freeman and Joseph Redinger, *Phys. Rev. B.* **40**, 4442 (1989).
- [57] J.P. Julien, A Pasturel, D. Mayou, F. Cyrot-Lackmann and D. Papaconstantopoulos, *Physica Scr.* **42**, 359 (1990).
- [58] For the unoccupied part of the spectrum the results are exactly similar to those in Ref. 47.
- [59] K. Kitazawa, A. Katsui, A. Toriumi and S. Tanaka, *Solid State Comm.* **52**, 459 (1984).
- [60] S. Tajima, S. Uchida, A. Masaki, H Takagi, K. Kitazawa, S. Tanaka and S. Sugai *Phys. Rev. B.* **35**, 696 (1987).
- [61] T. Claeson, J.B. Boyce, F. Bridges, T.H. Geballe, J.M. Remeika, A.W. Sleight, *Physica C* **162-164**, 544 (1989).
- [62] S.M. Heald, D. DiMarzio, M. Croft, M.S. Hegde, S. Li, M. Greenblatt, *Phys. Rev. B.* **40**, 8828 (1989).
- [63] G.K. Wertheim, J.P. Remeika and D.N.E. Buchanan, *Phys. Rev. B.* **26**, 2120 (1982).
- [64] Z.-X. Shen, P.A.P. Lindberg, B.O. Wells, D.S. Dessau, A. Borg, I. Lindau, W.E. Spicer, W.P. Ellis, G.H. Kwei, K.C. Ott, J.-S. Kang and J.W. Allen, *Phys. Rev. B.* **40**, 6912 (1989).
- [65] P.A.P. Lindberg, Z.-X. Shen, B.O. Wells, D.S. Dessau, W.P. Ellis, A. Borg, J.-S. Kang, D.B. Mitzi, I. Lindau, W.E. Spicer and A. Kapitulnik, *Phys. Rev. B.* **40**, 8840 (1989).
- [66] H. Matsuyama, T. Takahashi, H. Katayama-Yoshida, Y. Okabe, H. Takagi and S. Uchida, *Physica C* **162-164**, 1319 (1989).
- [67] H. Matsuyama, T. Takahashi, H. Katayama-Yoshida, Y. Okabe, H. Takagi and S. Uchida, *Phys. Rev. B.* **40**, 2658 (1989).
- [68] M.W. Ruckman and D. DiMarzio, Y. Jeon, G. Liang, J. Chen, M. Croft and M.S. Hegde, *Phys. Rev. B.* **39**, 7359 (1989).
- [69] T.J. Wagener, H.M. Meyer III, D.M. Hill, Yogjun Hu, M.B. Jost, J.H. Weaver, D.G. Hinks, B. Dabrowski and D. R. Richards, *Phys. Rev. B.* **40**, 4532 (1989).
- [70] Hirokazu Sakamoto, Hirofumi Namatame, Tamiko Mori, Koichi Kitazawa, Shoji Tanaka, Shigemasa Suga, *J. Phys. Soc. Jap.* **56**, 365 (1987).
- [71] H. Petersen, *Nucl. Instr. Meth. A.* **246**, 260 (1986).
- [72] J.Fink, Th. Muller-Heinzerling, B. Scheerer, W. Speier, F.U. Hillebrecht, J.C. Fuggle, J. Zaanen and G.A. Sawatzky, *Phys. Rev. B.* **32**, 4899 (1985).
- [73] F.M.F. de Groot et al, unpublished results.
- [74] *Unoccupied Electron States*, Eds. J.C. Fuggle and J. Inglesfield, (Springer Verlag, Berlin, 1991).
- [75] C.L. Lin, S.L. Qiu, Jie Chen, M. Strongin, Gang Cao, Chan-Soo Jee and J.E. Crow, *Phys. Rev. B.* **39**, 9607, (1989).
- [76] F.M.F. de Groot et al, unpublished results taken with the DRAGON monochromator with ~ 0.1 eV (hwhm) resolution.
- [77] O Strebelt et.al., unpublished results taken with the SX700(II) monochromator with ~ 0.1 eV (hwhm) resolution.
- [78] P.J.W. Weys, M.T. Czyzyk, J.F. van Acker, W. Speier, J.B. Goedkoop, H. van Leuken, H.J.M. Hendriks, R.A. de Groot, G. van der Laan, K.H.J. Buschow, G. Wiech and J.C. Fuggle, *Phys. Rev. B.* **41**, 11899 (1990). For an oxygen $1s$ -core hole the only multipole term is the G_{1s2p}^1 Slater Integral (or exchange interaction), but no detectable effects have been found in other systems; see F.M.F. de Groot, J.C. Fuggle, B.T. Thole and G.A. Sawatzky, *Phys. Rev. B.* **41**, 928 (1990).
- [79] R.W. Godby, M. Schluter and L.J. Sham, *Phys. Rev. B.* **37**, 10159 (1988).

- [80] R.J. Cava, P. Gammel, J.J. Krajewski, W.F. Peck Jr., L.W. Rupp Jr., R. Felder and R.B. van Dover, *Phys. Rev. B* **42**, 4815 (1990).
- [81] J.M. van Ruitenbeek et al, unpublished results.
- [82] J.S. Faulkner in *Progress in Materials Science*, Eds. J.W. Christian, P. Haasen and T.B. Massalski (Pergamon, Great Brittain, 1982), Vol. 27.
- [83] G.A. Waychunas, *American Mineralogist* **72**, 89 (1987).
- [84] P. Hartman, *Minerological Magazine* **37**, 366 (1969).
- [85] J.R. Günter and G.B. Jameson. *Acta Cryst. C* **40**, 207 (1984).
- [86] E.R. Whipple, *American Mineralogist*, **64**, 1311 (1979).
- [87] O. Dürmeyer, J.P. Kappler, E. Beaurepaire, J.M. Heintz and M. Drillon, *J. Phys. Cond. Matter*, **2**, 6127 (1990).
- [88] G.A. Waychunas, *Prog. Geol. Soc. Am. Annu. Meet.* **12**, 545 (1980).
- [89] R.D. Leapman, L.A. Grünes, and P.L. Fejes, *Phys. Rev. B* **26**, 614 (1982).
- [90] R. Brydson, H. Sauer, W. Engel, J.M. Thomas, E. Zeitler, N. Kosugi and H. Kuroda, *J. Phys. Cond. Matter* **1**, 797 (1989).
- [91] H. Petersen, *Nucl. Instr. Meth. A* **246**, 260 (1986).
- [92] C.T. Chen and F. Sette, *Physica Scripta* **T31**, 119 (1990).
- [93] F.M.F. de Groot, *Selected experiments in Condensed Matter Physics with Synchrotron radiation*, Ed. C.J. Czaja, (Birkhäuser Verlag, Basel, 1991).
- [94] P.J.W. Weijs, M.T. Czyżyk, J.F. van Acker, W. Speier, J.B. Goedkoop, H. van Leuken, H.J.M. Hendrix, R.A. de Groot, G. van der Laan, K.H.J. Buschow, G. Wiech and J.C. Fuggle, *Phys. Rev. B* **41**, 11899 (1990).
- [95] R. Natoli and M. Benfatto, *J. Physique. Coll. C8* **47**, 11 (1986).
- [96] R.D. Cowan, *The Theory of Atomic Structure and Spectra* (Univ. of California Press, Berkeley, 1991).
- [97] F.M.F. de Groot, J.C. Fuggle, B.T. Thole and G.A. Sawatzky, *Phys. Rev. B* **41**, 928 (1990).
- [98] M. Abbate, F.M.F. de Groot, J.C. Fuggle, A. Fujimori, Y. Tokura, Y. Fujishima, O. Strebel, M. Domke, G. Kaindl, J. van Elp, B.T. Thole, G.A. Sawatzky, M. Sacchi and N. Tsuda, Submitted to *Phys. Rev. B*.
- [99] F.M.F. de Groot, J.C. Fuggle, B.T. Thole and G.A. Sawatzky, *Phys. Rev. B* **42**, 5459 (1990).
- [100] F.M.F. de Groot, M. Grioni, J.C. Fuggle, J. Ghijsen, G.A. Sawatzky and H. Petersen, *Phys. Rev. B* **40**, 5715 (1989).
- [101] C. Palache, H. Berman and C. Frondel, (John Wiley, London, 1944), page 834.
- [102] W.H. Newhouse, *Bul. Geol. Soc. Am.* **47**, 1 (1936).
- [103] C.L. Silva, *Com.Serv. Geol. Portugal*, **LXII**, 35 (1977).
- [104] C.L. Silva, private comm.
- [105] C.L. Silva and M.L. Ubaldo, *Sor. Geol.* **8**, 1 (1985).
- [106] A. Machado-Corta, *Inventory of Minerals: Mineralogical and Geological Museum, Lisbon University, Portugal* (1936), page 361.
- [107] M. Horn, C.F. Schwerdtfeger and E.P. Maegher, *Z. Krist.*, **136**, 273 (1972).
- [108] D.T. Cromer and K. Herrington, *J. Am. Chem. Soc.* **77**, 4708 (1955).
- [109] W.H. Baur, *Acta Cryst.* **14**, 214 (1961).
- [110] B.A. Wechsler and C.T. Prewitt, *Am. Min.* **69**, 176 (1984).
- [111] J.A. Speer and G.V. Gibbs, *Am. Min.* **61**, 238 (1976)
- [112] M. Kitamura, M. Tokonami and N. Morimoto, *Contr. Min. and Petr.* **51**, 167 (1975).
- [113] M. Kitamura and M. Tokonami, *Tohoku University Science Reports* **11**, 125 (1971)

- [114] F.C. Hawthorne and H.D. Grundy, *Min.Mag.* **39**, 390 (1973)
- [115] G.A. Novak and G.V. Gibbs, *Am. Min.* **56**, 791 (1971)
- [116] J. Lima de Faria, *Estud. Ens. e Doc.* **112**, 1 (1964)
- [117] M. Grioni, M.T. Czyżyk, F.M.F. de Groot, J.C. Fuggle and B.E. Watts, *Phys. Rev. B.* **39**, 4886 (1989).
- [118] O. Durmeyer, J.P. Kappler, E. Beaurepaire, J.M. Heintz and M. Drillon, *Conf.Proc. Vol 25, "2nd European Conference on Progress in X-ray Synchrotron Radiation Research*, Eds. A. Balerna, E. Bersiani and S. Mobilio, (SIF, Bologna, 1990).
- [119] F. Al-shamma and J.C. Fuggle, *Physica C.* **169**, 325 (1990).
- [120] F. Sette, B. Sinkovic, Y.J. Ma and C.T. Chen, *Phys. Rev. B.* **39**, 11125 (1989).
- [121] M. Abbate, J.B. Goedkoop, F.M.F. de Groot, M. Grioni, J.C. Fuggle,, S. Hoffman, H. Petersen, and M. Sacchi; submitted.
- [122] S.P. Cramer, O. Tench, M. Yocum and G.N. George *Nucl.Instr. Meth. A.* **266**, 586 (1988).
- [123] S.P. Cramer, S.J. George, H. Kraner, L. Rogers, S. Rescia, V. Radeka, M. Yocum, J. Colaresi, O. Tench and O.C. Mullins, *X-ray Absorption Fine Structure*, Ed. S.S. Hasnain, (Ellis Horwood Publ., Chichester, 1991), page 640.
- [124] A. Taftø, and O.L. Krivanek, *Phys. Rev. Lett.* **48**, 560 (1982).
- [125] K. Tohji and Y. Udagawa, *Phys. Rev. B* **39**, 7590 (1989).

SUMMARY

X-ray absorption experiments on a wide variety of materials have been presented, in an attempt to define which theoretical models are appropriate under which circumstances and to illustrate the range of information which can be obtained from the combination of the new theoretical and experimental possibilities. The x-ray absorption experiments have been performed with the DRAGON monochromator at NSLS-Brookhaven and the SX700 monochromators at BESSY-Berlin. These monochromators reach an unprecedentedly high resolution of $1 : 10^4$ which created the opportunity to detect a great deal of fine structure without which a detailed investigation of the theoretical models would have been impossible.

At the outset of this study various models to explain the x-ray absorption spectral shape were available, but had not been widely tested. As indicated in the motivation, the extreme cases of weakly and strongly correlated systems could be described in great detail, but a large number of materials revealed their limitations. In this study these limitations have been investigated in detail, with the aim to improve the models to explain the spectral shapes of both the metal $2p$ and oxygen $1s$ x-ray absorption edges.

The metal $2p$ x-ray absorption spectra have been interpreted on the basis of a crystal field multiplet model, which originates from the strongly correlated limit in which the dominating local potential (the cubic crystal field) has been included. It has been shown that the crystal field model explains the spectra of $3d$ -metal fluorides in a surprisingly detailed fashion. In case of more covalent materials like the $3d$ -metal oxides the main characteristics have been reproduced, which illustrates the dominance of the core hole multipole interactions. The analysis with the crystal field multiplet model yields important parameters such as the valency of the metal ions (that is the number of filled $3d$ -states), the spin state and the cubic crystal field strength. Additionally polarization dependent measurements yield directional dependent information such as the crystal field parameters of lower symmetries. To simulate covalency effects the Slater integrals can be reduced from their atomic values. This approach has been compared with the more rigorous impurity calculations which include charge transfer-like configuration interaction and it has been found that in the case of divalent nickel halides, Slater integral reduction reproduces correctly the main modifications of the spectral shape. The effects of $3d$ spin-orbit coupling have been shown to be essential for the determination of the spectral shape of divalent cobalt ions, and for trivalent manganese oxides it gives rise to a ground state which is described by an admixture of high-spin and low-spin configurations. The effects of non-cubic symmetries have been investigated with angular dependent measurements. It was found that in case of the calcium $2p$ edges of the CaF_2 the effects of the surface can be explained in detail. Also it has been shown that in case of the layer-compound BaCoF_4 the temperature dependent linear dichroism effects

can be simulated correctly.

In contrast to metal $2p$ x-ray absorption, the oxygen $1s$ x-ray absorption spectra have been interpreted on the basis of one-electron models. The reasons are that the core hole bears no angular momentum, hence there are no multipole interactions, and furthermore the core hole is located on the oxygen, while the $3d$ -states are mainly located on the metal sites. It has been shown that for SrTiO_3 , LaTiO_3 , CuO and LiCoO_2 the ground state density functional calculations reproduce the main features of the spectral shapes. The inclusion of the core hole potential will further enhance the agreement as has been shown for LiCoO_2 . Other approaches are under investigation and specifically the study of the effects of the dd -correlations, which are important for a correct description of the ground state, need more study. However it has been shown that the one electron density of states calculations supply a sufficient basis for a first order interpretation of the spectra. Additionally it has been shown that this analysis yields significant information concerning the electronic structure.

In conclusion it can be stated that the metal $2p$ spectra as well as the oxygen $1s$ spectra of the $3d$ metal oxides yield useful information. The oxygen $1s$ spectra via the one electron interpretation and the metal $2p$ spectra via the analysis with the crystal field multiplet model. Because it has been found that the crystal field multiplet model yields interesting parameters (as indicated above), metal $2p$ x-ray absorption has been applied to other fields of research. Fields of research for which these results can be important include the role of metal-centers in enzymes and other biological materials, the electronic structure of minerals, the design of new ceramics and the electronic structure of surfaces and interfaces. Studies in these fields of research have been performed in collaboration with other groups.

SAMENVATTING

In dit proefschrift wordt verslag gedaan van een röntgenabsorptie onderzoek aan een groot aantal materialen. Door combinatie van nieuwe theoretische en experimentele methoden was het mogelijk om de modellen voor de interpretatie van de spectra aanmerkelijk te verbeteren. De röntgenabsorptie experimenten werden gedaan met de DRAGON monochromator in Brookhaven en de SX700 monochromator in Berlijn. Deze monochromatoren hebben een sterk verbeterde resolutie van 1 op 10.000 en maken het hierdoor mogelijk een grote hoeveelheid aan nieuwe structuren waar te nemen. Zonder deze verbeterde resolutie zou een gedetailleerd onderzoek naar de theoretische modellen onmogelijk zijn geweest.

Bij de aanvang van deze studie waren verschillende modellen om de röntgenabsorptie spectra te verklaren beschikbaar. Echter, deze modellen waren veelal nog niet getoetst aan de praktijk. Zoals is aangegeven in de motivatie konden de extreme gevallen van de zwak en sterk gecorreleerde systemen in detail worden beschreven, maar een groot aantal materialen gaf de beperkingen van deze extremen duidelijk aan. In dit proefschrift worden deze beperkingen in detail bestudeerd, met als doel een betere beschrijving te geven van de vorm van de metaal- $2p$ - alsmede de zuurstof- $1s$ -röntgenabsorptie spectra.

De metaal- $2p$ -röntgenabsorptie spectra zijn geïnterpreteerd met behulp van een kristalveld-multipletmodel. In dit model is naast de atomaire interacties ook de dominante locale kristal-potentiaal meegenomen. Het is aangetoond dat het kristalveld-multipletmodel de spectra van de $3d$ -metaalfluoriden tot in de kleinste details verklaard. In het geval van meer covalente verbindingen zoals oxiden worden de belangrijkste structuren gereproduceerd. Dit geeft aan dat de multipool interacties van het rompgat met de valentie electronen de vorm van het spectrum in hoge mate bepalen. De analyse van het kristalveld-multipletmodel levert belangrijke parameters op, zoals de valentie van het metaalion (dat wil zeggen het aantal gevulde $3d$ -toestanden) de spin-toestand en de sterkte van het kubische kristalveld. Tevens geven polarizatie-afhankelijke metingen hoekafhankelijke informatie, bijvoorbeeld de kristalveldparameters van lagere symmetrieën. Om de effecten van de covalentie in rekening te brengen, kunnen de Slater integralen verkleind worden. Deze methode is vergeleken met de meer algemene onzuiverheidsberekeningen die de interactie van verschillende ladingsoverdracht-configuraties in rekening brengen. Het blijkt dat voor de tweewaardige nikkelhaliden de belangrijkste veranderingen in de vorm van de spectra op de juiste wijze worden beschreven als de Slater integralen worden verkleind. Het is aangetoond dat de effecten van de $3d$ -spinbaan-koppeling essentieel zijn voor de juiste beschrijving van de spectra van de tweewaardige cobaltverbindingen. Tevens zijn het deze spinbaan-koppelingen die in het geval van de driewaardige mangaanoxiden aanleiding geven tot een menging van configuraties van een hoge en een lage spintoestand. Ook zijn de effecten

van niet-kubische symmetriën onderzocht, in het bijzonder met hoekafhankelijke metingen. In het geval van de calcium- $2p$ -spectra van CaF_2 is aangetoond dat de effecten ten gevolge van het oppervlak in detail kunnen worden verklaard. Tevens is aangetoond dat in het geval van de laagverbinding BaCoF_4 , de temperatuurafhankelijke lineaire tweekleurigheids effecten op de juiste manier beschreven kunnen worden.

In tegenstelling tot de metaal- $2p$ -spectra worden de zuurstof- $1s$ -spectra geïnterpreteerd aan de hand van één-electron modellen. De reden hiervoor is dat een $1s$ -rompgat geen hoekmoment heeft hetgeen betekent dat er geen multipool interacties met de valentieband zijn. Bovendien bevindt het rompgat zich op het zuurstof terwijl de $3d$ -toestanden vooral op de metaalionen gelocaliseerd zijn. Het is aangetoond dat de berekeningen van de grondtoestandsdichtheidfunctie de belangrijkste structuren in de spectra kunnen verklaren voor SrTiO_3 , LaTiO_3 , CuO en LiCoO_2 . Als de potentiaal van het rompgat wordt meegenomen treedt een verdere verbetering van deze overeenkomsten op, zoals is aangetoond in het geval van LiCoO_2 . Andere benaderingen worden momenteel onderzocht. Met name de studie van de effecten van de dd -correlaties, die belangrijk zijn voor een juiste beschrijving van de grondtoestand, verdient meer aandacht. Desalniettemin is aangetoond dat de berekeningen van de ééndeeltjes-toestandsdichtheid een voldoende basis geven voor een eerste-orde-interpretatie van de spectra. Daarnaast is aangetoond dat deze analyse belangrijke informatie verschaft inzake de elektronische structuur.

Concluderend kan worden gezegd dat zowel de metaal- $2p$ - als de zuurstof- $1s$ -spectra van de $3d$ -metaaloxiden nuttige informatie verschaffen. De zuurstof- $1s$ -spectra met behulp van de ééndeeltjes interpretatie en de metaal- $2p$ -spectra met behulp van de analyse met het kristalveld-multipletmodel. Omdat (zoals hiervoor is besproken) het kristalveld-multipletmodel interessante parameters oplevert, is naar mogelijkheden gezocht om metaal $2p$ -röntgenabsorptie te gebruiken voor andere gebieden van onderzoek. Onderzoeksgebieden waarvoor de resultaten van belang zouden kunnen zijn, betreffen het onderzoek naar de rol van metaal-centra in enzymen en andere biologische materialen, de studie van de elektronische structuur van mineralen, het ontwikkelen van nieuwe keramische materialen en de studie van de elektronische structuur van oppervlakken en grensvlakken. In samenwerking met andere groepen zijn op deze onderzoeksterreinen röntgenabsorptie experimenten gestart. De voorlopige resultaten hiervan zijn besproken.

LIST OF PUBLICATIONS

J.B. Goedkoop, B.T. Thole, G. van der Laan, G.A. Sawatzky, F.M.F. de Groot and J.C. Fuggle,

Calculations of magnetic x-ray dichroism in the 3d XAS spectra of rare earth compounds
Physical Review B. **37**, 2086 (1988).

P. Kuiper, G. Kruizinga, J. Ghijsen, M. Grioni, P.J.W. Weijs, F.M.F. de Groot, G.A. Sawatzky, H. Verweij, L.F. Feiner and H. Petersen,

X-ray absorption study of the oxygen 2p hole concentration dep. on stoichiometry in $YBa_2Cu_3O_x$,
Physical Review B **38**, 6483 (1988).

S.W. Kortboyer, J.B. Goedkoop, F.M.F. de Groot, M. Grioni, J.C. Fuggle and H. Petersen,

Experimental resolution in soft x-ray monochromators,
Nuclear Instruments and Methods A. **257**, 435 (1988).

M. Grioni, J.B. Goedkoop, R. Schoorl, F.M.F. de Groot, J.C. Fuggle, F. Schäfers, E.E. Koch, G. Rossi, J.-M. Esteva and R.C. Karnatak,

Studies of copper valencies with copper L_3 x-ray absorption spectroscopy,
Physical Review B. **39**, 1541 (1989).

M. Grioni, M.T. Czyżyk, F.M.F. de Groot, J.C. Fuggle and B.E. Watts,

Unoccupied electronic states of CuO: an oxygen 1s x-ray absorption spectroscopy investigation,
Physical Review B. **39**, 4886 (1989).

M. Pedio, J.C. Fuggle, J. Somers, E. Umbach, J. Haase, Th. Lindner, U. Höfer, M. Grioni, F.M.F. de Groot, B. Hilert, L. Becker and A. Robinson,

Covalency in oxygen chemisorption as probed by x-ray absorption,
Physical Review B. **40**, 7924 (1989).

P.E.S. Wormer and F. de Groot,

The potential energy surface of triplet H_3^+ : A representation in hyperspherical coordinates,
Journal of Chemical Physics **90**, 2344 (1989).

F.M.F. de Groot, M. Grioni, J.C. Fuggle, J. Ghijsen and G.A. Sawatzky,
Oxygen 1s x-ray absorption edges of transition metal oxides,
Physical Review B. **40**, 5715 (1989).

F.M.F. de Groot, J.C. Fuggle, B.T. Thole and G.A. Sawatzky,
 *$L_{2,3}$ x-ray absorption edges of $3d^0$ compounds:
 K^+ , Ca^{2+} , Sc^{3+} and Ti^{4+} in O_h (octahedral) symmetry,*
Physical Review B. **41**, 928 (1990).

F.M.F. de Groot, J.C. Fuggle, B.T. Thole and G.A. Sawatzky,
*2p x-ray absorption of 3d transition metal compounds:
An atomic multiplet description including the crystal field,*
Physical Review B. **42**, 5459 (1990).

F.J. Himpsel, U.O. Karlsson, A.B. McLean, L.J. Terminello, F.M.F. de Groot, M. Abbate,
J.C. Fuggle, J.A. Yarmoff, B.T. Thole and G.A. Sawatzky,
Fine structure of the calcium 2p x-ray absorption edge for bulk compounds, surfaces and interfaces,
Physical Review B. **43**, 6899 (1991).

M. Abbate, F.M.F. de Groot, J.C. Fuggle, Y.J. Ma, C.T. Chen, F. Sette, A. Fujimori, Y.
Ueda and K. Kosuge,
Soft x-ray absorption studies of the electronic structure changes through the VO_2 phase transition,
Physical Review B. **43**, 7263 (1991).

F.M.F. de Groot, J.C. Fuggle and J.M. van Ruitenbeek,
Oxygen 1s x-ray absorption of $BaPb_{1-x}Bi_xO_3$,
Physical Review B., accepted for publication.

S.P. Cramer, F.M.F. de Groot, Y. Ma, C.T. Chen, F. Sette, C.A. Kipke, D.M. Eichhorn,
M.K. Chan, W.H. Armstrong, E. Libby, G. Christou, S. Brooker, V. McKee, O.C. Mullins
and J.C. Fuggle,
Ligand field strengths and oxidation states from manganese L-edge spectroscopy,
Journal of the American Chemical Society; accepted for publication.

M. Abbate, F.M.F. de Groot, J.C. Fuggle, A. Fujimori, Y. Tokura, Y. Fujishima, O. Strebel,
M. Domke, G. Kaindl, J. van Elp, B.T. Thole, G.A. Sawatzky, M. Sacchi and N. Tsuda,
*Soft x-ray absorption studies of the location of extra charges induced by substitution in controlled-
valence materials,*
Physical Review B.; accepted for publication.

F.M.F. de Groot, M.O. Figueiredo, M.J. Basto, M. Abbate, H. Petersen and J.C. Fuggle,
2p x-ray absorption of titanium in minerals,
Physics and Chemistry of Minerals; submitted.

M. Abbate, J.B. Goedkoop, F.M.F. de Groot, M. Grioni, J.C. Fuggle, S. Hoffman, H. Petersen, M. Sacchi,
Probing depth of soft x-ray absorption spectroscopy measured in total electron yield mode,
Surface and Interface Analysis; submitted

J. van Elp, J.L. Wieland, H. Eskes, P. Kuiper, G.A. Sawatzky, F.M.F. de Groot, M. Abbate and T.S. Turner,
The electronic structure of CoO, Li doped CoO and LiCoO₂,
Physical Review B.; submitted.

M. Abbate, F.M.F. de Groot, J.C. Fuggle, A. Fujimori, O. Strebler, F. Lopez, M. Domke, G. Kaindl, B.T. Thole, G.A. Sawatzky, M. Takano, Y. Takeda, H. Eisaki, S. Uchida,
Controlled-valence properties of La_{1-x}Str_xFeO₃ and La_{1-x}Str_xMnO₃ studied by soft x-ray absorption spectroscopy,
Physical Review B.; submitted.

Conference Proceedings

F.M.F. de Groot, J.C. Fuggle, B.T. Thole and G.A. Sawatzky,
Ligand field effects in x-ray absorption of 3d transition metal compounds,
2nd European Conference on Progress in X-ray Synchrotron Radiation Research, Rome, November 1989; Eds. A. Balerna, E. Bernieri and S. Mobilio, (SIF, Bologna, 1990); page 51.

F.M.F. de Groot, J.C. Fuggle, B.T. Thole and G.A. Sawatzky,
2p x-ray absorption of 3d transition metal compounds,
X-ray Absorption Fine Structure, Proceedings of XAFS IV Conference, York, August 1990. Ed. S.S. Hasnain, (Ellis Horwood, Chichester, 1991); page 48.

F.M.F. de Groot,
Theory of x-ray absorption: the crystal field multiplet approach,
Selected Experiments in Condensed Matter Physics with Synchrotron Radiation, Ascona, July 1990. Ed. C.J. Czaja, (Birkhäuser Verlag, Basel, 1991)

ACKNOWLEDGEMENTS

There remains the pleasant task of thanking all the persons who helped me so greatly:

In the first place I thank John Fuggle, who gave me as much inspiration for my work as perspiration during it. Thanks to his stimulation and efforts to supply an almost continuous opportunity for international contacts, it became possible to learn so much in such a pleasant way. However, I have to admit there have been days on which I did not obey his motto: 'Good science is achieved by sweating blood every day for years'⁴.

I am greatly indebted to George Sawatzky for his discussions and lectures, which stimulated me to come up with new explanations, that turned out to be not always completely wrong.

Jeroen Goedkoop and Marco Grioni skilfully explained to me the attitude to and performance of synchrotron experiments. Also I would like to thank Jeroen for the many discussions concerning our doubts about, as well as passion for, science.

I would like to thank Theo Thole for his great help on the crystal field multiplet program. Science would be even nicer if more people had Theo's approach to it.

I thank Miguel Abbate for the enjoyable cooperation during our 'synchrotron sessions' in Berlin and Brookhaven. I have learned much from our numerous discussions.

John Inglesfield's stimulating and enthusiastic way of discussing physics is an example for everyone. Also he served as a sharp-eyed critic in the reading of the manuscript.

Much of my work has been made possible through the work of my former colleagues Hans van Acker, Harry Borsje, Pieter Weijs and Jeroen. I would like to thank them, together with John and especially Wiesiek Szweryn, for creating a congenial and stimulating working atmosphere. I would like to thank Ronald Kappert for many discussions and for his great help in introducing me to the world of TEX. Also I would like to thank Klaus Brodt, Jan Vogel, Michiel van Buuren, John Michiels and Leonardo Soriano. I have enjoyed very much the discussions with Susanne Kortboyer and Erwin Lindeyer.

I thank Marek Czyżyk who helped me with the use of his band structure programs.

⁴quoted from a postcard to the group

I would like to thank Jan van Elp, Pieter Kuiper, Jacques Ghijsen, Rudolf Potze, Barry Searle and Henk Eskes from the Groningen group for the numerous collaborations and discussions. It was a pleasure to work with Jan, Pieter and Jacques at the synchrotrons. During our 'synchrotron-experiences' many ideas concerning the interpretation of the spectra were developed and exchanged.

I have drawn from the ideas of Jan Zaanen and Gerrit van der Laan, in discussions as well as in writing.

I thank Jan van Ruitenbeek for the cooperation on the x-ray absorption experiments of the superconductors.

I thank Oliver Strebel, Francesca Lopez, Clemens Laubschatz, Michael Domke and Prof. Kaindl from the Freie Universität Berlin, for their hospitality and help during the experiments with the SX700(II) monochromator at BESSY. Also I thank the staff of BESSY for their help during our experiments. Especially I would like to thank Dr. W. Braun and Dr. H. Petersen.

I thank Alain Fontaine, Maurizio Sacchi, Susana Gota, Marie-Emanuelle Couprie and Helio Tolentino from LURE, for their hospitality and nice dinners during my visits to Paris. Special thanks to Helio, Susana and Francesca who became dear friends.

I have enjoyed the collaboration with Christian Brouder. I also would like to thank Stumm von Bordwehr for his 'history' and Gerard Krill for his enthusiasm.

I thank Olle Gunnarsson for his hospitality and help during my stay in Stuttgart.

Special thanks to Steve Cramer for the pleasure of working with him on the bioinorganic studies. Also I would like to thank him for his kind hospitality during my stay in Brookhaven.

I thank Yan-Jun Ma, Francesco Sette, Chien-Te Chen and Boris Sinkovic from AT&T Bell Labs. for their support and our discussions during the experiments with the DRAGON monochromator at Brookhaven.

I thank Franz Himpsel for the enjoyable cooperation on the interpretation of the CaF_2 -data and for his hospitality during my visit to IBM Yorktown Heights.

With pleasure I thank Marie-Ondina Figueiredo and Marie-João Basto for the cooperation on the x-ray absorption experiments of minerals. Also I would like to thank them very much for their kind hospitality during my stay in Lisboa, where I enjoyed the fortunate opportunity to learn as much about mineralogy as about Portugal.

Metal 2p x-ray absorption spectra

Potassium	Page	Manganese	Page
KBr	53	$K_4Mn(CN)_6$	185
KCl	53	$LaMnO_3$	147
KF	53	$La_{1-x}Sr_xMnO_3$	147
KI	53	$LiMnO_2$	133
Calcium		$LiMn_2O_4$	133
Ca	215	Li_2MnO_3	133
$Ca/(Si(111))$	215	$Mn(acen)(NO_2)$	186
CaF_2	53, 215	MnF_2	64, 184
$CaF_2(111)$	216	$Mn(hl)_2(ClO_4)_2 \cdot H_2O$	186
$CaF_2/Si(111)$	217	MnO	133
CaO	215	$MnO_2(pic)_4$	186
$CaSi_2$	215	MnS	184
Scandium		$(NEt_4)_2MnCl_4$	184
ScF_3	52	Piemontite	186
Sc_2O_3	52	$(pz)_2Mn$	184
Titanium		$(pz)_2Mn(ClO_4)_2$	186
Anatase	206	$SrMnO_3$	147
Augite	207	Iron	
Brookite	206	$LaFeO_3$	148
$CaTiSiO_5$	207	$La_{1-x}Sr_xFeO_3$	148
$FeTiO_3$	50, 206	$SrFeO_3$	148
Ilmenite	206	Cobalt	
Kaersutite	207	$BaCoF_4$	75
$LaTiO_3$	145	CoF_2	64
$La_{1-x}Sr_xTiO_3$	145	CoO	69, 129
Melanite-schorlomite	207	$LaCoO_3$	151
Rutile	206	$La_{1-x}Sr_xCoO_3$	151
$SrTiO_3$	145, 202	$Li_{0.1}Co_{0.9}O$	129
TiO_2	51, 206	$Li_{0.2}Co_{0.8}O$	129
Titanite	207	$LiCoO_2$	129
Vanadium		$SrCoO_3$	151
V_2O_3	162	Nickel	
VO_2	162, 171	$NiBr_2$	85
$VO_2(120^\circ C)$	171	$NiCl_2$	85
V_2O_5	162	NiF_2	85
$Zn_{1-x}Li_xV_2O_4$	164	NiI_2	85
VF_3	64	NiO	85

Oxygen 1s x-ray absorption spectra

Scandium	Page
Sc ₂ O ₃	119
Titanium	
LaTiO ₃	152
La _{1-x} Sr _x TiO ₃	152
SrTiO ₃	94, 152
TiO ₂	119
Ti ₂ O ₃	119
Vanadium	
V ₂ O ₃	119, 163
VO ₂	119, 163
VO ₂ (120°C)	170
V ₂ O ₅	163
Zn _{1-x} Li _x V ₂ O ₄	165
Chromium	
Cr ₂ O ₃	119
Nickel	
NiO	119
Copper	
CuO	96, 119
Others	
BaBiO ₃	193
BaPbO ₃	193
BaPb _{1-x} Bi _x O ₃	193

Manganese	Page
LaMnO ₃	156
La _{1-x} Sr _x MnO ₃	156
LiMnO ₂	140
LiMn ₂ O ₄	140
Li ₂ MnO ₃	140
MnO	140
MnO ₂	119
SrMnO ₃	156
Iron	
Fe ₂ O ₃	119
Fe ₃ O ₄	119
LaFeO ₃	158
La _{1-x} Sr _x FeO ₃	158
SrFeO ₃	158
Cobalt	
CoO	69, 138
LaCoO ₃	151
La _{1-x} Sr _x CoO ₃	151
Li _{0.1} Co _{0.9} O	138
Li _{0.2} Co _{0.8} O	138
LiCoO ₂	138
SrCoO ₃	151

CURRICULUM VITAE

Born in Eindhoven on Februari 10 1964, I lived the first 18 years in Nuenen and enjoyed high school at the Augustinianum in Eindhoven, where I passed the Atheneum exam June 1982.

I studied chemistry at the Catholic University of Nijmegen and passed the doctoral exam in June 1987, with specializations theoretical chemistry, molecular spectroscopy and philosophy of science. The last four years I worked in the group Spectroscopy of Solids and Surfaces of Prof. J.C. Fuggle. The subject of my study has been the use of x-ray absorption spectroscopy, and for this purpose I performed experiments at the synchrotrons in Berlin, Orsay and Brookhaven.

